Albumin Conjugated Upconversion Nanoparticles for Photodynamic Therapy Applications

Tarek Sabri

A Thesis
In
The Department
of
Chemistry and Biochemistry

Presented in Partial Fulfillment of the Requirements
For the Degree of
Doctor of Philosophy (Chemistry) at
Concordia University
Montreal, Quebec, Canada

January, 2022

© Tarek Sabri, 2022

CONCORDIA UNIVERSITY

SCHOOL OF GRADUATE STUDIES

This is to certify that the thesis prepared

By: **Tarek Sabri**

Entitled: **Albumin Conjugated Upconversion Nanoparticles for Photodynamic Therapy Applications**

and submitted in partial fulfillment of the requirements for the degree of

Doctor Of Philosophy (Chemistry)

complies with the regulations of the University and meets the accepted standards with respect to originality and quality.

Signed by the final examining committee:

_____Chair
Dr. Virginia Penhune

_____ External Examiner
Dr. Marco Bettinelli

_____ External to Program
Dr. William Bukowski

_____ Examiner
Dr. Christine DeWolf

_____ Examiner
Dr. Pat Forgione

_____Thesis Supervisor
Dr. John A. Capobianco

_____Thesis Co-Supervisor
Dr. Peter D. Pawelek

Approved by _____
Dr. Yves Gelinas, Graduate Program Director

February 1, 2022

_____
Dr. Pascale Sicotte, Dean Faculty of Arts and Science

ABSTRACT

Albumin Conjugated Upconversion Nanoparticles for Photodynamic Therapy Applications

Tarek Sabri, Ph.D.

Concordia University, 2022

Photodynamic therapy (PDT) is the least invasive therapeutic procedure that can exert a selective cytotoxic activity toward malignant cell. The procedure involves administration of photosensitizer, a light absorbing molecule, that upon irradiation by a specific wavelength will produce reactive singlet oxygen that induces cell death or tissue damage. Major limitations include poor selectivity of photosensitizers toward tumors, and radiation using visible light that weakly penetrates tissues. Hence, effectiveness of PDT is limited to superficial treatments, and its validity to treat deeper tissues is very limited.

Lanthanide upconverting nanoparticles (Ln-UCNP) are efficient energy transducers that can absorb light efficiently in the near infrared (NIR), while emitting *via* the process of upconversion in the UV-VIS-NIR regions of spectrum. NIR light excitation permits light penetration deeply in tissues, without causing any photodamage to biological entities. However, any foreign entity entering the body are coated by group of serum proteins (coronas). This will result in aggregation that might induce toxicity or change circulation fate of the nanoparticles lowering PDT efficacy. Albumin (ALB) the most abundant protein in serum, has been approved as a passive drug delivery loading modality. Herein, A modified version of desolvation method

was developed to render Ln-UCNPs ($NaGdF_4$: Yb^{3+}, Er^{3+}) dispersible in biological relevant media and biocompatible for PDT. The approach generated a uniform ~2 nm thick shell with approximately 112 molecules of ALB were present to cover 15290 nm^2 area of single $NaGdF_4$: Yb^{3+}, Er^{3+}. Additionally, Rose Bengal (RB) photosensitizer was structurally modified, and energy transfer of different RB loaded on $NaGdF_4$: Yb^{3+}, Er^{3+} surface was studied under 980 nm irradiation. Further, *in vitro* studies using human alveolar lung cancer cells (A549) showed that RB presence solely allowed cellular internalization of ALB coated $NaGdF_4$: Yb^{3+}, Er^{3+}. Also, cellular toxicity was induced under 980 nm excitation within a period of 10-minute exposure time.

New model of ALB conjugated to Ln-UCNPs is also developed. Bifunctional linker possessing maleimide group grafted on $NaGdF_4$: Yb^{3+}, Er^{3+} surface, and employed to target thiol group present on ALB cysteine 34. Albumin presence rendered Ln-UCNPs biocompatible and dispersible in aqueous environment and permitted the loading of different RB concentrations. Spectrophotometric analysis of the RB photoreaction processes identified both type I & II energy transfer mechanism, through the release of hydroxyl radical ($HO^{\bullet}$) , and $^1O_2$ respectively.

In vitro evaluation of the cellular activity of ALB presence on $NaGdF_4$: Yb^{3+}, Er^{3+} revealed a substantial selective cellular internalization effect using glioblastoma tumor cells (U251N), in comparison to A549 cells. Further, cellular toxicity assay of the nanoconstruct using U251N irradiated with 980 nm, revealed an intense cellular toxicity effect as a result of the enhanced cellular uptake, and the release of various toxic reactive oxygen radicals. Thus, RB modified ALB-$NaGdF_4$: Yb^{3+}, Er^{3+} provided biocompatible surface coating, targeting and cytotoxicity capabilities that all enhance PDT efficacy.

ACKNOWLEDGMENTS

First, Thank God I made it to this point healthy especially during the hard time we encountered with COVID-19 outbreak.

I want to thank my professor John A. Capobianco for the opportunity and his guidance through all my PhD program. Prof. Capobianco considered us as family in his lab and make every effort for all lab members to be successful. Prof. Capobianco is open to new ideas, and research methodologies that extended our knowledge in the field. He was always pleased to assist, discuss, and edit our research outcome. Also, he always adds his personal insights to our work that levitates our learning experience. Especial thank to my co-supervisor Prof. Peter Pawelek to his support that dates back when I was undergraduate student at Concordia university. I want to thank my committee members Prof. Christine DeWolf, and Prof. Pat Forgione to their support, insights, and guidance during my program.

Concordia colleagues and lab members. The list is huge and I hope I do not miss anyone. Prof. Capobianco group past and current members, especially Dr. Gabriella Tessitore, Steven Maurizio, and Gabriella Mandle for their support and the research we carried out together. Especial thank to Prof. Forgione group for their organic chemistry insights by Dr. Franklin Chacon-Huete, and Dr. Mohammad Askari. I also want to thank, Prof. John Oh and his group particularly my friend Dr. Arman Moini Jazani for their kindness and assisting in using lab equipment.

Especial thank to the hidden person that was a part of all our research, Dr. Jean-Philippe Masse at the Centre for Characterization and Microscopy of Materials $(CM)^2$ at university of Montreal for TEM analysis, imaging, and training. I want to thank Dr. Min Fu molecular imaging at McGill University Health Center for her kindness in assisting in using the cell imaging platform.

To my lovely family Captain Imad Sabri, Ali and Hiba for their support during my program. To an equally contributing person of this work my dear lovely hard working mother for her assistance, management, prayers, and blessings that without her this work couldn't be done.

TABLE OF CONTENT

ABSTRACT III
AUTHORS CONTIBUTIONS X
LIST OF FIGURES XIII
LIST OF SCHEMES XVIII
LIST OF TABLES XIX
Chapter 1. Introduction 1
1.1 Lanthanide Theory 1
1.1.1 Rare earth Elements (Lanthanides) 1
1.1.2 Lanthanides Doped Upconverting Nanoparticles (Ln-UCNPs) 2
1.1.3 Multiphoton upconversion mechanisms 4
1.1.4 Upconversion luminescence efficiency 6
1.2 Photodynamic therapy history 10
1.2.1 Oxygen Excited States 10
1.2.2 Photosensitizers (PS) 11
1.2.3 Photosensitizer activation 14
1.2.4 Light Penetration Depth 15
1.3 Literature Review 18
1.3.1 Nanocarriers in PDT 18
1.3.2 Ln-UCNPs $NaGdF_4$: Yb^{3+}, Er^{3+} 19
1.3.3 Ln-UCNPs surface coating strategies (approaches) for PS loading 21
1.3.4 Delivery modes of NP in vivo 25
1.3.5 Protein Corona and NP delivery 33
1.3.6 Albumin 35
1.4 Statement of the problem 38
Chapter 2. Dual Activity of Rose Bengal Functionalized to Albumin-Coated Lanthanide-Doped Upconverting Nanoparticles: Targeting and Photodynamic Therapy 40
2.1 Abstract 41
2.2 Introduction 42
2.3 Results and Discussion 45
2.4 Experimental Section 55
2.4.1 Synthesis of $NaGdF_4$: Yb^{3+}/Er^{3+} (Ln-UCNPs) 55

2.4.2 Transmission electron microscopy and negative staining 56
2.4.3 X-Ray powder diffraction 57
2.4.4 Bovine serum albumin (BSA) coated $NaGdF_4$: Yb^{3+}/Er^{3+} 57
2.4.5 Thermogravimetric Assay (TGA) 57
2.4.6 Primary amine quantification 58
2.4.7 Luminescent intensity $NaGdF_4$: Yb^{3+}/Er^{3+} 58
2.4.8 Rose Bengal linker addition, and surface conjugation 59
2.4.9 Energy transfer measurements 59
2.4.10 Singlet oxygen measurement 60
2.4.11 In vitro localization assay 60
2.4.12 Cell viability assay 60
2.5 Supporting Information 62
Chapter 3. Selective glioblastoma cellular uptake of upconverting nanoparticles using an albumin-based targeted PDT surface coating 68
3.1 Abstract 69
3.2 Introduction 70
3.3 Results and Discussion 72
3.4 Experimental Procedures 80
3.4.1 Materials 80
3.4.2 Thermal Decomposition Synthesis of $NaGdF_4$: Yb^{3+}, Er^{3+} 80
3.4.3 Transmission electron microscopy (TEM) 81
3.4.4 X-ray Powder Diffraction 81
3.4.5 $NaGdF_4$: Yb^{3+}, Er^{3+} upconversion emission spectra 81
3.4.6 Oleate removal and linker coordination on $NaGdF_4$: Yb^{3+}, Er^{3+} 82
3.4.7 Fourier transform infrared spectroscopy (FT-IR) 82
3.4.8 BSA surface coupling, and Rose Bengal photosensitizer loading 83
3.4.9 Tryptophan emission spectra 83
3.4.10 Thermogravimetric analysis of surface ligand 83
3.4.11 Energy transfer measurements 83
3.4.12 Singlet oxygen detection 84
3.4.13 Free Radicals detection with Electron paramagnetic resonance spectroscopy (EPR) 84
3.4.14 In vitro localization assay 85

3.4.15 Cell viability assay 85
3.5 Supporting Information 86
Chapter 4. An intense, narrow, and sharp blue light emissive band from ultra-small lanthanides upconversion nanoparticles with active and inert shells 92
4.1 Abstract 93
4.2 Introduction 94
4.3 Discussion 96
4.4 Experimental Procedures 103
4.4.1 Synthesis Core $NaGdF_4$: 20 % Yb^{3+}, 0.5 % Tm^{3+} 103
4.4.2 Synthesis of First Active Shell $NaGdF_4$: 20 % Yb^{3+} 103
4.4.3 Synthesis of Second Inert shell $NaYF_4$ 104
4.4.4 X-Ray Powder Diffraction 104
4.4.5 Transmission Electron Microscopy 104
4.4.6 Emission Spectra and Excited State Decay Times of Upconverting nanoparticles 104
4.4.7 Oleate removal and Riboflavin coating 105
4.4.8 Thermogravimetric assay 105
4.4.9 Singlet Oxygen generation and detection 105
4.5 Supporting Information 106
Chapter 5. Conclusions 112
Chapter 6. Future Directions 116
APPENDIX 119
REFERENCES 212

AUTHORS CONTIBUTIONS

Manuscript 1: "Dual Activity of Rose Bengal Functionalized to Albumin-Coated Lanthanide-Doped Upconverting Nanoparticles: Targeting and Photodynamic Therapy"

T. Sabri: Experimental work and manuscript preparation

P. D. Pawelek: project collaborator

J. A. Capobianco: project supervisor

Manuscript 2: "Selective glioblastoma cellular uptake of upconverting nanoparticles using an albumin-based targeted PDT surface coating"

T. Sabri: Experimental work and manuscript preparation

G. A. Mandl: Carried EPR measurments

P. D. Pawelek: project collaborator

J. A. Capobianco: project supervisor

Manuscript 3: "An intense, narrow, and sharp blue light emissive band from ultra-small lanthanides upconversion nanoparticles with active and inert shells"

T. Sabri: Experimental work and manuscript preparation

S. Maurizio: Lifetime measurments, and assisted in discussion

J. A. Capobianco: project supervisor

Additional Publications (Appendix)

Manuscript 4: "Intrinsic Time-Tunable Emissions in Core-Shell Upconverting Nanoparticle System"

Gabriella Tessitore: Spectroscopy measurements and manuscript preparation

S. Maurizio: Spectroscopy measurements and manuscript preparation

T. Sabri: Nanoconstructs design and characterization, and manuscript preparation

J. A. Capobianco: project supervisor

Manuscript 5: "The key role of intrinsic lifetime dynamics from upconverting nanosystems in multi-emission particle velocimetry"

Gabriella Tessitore: Experimental work and manuscript preparation

S. Maurizio: Aided in spectroscopy measurments

T. Sabri: Nanoconstructs design and characterization

C. D. Skinner: project collaborator

J. A. Capobianco: project supervisor

Manuscript 6: "Wavelength-Selective Nonlinear Imaging and Photo-Induced Cell Damage by Dielectric Harmonic Nanoparticles"

G. Campargue: aided in experimental work

I. Fureraj: aided in experimental work

S. Sakong: aided in experimental work

T. Sabri: Aided in nanoparticles synthesis, generated surface coatings, characterization

F. Riporto: aided in experimental work

A. Vieren: aided in experimental work

Y. Mugnier: aided in experimental work

C. Mas: aided in experimental work

D. Staedler: aided in experimental work

J. M. Collins: aided in experimental work

L. Bonacina: project collaborator

A. Vogel: aided in experimental work

J. A.Capobianco: project collaborator

J. P. Wolf: project collaborator

V. Kilin: Project Supervisor

LIST OF FIGURES

Figure 1.1 Dieke diagram for $4f^n$ energy levels of Ln^{3+} in $LaCl^{3+}$ 3

Figure 1.2 Schematic representation of upconversion excited state absorption (ESA) mechanism5

Figure 1.3 Schematic representation of energy transfer upconversion (ETU) mechanism. 5

Figure 1.4 Host lattice influence on the phonon energy of Ln^{3+}dopant ion 8

Figure 1.5 Oxygen electronic configuration with two excited singlet states and their corresponding energy above ground triplet state. 11

Figure 1.6 Backbone structure of porphyrin photosensitizer and its derivatives with π electrons difference highlighted in colors for Chlorin and Bacteriochlorin. 12

Figure 1.7 Energy state diagram illustrating the increasing number of electrons in a ring system is the energy of excited states. N is the number of electrons, and n is the number of excited states. 13

Figure 1.8 Jablonski diagram of excited photosensitizer for the release of reactive singlet oxygen. IC: internal conversion, ISC: intersystem crossing, T_1: triplet state of photosensitizer 15

Figure 1.9 molar absorptivity coefficient of water, oxyhemoglobin HbO_2, and deoxyhemoglobin Hb at different wavelength. 17

Figure 1.10 Different PS loading strategies. (a,d, e) are based are hydrophobic interaction of PS with core NPs. (b,c) hydrophobic or covalent coupling depending in PS 19

Figure 1.11 Upconversion mechanism energy diagram for $NaGdF_4$: Yb^{3+}, Er^{3+} 21

Figure 1.12 Different phosphate surface coated ligand for Ln-UCNPs dispersibility in aqueous media. OPLT: O-phospho-L-threonine 23

Figure 1.13 Surface modification of $NaYF_4$:Yb^{3+}, Er^{3+}@$NaYF_4$ (UCNPs) using Tween 80. (a) Oleate capped UCNP, (b) tween addition, (c) Tween 80 structure with amphiphilic properties. 25

Figure 1.14 Enhanced permeability and retention (EPR) effect diagram showing leaky endothelial cells around tumor site. Non targeted NPs corresponds to passive diffusion with bare surface targeting ligand 26

Figure 1.15 Confocal images of Hela cells. (a) Cells alone, (b) Folate-Ln-UCNPs , (c) Folate-Ln-UCNPs-Dox, (d) 980 nm excited Folate-Ln-UCNPs-Dox. Alexa 488 used for phalloidin staining, DAPI for nucleus [67] 30

Figure 1.16 In vivo fluorescence images of Ln-UCNPs loaded with RGD peptide for tumor targeting and PDT therapy. 1D, 2D, and 7D represents the number of day nanoparticles retained in tumor tissues. 33

Figure 1.17 Protein corona adsorption on the surface of NPs. Stealth coating formed by high affinity protein. Low affinity binding form soft corona with different kinetic (k). and thermodynamic (K) function..... 34

Figure 1.18 Caveolin mediated endocytosis utilizing gp60 for trafficking ALB-NP inside endothelial cells. SPARC released bind ALB-NP near tumor cells for enhanced retention 37

Figure 2.1 Transmission electron microscopy (TEM) of water dispersible BSA conjugated $NaGdF_4$: Yb^{3+}/Er^{3+} (BSA-Ln-UCNPs) 0.1 mg/ml in H_2O. (A,B) BSA coated nanoaggregates of BSA-Ln-UCNPs using desolvating agent with ethanol only. (C,D) BSA-Ln-UCNPs desolvation in presence of 4uL of 8% glutaraldehyde. (E) Negative staining TEM using uranyl formate. (F) High resolution TEM revealing the deposition of 2 nm BSA on the surface. 46

Figure 2.2 Thermogravimetric assay (TGA): (A) Oleate capped $NaGdF_4$:Yb^{3+}/Er^{3+} with a 2.65 % oleate loss between 320-500 ^{o}C. (B) BSA coated $NaGdF_4$: Yb^{3+}/Er^{3+}shows 15.24 % mass loss for a net of 120.6 µg of BSA for 1 mg nanoparticles. 48

Figure 2.3 Circular dichroism (CD) analysis of native BSA shown in red, and BSA-Ln-UCNPs. Two minima between 215-225 nm represents α-helices region. 49

Figure 2.4 Energy transfer spectrum of different RB conjugated to surface of BSA coated $NaGdF_4$: Yb^{3+}/Er^{3+}under 980 nm excitation. Values at the legend represent the concentrations of 1 mg/mL of RB-BSA-Ln-UCNPs in H_2O. 52

Figure 2.5 Confocal images of A549 cancer cell line. All red colored images represent emission from RB with excitation 548 nm, and green images represents emission from Ln-UCNPs with 980 nm excitation. (Top) Localization of modified RB, shown from the merged image RB localize in the cytosol. (Middle) Represent localization of BSA coated NaGdF4: Yb^{3+}/Er^{3+}(BSA-Ln-UCNPs). (Bottom) RB-BSA-Ln-UCNPs localization, merged image show that RB-BSA-Ln-UCNPs localize inside the cells occupying the cytosol of A549 cells..... 53

Figure S 2.1 X-ray powder diffraction pattern of $NaGdF_4$: Yb^{3+}/Er^{3+} (Black). Spectrum comparisons are drawn to reference hexagonal and cubic phases shown in red and blue respectively. 62

Figure S 2.2 TEM image of $NaGdF_4$: Yb^{3+}/Er^{3+} ,1% solution in Toluene. Average size of the particle is 78 nm +/-2.9 nm (scale 500 nm). 63

Figure S 2.3 Luminescent intensity measurements using 980 nm excitation. Same concentration of BSA coated $NaGdF_4$: Yb^{3+}/Er^{3+}used for both measurements (1mg/ml). In red sample in D_2O, and black in H_2O..... 64

Figure S 2.4 MALDI-MS for hexanoic acid modified RB. (M-H) ionization peak at 1086.6421 represents the expected molecular weight for the modified RB. 65

Figure S 2.5 Overlap spectrum of $NaGdF_4$: $Yb^{3+}/Er^{3+}$and RB. Luminescence emission using 980 nm excitation shown in black, and RB absorption shown in red. 65

Figure S 2.6 TNBS assay for primary amine quantification. Lysine used as standard with different concentrations. BSA-Ln-UCNPs (1 mg/ml, H_2O) unknown primary amine concertation shown in red. 66

Figure S 2.7 DPBF absorption decrease as a function of irradiation time using 980 nm. 1mg/ml nanoparticles in deuterated DMSO and D_2O (1:1) with 35 µM DPBF. 66

Figure S 2.8 Viability assay of A549 cell using different concentrations of RB-BSA-Ln-UCNPs. Blue columns without irradiation, and red columns under 980 nm excitation for 10 minutes period, using A549 cells. Four different concentrations 10, 40, 100, and 250 µg of nanoconstruct used.67

Figure 3.1 (A) TEM image of oleate capped UCNPs (NaGdF4: Yb^{3+} , Er^{3+}) 1 $mg.mL^{-1}$ dispersed in toluene. UCNPs measured between two opposite vertices giving average size distribution of 31.3 ± 1.6 nm as shown in the blue. (B) Thermogravimetric assay (TGA) in red MA-UCNPs, 6-maleimidohexanoic acid linker conjugated to NaGdF4: Yb^{3+}, Er^{3+} with a 1.29 % mass loss. Black curve represents albumin (ALB) conjugated with MA-UCNPs with a 3.86 % mass loss..... 73

Figure 3.2 (A) Energy transfer emission spectra of ALB conjugated UCNPs (ALB-UCNPs), and in the presence of different RB concentrations using 980 nm irradiation. Values at the legend corresponds to 2 mg.mL-1 nanoparticles in PBS solution, and the number of RB molecules present in a single nanoparticles(RB-ALB-UCNP). (B) Electron paramagnetic resonance of RB-ALB-UCNP with DMPO spin trap and the corresponding stimulated adducts..... 74

Figure 3.3 First row for each section (A,B, and C)represent confocal image of A549 , and second raw U251N. Blue color is the nuclei stain using DAPI, Green represents emission from UCNPs excited with 980 nm, and in Red is RB emission using 548 nm excitation. 200 $\mu g.mL^{-1}$ (of nanoconstruct is used. (A) cellular localization of ALB-UCNPs, F-merged represent fluorescent merged images. Overlay, is the merged images including bright field showing internalization of ALB-UCNPs into the cytosol. (B) cytosolic localization or RB without the nanoconstruct. (C)

Represent RB-ALB-UCNPs localization, where cell uptake noticed for merged U251N image. Scale bar shown in white represents 10 μm 76

Figure S 3.1 X-ray powder diffraction of $NaGdF_4$: Yb^{3+}, Er^{3+} compared to hexagonal phase pattern (JCPDS card 27-0699) in blue, and cubic phase pattern in red (JCPDS card 27-0697). All diffraction are assigned to the hexagonal β-phase. 86

Figure S 3.2 FT-IR spectroscopy (Black) 6-maleimidohexanoic acid (MA), (Red) $NaGdF_4$: Yb^{3+}, Er^{3+} conjugated with MA. All measurements were performed on powder samples. The free MA exhibits an intense carbonyl stretch at 1693 cm^{-1} which splits into two bands when conjugated on the UCNP surface, attributed to symmetric (υ_s) and asymmetric (υ_{as}) carboxylate stretches at 1578 cm^{-1}, and 1443 cm^{-1} respectively. Maleimide group stretching modes of C-N (υ_s 1405 cm^{-1}, υ_{as} 1109 cm^{-1}), and =C-H bending modes (830 cm^{-1}) are also observed for both coordinated and free MA confirming linker coordination 87

Figure S 3.3 Tryptophan fluorescence of native albumin (red) and ALB-MA-UCNPs (black) under λ_{exc} 280 nm in PBS buffer at pH 7.4. 87

Figure S 3.4 A) Emission spectrum of UCNPs (black) irradiated at 976 nm, and RB absorbance shown in red. B) Energy level diagram showing the upconversion process of $NaGdF_4$: Yb^{3+}, Er^{3+} nanoparticles. 88

Figure S 3.5 Calibration curve of RB concentrations with corresponding RB UV-vis absorption spectra shown in the inset. 88

Figure S 3.6 DPBF absorption spectra as a function of irradiation time at 976 nm of 2mg.mL^{-1} of RB-ALB-UCNPs dispersed in PBS solution. (A) without sodium azide. (B) with 20 mM sodium azide. (C) Percentage decrease of the maximum absorbance for A and B. 89

Figure S 3.7 A) confocal images of z-stack using U251N cells treated with ALB-UCNPs for 4 hours. B) Orthogonal projections representing cross sectional slices obtained from z-stack with 9 μM depth. Green is emission from ALB-UCNPs excited with 980 nm, with DAPI in blue as nuclear stain. 90

Figure S 3.8 Cell viability assays of different RB-ALB-UCNPs using U251N cancer cells without irradiation (blue) and with 976 nm irradiation (red). 91

Figure 4.1 (A) Studied nanoparticle compositions. (B) Particle size distributions. (C-F) Transmission electron microscopy images (TEM) of (C) $NaGdF_4$: Yb^{3+}, Tm^{3+} ,(D) $NaGdF_4$: Yb^{3+},

Tm^{3+} @ $NaGdF_4$: Yb^{3+} ,(E) $NaGdF_4$: Yb^{3+}, Tm^{3+} @ $NaGdF_4$: Yb^{3+} @ $NaYF_4$ and (F) High resolution dark field TEM image of "E"..... 96

Figure 4.2 Upconversion emission spectra of different nanoparticles under 980 nm excitation in powder..... 98

Figure 4.3 Nanoparticle luminescence decay curves, after a 200 μs pulse of 976 nm irradiation, of the (A) $^1G_4 \rightarrow {}^3H_6$ transition (475 nm) and the (B) $^3H_4 \rightarrow {}^3H_6$ transition (800 nm)..... 100

Figure 4.4 Thermogravimetric assay (TGA) of Riboflavin coated CSS nanoparticles. 45.29 % mass loss corresponding to 455 ug of Rf / 1 mg nanoparticles 102

Figure S 4.1 X-ray powder diffraction of (XRPD) of nanoparticles. C, CS and CSS represent $NaGdF_4$: Yb^{3+}, Tm^{3+} / $NaGdF_4$: Yb^{3+}, Tm^{3+} @ $NaGdF_4$: Yb^{3+} / and $NaGdF_4$: Yb^{3+}, Tm^{3+} @ $NaGdF_4$: Yb^{3+} @ $NaYF_4$ respectively. At the bottom are theoretical patterns of hexagonal and cubic phase. 106

Figure S 4.2 : Energy level diagrams of Yb^{3+}, Tm^{3+} and Gd^{3+}, depicting energy transfer upconversion between Yb^{3+} and Tm^{3+}..... 107

Figure S 4.3 Unit cell parameters and structure of β-$NaGdF_4$..... 107

Figure S 4.4 Emission spectra for all compositions studied, upon 976 nm excitation, normalized to the $^3H_4 \rightarrow {}^3H_6$ transition indicated by the asterisk..... 108

Figure S 4.5 Spectral overlap of CSS nanoparticles emission upon 976 nm excitation shown in black, and riboflavin absorbance in red 109

Figure S 4.6 FTIR of CSS nanoparticles surface coated with phosphate riboflavin. In black native phosphate riboflavin, and Rioflavin coated CSS shown in red 109

Figure S 4.7 DPBF absorption after irradiation of Rf-CSS nanoparticles with 980 nm. 2 mg/mL of nanoparticles are dispersed in (1:1) deuterated DMSO and D_2O in the presence of 37 μM DPBF 110

LIST OF SCHEMES

Scheme 2.1 Graphical content of PDT nanoprobe. Rose Bengal conjugated to albumin $NaGdF_4:Yb^{3+}$, Er^{3+} upconversion nanoparticles. 41

Scheme 3.1 Schematic representation of selective cellular uptake of RB albumin conjugated Ln-UCNPs 69

Scheme 4.1 Graphical representation of sub 10 nm core $NaGdF_4:Yb^{3+},Tm^{3+}$ with active $NaGdF_4:Yb^{3+}$ and inert $NaYF_4$ shell. 93

LIST OF TABLES

Table 4.1 Luminescence decay times from the curves in Figure 3……..100

Table S 4.1 Luminescence rise times from the curves in Figure 3 108

LIST OF ABBREVIATIONS

ESA	Excited state upconversion
ETU	energy Transfer upconversion
FTIR	Fourier transform infrared spectroscopy
HNP	Harmonic nanoparticles
Ln	Lanthanides
Ln-UCNP	Lanthanides upconversion nanoparticles
MALDI-MS	Matrix assisted laser desorption ionization- mass spectrometry
NIR	Near infrared
NP	nanoparticles
PDT	photodynamic therapy
PS	photosensitizer
RB	Rose Bengal
SPARC	Secreted protein acidic and rich in cysteine
TEM	Transmission electron microscopy
TGA	Thermogravimetric analysis
VEGED	Vascular endothelial growth factor
XRPD	X-ray powder diffraction

Chapter 1. Introduction

1.1 Lanthanide Theory

1.1.1 Rare earth Elements (Lanthanides)

Lanthanides (Ln) belong to consecutive elements in periodic table starting from Lanthanum and ending with Lutetium (atomic number Z= 51-57). Scandium and yttrium are included with lanthanides due to the similar electronic configuration. Lanthanides with trivalent oxidation state (Ln^{3+}) are the most stable. The electronic ground state configuration of Ln^{3+} is [Xe]4f^n where n is between 0 and 14. This give large number of electronic configurations of the electrons (n^{th}) in the f orbitals (14! /[n!(14-n)!]). Ln^{3+} are characterized by Xenon (Xe) core with 54 electrons shielding the 4*f* orbital of Ln^{3+} from its external chemical environment, and the partially filled *f* orbitals are not present in the outermost shell. This fact is due to the expansion of the filled $5s^2$ and $5p^6$ subshells exceeding the 4f orbitals [1]. This permits Ln^{3+} to retain free ions optical properties when doped into crystalline materials where the crystal field is minimally affected by the environment. As a result, 4*f*-4*f* transitions exhibit sharp, and narrow emission bands as observed in gas spectra due to the weak crystal field effect on the electronic cloud of Ln^{3+} [1].

The assignment of 4*f*-4*f* energy levels of free Ln^{3+} can be described by the Russel Saunders coupling scheme also known as LS coupling. This simply specifies a coupling scheme of electronic spin and orbital angular momenta. In the case of multi electron atoms where the spin orbit coupling is weak it can be presumed that the orbital angular momenta of the individual electrons add resulting in the total orbital angular momentum, L (S=0, P=1, D=2, F=3, etc.) In addition, the spin angular momenta also couple resulting in the total spin angular momentum, S. The coupling between L and S result in the total angular momentum, J given by J = |L = S|, |L + S - 1|,…..|L-S|

. The labels on the energy level diagram of the lanthanides are based on the Russell Saunders term symbol, $^{2S+1}L_J$. Detailed experimental work was carried by Dieke and coworkers tabulating energy levels of all trivalent ions lanthanides (Figure 1.1) [2]. It is worth mentioning that splitting of the energy levels are influenced with the environment (ligand) that generate a crystal field with less magnitude in comparison to coulombic force (electrostatic interaction), or spin-orbit coupling. The crystal field is in the order of 10^2 cm^{-1} [3].

1.1.2 Lanthanides Doped Upconverting Nanoparticles (Ln-UCNPs)

Ln-UCNPs are luminescent nanocrystals with narrow emission profiles and unique physical and chemical features. Ln-UCNPs are insulators, implying that they possess a large bandgap in which the quantum confinement effect is not observed.

In general, luminescent probes rely on single photon excitation using high energy sources, resulting in Stokes emission of low energy radiation. Although multiphoton luminescence may be possible with quantum dots and dyes, they require a high photon density excitation source. Ln-UCNPs ions can be excited using lower power densities and low energy light, for example Near-infrared (NIR). Using low energy excitation the lanthanides undergo the process of upconversion where low energy light is converted to higher light such UV, visible or NIR (wavelength lower than the excitation source).

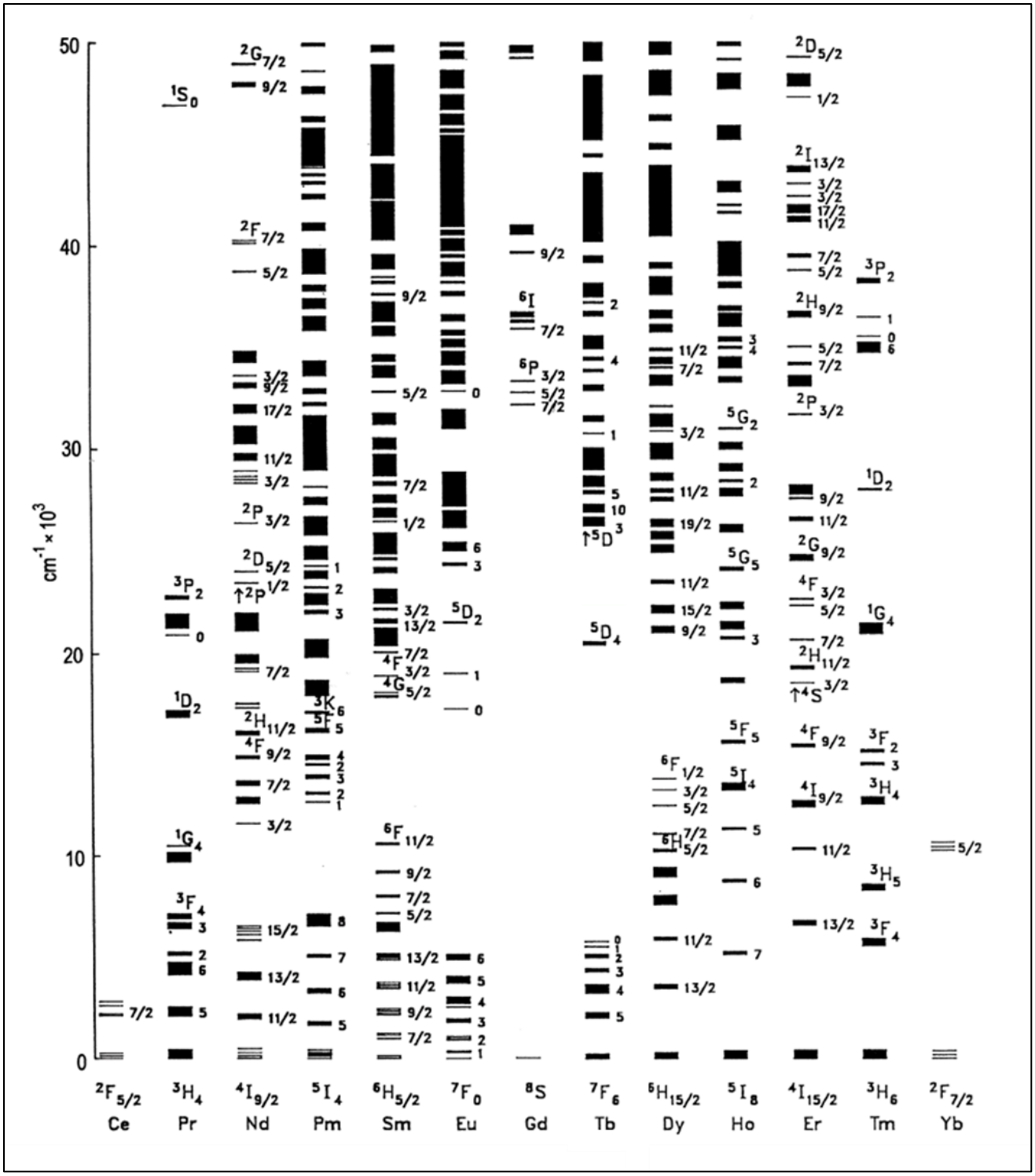

Figure 1.1 Dieke diagram for $4f^n$ energy levels of Ln^{3+} in $LaCl^{3+}$ [1]

1.1.3 Multiphoton upconversion mechanisms

Upconversion can occur *via* two major mechanism: excited state upconversion (ESA), and energy transfer upconversion (ETU).

1.1.3.1 Excited state upconversion (ESA)

Excited state absorption was the first mechanism identified in 1959 by Bloembergen where he proposed that infrared photons could be detected through the sequential absorption within levels of an ion in a solid. The mechanism involves the sequential absorption of two or more photons to promote the ion to an excited state with the subsequent radiative emission to the ground state. The process is initiated with the excitation of a single ion (X) with resonance energy photon matching the energy gap of the ground state (G) and the first excited state E1. E1 is a metastable long lived excited state acting as an energy reservoir permitting sufficient time for second photon to excite the ion from E1 to higher energy level E2 (assuming energy gap of G-E1 matching E1-E2 state) followed by higher energy radiative emission to the ground state (Figure 1.2). Lanthanides are characterized by a ladder like energy level structure with resonant energy gaps between ground state and excited state thus, ESA would be allowed when using a single pump source with resonant energy gap [4].

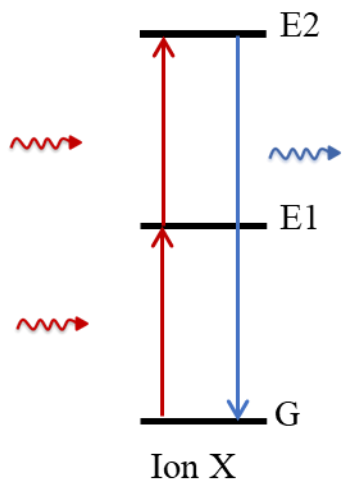

Figure 1.2 Schematic representation of upconversion excited state absorption (ESA) mechanism

1.1.3.2 Energy transfer (ETU)

Energy transfer upconversion was proposed by Auzel and Ovsyankin et al. independently in 1966 [5, 6]. Auzel called it APTE (Addition de Photons par Transferts d'Energie). ETU is a far

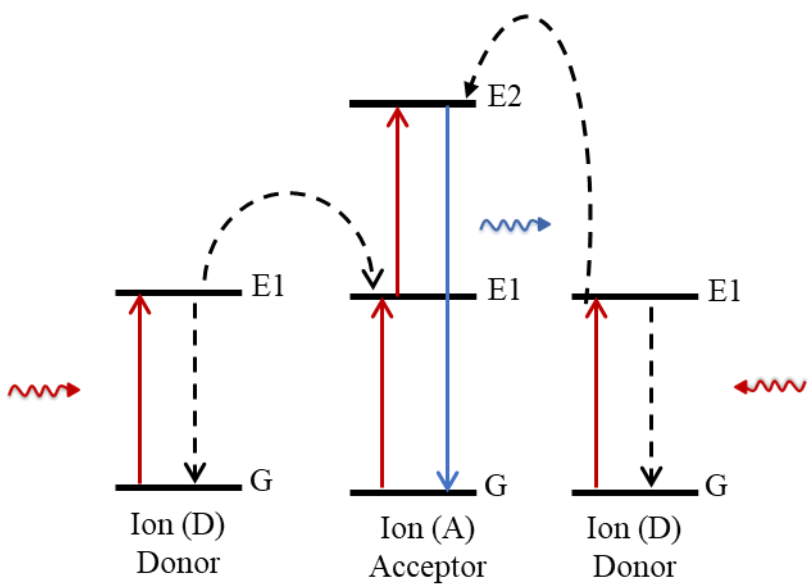

Figure 1.3 Schematic representation of energy transfer upconversion (ETU) mechanism.

more efficient than ESA. The mechanism is shown in Figure 1.3 and is of particular interest in this dissertation. ETU is realized by nonradiative energy transfer between two neighboring ions donor (activator), and acceptors. The first ion is the sensitizer (e.g. Yb^{3+}) also known as the donor, and the second ion is the activator (acceptor) such as, Er^{3+}, Ho^{3+}, Tm^{3+}.The sensitizer possess a high absorption cross section at the excitation wavelength. The initial process is the same as ESA in ground absorption, however, incoming photon populate intermediate states (E1) for both donor and activator ions.

The first radiative process could occur from the acceptor ion (A), where sequential photon absorption from E1 populate ions to E2 in a similar fashion as ESA assuming G-E1, and E1-E2 have same energy gap. The first radiative decay to the ground state occurs from E2 of the A ion alone. The second radiative pathway arise from the non-radiative energy transfer of the excited donor ion (D) metastable E1 state to (A) ion E1. Another incoming photon will pump the ion in (A) to higher energy state E2 where a radiative relaxation could occur from E2-G. The third route depends on the (D) G-E1 and (A) E1-E2, when the energy gap is similar non-radiative energy transfer occur from (D)-E1 to (A)-E2 where a radiative decay to ground state could occur. In ETU, emission intensity from acceptor ion is magnified comparing to ESA, due to the energy loop provided by (D) ion present in host material [7]. The energy transfer processes are based on electric dipole interactions. ETU is on the order of $10^{-3}cm^2/W$ that is two orders of magnitude higher than ESA.

1.1.4 Upconversion luminescence efficiency

1.1.4.1 Host Material Phonon Energy

The most common host used for lanthanide-doped UCNP are fluoride based materials ($NaYF_4$, $NaGdF_4$, and $LiYF_4$). In contrast to oxides and phosphates, fluoride hosts have low

phonon energies. Phonon energy is referred to the resonant oscillation/vibration of atoms in crystal lattice. Phonons are non-radiative energy that directly affect the depopulation of excited states of lanthanides doped in host material. Previously, we described upconversion processes radiative decay to ground state without taking into account the rate of phonon assisted transition (ω) that can affect the radiative relaxation state from different excited state to the ground state as shown in equation (1.1)

$$\omega \propto \exp(-k\Delta E/h\nu_{max}) \qquad (1.1)$$

where k is the Boltzmann constant, ΔE is the energy gap between the excited state and its lowering energy level, and $h\nu_{max}$ represents the phonons linked to the radiative levels [8, 9]. As ΔE increases between excited state of interest (E1-E2), the probability of multi phonon relaxation decreases since more phonons are required to bridge the gap between the two excited state. Thus, phonon assisted transitions (ω) decrease the non-radiative decay from the higher excited state (E2) (Figure 1.4). Fluoride hosts have a phonon energy of 350 cm^{-1}. For example, when E1-E2 transitions possess 1500 cm^{-1} energy gap this require more than four phonons to non radiatively decay from E2-E1 which less likely process to occur. In contrast, high phonon energy crystals such as phosphate (1000 cm^{-1}) require one photon to bridge this gap and quenching the emission from E2. Thus, low phonon energies is essential to minimize the non-radiative relaxation resulting in high upconversion luminescence efficiency [10, 11].

1.1.4.2 Host lattice crystal phase

Crystal field symmetry is one of the major contributors for enhanced upconversion luminescence intensity. Ln^{3+} ions electric dipole transition is parity forbidden ($4f^N$-$4f^N$). The presence of Ln^{3+} ions in low symmetry sites permits the degeneracy of Ln^{3+} ions to be removed.

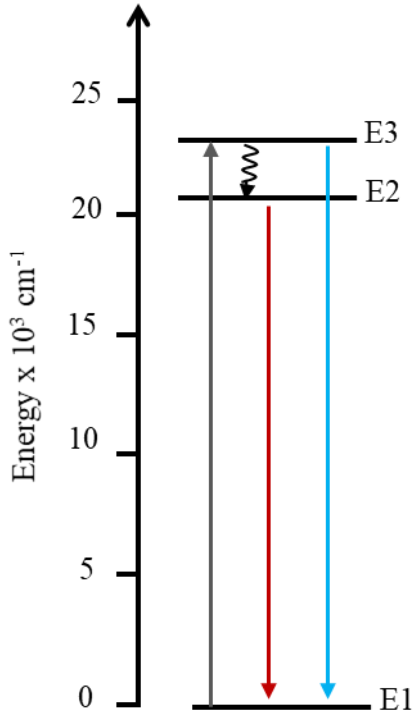

Figure 1.4 Host lattice influence on the phonon energy of Ln^{3+}dopant ion

Ln^{3+} ($4f^N$ state) interact with opposite parity, leading to a mixed parity states where various parity forbidden states become allowed [12]. The outcome of this parity mixing improves optical absorption and emission probabilities in Ln^{3+} [12]. In principle, increasing the degree of asymmetry will enhance parity mixing transition and Ln^{3+} optical activity. For example, the transition of $NaYF_4$ from cubic to hexagonal phase causing the symmetry of Er^{3+} dopants to change from O_h to C_{3h} respectively, permitting 10 fold increase in luminescence intensity under same doping concentration [13, 14].

1.1.4.3 Dopant Concentration

Optimizing Ln^{3+} doping concentrations is one of the major factors that influence the luminescence intensity of a given host. Yb^{3+} is the most used donor ion at a relatively high concentration (20 mol%) compared to acceptors (Er^{3+}, Tm^{3+}, Ho^{3+}) that are sub-2 mol%. Yb^{3+} has the highest absorption cross-section of all lanthanides, with single excited state $^2F_{7/2} \rightarrow {}^2F_{5/2}$ that allows NIR excitation [7]. This unique energy state diminishes cross relaxation effect of neighbouring Yb^{3+} ions present in same host crystals, that results in higher absorption of NIR. In addition, the $^2F_{7/2} \rightarrow {}^2F_{5/2}$ excited state has a phonon energy of 10^4 cm^{-1} compared to 350 cm^{-1} of the fluoride host materials. This huge difference in phonon energy decreases the probability of non-radiative decay to occur, thus enhancing the upconversion luminescence. On the other hand, acceptor ions have many excited states compared to Yb^{3+}. Therefore, at higher doping concentration of the acceptor ion there is an increase in the non radiative resonance energy transfer between similar acceptors (emitting ions), that is a major factor resulting in upconversion quenching [15].

1.2 Photodynamic therapy history

Light as a therapeutic tool has been employed over thousands of years in ancient civilizations such as India, Egypt, and Greek for skin diseases, cancer, rickets, and psychosis treatments [16, 17]. However, the first scientific concept of utilizing light and organic molecules for treatments dates to the accidental discovery made by Oscar Raab a German medical student (1900) studying acridine lethal activities on paramecium [17]. Raab noticed that when performing experiments in the dark, acridine did not demonstrate any adverse effect on paramecium. It took several decades until the milestone of photodynamic therapy (PDT) started by Dr. Thomas Dougherty (1975) at the Roswell Park Cancer institute in U.S.A, Buffalo, NY. Dougherty et al. used hematoporphyrin derivative (HpD) in combination with a red light as an excitation source to induce cytotoxic effect to cure mice carrying mammary tumors [18].

Currently, (PDT) is regarded as the least invasive therapeutic procedure compared to conventional cancer treatments such as chemotherapy or radiotherapy. PDT makes use of three components, light of a specific wavelength, a photosensitizer (**PS**) that is a light sensitive molecule, and oxygen. Individually, these three components are harmless however when combined, the putative cytotoxic reactive oxygen species are generated to induce cytotoxic reactions in the cells *via* apoptosis or necrosis, leading to the self-destruction of tumor cells. Production of free radicals induce vascular distortion resulting in tumor tissue death. Simultaneously, toxic radicals directly eradicate cancer cells by rupturing cell membrane, or internal organelles.

1.2.1 Oxygen Excited States

Molecular oxygen has three electronic configuration that are differ by occupancy of electrons in the π-antibonding orbitals (π^*). In its ground state oxygen is in triplet state $^3O_2$ ($^3\sum_g^-$)

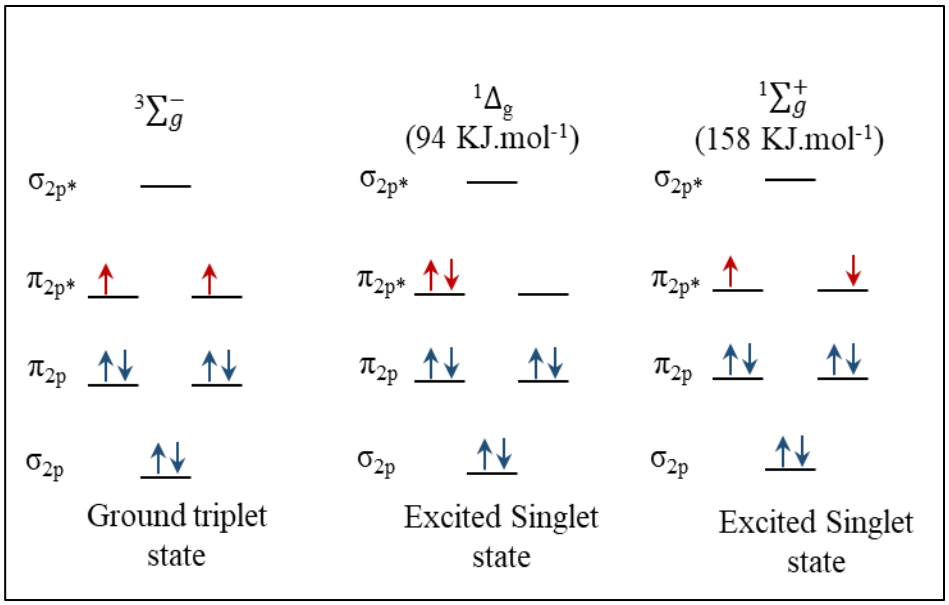

Figure 1.5 Oxygen electronic configuration with two excited singlet states and their corresponding energy above ground triplet state.

where electrons have parallel spin distributed in different π^* orbitals. $^3\Sigma_g^-$ has two low lying excited states differ in electron spin in two degenerate π anti-bonding orbital. The first is $^1\Delta_g$ referred as singlet oxygen ($^1O_2$) where opposite electron spin are residing within the same π^* orbitals. The transition between $^1\Delta_g \rightarrow {}^3\Sigma_g^-$ is spin forbidden, this behaviour generates relatively stable long lived species with life time of 1µs-1ms depending [19]. The second excited state is $^1\Sigma_g^+$ where electrons are in opposite spin in the π^* orbitals (Figure 1.5). The transition of $^1\Sigma_g^+ \rightarrow {}^1\Delta_g$ is spin allowed and short lived with a lifetime below 1ps [20].

1.2.2 Photosensitizers (PS)

PS are light absorbing molecules mainly in the UV-Vis region. PS for PDT are characterized by high absorption coefficient with long lived triplet state lifetime in the µs domain, with an energy gap ($E_T \geq 95$ KJ/mol) matching the oxygen triplet state $^3O_2$. These characteristics will provide efficient energy transfer to neighbouring substrate/oxygen molecules that induces the production of reactive oxygen species (ROS) [21]. Most of the clinically approved PS are classified

mainly as porphyrin or porphyrin like derived compounds such as chlorin, and bacteriochlorin [22]. The backbone skeleton of these PS are derived from blood hemoglobin, consisting of tetrapyrroles with 22 π (porphyrin), 20 π (chlorin), and 18 π (bacteriochlorin) electrons in a highly conjugated heterocyclic macrocycle [22]. This basic structure allows porphyrin PS and its derivatives to acquire long and different wavelength absorption profiles (figure 1.6). All porphyrin PS show a maximum absorption band in the 350-450 nm region known as the Soret band, and weaker Q-bands with absorption bands centered at 630nm, 650 nm, 710 nm for porphyrin, chlorin, and bacteriochlorin, respectively.

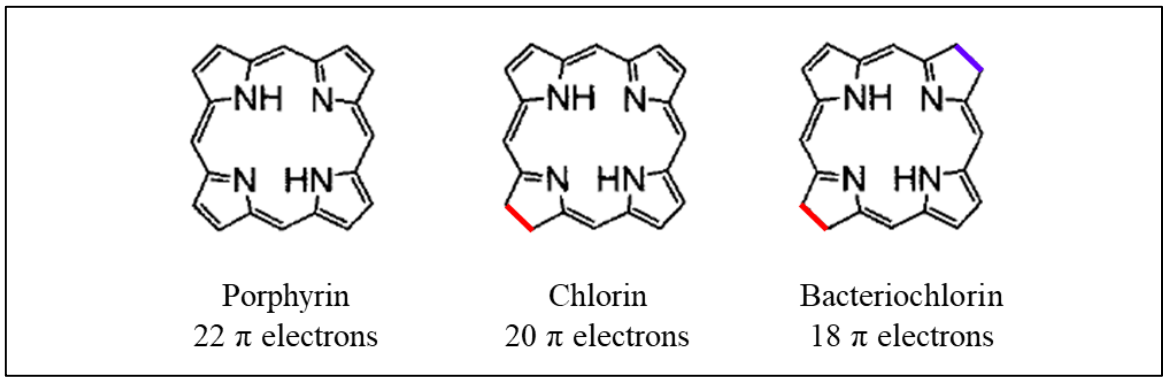

Figure 1.6 Backbone structure of porphyrin photosensitizer and its derivatives with π electrons difference highlighted in colors for Chlorin and Bacteriochlorin.

The difference in maximum absorption profile is a result of different delocalized π electrons present in each derivative, which can be explained by Hoffman square one dimensional potential well [23]. Herein, it is assumed that aromatic ring presence with delocalized π electrons behave as one particle. Energy level (E_n) calculation of different absorption bands could be derived using a square potential in a confined region (L) as shown in equation 1.2

$$E_n = \frac{h^2(n+1)^2}{8\,mL^2} + E(n, N) \qquad (1.2)$$

where h is Plank's constant, n is the energy state valence ensemble electrons, and m is the mass of the electron. E(n, N) is related to electron interaction that cause perturbation to the energy level from ground state (n =0) to higher excited state (n= 1,2,3,..n) in the presence of number of electron (N>1) . This term is equal to zero in the presence of single electron in a potential well. However, E_n increase upon the addition subsequent electrons. Since energy is inversely proportional to wavelength, the presence of high numbers of π electrons require shorter wavelength for exciting PS as shown in figure 1.7.

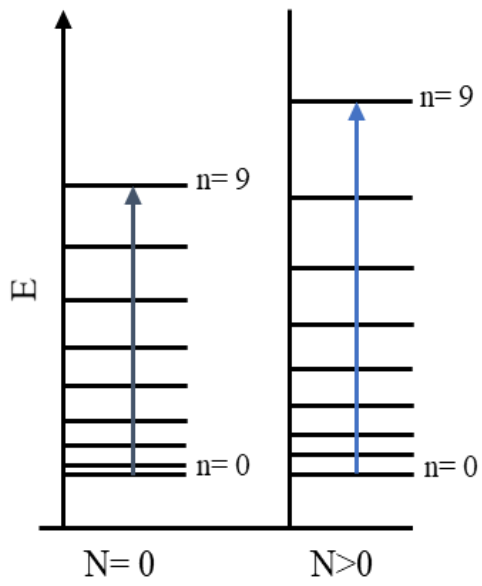

Figure 1.7 Energy state diagram illustrating the increasing number of electrons in a ring system is the energy of excited states. N is the number of electrons, and n is the number of excited states.

As a result, porphyrin with 22 π electrons show a blue shifted (hypsochromic) wavelength absorption compared to chlorin and bacteriochlorin with 20 and 18 π electrons, respectively. Furthermore, porphyrin PS are considered the least cytotoxic compared to other photosensitizers because they are derived from naturally occurring blood hemoglobin. However, porphyrin efficacy is restricted to superficial cancer treatments, due to the need of higher energy radiation for activation [22].

1.2.3 Photosensitizer activation

Photosensitizer activation requires light with appropriate wavelength matching the energy gap of the ground state (S_0) and the higher excited singlet state (S_n). Upon illumination the photosensitizer is excited from the ground state (S_0) to the short lived excited state (S_n) in the nanosecond time domain. The Jablonski diagram in Figure 1.8 shows the electronic states and the radiative and non-radiative transitions that the photosensitizer can undergo: (i) non-radiative vibrational relaxation between two electronic states with the same spin multiplicity known as internal conversion (IC), which occurs on a timescale of 10^{-11} to 10^{-9} s (ii) fluorescence, a radiative transition between two electronic states of the same spin multiplicity, which occurs on a lifetime of 10^{-10} to 10^{-7} s, (iii) intersystem crossing (ISC) a non-radiative transition between two isoenergetic vibrational levels belonging to electronic states of different spin multiplicity (S_1 to the T_1, (iv) phosphorescence, a radiative transition between two electronic states of different spin multiplicity, T_1 to S_0, with lifetimes in the 10^{-6} to 10 s. The excited triplet state may lose its energy either *via* phosphorescence or quenching. The long lifetime of the triplet state allows the photosensitizer to react with surrounding molecules (e.g. oxygen) that generates cytotoxic agents such as singlet oxygen as shown in Figure 1.8, which is known as a Type II photoreaction process [24]. The activated photosensitizer could also undergo a Type I photoreaction, which involves hydrogen atom extraction or electron transfer reactions between the photosensitizer's excited state and a substrate (S) such as biomolecules, to produce radicals and radical ions. These radicals may interact with molecular oxygen to produce superoxide anion or with hydrogen peroxide to produce hydroxyl radical ($HO^{\bullet}$) [25]. These species are cytotoxic and lead to cell death.

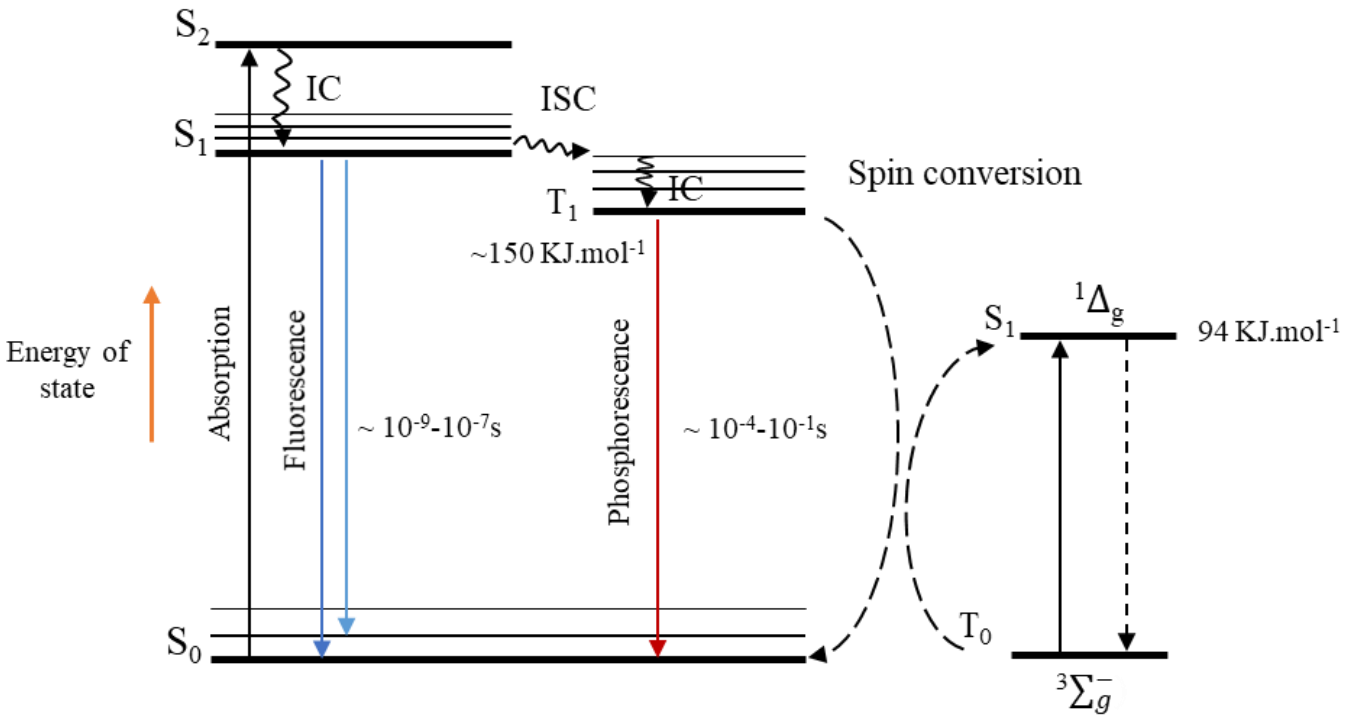

Figure 1.8 Jablonski diagram of excited photosensitizer for the release of reactive singlet oxygen. IC: internal conversion, ISC: intersystem crossing, T_1: triplet state of photosensitizer

1.2.4 Light Penetration Depth

Being able to target tissue at depth is an important consideration in photodynamic therapy to maximize effectiveness. In addition, to the penetration depth of light the wavelength used must meet the requirements for efficient excitation of the photosensitizer. In general, photosensitizers have two main absorptions, the Soret band and the Q-bands. The Soret band is in the 400 nm region and the Q-band in the 630 nm region. Neither of these regions take advantage of the biological optical window (650 to 1000nm). In this region, water, hemoglobin, and oxyhemoglobin show the lowest absorption (Figure 1.9).

As mentioned previously the attenuation of light plays a major role in the effectiveness of photodynamic therapy. Light used to excite the photosensitizer is attenuated at different tissue levels before reaching target site. For instance, illuminating skin tissues with visible radiation, a portion of light is reflected the remaining is absorbed and scattered by biological tissue [26]. The extent of tissue penetration is dependent on the wavelength and optical properties of the illuminated tissue, which is defined as fluence rate depth (Ψ) in a volume of scattering media given by following equations which is derived from diffusion theory [27, 28].

$$\Psi = \psi_0 \frac{e^{-\alpha r}}{r} \qquad (1.3)$$

$$\delta = \alpha^{-1} = [3\mu_a (\mu'_s + \mu_a)]^{-1/2} \qquad (1.4)$$

$$\delta = [3(\mu_a + \varepsilon Cr)(\mu'_s + (\mu_a + \varepsilon Cr))]^{-1/2} \qquad (1.5)$$

Where ψ_0 is standard fluence rate at a given wavelength, (r) is the depth from light source. [α (cm^{-1})] is the attenuation coefficient of light dependent on the nature of the tissue to absorb and scatter light. This is experimentally determined for different biological entities [29, 30] . α is dependent on the sum of all optical absorption coefficients (μ_a) for all tissues and fluids present in a given area such as, hemoglobin oxygenated/deoxygenated, fat, and water content. μ'_s is the reduced scattering coefficient. The inverse of (α) is the attenuation depth [δ (cm)]. The fluence rate is inversely proportional *r*. This implies that as tissues thickness increases (*r*), the light fluence rate become weaker, and the less likely that the photosensitizer is activated. Similarly, to a larger extent, a slight change is the attenuation tissue coefficient which results from an increase in the absorption/scattering (μ_a and μ'_s) will cause exponential decrease of the fluence rate, and an increase in the attenuation depth (δ). However, decreasing δ at a specific distance *r* could be enhanced by utilizing higher concentration (C) of the photosensitizer (Equation 1.5) [28] .

There have been numerous studies reporting the penetration depth of UV, visible and near infrared light in tissue. Near infrared light in the 800 nm region has been shown to provide the best results with respect to penetration depth, since light in minimally attenuated due to tissues absorbance [26].

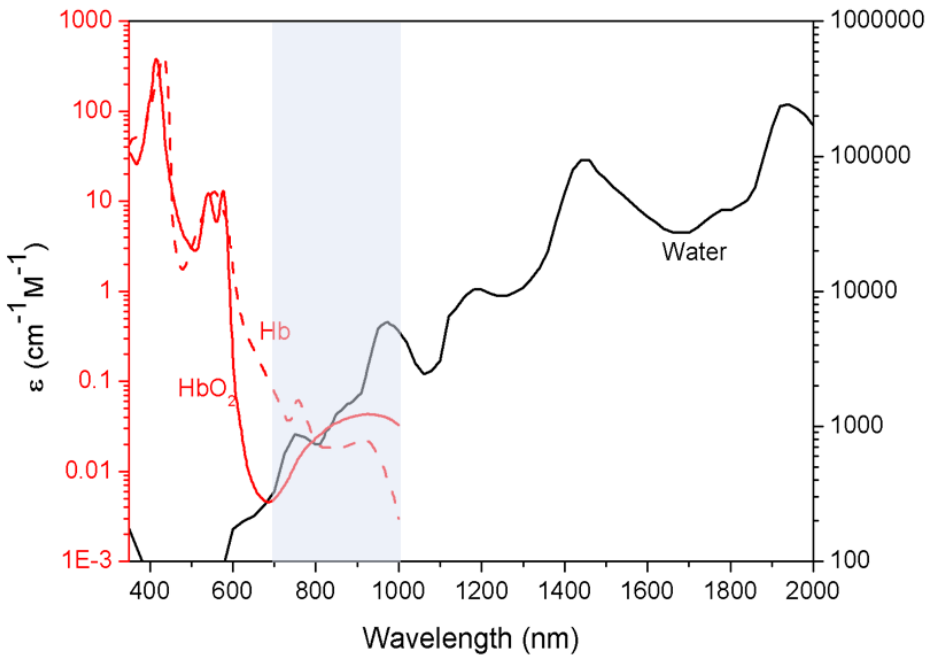

Figure 1.9 Molar absorptivity coefficient of water, oxyhemoglobin HbO_2, and deoxyhemoglobin Hb at different wavelength [24].

1.3 Literature Review

1.3.1 Nanocarriers in PDT

Like any cancer treatment PDT faces major challenges in activating and delivering photosensitizer (PS) molecules towards their target tissues. Most PS are hydrophobic in nature with poor solubility in aqueous environment (serum) and require loading carrier to enhance their selective delivery toward tumor site. Photosensitizer are below ~5 nm in size which contributes to rapid kidney clearance through renal filtration [31], and potentially reduce their PDT efficacy. Notwithstanding the fact that the majority of photosensitizer are non-selective to tumor tissue, and induce cellular toxicity when present in a healthy tissue environment. Nanocarriers can contribute to overcome these obstacles and enhance loading, and targeting of PS into tumor sites.

Nanocarriers have high surface area to volume ratio, that permits the loading of significant number of PS either through encapsulation, or surface conjugation with ligand on nanoparticles (NP) surface. This will prevent the significant loss of PS before reaching their target sites. Further, NPs could be functionalized with a cellular targeting surface ligand such as antibodies, peptides or aptamers, and folic acid receptors that are highly expressed on cancer surface that improve delivery of PS to cellular targets [32-34]. Also, NPs could passively target tumors through the enhanced permeability and retention effect (EPR). The EPR effect is the result of abnormal regulation of tumor tissues caused by hyper proliferation growth of cell with rapid vascularization, and inefficient lymphatic drainage [35]. Currently, there are many NPs that act as loading and delivery systems for cancer drugs and photosensitizers, such as liposomes, dendrimers, polymeric micelle, and silica (figure 1.10). Although these models are successfully utilized for PS, optically inactive NPs require high energy radiation excitation for PS activation, this limits their utility for deep tissue tumor treatments.

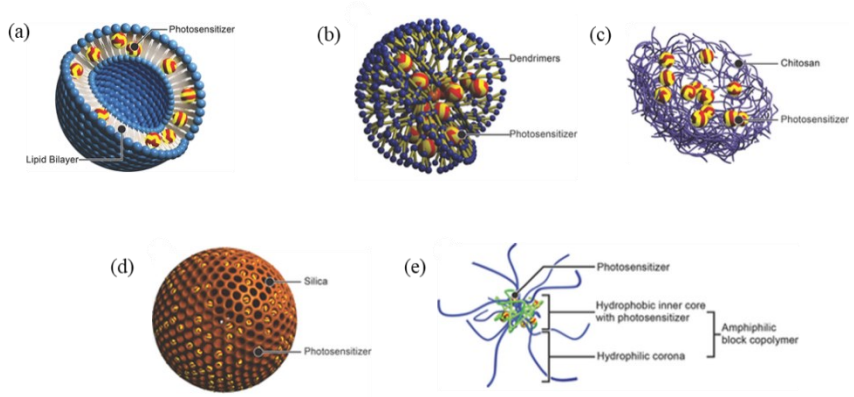

Figure 1.10 Different PS loading strategies. (a,d, e) are based are hydrophobic interaction of PS with core NPs. (b,c) hydrophobic or covalent coupling depending in PS.

1.3.2 Ln-UCNPs $NaGdF_4$: Yb^{3+}, Er^{3+}

Fluoride based host materials have low phonon frequencies (350 cm^{-1}), an important factor that affects the luminescence efficiency of Ln^{3+} where non radiative relaxation occurs due to multi-phonon relaxation. Thus, fluoride materials such as $NaGdF_4$ and $NaYF_4$ have been used extensively as ideal host for luminescent ions showing upconversion. In addition, fluoride host materials have high chemical stability, long luminescence lifetime, tunable emission wavelength, low cellular toxicity. In addition, the absence of autofluorescence and blinking permits fluoride based upconversion nanoparticles as the ideal nano-medicine applications.

Owing to their unique optical properties, different synthesis routes have been developed to produce fluoride based upconversion nanoparticles. These strategies generated well-defined crystal phase nanoparticles with high crystallinity and narrow particle size distribution. The most investigated synthetic procedures are thermal decomposition [36], and coprecipitation[37].

Nanoparticles such as $NaGdF_4$ produced by these methods allow for excellent control of the size ranging from the ultra small 2.5 nm up to 100 nm size diameter [38]. A unique optical feature of $NaGdF_4$ nanoparticles, is the presence of Gd^{3+} ions that can act as an intermediate sensitizer in host matrix by permitting energy transfer to neighbouring lanthanides activators (Tm^{3+}, Tb^{3+}, Sm^{3+}, Dy^{3+}) enhancing the radiative emission of visible light emissions [39]. Apart from optical feature, Gd^{3+} ions are paramagnetic relaxation agent imparting multimodal characteristics thus can be used as contrast agent for magnetic resonance imaging (MRI).

The common binary dopants of $NaGdF_4$ host for PDT applications are 20 moles % Yb^{3+} for NIR absorption at 980 nm, and 2% mole Er^{3+} acting as emitting centers in the visible region. The combination permits a strong emission profile in the green and red region of spectrum. The Er^{3+} emission bands are either a result of energy transfer from $Yb^{3+} \rightarrow {}^2F_{5/2}$ transition to $Er^{3+} \rightarrow {}^4F_{7/2}/{}^4F_{9/2}$ or by two photon absorption of Er^{3+} through ${}^4I_{15/2} \rightarrow {}^4I_{11/2} \rightarrow {}^4F_{7/2}$ transitions. Non-radiative decay from ${}^4F_{7/2}$ to lower excited states ${}^2I_{11/2}$, ${}^4S_{3/2}$, and ${}^4F_{9/2}$ show emission bands centered at 524 nm, 546 nm, and 658 nm respectively (Figure 1.11). However, the emission profile of $NaGdF_4$: Yb^{3+}, Er^{3+} should overlaps with the PS absorption spectrum, which is required for the activation (excitation) of PS, and subsequently the production ${}^1O_2$. An example is the FDA approved PS for metastatic melanomas Rose Bengal (RB) shows a maximum overlap around 548 nm [40].

1.3.3 Ln-UCNPs surface coating strategies (approaches) for PS loading

1.3.3.1 Organic functional ligands (Electrostatic interaction)

High quality $NaGdF_4$ nanocrystals can be produced using the thermal decomposition method. The synthesis involves the decomposition of fluoro-organic acid salts of lanthanides (usually trifluorocetate) oleic acid (ligand) and 1-octadecene (a high boiling solvent). The surface of resulting nanoparticles are oleate capped, therefore are hydrophobic. For biological applications

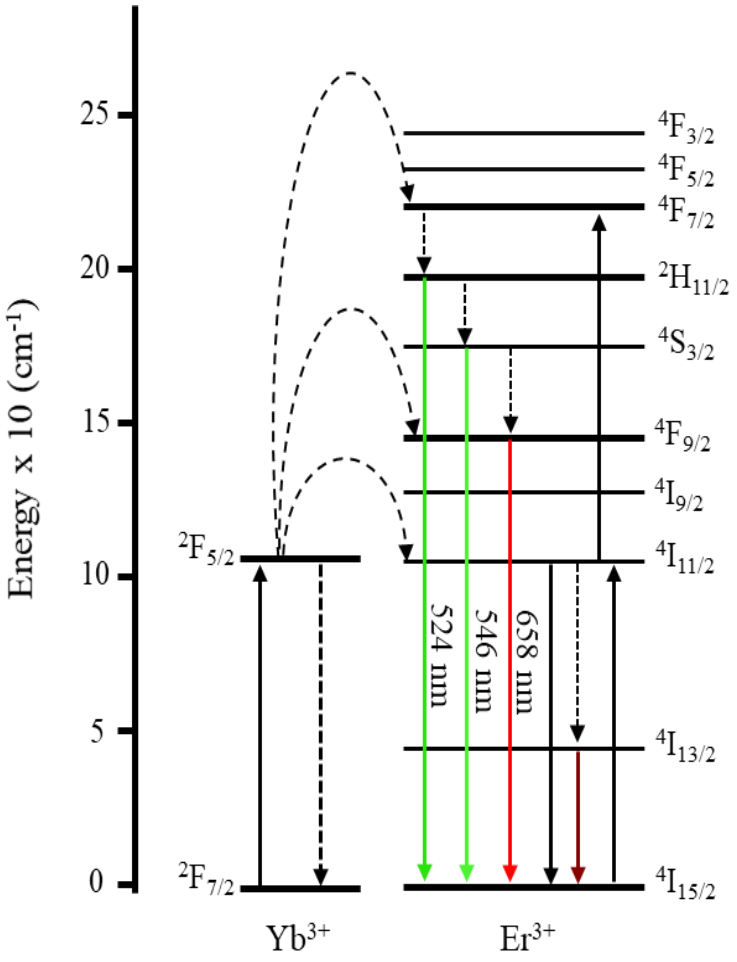

Figure 1.11 Upconversion mechanism energy diagram for $NaGdF_4$: Yb^{3+}, Er^{3+}

surface modifications of the nanoparticles are required to enable dispersion in hydrophilic solvents.

In order to achieve dispersibility of oleate capped nanoparticles Bogdan et al. developed a novel and facile approach that used a mild acidic conditions (pH 4.0, 0.1 M HCl) to protonate the oleate carboxylate moiety on Ln-UCNPs surface [41]. Protonation of the oleate produces oleic acid which is freed from the surface leaving a positively charged surface rendering Ln-UCNPs dispersible in a hydrophilic environment. An alternative approach of generating a positively charged water dispersible surface is the use of nitrosonium tetrafluoroborate ($NOBF_4$) in presence of dimethylformamide (DMF) solution [42]. $NOBF_4$ generates nitrous acid (HNO_2) that protonates oleate ligand, and tetrafluoroborate (BF_4^-) ions will electrostatically interact with positively charged surface enhancing dispersibility in aqueous environment.

Uncapped Ln-UCNPs have a positively charged surface that utilized to load PS directly via electrostatic interaction. However, for direct surface conjugation, PS must possess carboxylate, phosphate, or sulfonate functional groups that have strong affinity to the Ln-UCNPs surface. For example, Chen et al. modified PS phthalocyanine zinc (ZnPc) to β-carboxy phthalocyanine zinc by adding a single carboxyl group functionality (ZnPc-COOH)[43]. This modification was used by Wang et al. to effectively graft ZnPc-COOH on the oleate free $LiYF_4$: Yb^{3+}, Er^{3+} and showed the production of reactive singlet oxygen species under NIR irradiation [44]. In a relatively similar approach, Yu et al. electrostatically functionalized $LiYF_4$: Yb^{3+}, Tm^{3+} with benzoic acid modified FDA approved Foscan®. Yu et al. showed that the overlap of the emission band of Tm^{3+} in the blue region overlaps with the Soret absorption band of the photosensitizer resulted in energy transfer from the donor (Ln-UCNP) to the acceptor (photosensitizer), which activated the photosensitizer to produce $^1O_2$ and induced Hela cells toxicity [45].

Although functionalization of the PS to the Ln-UCNP surface using electrostatic interaction shows the production of $^1O_2$, undesirable premature release (leakage) remain the main

challenge for *in-vivo* applications [46]. In addition, excessive loading of PS on the surface of Ln-UNCPs will induce self quenching and decrease the efficiency of $^1O_2$ production. To overcome these limitations, the positively charged surface of the nanoparticles are functionalized with a surface ligand with dual functionality. First, a functional group such as phosphate, thiol, and carboxylate with free negative charge that can electrostatically interact with the positively charged nanoparticles surface. Phosphates is considered to provide an enhanced ligand stability in biological environment in comparison to carboxylate and thiol moieties. [47] . The second functional moiety of the ligand should be a primary amine or hydroxyl group to target carboxyl functional groups present in PS such as alendronate ligand as shown in figure 1.12 [48].

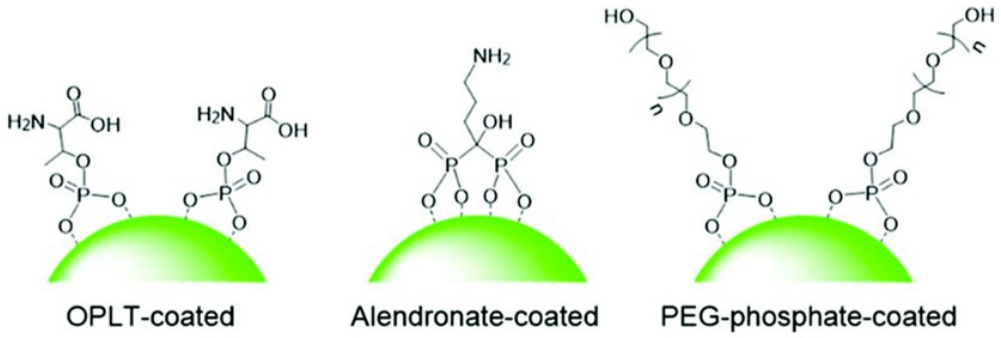

Figure 1.12 Different phosphate surface coated ligand for Ln-UCNPs dispersibility in aqueous media. OPLT: O-phospho-L-threonine [46]

1.3.3.2 Long chains amphiphilic polymer coatings

Despite the stability of adding a functional ligand on the surface of Ln-UCNPs, grafting of hydrophilic or amphiphilic long chains molecules (AC) such as, poly (ethylene glycol)[49], silica[50], poly (allyl amine) or poly (acrylic acid) (PAA) [51], poly (ethylene imine) (PEI) [52] provides further

advantages for the above-mentioned organic surface ligands for PDT therapy. Adding AC doesn't require the removal of the oleate capping ligand from the surface of the Ln-UCNPs through acidic conditions, which may cause etching of nanoparticle surface. AC alky chain provide a stealth surface coating through hydrophobic interaction with oleate chain present in the surface of Ln-UCNPs. In addition, AC provides a full surface coverage, and the thickness can be controlled on the surface of the Ln-UCNPs. The significance of full surface coverage on Ln-UCNPs relies on preventing solvent phonon quenching by shielding the surface from the surrounding environment media. This enhances the luminescence intensity required for PS activation and singlet $^1O_2$ production. Moreover, AC possess functional moieties, which may be used for PS coupling, and dispersibility in biological aqueous environment. For example, Ren et al. utilized commercial available nontoxic food additive TWEEN-80 surfactant to coat Ln-UCNPs without the use of surface pre-treatments for loading hydrophobic drugs or PS molecules [53]. TWEEN-80 hydrophobic tails were grafted on $NaYF_4$:Yb^{3+}, Er^{3+}@$NaYF_4$ via intercalating with the oleate surface ligand (Figure 5). The other side chain of TWEEN-80 aliphatic ester provide hydrophilicity rendering NPs stable in biologically relevant media such as, fetal bovine serum (FBS), saline buffered solution (PBS), and *in vitro* cell culture amino acid media [53].

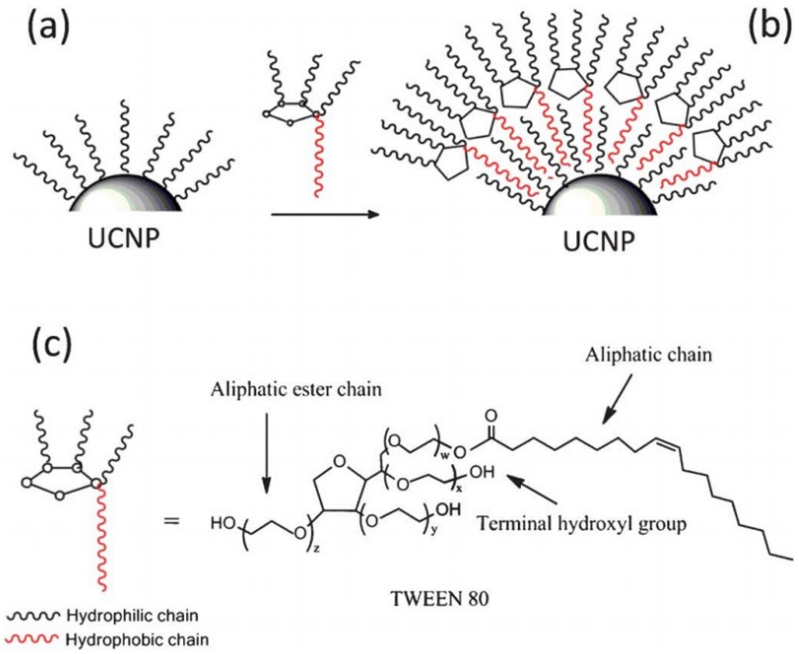

Figure 1.13 Surface modification of $NaYF_4$:Yb^{3+}, Er^{3+}@$NaYF_4$ (UCNPs) using Tween 80. (a) Oleate capped UCNP, (b) tween addition, (c) Tween 80 structure with amphiphilic properties [51].

1.3.4 Delivery modes of NP in vivo

1.3.4.1 Passive targeting

Vascular endothelium (VE) is one of the barriers encountered by NPs to reach the tumor site. VE is defined as the biological boundary between circulating blood and the surrounding underlying tissue that is responsible for the diffusion of blood component towards tissues. Injured, inflamed, and cancer tissues show leaky VE due to the large fenestration between endothelial cells that ranges from 10 nm to greater than µm [54]. These endothelial gaps are the passive routes responsible for therapeutic NPs delivery towards tumor sites and reducing nonselective delivery into normal tissues. Furthermore, tumor tissues with massive proliferation rate may lose lymphatic drainage function, which is the existing pathway leading to increased NP retention [54]. In other

words, vessel leakiness and minimal tissue efflux is referred to the enhanced permeability and retention (EPR) effect (figure 1.14). Therapeutic NP are designed to pass the tumor endothelial cells, at the same time have threshold above the normal fenestration present in normal tissues. For instance, NPs less than 6 nm in diameter are removed from circulation by kidneys through renal filtration [55]. Also, hepatic clearance through the liver represents a primary route for efficiently capturing and excreting of NPs (10-20 nm) present in blood[55]. Thus, consideration relative to size of the NP are essential for enhancing nanoparticles delivery system.

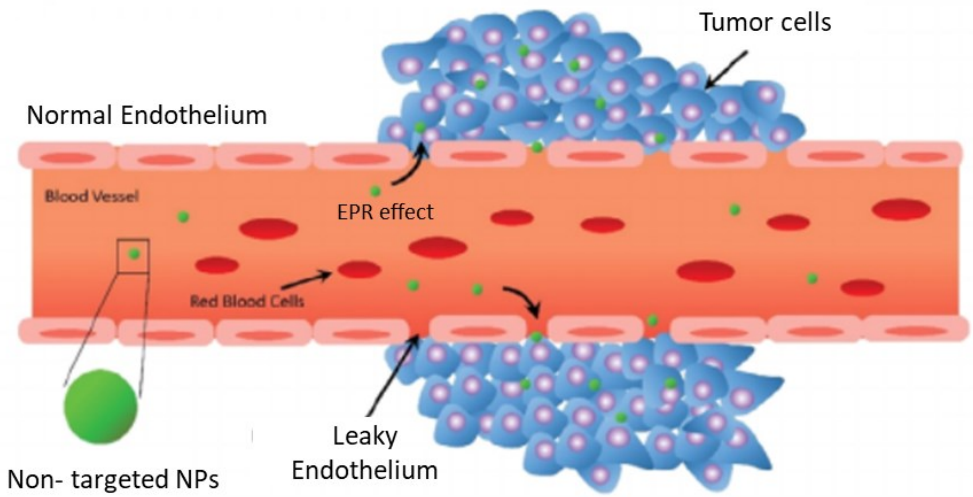

Figure 1.14 Enhanced permeability and retention (EPR) effect diagram showing leaky endothelial cells around tumor site. Non targeted NPs corresponds to passive diffusion with bare surface targeting ligand [53].

For example, using a lung carcinoma model Tang et al. showed that silica NPs of 50 nm had the highest tumor penetration in comparison compared to 200 nm silica-NPs that was regarded as the best cut-off for tumor penetration by the EPR effect [56]. In a similar approach, Park et al.

showed that a 42 nm $NaYF_4:Yb^{3+}$, Er^{3+} @ $NaGdF_4$ coated with PEG phospholipid loaded with PS chlorin e6 (Ce6) was readily accumulated in tumor (glioblastoma) by the EPR effect, which could be used for both imaging and PDT [57]. Although size consideration is highly significant in tumor passive targeting, physicochemical properties of NPs such as hardness, shape, surface charge and coating affect NPs organ distribution, toxicity, and cellular localization. To elaborate on hardness, Anselmo et al. used a 200 nm PEG-NP with different elastic moduli, and demonstrated that harder NPs ($3x10^3$ kPa) showed diminished targeting ability compared to a softer 10 kPa PEG-NP that resulted in an extended blood circulation and passive targeting *in vivo* [58].

Moreover, tumor exhibit intra/intertumoral heterogeneity with different vascular leakiness between periphery and hypoxic core that have implications in NP passive delivery. Adjustments of the heterogeneity of vascular permeability may be enhanced by vasodilants such as vascular endothelial growth factor (VEGF), nitric oxide (NO), LPS (lipopolysaccharide), and thrombin that disrupt endothelial cell barrier function [59]. VEGF is most attractive vasodilants since it exhibits elevated level or overexpression of its receptor in tumors such as pancreatic, and breast cancer. VEGF activates vascular permeability by triggering disassembly of the inter-endothelial cell junctions causing increase in intracellular gaps that potentially augment the uptake of NPs [59].

1.3.4.2 Active Targeting

Active targeting is complementary to passive targeting and involves grafting targeting ligand in the surface of NPs that permits biological interaction with the target cell. There are numerous biological ligands that provide NPs with active targeting and facilitate cellular internalization and increase retention and therapeutic efficacy. Herein the focus will be on the most significant targeting ligand used for targeting cancer cells.

(a) Aptamers

The term aptamers are derived from Latin that means 'to fit'. Aptamers are class non-biological nucleotides (DNA or RNA) characterized by short size sequence between 20 and 100 nucleotide residues. Apartments "synthetic antibodies" target many protein families such as proteases, cytokines, kinases, and more notably cell-surface receptors [60]. Aptamers are relatively non-immunogenic, chemically stable due to their phosphodiester bond, and easily conjugated with organic molecules such as photosensitizer that can be introduced during synthesis [60]. There are currently many aptamers in clinical phase trials, with one FDA approved Pegaptanib (Pfizer) composed of 27 nucleotides that target VEGF receptor. Conjugated with 40 kDa PEG, Pegaptanib is used for treating aberrant angiogenesis of age related macular degeneration (AMD) [61]. Another promising candidate is the sgc8c aptamer that can recognize protein tyrosine kinase 7 (PTK7), a transmembrane receptor that is highly expressed in lymphoblastic leukemia CEM cancer cells [62]. Hou et al. elegantly utilized sgs8c aptamer by extending its sequence with poly T (thymine) bases possessing thiol end, and embedded primary amine functionality. The former group form disulfide bridge with UCNPs ($NaYF_4$: Yb^{3+}, Er^{3+}) surface, and the latter applied to couple PS-Ce6 (Chlorin e6) for PDT application [63]. The system provided with sgs8c a surface recognition site permitting UCNPs CEM cell entry, the UCNPs-Ce6 was activated *via* energy transfer, which induced cellular toxicity under 980 nm NIR irradiation.

(b) Small molecules

Although there are many molecules used as a targeting surface ligand such as mannose, galactose and biotin [64], folic acid remains the most used ligand for targeting tumor cells. Folate receptor (FR) family are membrane associated glycoprotein cysteine rich cell surface receptors that are responsible for folic acid (vitamin B9) cellular uptake. Folic acid is essential for cell cycle as it interferes with the biosynthesis of DNA, and RNA. There are four FR isoforms FRα, FRβ,

FRγ, and FRδ [65]. Among the four, FRα is expressed in tubular epithelial linings along with FRβ and are responsible for most FA shuttling inside the cells. Since cancer cells have high proliferation rate in comparison to normal cells, FR are highly expressed in the cancer cell surface to accommodate for the excessive need of FA that is needed for DNA synthesis for dividing cells [66]. Although FR receptors are present in normal tissues, their expression levels are considered negligible compared to cancer tissues. For example, the levels of FR receptors in ovarian fallopian tube cancer tissue are 13 times more than in normal tissues[66]. Another significant finding was observed in colorectal metastatic cancer cells where FRα is overexpressed compared to normal colorectal tissues where expression level is not observed [67].

These FR are employed in active targeting strategies for delivering therapeutic nanocarriers. Chien et al designed a complex photocage system of SiO_2-Ln-UCNPs ($NaYF_4$:Yb^{3+},Tm^{3+}) linked with PEG to deliver doxorubicin (Dox) a chemotherapeutic agent [68]. To enhance cellular targeting and delivery of the drug, the targeting ligand FA was conjugated the NP system. Using amidation coupling, FA was covalently linked with PEG, permitting cellular internalization of the Ln-UCNP in Hela cells (confocal image Figure 7), and the release of Dox inside the cells under 980 nm irradiation [68].

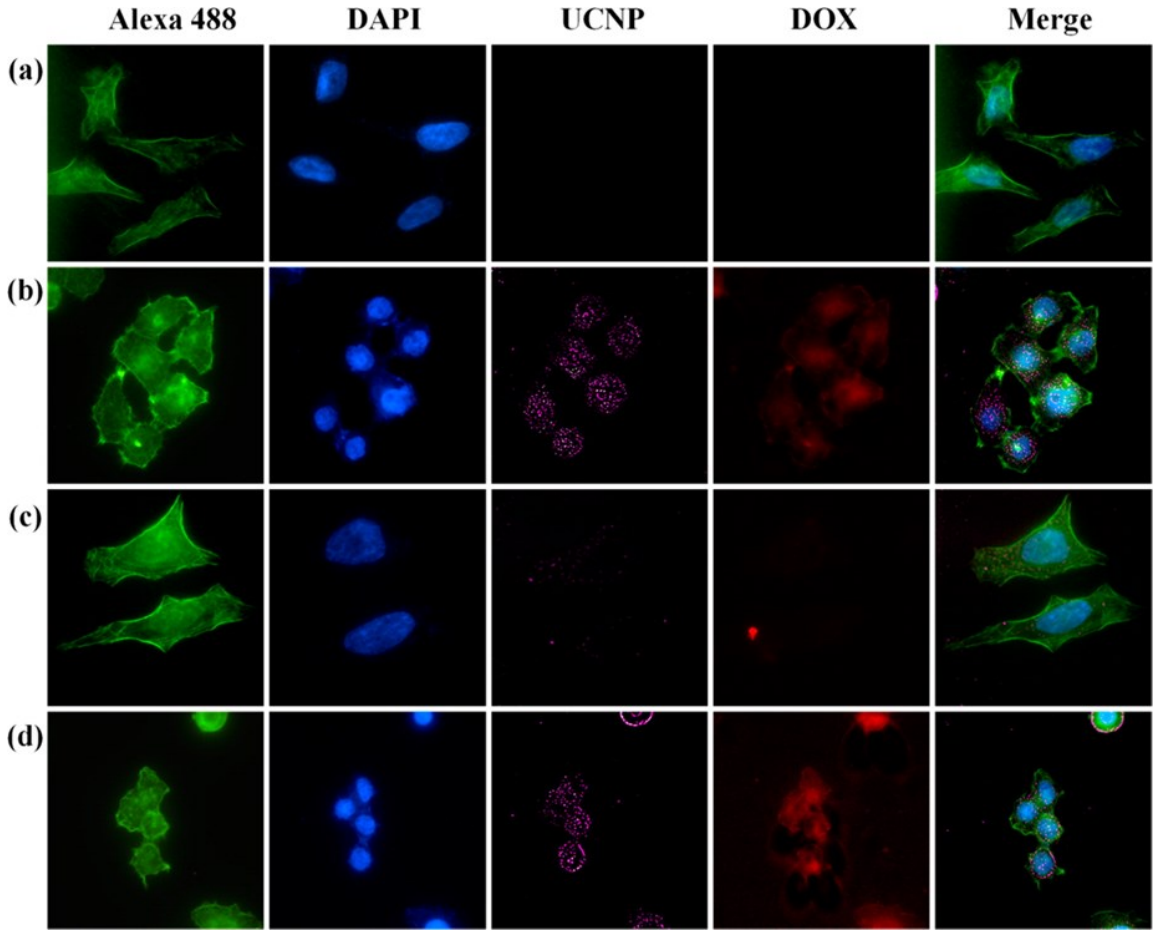

Figure 1.15 Confocal images of Hela cells. (a) Cells alone, (b) Folate-Ln-UCNPs, (c) Folate-Ln-UCNPs-Dox, (d) 980 nm excited Folate-Ln-UCNPs-Dox. Alexa 488 used for phalloidin staining, DAPI for nucleus [66].

Another promising candidate, is 18β-Glycyrrhetinic acid (GA) derived from the hydrolysis of naturally occurring glycyrrhizin present in the roots of licorice that is used in Chinese medicine [69]. This emerging molecule for enhanced targeted delivery has been selectively used for targeting hepatocellular carcinoma (HCC) and are currently extensively investigated in nanoparticles delivery systems [70]. Glycyrrhetinic acid receptor (GA-R) expression on the sinusoidal surface of hepatocytes has been identified as the target receptor responsible for shuttling nanoparticles inside the cells [70]. There are many emerging and successful reports on utilizing GA for delivering

nanoparticles for therapeutic approaches such as liposomes, micelles, and graphene oxide [71]. A relevant example related to Ln-UCNPs, is $Li(Gd,Y)F_4:Yb^{3+}$, Er^{3+} with an active core, and inert shell coated with PEG modified GA for imaging hepatic cancer cells [72]. Using *in vitro* and *in vivo* model with HepG2 liver cancer tumor, GA-Ln-UCNPs was efficiently delivered to the tumor/cell site and could be imaged using 980 nm excitation [72].

There are more emerging small targeting molecules that are important in delivering therapeutic nanomaterials for different target tissues. For example, bisphosphonates ligand with Ln-UCNPs have been used for bone active targeting [73]. Although small targeting molecules are a growing interest due to their feasible preparation and coupling on nanomaterial surface, their major challenge is identifying new surface targeting ligands that are solely specific for certain type of cancer tissue.

(c) **Antibodies and peptides**

Antibodies belong to immunoglobulin superfamily with known function in neutralizing foreign antigens and stimulating immune responses. Due to their extreme specificity toward cell surface antigens (epitopes), their uses in cancer therapy have grown enormously, and currently there are more than 40 FDA approved Abs therapeutics for a wide range of cancerous tissues [74]. The general mechanism of Abs in cancer cell eradication is binding to the surface of growth factor signalling receptors such as EGFR that is responsible for tumor cell proliferation, migration, and invasion. Abs binding block the signaling activity of the receptor, and induce cellular toxicity [74]. It is worth mentioning, that there are significant number of Abs that have diagnostic properties that target biomarkers present in specific cancer cells, and lack the therapeutic activity , as an example is the p53-Ab that is an early marker for lung cancer [75].

Abs can be loaded to the surface of Ln-UCNPs. Jin et al. targeted carcinoembryonic antigen (CEA) that is highly expressed in colon cancer with CEA-Abs grafted on the surface of the Ln-UCNPs. The core shell nanoparticles designed ($NaYF_4$:Yb^{3+}, Er^{3+} @ $NaGdF_4$) represented a selective bimodal imaging probe (Fluorescence/MRI) for selectively detecting colon cancer *in vivo* [76]. The same core shell Ln-UCNPs were applied by Liang et al. using EpCAM-Ab (epithelial cell adhesion molecule transmembrane glycoproteins) to target colorectal adenocarcinoma HT-29 cells. Also, PS can be grafted to induce highly selective local PDT toxicity with $^1O_2$ released under NIR irradiation[77].

Although Abs conjugated to Ln-UCNPs are promising there are some major challenges that limit their effectiveness. First, the production of Abs is associated to very high costs. Abs are large protein molecules normally above 150 KDa that effects the number that can be conjugated on the nanoparticles surface. Moreover, Abs require specific orientation to identify epitopes present on target protein molecules, which might be lost or limited when present on nanoparticles surface [74]. A very promising alternative is the use of short low molecular weight peptides that can target cell surface receptors. RGD (arginine-glycine-aspartic acid) is the most commonly used peptide that target tumors endothelial adhesion integrin receptor $\alpha v\beta_3$. Jin et al. designed a very elegant system for targeting an aggressive tumor *in vivo,* triple negative breast cancer cells (MDA-MB-231). The design combined Ln-UCNPs ($NaYF_4$: Yb^{3+}, Er^{3+}) with amphiphilic surface coating conjugated with PS, and RGD [78]. Selective nanoparticles targeting, and retention was observed up to seven days in mice bearing tumors (Figure 1.16). There are some other proteins used in active targeting, albumin is one such biomolecule that will be covered in detail in section 1.3.6 due to the relevance to this thesis.

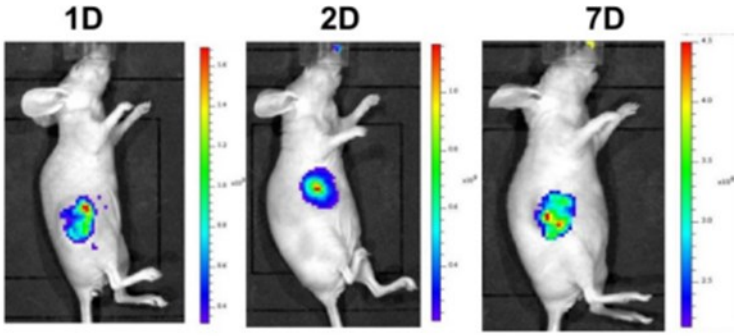

Figure 1.16 In vivo fluorescence images of Ln-UCNPs loaded with RGD peptide for tumor targeting and PDT therapy. 1D, 2D, and 7D represents the number of day nanoparticles retained in tumor tissues [76].

1.3.5 Protein Corona and NP delivery

Although the above-mentioned delivery strategies prove to be efficient in delivering NPs towards tumor sites, there are additional challenges that reduce or prevent the amount of injected dose to reach their target sites. Foreign entities nanoparticles entering the blood stream are exposed to biomolecules (proteins) that adsorb into their surfaces. There are two types of protein that adsorb on NPs. First, high affinity proteins with long retention time and high interaction ability with NPs. These proteins remain intact with the NPs forming a permanent structure known as hard corona. Second, low affinity (transient) proteins that weakly bind to NPs hard corona (figure 1.17), which can be easily exchanged or released in the biological media forming soft corona [79]. Presence of hard corona is the major contributor compared to soft corona that will affect the biological fate, and the identity of nanoparticles [79]. Corona deposition will increase the size of the nanoparticles, and may engulf many nanoparticles forming clusters or aggregates. Also, corona presence will mask the targeting ligand grafted on the nanoparticles. Thus, diminishing passive or targeted delivery efficiency towards tissues of interest.

The nature of protein corona deposited on the surface of the NPs is dependent on the physiochemical properties of the NPs. Walkey et al. generated a library of 63 different nanoparticles, and reported more than 100 proteins could be present in a single nanoparticles. The majority are transient proteins, and only 6 proteins are intact with high affinity and high abundance such as apolipoprotein AI, Albumin, and fibrinogen [80]. Recently, in similar study with Au-NPs Vitali et al. identified that albumin is a major constituents of the HC reaching up to 75 % protein composition on the surface of gold nanoparticles [81].

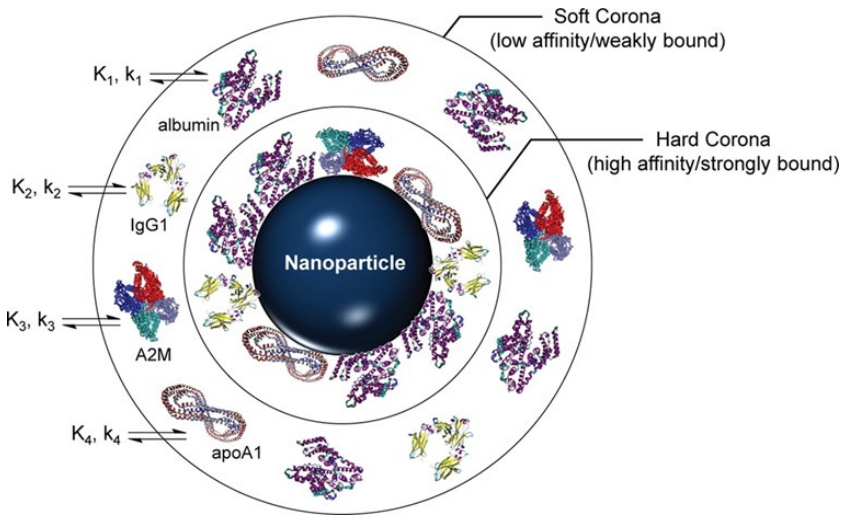

Figure 1.17 Protein corona adsorption on the surface of NPs. Stealth coating formed by high affinity protein. Low affinity binding form soft corona with different kinetic (k). and thermodynamic (K) function [77].

1.3.6 Albumin

1.3.6.1 Biological Properties

Albumin (ALB) is the most abundant protein present in human blood. It is estimated that up to 15g of ALB produced predominantly in the liver and distributed in the vascular tissues daily, albumin has a circulating half life of 19 days [82]. ALB is composed of 585 amino acids arranged in three domains (DI, DII, and DIII) forming a heart shape structure. Each domain is composed of two subdomains A, and B each consisting of 4, and 6 α-helices respectively. ALB has no β-sheets with 17 disulphide bridges, and unique free thiol at cysteine 34 present in DI. These features give ALB high stability in variable pH, denaturation solvents, and heat. ALB is very soluble in aqueous media due to the nature of the charged amino acids present with 99 acidic, and 83 basic residues [82]. These characteristics permit ALB to have significant biological functions such as lipid metabolism by acting as solubilization agent of fatty acid, transportation of metals (copper, calcium, nickel, zinc), osmotic pressure in blood, and its own catabolic reactions that provide energy to tissues [82].

1.3.6.2 Surface receptors and trafficking

There are six known receptors present on different cell type surface that recognize ALB and mediate its cellular internalization, degradation, and recycling. Secreted protein acidic and rich in cysteine (SPARC), glycoprotein receptors (gp18, gp30, gp60), neonatal Fc receptor (FcRn), and cubilin-megalin complex are all ALB surface receptors. The gp18, and gp30 are expressed mainly in liver endothelial cell membranes. These two receptors are known as scavengers responsible for binding modified or altered ALB with high affinity (1000x) compared to native ALB [83]. The gp60 are present in vascular endothelial membrane, which regulates permeability of circulating lipids,

and proteins including native non modified ALB [84]. Gp60 utilize caveolae meditated endocytosis to transport ALB. Caveolae (little caves) are plasma membrane invagination reaching up to 80 nm in size are capable of harvesting extracellular matrix serum components. Caveolae dependent mediated endocytosis entering the cell escape lysosomal vesicles [85]. This pathway protects the loaded contents from lysosome hydrolytic degradation, which is one of the most significant routes for the development of therapeutic nanoparticles. FcRn receptor is expressed in a wide range of epithelial tissues (alveolar, vascular, brain, and renal), and have similar activity to gp60 receptor. At low endosome pH, FcRn binds ALB with high affinity preventing its degradation, increasing the half lifetime, and recirculating ALB to extracellular matrix.

SPARC is an extracellular secreted glycoprotein, and its expression is restricted to stressed tissues undergoing remodelling, repair, in a wide range of cancerous tissues such as, colon, glioma, breast, head, and lung. SPARC is released in the vicinity of the tumors extracellular matrix, bind albumin with high affinity, and assist in tumor growth suppression and restrict metastasis of cancer cells [86]. Thus, accumulation of ALB in tumors through SPARC binding is a key element in designing ALB nanovehicle therapeutics for targeting wide range of tumors.

1.3.6.3 Albumin NPs in cancer therapy

As a result of the abovementioned characteristics, albumin is becoming a unique naturally occurring protein for cancer therapeutics. The usefulness of ALB relies on its ability to combine active (receptor mediated) and passive (EPR) delivery modes when present in nanocarriers. More importantly, providing surface protection from surface deposition of serum protein corona. One of the landmark example, is the novel FDA approved ALB nanoparticles Abraxane® (ALB-paclitaxel) used for treating metastatic breast cancer. The formulation is based on fusing ALB under high pressure with paclitaxel (PTX) a chemotherapeutic cancer drug. The approach

produced ALB-NPs with an average size of 130 nm which are employed using the passive targeted EPR effect. In addition, both gp60 and SPARC surface receptor were employed to provide enhanced cell targeting and ALB-NPs retention (Figure 1.18) [87].

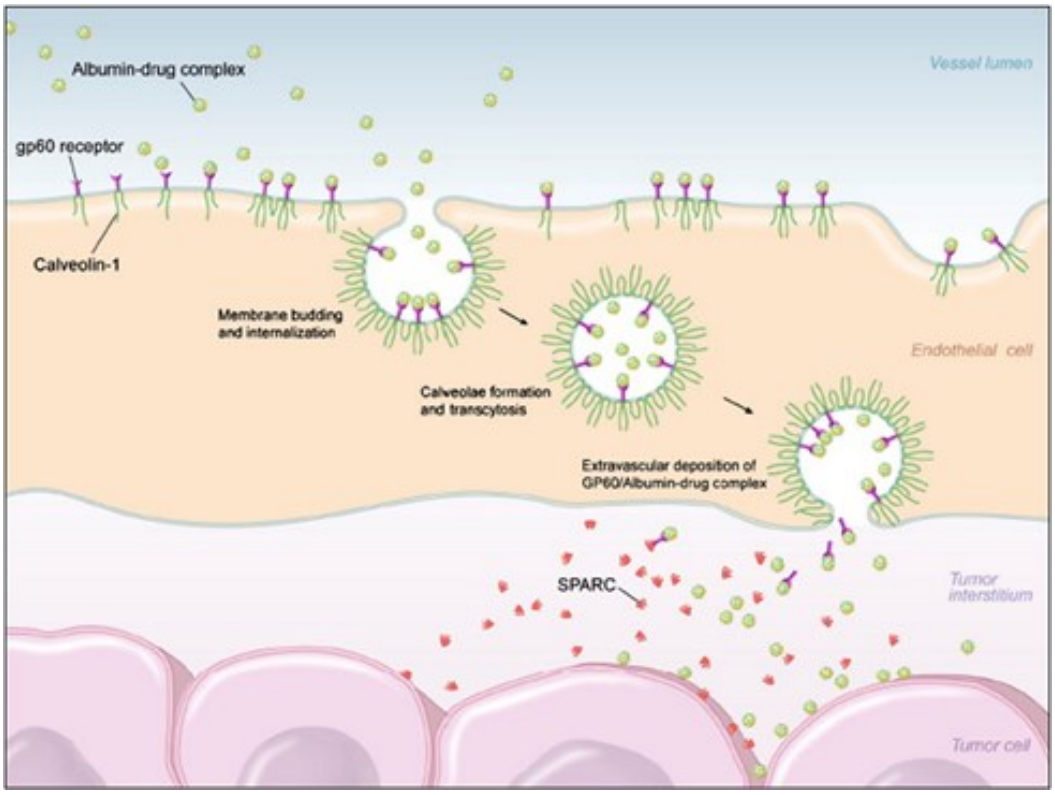

Figure 1.18 Caveolin mediated endocytosis utilizing gp60 for trafficking ALB-NP inside endothelial cells. SPARC released bind ALB-NP near tumor cells for enhanced retention [85].

Inspired by the Abraxane® model, different ALB-NPs systems are emerging for use as a multimodal nanoprobes for cancer therapeutics. Lie et al. used CTAB-Au nanorods covalently linked with ALB for combining photothermo-chemotherapy [88]. Au provided photothermal cancer cell ablation under NIR excitation, and the presence of ALB permits the loading of the chemotherapeutic agent PTX *via* hydrophobic interaction. In addition, ALB acted as biomimetic

transportation of Au-NPs utilizing SPARC targeted pathway to human colon cancer cells (HCT116).

1.4 Statement of the problem

Cancer is regarded as one of the deadliest and most challenging disease that faces mankind. The current conventional invasive treatments such as, radiotherapy and chemotherapy have major drawbacks such as, recurrence, and the use of indiscriminately drug molecules that induce toxicity to healthy tissues present in the body. PDT is a treatment that has garnered great attention, which utilizes individually nontoxic components (light, PS, and oxygen) that are activated in a spatiotemporal manner to induce a local cancer cell destruction.

Currently, PDT success is limited to superficial treatments, and face major challenges to translate the treatment to deeper tumor tissues. For example, the irradiation source used in PDT to activate most PS are far from the ideal biological optical window. PS activation lies in the UV-Vis spectral region where light has very limited tissue penetrance. Also, PS injected in the blood are removed from circulation through RES, and renal filtration. As a result, higher dose is required to circumvent PS lost by circulation, which could possibly induce toxicity to healthy tissues. Although cargo nanovehicle may assist in loading high concentration and suppress renal filtration, presence of blood serum protein biomolecules (corona) will change NPs identity and cellular target fate. Thus, PS would not reach their target tissues and will diminish the efficacy of PDT in deeper tissues.

Herein, lanthanides upconversion nanoparticles (Ln-UCNPs) are used as an optically active NIR energy transducer, and nanocarrier to enhance PDT utility for deeper tissue treatment. NIR excitation provide deeper tissue penetration, compared with excitation sources used presently for most PS (photosensitizer). Upconversion of Ln-UCNPs provide a selective tailored emission

to excite an FDA approved PS Rose Bengal. Ln-UCNPs are noncompatible in biologically aqueous media. Thus, different surface coating strategies are required to be optimized to load protein albumin onto the surface on the nanoparticles. Albumin was selected because of its natural abundance in blood serum providing dispersibility in biological media, and providing surface functionality for PS loading. Further, albumin presence will mimic the adsorption of blood serum proteins, which has implications in Ln-UCNPs targeting. PS modifications, and coupling strategies are used to study energy transfer, and activation processes responsible for toxic radicals generation. Cellular studies using different cancer cells line glioblastoma, and alveolar lung carcinoma (A549) are employed to study cellular targeting, and toxicity under NIR irradiation. Both unfolded and native albumin present on Ln-UCNPs cellular internalization studies are conducted. In both cancer cells lines studied, cellular toxicity assays under NIR irradiations were explored showing an enhanced PDT effect. These studies improve the use of Ln-UCNPs as optically active vehicle for loading and activating PS. The model is not limited to PDT, and could be extended to be used as a novel biocompatible nanocarrier for different cancer therapeutics.

Chapter 2. Dual Activity of Rose Bengal Functionalized to Albumin-Coated Lanthanide-Doped Upconverting Nanoparticles: Targeting and Photodynamic Therapy

Published as:

Tarek Sabri, Peter D. Pawelek, John A. Capobianco*

ACS Applied Materials & Interfaces. 2018, 10(32), 26947-26953

Department of Chemistry and Biochemistry, and Centre for NanoScience Research, Concordia University. 7141 Sherbrooke St. West, Montreal, Quebec H4B 1R6, Canada.

2.1 Abstract

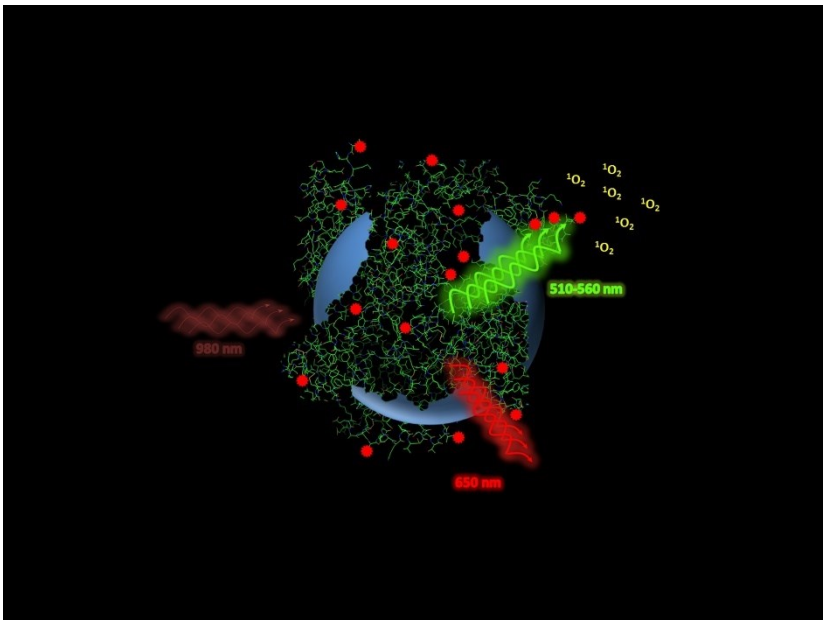

Scheme 2.1 Graphical content of PDT nanoprobe. Rose Bengal conjugated to albumin $NaGdF_4$:Yb^{3+}, Er^{3+} upconversion nanoparticles.

A modified version of a desolvation method was used to render lanthanide doped upconverting nanoparticles $NaGdF_4$: Yb^{3+}/Er^{3+} (Ln-UCNPs) water dispersible and biocompatible for photodynamic therapy. Bovine serum albumin (BSA) was used as surface coating with a direct conjugation to $NaGdF_4$: Yb^{3+}/Er^{3+} nanoparticles forming a ~2 nm thick shell. It was estimated that approximately 112 molecules of BSA were present and crosslinked per $NaGdF_4$: Yb^{3+}/Er^{3+} nanoparticle. Analysis of the BSA structural behavior on the Ln-UCNPs surfaces displayed up to 80% loss of α-helical content. Modification of the Ln-UCNPs with a BSA shell prevents luminescence quenching from solvent molecules (H_2O) with high energy vibrations that can interact with the excited states of the optically active ions Er^{3+} and Yb^{3+} via dipole-dipole interactions. Additionally, the photosensitizer Rose Bengal (RB), was conjugated to albumin on

the surface of the Ln-UCNPs. Emission spectroscopy under 980 nm excitation was carried out and an energy transfer efficiency of 63% was obtained. *In vitro* cell studies performed using human lung cancer cells (A549 cell line) showed that Ln-UCNPs coated with BSA were not taken by the cells. However, when RB was conjugated to BSA on the surface of the nanoparticles, cellular uptake was observed and cytotoxicity was induced by the production of singlet oxygen under 980 nm irradiation

2.2 Introduction

Photodynamic therapy (PDT) is a minimally invasive cancer treatment that involves the combination of light, photosensitizer (PS), and oxygen [89]. Individually the three components are harmless, however when combined reactive singlet oxygen ($^1O_2$) is generated, which induces cytotoxic reactions in cells resulting in cell death either *via* apoptosis or necrosis [89]. Unlike conventional treatments such as chemotherapy or radiotherapy, PDT presents remarkably reduced side effects, and improved selectivity towards cancer cells. However, the efficacy of PDT is limited since the majority of currently available photosensitizers are excited using UV/visible light [90-92]. In this range of spectrum, light has a lower tissue penetration depth of typically 1-3 mm due to scattering and the absorption of visible light by melanin and hemoglobin [93]. Thus, PDT is currently restricted to superficial treatments since deep-tissue penetrance is so poor. Substantial effort has been invested in designing photosensitizers that have absorption profiles lying in the biological optical window corresponding to the near infrared region (NIR) of the spectrum (750-1300 nm). In this region of the spectrum, both scattering and absorption by biological entities found in tissues are reduced [94].

Various challenges have been encountered in the effort to develop NIR-active photosensitizers. First, modifying the structure of the photosensitizer diminishes targeting specificity and may enhance toxicity. Second, the energy of NIR photons used to excite the PS is not sufficient to induce the production of $^1O_2$ [95, 96]. This has driven research in the area of developing efficient light or energy transducers that can strongly absorb in the near infrared region, and simultaneously emit in different regions of the spectrum, which could activate a broad range of PSs with different absorption profiles.

Lanthanide-doped upconverting nanoparticles with unique optical properties have garnered attention in biomedical applications such as photodynamic therapy [45, 91, 97], bioimaging, sensing [98, 99], and other fields such as photovoltaics devices [100], and security inks [101]. Upconversion is the conversion of long-wavelength radiation (NIR) into short wavelength (UV/visible) *via* a sequential two-photon or multiphoton mechanism. NIR excitation provides a number of advantages in biological applications, which include: higher tissue penetration, lack of cytotoxicity, and improved detection sensitivity due to the absence of autofluorescence [93]. Additionally, lanthanide-doped upconverting nanoparticles possess a number of attractive features such as stability with respect to photobleaching, long photoluminescence lifetimes, low cytotoxicity, sharp f-f absorption and emission peaks, and tunable emission that are extremely useful for biological applications [102]. Moreover, the large surface to volume ratio of these nanoparticles can act as a scaffold upon which to build new functionalities such as conjugation with targeting molecules and drugs [103].

Despite the attractive properties of Ln-UCNPs that make them excellent potential candidates for possible photodynamic therapy applications, as synthesized Ln-UCNPs are hydrophobic, which limits their utilization in biological applications. Different surface modification strategies have

been used to achieve dispersibility in aqueous environments and enhance PS loading. Common functional surface coating include adding a silica [104], or poly(ethylene glycol) shell [105], rendering Ln-UCNPs dispersible in aqueous environment. For example, Zhao et al. used a silica coated core shell $NaGdF_4:Yb^{3+}/Er^{3+}$@ $NaGdF_4$ for incorporating a modified phthalocyanine PS in PDT applications [106]. In a recent work Dou et al. covalently attached Chlorin e6 (PS) to amine functionalized silica coated $NaYF_4:Yb^{3+}/Er^{3+}$, showing a promising photodynamic effect at low nanoparticles concentration [107]. Very recently, another surface coating for $NaYF_4:Yb^{3+}/Er^{3+}$ using polymer poly(allyamine) conjugated to RB was proposed as a model to enhance tissue photochemical regeneration and possible application in PDT [108] . In a different approach our group reported the utilization of oleate-free Ln-UCNPs [41], to electrostatically graft the modified PS temoporfin on the surface of $LiYF_4:Yb^{3+}/Tm^{3+}$ for the production of singlet oxygen [45].

Surface modifications have been used as enhanced application of Ln-UNCPs in drug delivery and cancer targeting. However, nanoparticulate foreign entities entering the body are typically coated by various proteins in the serum to form a corona [79]. Furthermore, the corona can be divided into two types: a 'hard' corona, consisting of proteins adsorbed to NPs with high affinity, and a 'soft' corona, consisting of more loosely bound proteins passively acquired from the serum of the host. Soft coronas adsorbed to the surface can cause aggregation, affecting both the biological identity of the nanoparticles and their therapeutic effects [109]. Albumin, the most abundant protein in serum, has received considerable attention recently because it has been demonstrated to increase biocompatibility and stability in aqueous environments when adsorbed to the surface of nanoparticles [110]. Furthermore, it has been proposed that pre-loading of purified albumin onto NPs as a hard corona can confer a 'stealth' property onto an NP, preventing unwanted and uncontrolled accumulation of various host serum proteins to form an adventitious corona blocking cellular

uptake [111]. In addition, albumin-coated nanoparticles have been shown to be effectively loaded with drugs and to accumulate in cancer tissues through passive targeting [110].

In this work, we present NIR excited upconverting nanoparticles $NaGdF_4:Yb^{3+}/Er^{3+}$ coated with bovine serum albumin (BSA) for dispersibility in aqueous medium, biocompatibility and loading capability. By targeting free amine groups on the BSA surface we covalently bonded Rose Bengal (RB) modified with a hexanoic acid chain. Herein, we show that efficient energy transfer occurred between Ln-UCNPs and RB under 980 nm excitation, producing singlet oxygen that can be detected via a 1,3 diphenylisobenzofuran (DPBF) trap. Optimization of the concentration of RB on nanoparticles was carried out, and the energy transfer process was monitored by the decrease in the emission intensity of the $^4S_{3/2}$-$^4I1_{5/2}$ transition. In addition, the stoichiometry and structural conformation of BSA molecules bound to Ln-UCNPs surface were examined. Circular dichroism spectroscopy demonstrated a major loss of BSA helical structure on the surface of the nanoparticles. Transmission electron microscopy (TEM) studies revealed the thickness of the BSA shell on the nanoparticles to be ~2 nm. Moreover, *in vitro* cellular uptake and toxicity tested using A549 lung cancer cell line were carried out. BSA coated Ln-UCNPs (BSA-Ln-UCNPs) showed no cellular internalization. Most significantly, conjugating RB to the BSA coated nanoparticles, resulting in the nanoconstruct "RB-BSA-Ln-UCNP" imparted targeting ability that facilitated cellular uptake. Following uptake, RB-BSA-Ln-UCNP induced cellular toxicity upon irradiation with 980 nm infrared light.

2.3 Results and Discussion

In the present study, we synthesized hexagonal phase oleate capped lanthanide-upconverting nanoparticle $NaGdF_4$: Yb^{3+}/Er^{3+} (oleate capped-Ln-UCNPs) (Fig. S2.1, ESI) using a thermal

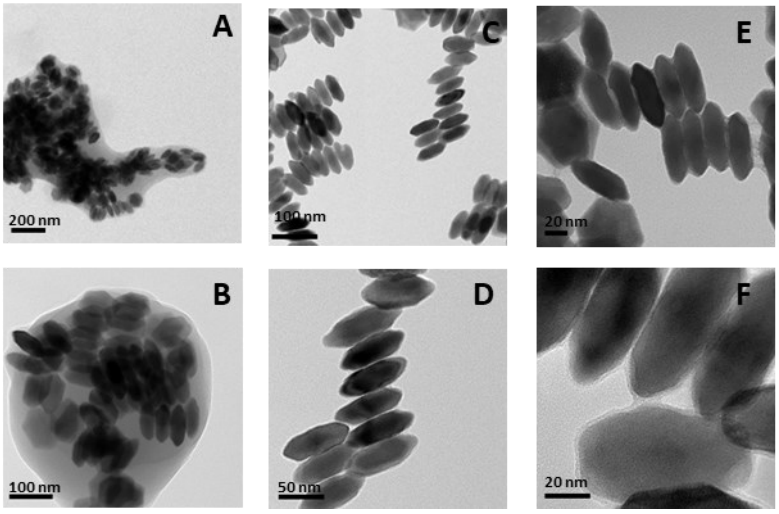

Figure 2.1 Transmission electron microscopy (TEM) of water dispersible BSA conjugated $NaGdF_4$: Yb^{3+}/Er^{3+} (BSA-Ln-UCNPs) 0.1 mg/ml in H_2O. (A,B) BSA coated nanoaggregates of BSA-Ln-UCNPs using desolvating agent with ethanol only. (C,D) BSA-Ln-UCNPs desolvation in presence of 4uL of 8% glutaraldehyde. (E) Negative staining TEM using uranyl formate. (F) High resolution TEM revealing the deposition of 2 nm BSA on the surface.

decomposition method previously reported by our group [112]. The oleate capped-Ln-UCNPs have hexagonal morphology with a length of 78 nm between opposite vertices (Fig. S2.2, ESI). As synthesized Ln-UCNPs are freely dispersible in non-polar organic solvent due to the oleate ligand present on the surface of the nanoparticles. To enhance biocompatibility and dispersibility in physiologically-relevant aqueous environments, BSA was used as a surface coating using a modified version of an ethanol-based desolvation method reported previously [113]. This approach produced monodisperse albumin coated nanoparticles with different shell thickness depending on the desolvating (ethanol) and cross-linking agents (glutaraldehyde) used [113]. The technique is similar to micellar production in polar solvents [114]. Specifically, the presence of the desolvating agent promoted local unfolding of BSA, exposing the majority of the amino acid side chains in an amphipathic manner. Amino acid residues with non-polar side chains form an interior-facing non-polar surface interacting with non-polar oleate groups, while exterior-facing hydrophilic side chains are solvent-exposed, rendering BSA-coated Ln-UCNPs water dispersible. Initially, we used

a desolvation method employing ethanol alone with BSA in the presence of Ln-UCNPs. The BSA-coated Ln-UCNPs were examined by TEM, and large nanoparticle clusters were observed (Figs. 2.1A and 2.1B). In order to produce a well-defined surface coating per single nanoparticle, different concentrations of glutaraldehyde (4, 15, 20, 30 μL of an 8% (v/v) solution) was added to the reaction mixture. It was evident that 4 μL of glutaraldehyde was the optimal concentration to minimize the formation of nanoparticle aggregates, and to form a uniform 2 nm thick BSA coating as seen in high-resolution TEM images (Figs. 2.1C, 2.1D and 2.1F). Conversely, elevated concentrations of glutaraldehyde (20μL, and 30μL) induced precipitation of the BSA-Ln-UCNPs, presumably due to the formation of inter-particle crosslinks as well as an overall decrease in the surface polarity due to the loss of primary amines on targeted Lys residues of BSA.

Although TEM was effective in determining the structure, size and morphology of oleate capped-Ln-UCNPs and BSA-Ln-UCNPs, low-mass elements such as carbon, oxygen and nitrogen contributed to low contrast and difficulties in imaging. We therefore employed negative staining to enhance contrast as well as to mitigate sample damage due to electron beam irradiation. Nanoparticle surfaces were coated with uranyl formate followed by TEM imaging. Resulting

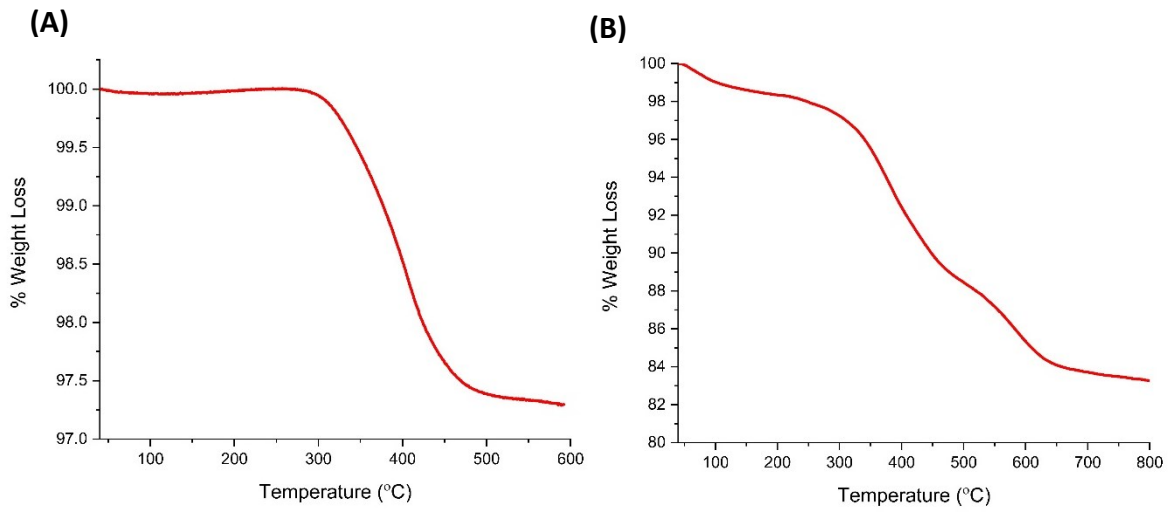

Figure 2.2 Thermogravimetric assay (TGA): (A) Oleate capped $NaGdF_4$:Yb^{3+}/Er^{3+} with a 2.65 % oleate loss between 320-500 °C. (B) BSA coated $NaGdF_4$: Yb^{3+}/Er^{3+} shows 15.24 % mass loss for a net of 120.6 µg of BSA for 1 mg nanoparticles.

images clearly showed that each nanoparticle is surrounded by a continuous layer of BSA, the thickness of which is ~ 2 nm (Figs. 2.1E and 2.1F).

Thermogravimetric analysis (TGA) of the oleate capped Ln-UCNPs indicated a weight loss of 2.65 %, which represents a mass of 26.4 µg of oleate molecules on the surface per 1 mg of nanoparticles (Fig. 2.2A), and a surface coverage of approximately 15 %. This result is based on comparing the surface area of Ln-UCNPs (15290 nm^2, ESI) to that of the surface area of the oleate that has been reported to be (0.4 nm^2) [115]. The same measurement was performed for BSA-Ln-UCNPs which showed a net mass loss of 15.24%, corresponding to 120.6 µg of BSA per 1 mg of nanoparticles (Fig. 2.2B), which corresponds to a stoichiometry of 112 BSA molecules per nanoparticle (Calculation, ESI). Given that the largest solvent-exposed surface of BSA is approximately 64 nm^2 (overall BSA dimensions approximately 8 nm x 8 nm x 3 nm (PDB code: 3V03) [116], 112 folded BSA molecules would cover approximately 7,200 nm^2, which is less than the surface area of a single Ln-UCNP nanoparticle (15,290 nm^2).

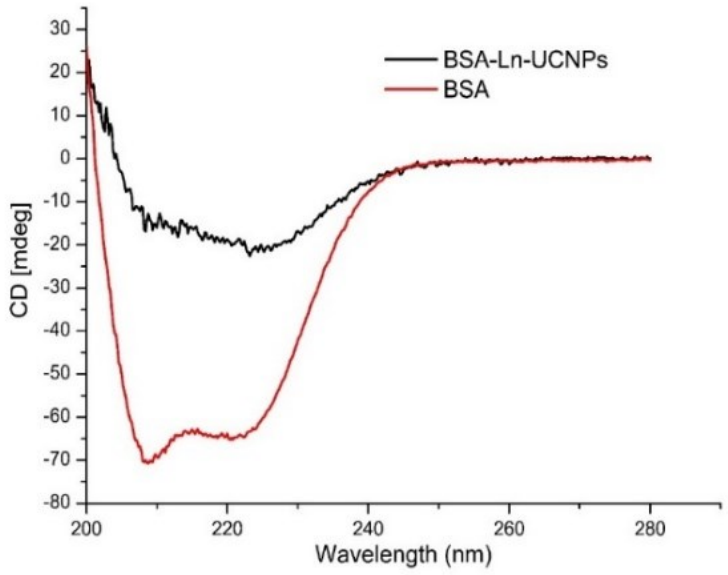

Figure 2.3 Circular dichroism (CD) analysis of native BSA shown in red, and BSA-Ln-UCNPs. Two minima between 215-225 nm represents α-helices region.

Since we observed a continuous layer of BSA coating Ln-UCNPs, we therefore reasoned that some degree of unfolding of BSA had occurred upon adsorption to the nanoparticle surfaces. Given that BSA is an α-helical protein, we used far-UV circular dichroism (CD) to determine helical content of BSA when adsorbed to the Ln-UCNPs. Far-UV CD spectra of BSA and BSA-Ln-UCNPs revealed a decrease in BSA helical content of approximately 80% when adsorbed to Ln-UCNPs in comparison with the same concentration of BSA in solution (Fig. 2.3). This supports our hypothesis that BSA undergoes unfolding upon adsorption to Ln-UCNP surfaces, resulting in the formation of a continuous BSA layer on the nanoparticle surfaces.

The synthesized nanoconstruct BSA-Ln-UCNPs is water dispersible, which is necessary for biological applications. To investigate the effect adding BSA on the surface of the Ln-UCNPs on upconversion spectra, measurements were performed on the BSA capped Ln-UCNPs nanoparticles dispersed in water (H_2O) as well as deuterated water (D_2O) (Fig. S2.3, ESI). We observed that both the peak positions in the green region centered at approximately 525 nm and

550 nm ascribed to the transitions $^2H_{11/2}$-$^4I_{15/2}$ and $^4S_{3/2}$-$^4I_{15/2}$ respectively remain the same in both solvents. Also, the peak position in the red region centered at 650 nm assigned to the transition from the $^4F_{9/2}$ excited state to the $^4I_{15/2}$ ground state remains the same. More importantly, no change is observed in the overall intensities of the peaks in the green and red region. These results provide evidence that BSA on the surface of the Ln-UCNPs provides excellent coverage of the surface of the nanoparticles thus preventing any interaction with the high-energy OH vibrational groups in H_2O , thus preventing the multiphonon relaxation from the $^2H_{11/2}$/$^4S_{3/2}$ to the $^4F_{9/2}$ state [41, 117]. If multiphonon relaxation was occurring an increase in the intensity of the transition at 650 nm ($^4F_{9/2}$ to the $^4I_{15/2}$) with the concomitant decrease of the intensity in the green region would have been observed.

RB is a well-known photosensitizer (PS) that exhibits the facile conversion of triplet oxygen to singlet oxygen is used [118]. The production of singlet oxygen is achieved upon irradiation with green light in the wavelength range 530 to 560 nm. At 549 nm RB has a high absorption cross section (99,800 $M^{-1}cm^{-1}$) and an excellent overlap with the green emission of the $NaGdF_4$: Yb^{3+}/Er^{3+} (Ln-UCNPs) from the $^2H_{11/2}$/$^4S_{3/2}$ to the $^4I_{15/2}$ state of the Er^{3+} ions (Fig S2.4, ESI). This overlap facilitates the energy transfer process from the upconverting Ln-UCNPs to the surface RB molecules that can trigger the production of singlet oxygen. Conjugation of a PS to the surface of a nanoparticle via hydrophobic or electrostatic interaction results in poor stability of the nanoplatform with the consequence that desorption/and or leakage may occur. Liu et al. demonstrated that electrostatic interaction of RB to the surface of $NaYF_4$:Yb^{3+}/Er^{3+} nanoparticles was an inefficient system due to the release of the PS. The authors reported that the amount of RB in the eluate to be one order of magnitude less for covalently bonded nanoparticle-photosensitizer, indicating less leakage occurs [119].

Conveniently, the presence of BSA on the surface of the Ln-UCNPs can be utilized as a scaffold which may be used to covalently conjugate the RB. The amine groups from lysine residues present on BSA are utilized to carry out amidation coupling to covalently link RB to the surface of the BSA-Ln-UCNPs. In order to covalently conjugate RB to the surface of the BSA-Ln-UCNPs, the RB hexanoic ester was synthesized by reacting RB with 6-bromohexanoic acid [119, 120]. The formation of the RB hexanoic ester was confirmed by MALDI-MS (Fig. S2.5, ESI). The conjugation of the RB hexanoic ester to the BSA-Ln-UCNPs was accomplished using a carbodiimide coupling reaction between the amino group of the BSA and the carboxylic acid group of the hexanoic acid ester of RB. The addition of hexanoic acid is required because the carboxylate group of the RB is sterically hindered by the adjacent chlorine which reduces the efficiency of the amidation reaction.

2,4,6-trinitrobenzene sulfonic acid (TNBS) has UV-active chromophore which were used to determine primary amine content following formation of 2,4,6-trinitrophenyl (TNP) lysine, which absorbs maximally at 346 nm [121]. A calibration curve to measure free Lys residues following trinitrophenylation was prepared (Fig. S2.6, ESI) and used to determine the number of free amine groups per BSA-Ln-UCNP nanoparticle. We determined that each BSA molecule attached to a Ln-UCNP contained 19 reactive free primary amine groups out of 60 Lys residues per BSA molecule. This represents a total of approximately 2128 primary amine conjugation sites per BSA-Ln-UCNP.

The upconversion emission spectra of a dispersion of BSA-Ln-UCNPs (0.1 wt% in H_2O and a solution of RB-BSA-Ln-UCNPs (0.1 wt% in H_2O) with different RB concentrations (30, 20, 3 μM equal 1292, 855, and 133 RB molecules per BSA-Ln-UCNP, respectively) are shown in Figure 2.4. We observe a significant difference in the intensities of the green peak centered at 550 nm of

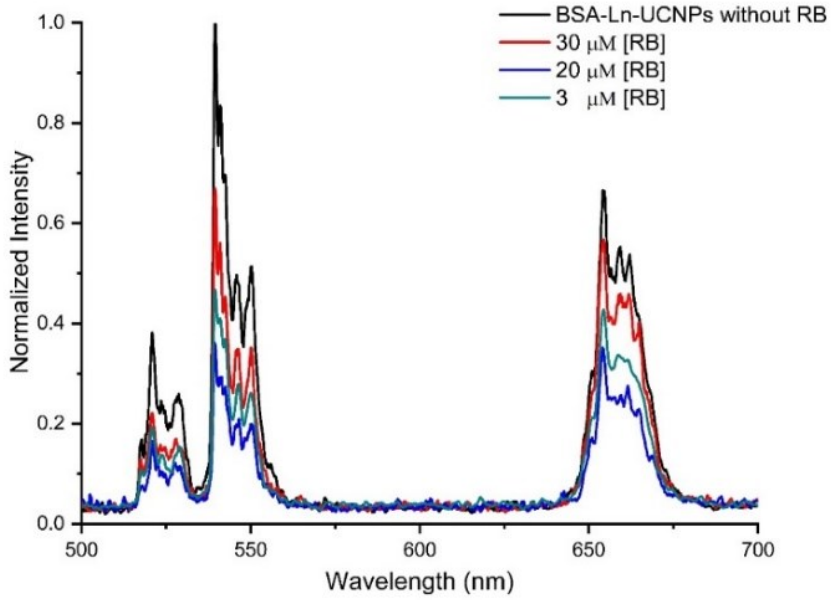

Figure 2.4 Energy transfer spectrum of different RB conjugated to surface of BSA coated $NaGdF_4$: Yb^{3+}/Er^{3+} under 980 nm excitation. Values at the legend represent the concentrations of 1 mg/mL of RB-BSA-Ln-UCNPs in H_2O.

the RB-BSA-Ln-UCNPs in comparison to the respective peaks for the BSA-Ln-UCNPs. This provides evidence of energy transfer from the Ln-UCNPs to the RB. The maximum energy transfer efficiency was calculated using the following equation,

$$E = 1 - (I_1/I_2)$$

where E is the energy transfer efficiency, I_1 is the intensity of RB-BSA-Ln-UCNPs at 550 nm, and I_2 is the intensity of the BSA-Ln-UCNPs at 550nm. The maximum energy transfer efficiency was calculated to be 68 %.

The nanoconstruct (RB-BSA-Ln-UCNPs) was assessed with respect to its production of $^1O_2$ under 980 nm excitation, using the standard reaction of 1,3-diphenylisobenzofuran (DPBF) with singlet oxygen, where the decrease in the absorption peak for DPBF at 415 nm represents the amount of singlet oxygen produced[35]. The nanoconstruct was irradiated with 980 nm light over a period of 90 minutes at 15 minute intervals. Assuming that the reaction between $^1O_2$ and DPBF

occurs in a 1:1 ratio, the number of $^1O_2$ molecules produced was calculated to be 5.9×10^{21} (Figure S7). This value is higher than the threshold required to induce cell damage that has been estimated to be 7×10^9 [122].

Using confocal microscopy, we evaluated the localization of RB hexanoic ester, BSA-Ln-UCNPs and RB-BSA-Ln-UCNPs in the mammalian cancer cell line A549. The confocal images

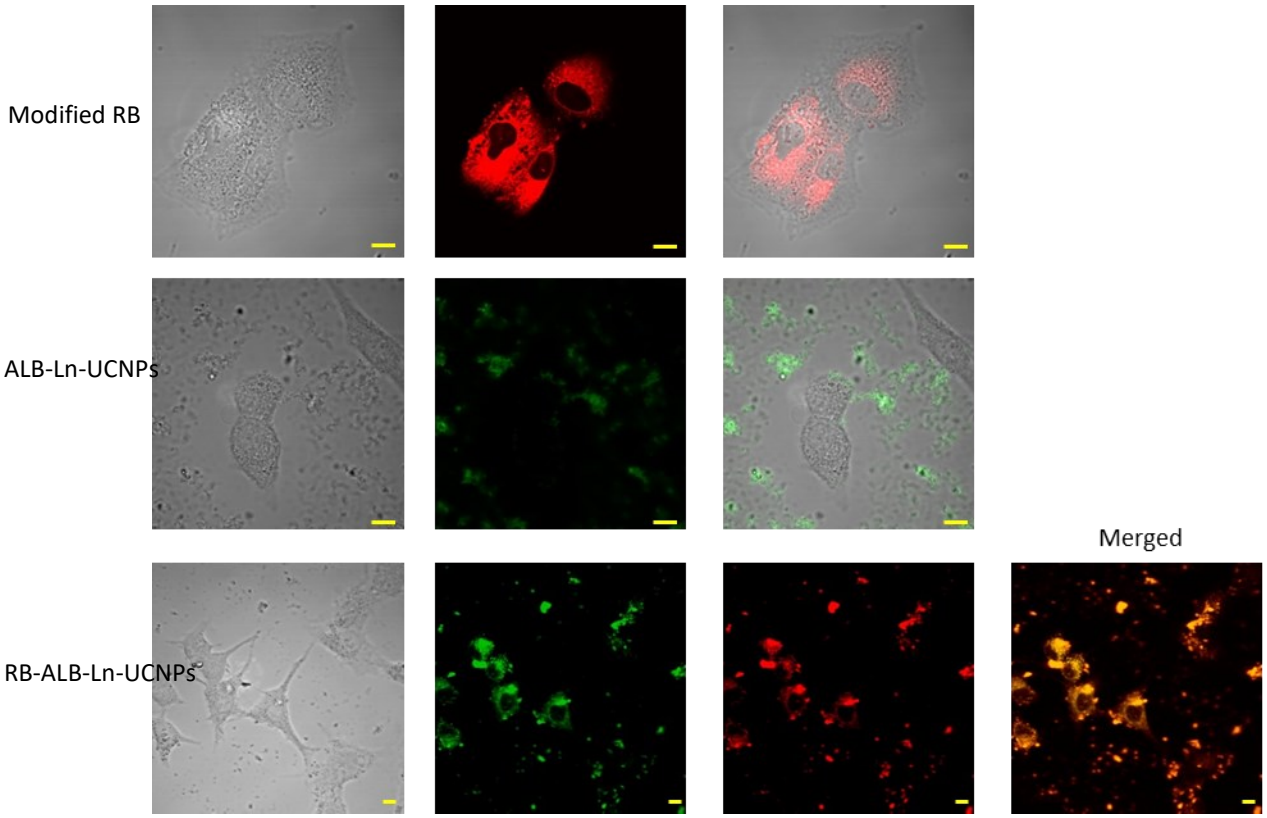

Figure 2.5 Confocal images of A549 cancer cell line. All red colored images represent emission from RB with excitation 548 nm, and green images represents emission from Ln-UCNPs with 980 nm excitation. (Top) Localization of modified RB, shown from the merged image RB localize in the cytosol. (Middle) Represent localization of BSA coated NaGdF4: Yb^{3+}/Er^{3+}(BSA-Ln-UCNPs). (Bottom) RB-BSA-Ln-UCNPs localization, merged image show that RB-BSA-Ln-UCNPs localize inside the cells occupying the cytosol of A549 cells.

(Fig. 2.5) clearly demonstrate that the RB-BSA-Ln-UCNPs are internalized by the A549 cells and reside in the cytosol. In contrast, BSA-Ln-UCNPs lacking RB were not internalized by the cells

rather they were found to be located around the membrane as clearly shown in the merged confocal image (Fig. 2.5). Collectively, these two results provided evidence that RB conjugation is necessary for the cellular uptake of BSA-Ln-UCNPs. Interestingly, albumin did not appear to be directly involved in cellular targeting of BSA-Ln-UCNPs, in contrast to reports of other albumin-coated NPs where uptake was thought to occur *via* albumin-binding 'scavenger receptors' [123]. Given that RB-dependent uptake of BSA-Ln-UCNPs into A549 cells occurred in a culture medium containing various serum proteins, the pre-loaded albumin hard corona appears to have played a 'stealth' role in preventing formation of an adventitious soft corona that could have interfered with cellular uptake. Taken together, our results support the idea that this nanoconstruct may have potential applications as a delivery vehicle of the RB that can be activated *via* energy transfer from the Ln-UCNPs to produce singlet oxygen for PDT. Furthermore, as a theranostic agent, this nanoconstruct can simultaneously be employed for deep tissue imaging.

In vitro cell viability tests using a MTT (3-(4,5-dimethylthiazol-2-yl)-2,5-diphenyltetrazolium bromide) tetrazolium reduction assay were carried out to ascertain the effect of different concentrations of RB-BSA-Ln-UCNPs on the cells in the absence and presence of 980 nm irradiation [124].

The A549 lung cancer cells were incubated with RB-BSA-Ln-UCNPs at concentrations of 10 to 250 μg mL^{-1} for 4 hours and were irradiated with 980 nm with power of 0.8 W for 10 minutes. In the absence of irradiation, the nanoconstruct demonstrated intrinsic cellular toxicity reaching 15 %. This similar activity has been recently shown for RB alone, that induces tumor regression and immunogenic cell death in human colon cancer cells while not affecting normal fibroblast cells [125]. However, following 980 nm excitation, an increase in toxicity was observed to be proportional to the nanoconstruct concentration (RB-BSA-Ln-UCNPs) and reached up to 36 %

cell death for a 10-minute exposure time using 250 µg concentration (Fig. S2.8, ESI). This toxicity level could be enhanced by increasing the concentrations of the nanoparticles, and exposure time.

CONCLUSION

In summary, we used a one-step approach we prepared BSA-coated monodisperse NaGdF4: Yb3+/Er3+ upconversion nanoparticles with a shell thickness of 2 nm, by crosslinking BSA on the surface of the nanoparticles in presence of glutaraldehyde and ethanol. Also, the structure of BSA attached to nanoconstruct surfaces was examined, and a loss of helical content was observed, indicating BSA unfolding. The number of BSA molecules and reactive primary amine groups were quantified, and this information was used to prepare RB-conjugated BSA-Ln-UCNP nanoconstructs. We demonstrated that RB conjugated to the surface of the BSA-Ln-UCNPs acquired a cellular targeting ability, facilitating cellular uptake of the nanoparticles. We also showed that energy transfer induces singlet oxygen release in vitro under 980 nm excitation and cause cellular toxicity of A549 cells within a 10-minute exposure time. The RB-BSA-Ln-UCNP nanoconstruct reported here provides additional targeting and cytotoxic capabilities to selectively detect and destroy tumor cells in deep tissue.

2.4 Experimental Section

2.4.1 Synthesis of $NaGdF_4$: Yb^{3+}/Er^{3+} (Ln-UCNPs)

Monodisperse upconverting $NaGdF_4$:Yb^{3+}/Er^{3+} nanoparticles were synthesised by thermal decomposition technique established by our group [41]. Erbium oxide (Er_2O_3, 99.99%), Gadolinium oxide (Gd_2O_3), Ytterbium oxide (Yb_2O_3), trifluoroacetic acid (CF_3COOH, 99%), Sodium trifluoroacetate ($NaCF_3COONa$, 98%), oleic acid (technical grade,90 %), and 1-octadecene (technical grade, 90%) were all purchased from Sigma-Aldrich and were used without any further

purification. First, lanthanides precursors are prepared by dissolving Gd_2O_3 (0.534 g, $9.75x10^{-4}$ mole, 78 mol %), Er_2O_3 (0.0096 g, $2.5x10^{-5}$ mole, 2 mol %), and Yb_2O_3 (0.0985 g, $2.5x10^{-4}$ mole, 20 mol %) in a 10 ml mixture of distilled water and trifluoroacetic acid (1:1) at 80 °C for 12 hours under reflux. The solvent was evaporated slowly at 60 °C for 16 hours to produce a white powder. Sodium trifluoroacetate (0.34 g, 2.5 $x10^{-3}$ mole) was added over the dried precursor and the solution is gradually heated up to 125 °C under vacuum in the presence of 7.5 mL oleic acid and 7.5 mL 1-octadecene. Meanwhile, a receiving flask containing 12.5 mL oleic acid and 12.5 mL 1-octadecene heated up to 150 °C under vacuum for 30 minutes, followed by a direct temperature increase up to 310 °C under inert atmosphere using gentle flow of argon gas. Heated precursors were injected to the receiving flask at rate of 1.5 mL/min using syringe and pump system and left stirring for an additional hour. The solution was cooled down to room temperature, and $NaGdF_4$: Yb^{3+}/Er^{3+} nanoparticles were precipitated with ethanol. Nanoparticles were isolated by centrifugation 3400 rpm for 15 minutes. For additional purification, collected pellet were washed twice with hexanes/ ethanol (1:4).

2.4.2 Transmission electron microscopy and negative staining

To determine the particle size and morphology, high resolution transmission electron microscopy using a Philips CM200 operated at 200kV equipped with a charge coupled device (CCD) camera (Gatan) was used. A solution of 0.1 wt % Ln-UCNPs was prepared in toluene and 15 µL of the solution was evaporated on a formavar/carbon film supported on a 200 mesh copper grid**.** Samples for the negative stain were prepared by adding 5 µL of BSA coated Ln-UCNPs in water (0.5

mg/mL) to copper grid, and sample left to air dry. Later, 5 uL of 1.5% uranyl formate solution in 5 M NaOH solution was added, incubated for 1 min and allowed to dry.

2.4.3 X-Ray powder diffraction

X-ray powder diffraction (XRPD) measurements was performed using Scintag XDS-2000 diffractometer equipped with Si(Li) solid state Peltier detector, a Cu Kα source using a generator power of 40mA and 45 kV, receiving beam slits (0.2-0.5 mm), and beam divergent (2 mm and 4 mm). The range of the scan was set between 20-80° 2θ with a 0.02° step size and a count time of 1 s.

2.4.4 Bovine serum albumin (BSA) coated $NaGdF_4$: Yb^{3+}/Er^{3+}

A modified version of BSA nanoparticle synthesis protocol [113], was used to produce water-monodisperse BSA coated $NaGdF_4$: Yb^{3+}/Er^{3+} (BSA-Ln-UCNPs). To prepare the coated nanoparticles, 2 mg of Ln-UCNPs were dispersed in 7 mL ethanol, sonicated for 10 minutes and injected using a syringe and pump system to a BSA (Bovine Serum Fraction V, Bioshop) solution 1mg/mL at a rate of 1 mL/min. Once the injection was terminated, different volumes (4, 15, 20, 30 µL) of (8%) glutaraldehyde solution was added, and the reaction stirred for an additional 4 hours. BSA-Ln-UCNPs were centrifuged (12470 g, for 5 minutes) and the white pellet washed 3 times with ultrapure water and stored in water at -20 °C.

2.4.5 Thermogravimetric Assay (TGA)

TGA was used to estimate the actual mass of BSA on the surface on of the Ln-UCNPs. The mass of oleate was quantified by measuring the mass loss of $NaGdF_4$: Yb^{3+}/Er^{3+} between 250-600 °C. Initial mass of the Ln-UCNPs used was 9.845 mg and showed a total weight loss of 2.65%. This represents 5.63×10^{16} molecules of oleate per 1 mg Ln-UCNPs, which corresponds to a surface coverage of approximately 15 % , based on the surface area of 0.4 nm^2 for the oleate molecule [115],

and 15290 nm^2 area of single Ln-UCNPs. The area of the Ln-UCNPs is calculated by measuring the average length of the hexagon prism shown by TEM. Similarly, TGA measurement was carried out for BSA-Ln-UCNPs and percent mass loss was recorded between 200 °C and 800 °C, showing a 15.24 % mass loss which represents 120.64 µg for 1 mg Ln-UCNPs. BSA has a molecular weight of 66 463 kDa, this will imply to 112 BSA molecules per single Ln-UCNP.

2.4.6 Primary amine quantification

Trinitrobenzenesulfonic acid (TNBS) a well-established method for primary amines quantification, and protein detection, was used to quantify free amine on BSA-Ln-UCNPs [121]. Briefly, 0.25 mL of TNBS solution in 0.01% $NaHCO_3$ was mixed with lysine standard solutions between 1-10 µg, for a total volume of 2 mL per sample to generate a standard curve. Mixtures were incubated for 2 hours at 37 °C, followed by addition of 0.25 mL 10% SDS, and 0.125 mL of 1M HCl generating an orange color that was quantified by measuring the absorbance at 346 nm. BSA-Ln-UCNPs quantification was obtained using the lysine standards. Based on calibration curve we estimated that 2128 primary amine sites per single BSA-Ln-UCNPs.

2.4.7 Luminescent intensity $NaGdF_4$: Yb^{3+}/Er^{3+}

To study the influence of water on the luminescence of the Er^{3+} ions of the BSA conjugated nanoparticles the emission spectra were recorded using ultra pure water and D_2O as the solvent. A 980 nm diode laser (F6 series fiber coupled, 0.5 W power) was used to excite the sample solution (1 wt %). The emission spectra were collected using a double monochromator (Jarrell-Ash Czerny Turner), photomultiplier tube (R943-02, Hamamatsu), SR440 (Standard research amplifier), SR400 (Gated photon counter), and SR465 (computer data acquisition software).

2.4.8 Rose Bengal linker addition, and surface conjugation

RB (Rose Bengal) was modified by adding a hexanoic acid linker to facilitate coupling with the primary amines of BSA that is coated on the nanoparticles surface [119]. In brief 50 mM RB and 125 mM 6-bromohexaonic acid were mixed in 70% acetone solution (20 mL) and refluxed at 60 °C for 18 hours. The reaction mixture was acidified with H_2SO_4 and extracted three times using dichloromethane (30 mL). The sample was dried under vacuum for 24 hours. Matrix assisted laser desorption ionization mass spectrometry (MALDI-MS) was used to confirm the modification to RB. In order to couple modified RB to BSA-Ln-UCNPs, 20 mM modified RB was mixed with 50 mM EDC (1-Ethyl-3-(3-dimethylaminopropyl)carbodiimide, Sigma-Aldrich) and 50 mM NHS (N-Hydroxysuccinimide, Sigma-Aldrich) in DMSO and stirred for three hours at room temperature. Different concentration of nanoparticles were added over the mixture and stirred overnight (in dark). Dialysis was performed using ultrapure water for 4 hours, and 16 hours using 12-14 kD membrane (Spectrum labs). RB-BSA-Ln-UNCPs are collected via centrifugation (14000 rpm), and washed three times using ultra pure water and the sample was stored at -20 °C.

2.4.9 Energy transfer measurements

The concentration of modified RB coupled to BSA-Ln-UCNPs was determined using RB calibration curve. Three different concentrations (30, 20, and 3 μM) were conjugated to BSA-Ln-UCNPs. For Luminescent intensity measurements, same concentration of Ln-UCNPs were optimized to 1 mg/ ml in water using ICP-MS (inductively coupled plasma mass spectrometry, Agilent 7500ce). BSA-Ln-UCNPs were used as standard emission under 980 nm excitation.

Energy transfer is attributed to the decrease in the intensity of $^4S_{3/2}$-$^4I_{15/2}$ transition at 540 nm for RB-Ln-UCNPs emission compared to BSA-Ln-UCNPs.

2.4.10 Singlet oxygen measurement

DPBF (1,3 dipenylisobenzofuran, Sigma-Aldrich) probe was used to detect singlet oxygen production [45]. RB-BSA-Ln-UCNPs (1mg/ml) are dispersed in 1:1 ratio in deuterated solvents of Dimethyl sulfoxide-d_6 (Sigma Aldrich), and D_2O (Sigma Aldrich). Absorbance of DPBF (35 μM) at 415 nm was measured prior to 980 nm laser irradiation. 980 nm excitation of RB-BSA-Ln-UCNPs was performed at 15 minute time intervals for a total time of 90 minutes. Assuming 1:1 ratio of singlet oxygen and DPBF, approximately 28 % of DPBF was consumed which was used to calculate the production of molecules of singlet oxygen (5.9×10^{21}).

2.4.11 In vitro localization assay

Cellular localization of the nanoconstruct was tested using A549 lung cancer cell lines. 35 mm cell culture dish cells are seeded with a density of 2.5×10^3 cells. After 24 hours, different concentration of RB-BSA-Ln-UCNPs were mixed with 2 mL cell culture medium that contained F-12k (Wisent Bioproducts) with 10% FBS (Thermofisher Scientific), and 1% Penicillin/ streptomycin (Thermofisher Scientific) (10, 000 U)/mL. RB-Ln-UCNPs were incubated for 4 hours, followed by isotonic saline washing using PBS (Thermofisher Scietific). Furthermore, cells are fixed with 10 % formalin (Sigma Aldrich) for 15 minutes, followed by washing with PBS twice. Fixed cells are stored at 4 °C, and imaged using a Zeiss LSM780 confocal microscope.

2.4.12 Cell viability assay

A549 lung cancer cells were seeded on 96-well plate with a density of 5000 cells/ well. The cells allowed to grow for 18 hours, followed by PBS wash and the addition of 100 μL cell culture medium (F-12k medium with 10% FBS and 1% Penicillin/streptomycin (10, 000 U)/mL).

Different concentrations of RB-BSA-Ln-UCNPs were incubated with A549 cells for 4 hours at 37 °C. The cells are washed with PBS and incubated for additional hour at 37 °C in cell culture medium. After this, cells are irradiated with 980 nm for a period of 10 minutes. A549 cells are allowed to grow for additional 18 hours. Later MTT ((3-[4,5-dimethylthiozol-2-yl]-2,5-diphenyltetrazoliumbromide, Thermo-Fisher Scientific) reagent (0.2 mg/mL in cell culture medium) was added to cells and incubated for 4 hours at 37 °C. Formazan crystals formed are dissolved by the addition of 150 μL of DMSO, and MTT absorbance at 590 nm measured using 96-well plate (BioTeK). Same procedure as above was done for RB-BSA-Ln-UCNPs but without irradiation to estimate the toxicity of nanoconstruct by itself for A549 cells.

2.5 Supporting Information

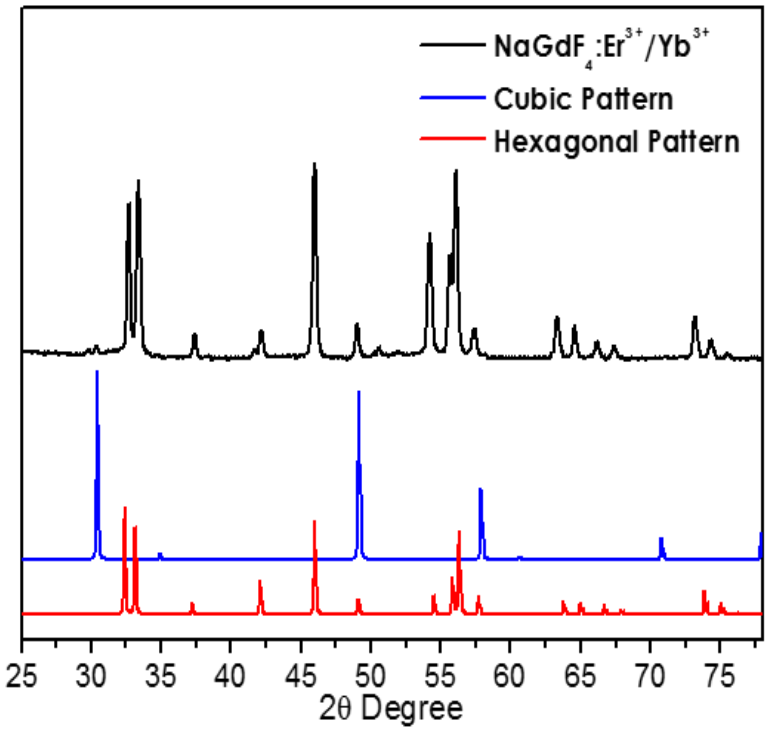

Figure S 2.1 X-ray powder diffraction pattern of $NaGdF_4$: Yb^{3+}/Er^{3+} (Black). Spectrum comparisons are drawn to reference hexagonal and cubic phases shown in red and blue respectively.

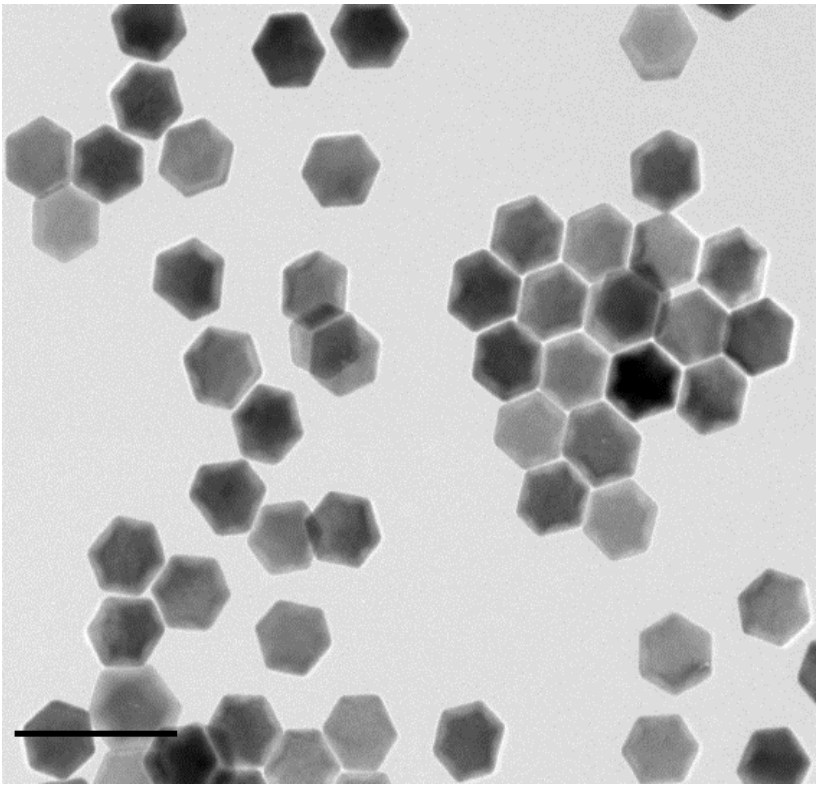

Figure S 2.2 TEM image of $NaGdF_4$: Yb^{3+}/Er^{3+} ,1% solution in Toluene. Average size of the particle is 78 nm +/-2.9 nm (scale 500 nm).

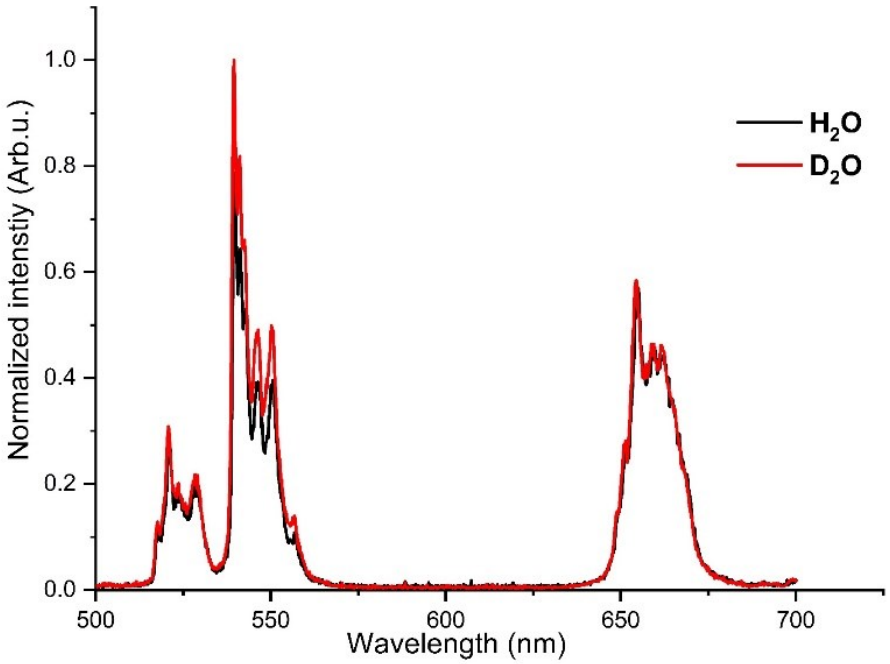

Figure S 2.3 Luminescent intensity measurements using 980 nm excitation. Same concentration of BSA coated $NaGdF_4$: Yb^{3+}/Er^{3+}used for both measurements (1mg/ml). In red sample in D_2O, and black in H_2O.

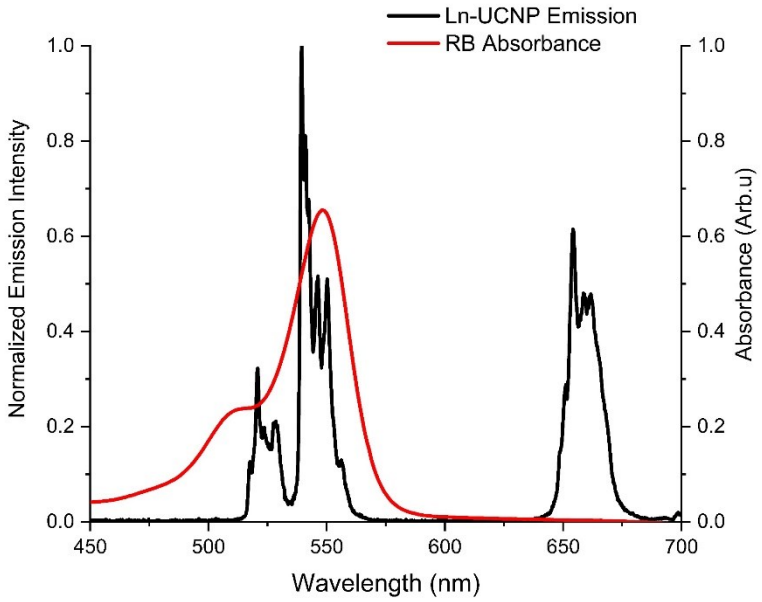

Figure S 2.5 Overlap spectrum of $NaGdF_4$: $Yb^{3+}/Er^{3+}$and RB. Luminescence emission using 980 nm excitation shown in black, and RB absorption shown in red.

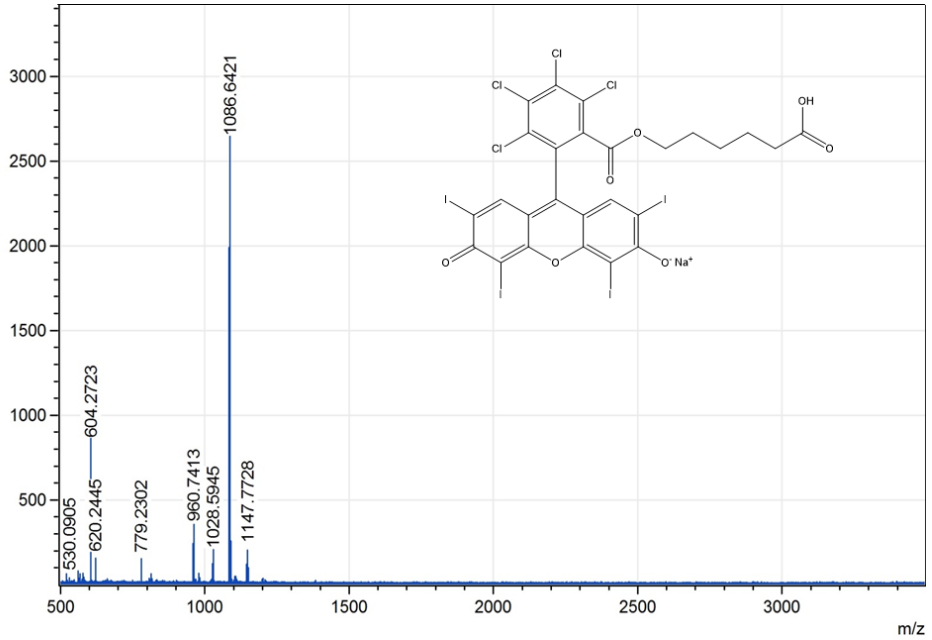

Figure S 2.4 MALDI-MS for hexanoic acid modified RB. (M-H) ionization peak at 1086.6421 represents the expected molecular weight for the modified RB.

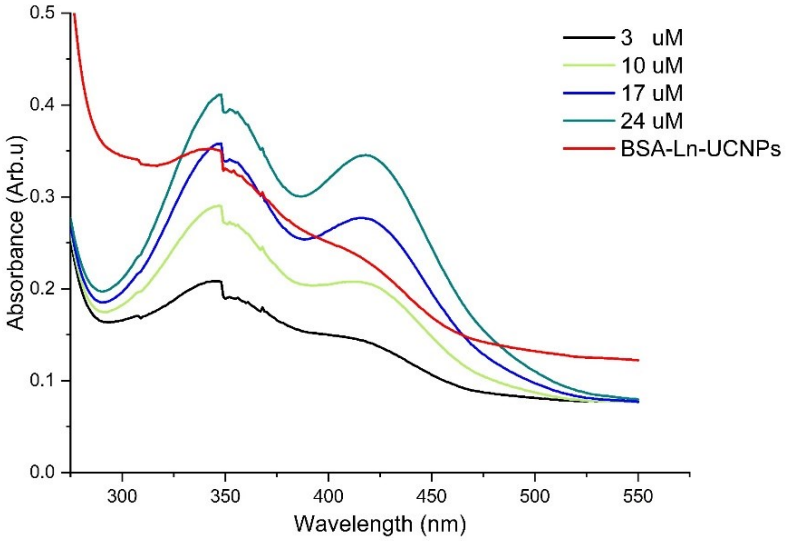

Figure S 2.6 TNBS assay for primary amine quantification. Lysine used as standard with different concentrations. BSA-Ln-UCNPs (1 mg/ml, H_2O) unknown primary amine concertation shown in red.

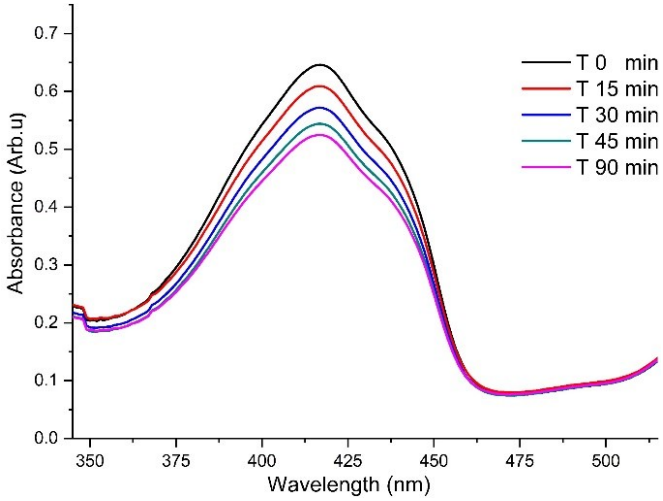

Figure S 2.7 DPBF absorption decrease as a function of irradiation time using 980 nm. 1mg/ml nanoparticles in deuterated DMSO and D_2O (1:1) with 35 μM DPBF.

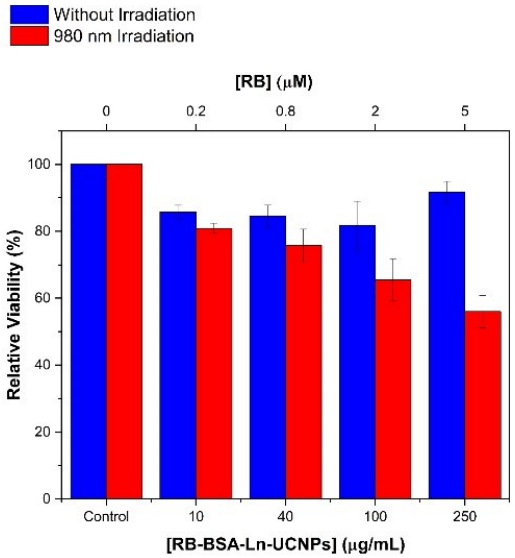

Figure S 2.8 Viability assay of A549 cell using different concentrations of RB-BSA-Ln-UCNPs. Blue columns without irradiation, and red columns under 980 nm excitation for 10 minutes period, using A549 cells. Four different concentrations 10, 40, 100, and 250 μg of nanoconstruct used.

Chapter 3. Selective glioblastoma cellular uptake of upconverting nanoparticles using an albumin-based targeted PDT surface coating

In preparation (ACS Applied Nano Materials)

Tarek Sabri, Gabrielle A. Mandl, Peter D. Pawelek, John A. Capobianco*

Department of Chemistry and Biochemistry, and Centre for NanoScience Research, Concordia University. 7141 Sherbrooke St. West, Montreal, Quebec H4B 1R6, Canada.

3.1 Abstract

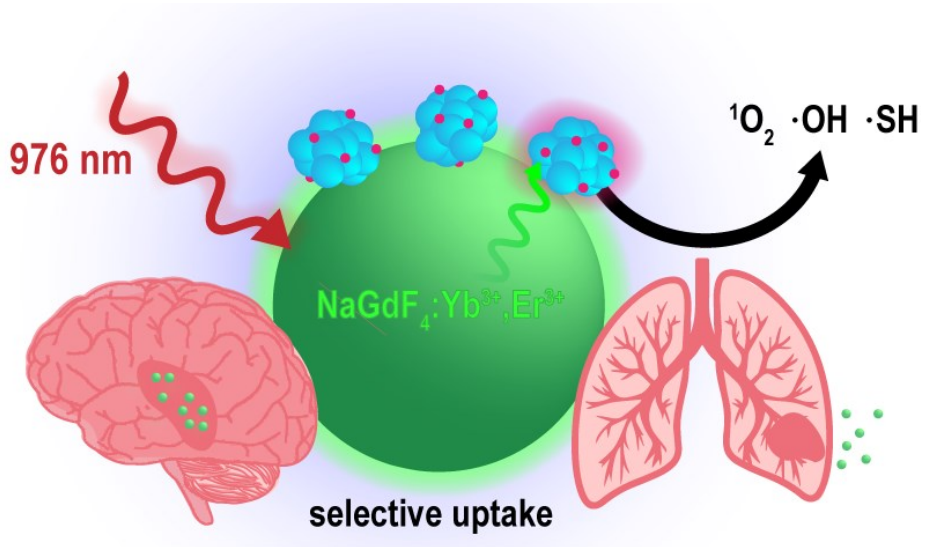

Scheme 3.1 Schematic representation of selective cellular uptake of RB albumin conjugated Ln-UCNPs

We report an approach to the conjugation of native albumin to the surface of upconverting nanoparticles, endowing the nanoconstructs with enhanced photosensitizer loading, and permitting selective delivery towards glioblastoma cells. Improved PDT efficacy was realized after nanoparticle internalization and the detection of ROS radicals under NIR irradiation was observed

3.2 Introduction

Although reactive oxygen species (ROS) are part of normal cellular metabolism, aberrant production of ROS can have significant effects on the cellular environment including redox homeostasis, cell functions and signalling pathways that regulate cell division and stress response systems[126]. Photodynamic therapy (PDT) is a non-invasive cancer treatment that induces ROS generation through the combination of photosensitizer (PS), light, and *in situ* oxygen to induce the production of singlet oxygen ($^1O_2$) and ROS that oxidizes lipids, proteins and DNA, destroying cellular and tumor vasculatures [127]. PDT has several disadvantages that affect its efficacy in cancer treatment. First, most of the commonly used PS that possess high $^1O_2$ yield are excited in the UV or visible range [128, 129]. This high-energy light can induce tissue damage, and has low tissue penetration depth[5]. Second, most PS lack the ability of tumor cell recognition, resulting in unintended uptake by healthy cells [130]. Third, due to an insufficient oxygen supply in tumors, $^1O_2$ production is limited, and consequently so is PDT efficacy [130].

Lanthanide doped upconversion nanoparticles (UCNPs) are near-infrared (NIR) energy transducers, undergoing a sequential absorption of two or more NIR photons that results in the emission of higher energy radiation (UV-Visible-NIR). NIR as an excitation source provides major advantages in the context of PDT. NIR radiation affords deeper tissue penetration due to reduced absorption and scattering [131, 132], and more importantly reduced photodamage of tissues by circumventing the requirement for the direct use of higher energy radiation [93]. Collectively, these features promote UCNPs as an excellent therapeutic tool for PDT, and other applications such as bioimaging [133], light mediated drug delivery [134, 135], biosensing [136], and optogenetics [137, 138].

However, effective delivery of nanoparticles (NPs) towards a specific biological target remains a major challenge for multiple reasons. First, the NP size, mechanical flexibility, surface charge, and functionality are all contributors for delivering NPs with their cargo to the target [139, 140]. Second, adsorption of serum protein (coronas) to NPs entering the body alters the biological identity of the NPs, diminishing targeting ability, as well as therapeutic efficacy [141].

Albumin (ALB) has garnered great attention as a loading and targeting nanocarrier for different cancer treatments. It is the most abundant protein in serum and is known to selectively accumulate in tumor tissue. It is also used as a major energy source for protein production in cancer cells [142]. ALB uptake in tumor vessels, malignant and stromal cells is dependent on the presence of albumin binding proteins (ABP), in particular the overexpression of metastasis-related extracellular matrix glycoprotein (gp 60), and SPARC (secreted protein acidic and rich in cysteine) receptors which have high binding affinity to native serum albumin[143]. In this regard, Zhao et al. determined the presence of overexpressed SPARC on human colon tumor cells (HCT8) has facilitated the cellular uptake of cancer drugs encapsulated in ALB NPs that demonstrated enhanced toxicity [144]. Inspired by ALB targeting abilities, and the biological relevance of UCNPs in PDT, we developed a covalent linking strategy without the use of coupling reagent to load native ALB onto the UCNP surface. ALB provides biocompatibility and dispersibility of UCNPs in aqueous environment. Rose Bengal (RB) was chosen as a PS for its strong ALB binding affinity and excellent spectral overlap with UCNPs, producing type II and I photoreaction processes. The latter bypass the oxygen requirement for ROS production, which is important in hypoxic tumor environments. Incorporation of RB with ALB-UCNPs had no

influence on the cellular uptake behaviour on lung cancer cells (A549). However, ALB presence solely selectively permits intracellular targeting ability of UCNPs towards glioblastoma cancer cells (U251N), permitting an intense upconversion PDT effect demonstrated upon the 976 nm irradiation.

3.3 Results and Discussion

$NaGdF_4$: Yb^{3+}, Er^{3+} UCNPs were synthesized using a thermal decomposition method known to produce monodisperse and highly crystalline nanoparticles[10]. The synthesized UCNPs exhibited a hexagonal prism morphology, with an average size of 31.3 ± 1.6 nm **(Fig. 3.1A)** and a hexagonal crystal phase **(Fig. S3.1)**.

The as-synthesized oleate-capped UCNPs are only dispersible in nonpolar organic solvents. To this end, oleate-free UCNPs were prepared and 6-maleimdohexanoic acid (MA) was introduced as a bifunctional linker to be grafted on the NP surface. The carboxylic acid moiety of MA coordinates with the positively charged surface of the oleate free UCNP surface, and the maleimide end acts as a thiol targeting group, forming a stable thioether adduct at pH 7.4 [145]. To confirm the grafting of MA linker, the stretching modes of free and conjugated MA are compared as shown in **Fig. S3.2**. Maleimide groups extending from the UCNPs surface were then used as anchors for the thiol group on bovine serum albumin at pH 7.4. Kratz et al. reported that albumin possesses a single thiol group (cysteine 34) at neutral pH, which is used for conjugating maleimide modified doxorubicin to ALB for enhancing chemotherapeutic drug delivery [146]. By mixing ALB with MA-UCNPs in PBS buffer at pH 7.4, coupling was performed, without the need for additional coupling reagents, to generate ALB-coupled MA-UCNPs (ALB-UCNPs). Thermogravimetric assays (TGA) were employed to estimate the number of ALB molecules loaded on UCNPs.

Initially, surface MA molecules were quantified, and determined to be 10.82 µg MA/mg UCNPs, corresponding to 2030 molecules per NP. Similarly, TGA was applied to ALB-UCNPs identifying the presence of 31.34 µg of ALB, giving resulting in approximately 18 ALB per NP (**Fig. 3.1B**). This translates to a 25.7 % surface coverage using 64 nm^2 as ALB surface area [116], with the calculated area of a single UCNP ~ 4488.4 nm^2. Liu et al. identified that carboxylate anions have a higher binding affinity towards lanthanide ions on the (100) facet of hexagonal phase NPs [147]. This indicates that the MA linkers are potentially asymmetrically grouped on one facet. Additionally, the globular size of ALB

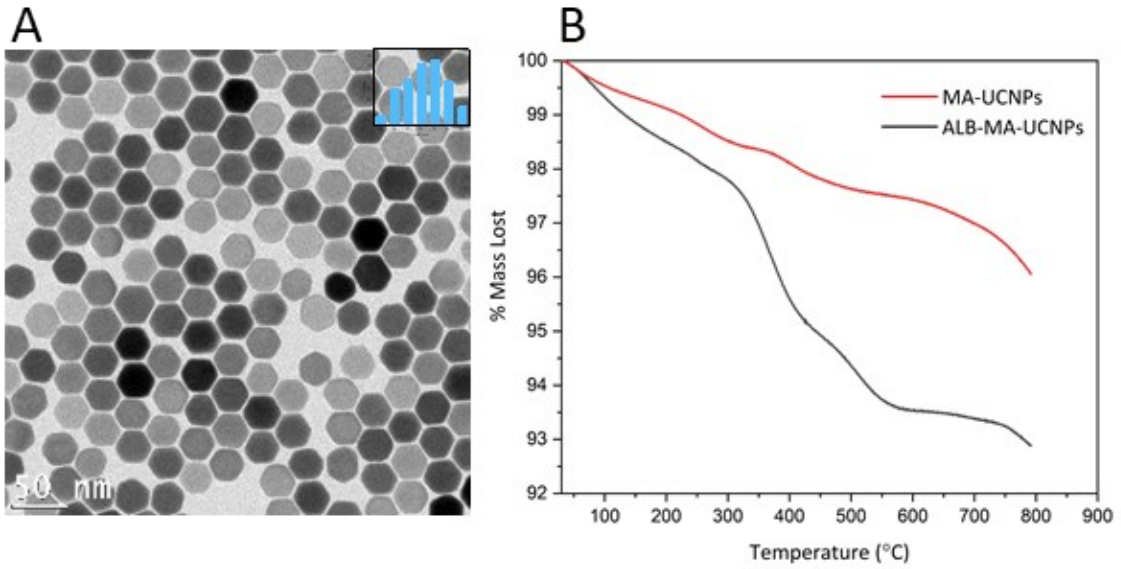

Figure 3.1 (A) TEM image of oleate capped UCNPs (NaGdF4: Yb^{3+} , Er^{3+}) 1 $mg.mL^{-1}$ dispersed in toluene. UCNPs measured between two opposite vertices giving average size distribution of 31.3 ± 1.6 nm as shown in the blue. (B) Thermogravimetric assay (TGA) in red MA-UCNPs, 6-maleimidohexanoic acid linker conjugated to NaGdF4: Yb^{3+}, Er^{3+} with a 1.29 % mass loss. Black curve represents albumin (ALB) conjugated with MA-UCNPs with a 3.86 % mass loss

prevents accessibility to neighbouring MA, consequently decreasing the UCNP percent

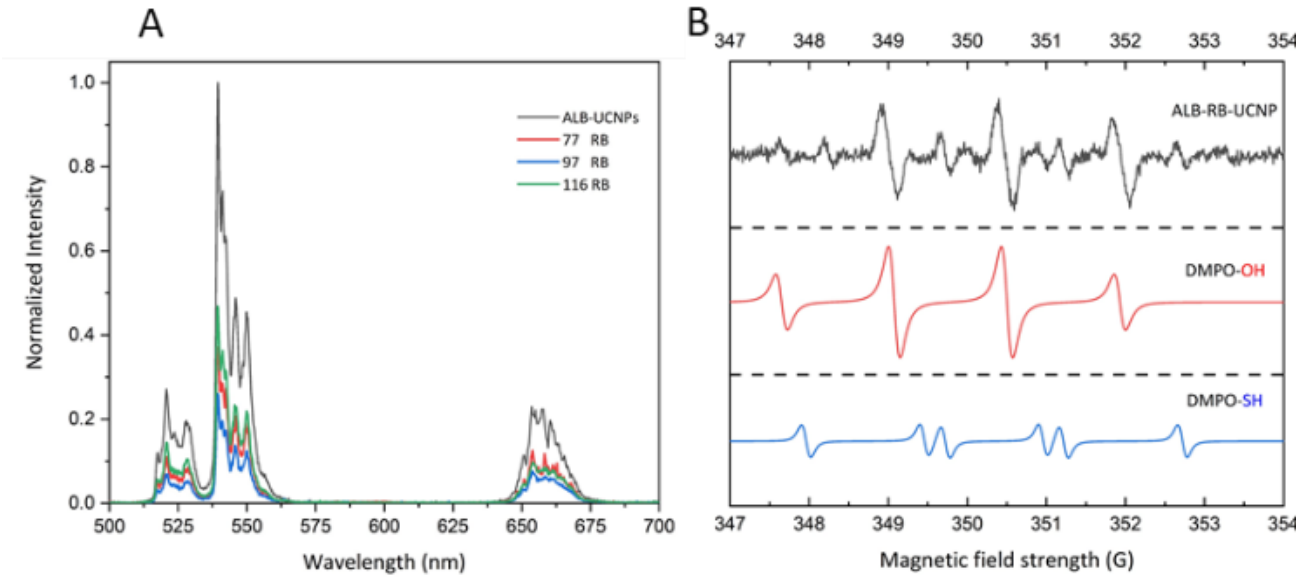

Figure 3.2 (A) Energy transfer emission spectra of ALB conjugated UCNPs (ALB-UCNPs), and in the presence of different RB concentrations using 980 nm irradiation. Values at the legend corresponds to 2 mg.mL-1 nanoparticles in PBS solution, and the number of RB molecules present in a single nanoparticles(RB-ALB-UCNP). (B) Electron paramagnetic resonance of RB-ALB-UCNP with DMPO spin trap and the corresponding stimulated adducts

surface coverage. This postulation was consistent with an observed shift in the intrinsic fluorescence maximum of tryptophan that showed a 6 nm blue shift (**Fig. S3.3**) , which has been used as a diagnostic landmark for ALB clustering [148].

In order to impart the ALB-UCNPs with PDT capability, Rose Bengal (RB) was chosen as a photosensitizer. RB has a high $^1O_2$ quantum yield and low rate of photodegradation, resulting in efficient ROS production [149]. Also, RB absorbance has a strong spectral overlap with the green emission from Er^{3+} in the UCNPs, with a maximum overlap centered at 540 nm (**Fig. S3.4A**) which is attributed to the $^4S_{3/2}$-$^4I_{15/2}$ transition of Er^{3+} (**Fig. S3.4B**). This spectral overlap is necessary for energy transfer to RB, and therefore for triggering the production of ROS. Apart from the advantages listed above, Alarcón et al. showed that RB possesses high binding affinity for native ALB, reaching up to 10 molecules of RB for a single ALB molecule, with a high $^1O_2$ flux at low RB concentrations [150]. To determine the optimal RB loading for the UCNP-PDT system, we loaded 3 different RB concentrations

onto the ALB; 1.96, 2.45, and 2.94 μM, corresponding respectively to approximately 77, 97 and 116 molecules for a single ALB-UCNP based on an RB standard curve (**Fig. S3.5**). The range studied permits the presence of less than 7 RB molecules per ALB, based on the total 18 ALB present on a single UCNP. Low RB concentrations are important to prevent stacking and triplet state quenching which are known to significantly affect ROS production[150]. Upconversion emission spectroscopy at 976 nm excitation of the different RB loaded concentrations (RB-ALB-UCNP) was performed, with maximum energy transfer (74.02 %) observed at 97 RB loaded per UCNP, corresponding approximately to 5 RB molecules for a single ALB molecule (**Fig. 3.2A**). Energy transfer was calculated based on the decrease in emission intensity from the $^4S_{3/2}$-$^4I_{15/2}$ Er^{3+} transition for UCNPs in the absence and presence of RB.

ROS production was first evaluated using DPBF (1,3-diphenylisobenzofuran), a known probe for activity towards different radicals [151], with higher sensitivity towards the detection of $^1O_2$ which is implicated in type II photoreactions [152]. The RB-ALB-UCNPs were irradiated for 20 minutes in the presence of 25 μM DPBF, and in the absence and presence of sodium azide (NaN_3), a known $^1O_2$ quencher (**Fig. S3.6A, S3.6B**). The nanoconstruct showed a 54.4 %, and 42.3 % decrease in DPBF absorbance in the absence and presence of NaN_3, respectively (**Fig. S3.6C**). This change in DPBF signal in the presence of NaN_3 gives clear indication for the release of different ROS, in addition to confirming $^1O_2$ production.

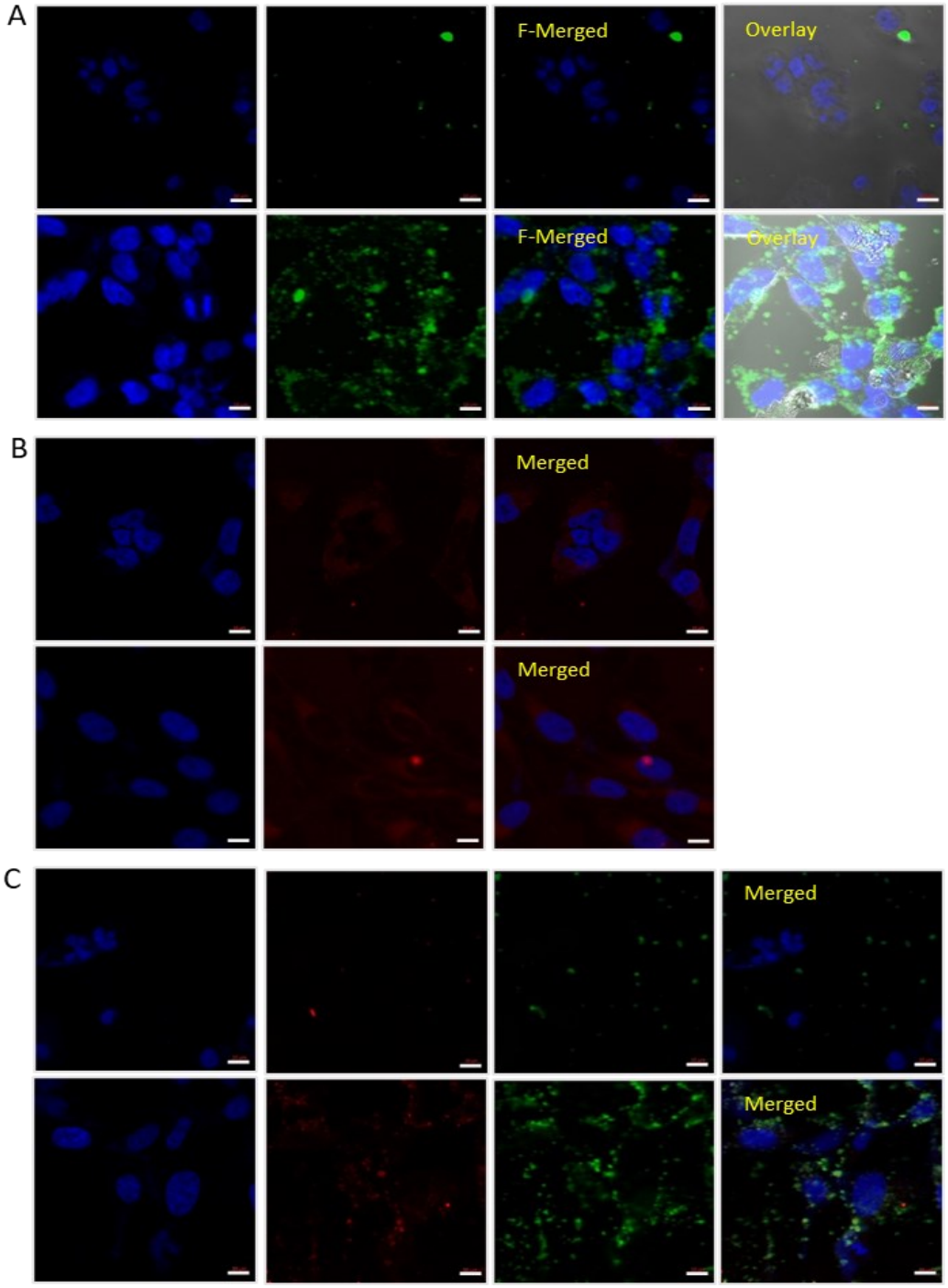

Figure 3.3 First row for each section (A,B, and C)represent confocal image of A549 , and second raw U251N. Blue color is the nuclei stain using DAPI, Green represents emission from UCNPs excited with 980 nm, and in Red is RB emission using 548 nm excitation. 200 $\mu g.mL^{-1}$ (of nanoconstruct is used. (A) cellular localization of ALB-UCNPs, F-merged represent fluorescent merged images. Overlay, is the merged images including bright field showing internalization of ALB-UCNPs into the cytosol. (B) cytosolic localization or RB without the nanoconstruct. (C) Represent RB-ALB-UCNPs localization, where cell uptake noticed for merged U251N image. Scale bar shown in white represents 10 µm

Electron paramagnetic resonance spectroscopy (EPR) is a technique that can be utilized to detect and identify the production of radical species through the use of a spin trap. The ROS produced by RB-ALB-UCNPs were evaluated using 5,5-dimethyl-1-pyrroline *N*-oxide (DMPO), a spin trap which forms adducts with oxygen, nitrogen and sulfur-based radicals, and 3,3,5,5-tetramethyl-1-pyrroline-N-oxide (TMPO), a spin trap that specifically reacts with superoxide radicals[153].

EPR spectra of an aqueous mixture of DMPO and the RB-ALB-UCNPs were obtained after 10 minutes of irradiation at 976 nm. As seen in **Fig. 3.2B**, the DMPO-OH radical adduct (α_N = 14.3 G, α_H = 14.3 G) was observed, confirming the production of type I photoreaction hydroxyl radicals by this system, in agreement with the RB-mediated production of hydroxyl radicals with X-PDT nanosystems [154]. The type I mechanism is oxygen-independent, which is a major advantage at deep tumor sites where oxygen is scarce[155], thus enhancing the efficacy of PDT. The DMPO-SH radical adduct (α_N = 15.0 G, α_H = 17.8 G) was also observed and can be attributed to the reaction of $^1O_2$ with the cysteine and methionine residues in the ALB coating the NPs [156]. The EPR results are thus in agreement with the absorbance-based assays for detecting ROS and $^1O_2$.

The efficacy of PDT is enhanced when ROS are produced inside the cells or at the vicinity of mitochondria [157]. However, different cancer cell lineages exhibit different expression levels of ALB binding proteins or receptors on their surfaces [158], consequently affecting the outcome of cellular trafficking of ALB NPs. Lin et al. reported that brain tumors overexpress SPARC, and gp60 proteins, which are responsible for cellular uptake of the ALB-modified paclitaxel cancer drug [159]. Two cancer cell lines, human alveolar epithelial

cancer (A549) and human glioblastoma (U251N), were used to evaluate the efficacy of the RB-ALB-UCNP for PDT, as these lines exhibit different expression levels of ALB binding proteins or receptors. Cellular uptake in each line was evaluated using the upconversion emissions of the ALB-UCNPs for NIR-excited confocal microscopy. Cellular uptake using A549 cancer cells showed no internalization behaviour, as observed by confocal microscopy (**Fig. 3.3A**). However, ALB- significant cellular uptake was observed in U251N as evidenced by the UCNP emissions spanning the area around the nuclei (**Fig. 3.3A**). To confirm that the ALB-UCNPs were residing in the cytosol, and not attached to the cellular membrane, orthogonal sections for z-stack confocal images show that the particles show heterogeneity in the cytosolic compartment (**Fig. S3.7**).

Further, we examined the effects of the presence of RB on cellular trafficking, as its presence was previously demonstrated to enhance the cellular uptake [160]. RB alone was shown to stain the cytosolic compartments for A549, and U251N cells (**Fig. 3.3B**) in both cell lines. Cellular localization of the RB-ALB-UCNPs in both lines showed similar uptake patterns as previously found for RB-free ALB-UCNPs (**Fig. 3.3C**). Since U251N was able to internalize the RB-ALB-UCNPs, the XTT cell viability assay was used to measure the intrinsic toxicity (without irradiation) and the PDT toxicity effect under 976 nm irradiation. A range of RB-ALB-UCNP doses from 10 to 120 μg/100 μL were evaluated. RB-ALB-UCNPs demonstrated intrinsic cellular toxicity at high concentrations of NPs (**Fig. S3.8**), which is in the accordance with the significant uptake of the nanoconstructs as shown by confocal microscopy. In contrast, low NP concentrations (60 μg/100 μL) did not show significant intrinsic cellular toxicity (**Fig. S3.8**). The same concentration ranges were applied to the U251N cells and excited with a 976 nm pulsed (5kHz) laser using a power

density of 0.3 W/cm^2 for 5 minutes. The RB-ALB-UCNPs demonstrated a very strong PDT effect at very low doses of NPs, inducing approximately 80 % decease in cellular viability for just 0.6 μg/100 μL of the nanoconstruct, as a result of the ROS ($^1O_2$, RS$^\bullet$, and HO$^\bullet$) released by RB excitation.

In conclusion, $NaGdF_4$:Yb^{3+}, Er^{3+} UCNPs were functionalized with native ALB without the use of coupling reagents, by utilizing the single thiol group present in cysteine 34 residues at physiological pH. We demonstrated that the presence of ALB on the UCNP surface induces a selective intracellular targeting ability towards glioblastoma U251N cells compared to A549 cells, owing to the presence of ALB binding proteins and receptors on the U251N surface. Incorporating RB PS with ALB revealed both type I and II PDT photoreactions confirmed by EPR and colorimetric measurements. *In vitro* toxicity using RB-ALB-UCNPs with 976 nm shows an intense PDT toxicity effect due to the internalization behaviour of U251N, and the released radicals that are in the vicinity of organelles within the cell. These results demonstrate an attractive approach in employing ALB as a surface loading carrier with selective targeted delivery towards cancer cell for enhanced PDT efficacy through the use of their intrinsic protein overexpression profile.

3.4 Experimental Procedures

3.4.1 Materials

All reagents used without further purification. Gd_2O_3 (99.99 %), Yb_2O_3 (99.99), Er_2O_3 (99.99), Sodium trifluoracetate, Oleic acid (90 %), 1-octadecene (90%), 1,3-Diphenylisobenzofuran (DPBF) (97%), Sodium Azide (99.5%), Deuterium oxide (99.99), 2-(4-Amidinophenyl)-6-indolecarbamidine dihydrochloride, Paraformaldehyde, and 6-Maleimidohexanoic acid were purchased from Sigma Aldrich. Rose Bengal was purchased from Alfa Aesar. 3,3,5,5-Tetramethyl-1-pyrroline-N-oxide (TMPO) (≥95%) and 5,5-Dimethyl-1-pyrroline-N-oxide (DMPO) (≥98%) were purchased from Santa Cruz Biotechnology and used without further purification. CyQUANT XTT cell Viability Assay, Bovine Serum Albumin, and phosphate buffered saline (PBS), Gibco GlutaMaX-DMEM (Dulbecco's modified eagle medium), FBS (fetal bovine serum), and Penicillin-Streptomycin (10,000 U/mL) were purchased from Fisher Scientific. 35 mm Dish Poly-D-Lysine coated coverslip was purchased from MatTek Life Sciences.

3.4.2 Thermal Decomposition Synthesis of $NaGdF_4$: Yb^{3+}, Er^{3+}

Monodisperse lanthanide-doped upconverting nanoparticles were synthesized using the thermal decomposition technique previously reported in the literature [11]. Trifluoroacetate precursors were prepared by refluxing lanthanide oxides Gd_2O_3 (78 mol %, 0.534 g, 9.75x 10^{-04} mol), Yb_2O_3 (20 mol %, 98.5 mg, 2.5 x 10^{-04} mol), and Er_2O_3 (2 mol %, 9.6 mg, 0.25 x10^{-04} mol) with 10 ml of trifluoroacetic acid and distilled H_2O (1:1) overnight (18 h) at 80 °C. The transparent solution evaporated at 60 °C for 16 h, forming a white precipitate. Oleic acid (7.5 mL), 1-octadecene (7.5 mL), and sodium trifluoroacetate (0.34g, 0.25 x10-04) were added to the white precipitate, and gradually heated to 125 °C under vacuum. Meanwhile, in another receiving flask, Oleic acid (12.5 mL), and 1-octadecene (12.5 mL) were degassed for 25 minutes at 150 °C. The temperature of the

receiving flask was increased to 310 °C under an inert atmosphere (Ar) at a rate of 10 °C / minute. Using a syringe pump, the precursor was injected into the receiving flask at a rate of 1.5 mL/min, and the reaction was stirred for 60 minutes at 310 °C under an inert atmosphere (Ar). The mixture was cooled down to room temperature under argon, followed by the addition of ethanol (99%, 60 mL), and the nanoparticles were centrifuged at 3600 rpm for 15 minutes. To remove solvent residues, nanoparticles were washed twice with hexanes/ethanol (1:4).

3.4.3 Transmission electron microscopy (TEM)

Electron microscopy images were acquired using a Jeol-JEM-2100F microscope operated at 200 kV equipped CCD (charge coupled device) camera. The sample was prepared by making a 0.1 % solution of $NaGdF_4$: Yb^{3+}, Er^{3+} in toluene and sonicating for 10 minutes. 15 µL of the nanoparticle dispersion was deposited onto a formavar/carbon film-coated 300-mesh copper grid.

3.4.4 X-ray Powder Diffraction

X-ray diffraction patterns were measured using a Scintag XDS-2000 diffractometer equipped with a Si(Li) Peltier-cooled solid state detector, Cu Kα source, at a generator power of 45 kV and 40 mA, beam divergent (2 mm and 4 mm), and receiving slits (0.2-0.5 mm). The measurement scan covered the range 10-90° 2θ with a step size of 0.01° and count time of 2 seconds. All samples were measured using a quartz zero background disk.

3.4.5 $NaGdF_4$: Yb^{3+}, Er^{3+} upconversion emission spectra

The luminescence emission of the $NaGdF_4$: Yb^{3+}, Er^{3+} UCNPs were measured following 976 nm excitation using a Coherent 6-pin fiber-coupled F6 series 980 nm laser diode coupled to a 100 µm (core) fiber. The upconverted luminescence emissions were obtained from a sample of 2 mg. mL^{-1} UCNPs in toluene, and for albumin conjugated UCNPs 2 $mg.mL^{-1}$ in PBS at pH 7.4 . The upconverted visible emissions were collected at 90° with respect to the incident beam and

dispersed by a double monochromator (1180 grooves/mm, Jarrell-Ash Czerny-Turner 25-102 1 m) coupled to a cooled Hamamatsu R943-02 photomultiplier tube. The photomultiplier signal was processed using a gated photon counter model SR400 Stanford Research Systems data acquisition system as an interface between the computer and the spectroscopic hardware.

3.4.6 Oleate removal and linker coordination on $NaGdF_4$: Yb^{3+}, Er^{3+}

A modified version of the protocol for generating oleate-free upconversion nanoparticles was used[41]. Oleate-capped $NaGdF_4$: Yb^{3+}, Er^{3+} nanoparticles (30 mg) were dispersed in 3 mL of 0.1 M HCl solution for 30 minutes. Hexane (5 mL) was added to the nanoparticles to extract oleic acid released into the solution. This extraction procedure was repeated 3-5 times until the solution becomes clear. The aqueous layer was collected and centrifuged with acetone (1:5) at 13000 rpm for 20 minutes. Nanoparticles were precipitated and washed twice with (1:1) water/ethanol solution, centrifuging at 13000 rpm for 20 minutes. Collected nanoparticles were redispersed in distilled water for further use. 5 mg of oleate-free nanoparticles were then dispersed in 3 mL distilled water and mixed with 5 mg of 6-maleimidohexanic acid (linker). The solution was stirred for 18 hours, and precipitated using centrifugation at 8700 rpm for 20 minutes. The precipitated nanoparticles are dialysed with 12-14 kD MWCO in distilled water for 24 hours. Collected nanoparticles were redispersed in 1x PBS (pH 7.4) solution.

3.4.7 Fourier transform infrared spectroscopy (FT-IR)

6-maleimidohexanoic acid and 6-maleimidohexanoic acid-conjugated on nanoparticles were dried under vacuum. Dried samples are deposited onto a diamond ATR crystal of an iS550 FT-IR spectrometer (Thermofisher Scientific) utilizing ATR (attenuated total reflectance) mode. Spectra are collected with 64 scans and 0.8 cm resolution covering 2800-700 cm^{-1} range.

3.4.8 BSA surface coupling, and Rose Bengal photosensitizer loading

Albumin (0.5 $mg.mL^{-1}$) in PBS was added dropwise to the nanoparticles solution in PBS and stirred for 2 hours at room temperature. ALB-MA-UCNPs were precipitated by centrifugation at 8000 rpm for 10 minutes, and washed twice with 1x PBS (pH 7.4). Three different concentrations of RB (1.96, 2.45, and 2.94 µM) were added to aliquots of 1 $mg.mL^{-1}$ of ALB-MA-UCNPs. The mixture was stirred for 24 hours at 4 °C, and dialysed with 12-14 kD MWCO for an additional 24 hours at 4 °C. Purified RB-ALB-$NaGdF_4$: Yb^{3+}, Er^{3+}(UCNPs) conjugates were collected by centrifugation at 13000 rpm for 10 minutes.

3.4.9 Tryptophan emission spectra

Fluorescence emission spectra of ALB and ALB conjugated to $NaGdF_4$: Yb^{3+}, Er^{3+} were measured using a Varian Cary eclipse fluorescence spectrophotometer equipped with a xenon flash lamp and set to an 880 Hz acquisition rate. The excitation wavelength was 280 nm and the entrance and exit slits were set to 5 nm. The ALB concentration was set to 0.3 $mg.mL^{-1}$ in PBS solution at pH 7.4.

3.4.10 Thermogravimetric analysis of surface ligand

TGA measurements were carried out using TA instrument Q50 analyzer. A dried pellet of nanoparticles and its conjugates (6-8 mg) were placed into a platinum pan, and heated under nitrogen flow from 25 to 800 °C at a heating rate of 10 °C/minute. The 6-maleimidohexanoic acid linker-conjugated nanoparticles showed a 1.92 % mass loss, corresponding to 10.82 µg/mg nanoparticles. ALB coupled to the surface linker showed a 3.86% weight loss, corresponding to a net of 31.34 µg ALB/mg nanoparticles.

3.4.11 Energy transfer measurements

Different RB loading amounts onto the surface of $NaGdF_4$: Yb^{3+}, Er^{3+} were calculated from a calibration curve. Different amounts of RB were added to ALB-$NaGdF_4$: Yb^{3+}, Er^{3+} using a

concentration of 1mg.mL^{-1} UCNPs. To estimate energy transfer under 976 nm excitation, the upconversion emission spectrum of ALB-$NaGdF_4$: Yb^{3+}, Er^{3+} without RB was compared to the emission spectrum of RB-ALB- $NaGdF_4$: Yb^{3+}, Er^{3+} nanoparticles. The decrease in the intensity of the $^4S_{3/2}$-$^4I_{15/2}$ transition at 540 nm provides an estimate of energy transfer that is attributed to different RB concentrations.

3.4.12 Singlet oxygen detection

The DPBF (1,3 dipenylisobenzofuran) assay was used to detect reactive oxygen species released by RB-ALB-$NaGdF_4$: Yb^{3+}, Er^{3+} nanoparticles under 976 nm irradiation[44]. 25 µM of DPBF is added to 2 mg.mL^{-1} of nanoparticles. The first absorption measurement was acquired without irradiation, which provides a baseline DPBF signal. The DPBF and nanoparticles were then excited with 976 nm, and the absorption was recorded at 5 minute intervals for a total of 30 minutes of irradiation. The same procedure is followed for the NaN_3 (20 mM) treated nanoparticles.

3.4.13 Free Radicals detection with Electron paramagnetic resonance spectroscopy (EPR)

EPR spectra acquired using a Bruker Elexsys E580 X band EPR spectrometer (Karlsruhe, Germany) equipped with a high-sensitivity resonator cavity. The aqueous samples were analyzed in a 150 µL Suprasil flat cell with a 0.3 mm thickness. 1 G modulation amplitude and 20 mW power were used for acquisition. All samples were analyzed at a concentration of 50 mM TMPO or DMPO and 2 mg/mL nanoparticles in pH 7 H_2O. Sample irradiation was performed using a continuous wave 976 nm diode laser at a power density of 3 W/cm^2 at a distance of 5 cm from the sample. Aqueous solutions of TMPO and DMPO were analyzed by EPR spectroscopy prior to the addition of the nanoconstruct to ensure the paramagnetic purity of the spin trap. Polynomial baseline corrections were performed on each spectrum prior to fitting. Spectra were fitted using

SimLabel EPR spectroscopy software and MatLab 2019b. All spectra were fit using an isotropic g value of 2.0087 and correlation time of 2.25×10^{-10} s.

3.4.14 In vitro localization assay

ALB conjugated to $NaGdF_4$: Yb^{3+}, Er^{3+} was tested for cellular localization using U251N, and A549 cell lines. Using 35 mm poly-lysine cover slip coated dishes, 5×10^4 cells are seeded and left to grow for 24 hours in DMEM cell culture media supplemented with 10% FBS and 1% Penicillin/streptomycin (10, 000 U/mL). 0.3 µg of ALB conjugated $NaGdF_4$: Yb^{3+}, Er^{3+} were added to the wells, and incubated for 4 hours. The cells were washed twice with PBS, and fixed with 4% formalin for 15 minutes at room temperature, followed by washing twice with PBS. Fixed cells were imaged using an LSM780 confocal microscope.

3.4.15 Cell viability assay

U251N cells were seeded at a density of 5000 cells/well on a 96 well plate. After 18 hours of incubation, cells were washed with PBS, and 100 µL of fresh media (DMEM, 10% FBS, and 1% Pencillin/Streptomycin) was added per well. Different concentrations of RB-ALB-$NaGdF_4$: Yb^{3+}, Er^{3+} conjugates were added and incubated for 4 hours. Cells were irradiated with a pulsed 976 nm laser with a power density of 0.3 W/cm^2 and frequency of 5 KHz for 5 minutes. The cells were left to grow for an additional 16 hours, washed with PBS and 100 µL of media was added. The XTT assay was performed as recommended by the manufacturer. Briefly, the XTT reagent was thawed at 37 °C, and combined with the electron coupling reagent and 70 µL of the mixture added to each well. After 4 hours of incubation, absorbance at 450 nm, and 660 nm recorded using a 96-well plate reader, and specific absorbance is calculated according to the equation (Specific Absorbance = [Abs_{450nm} (Sample) – Abs_{450nm} (blank)] – Abs_{660nm}(Sample)).

3.5 Supporting Information

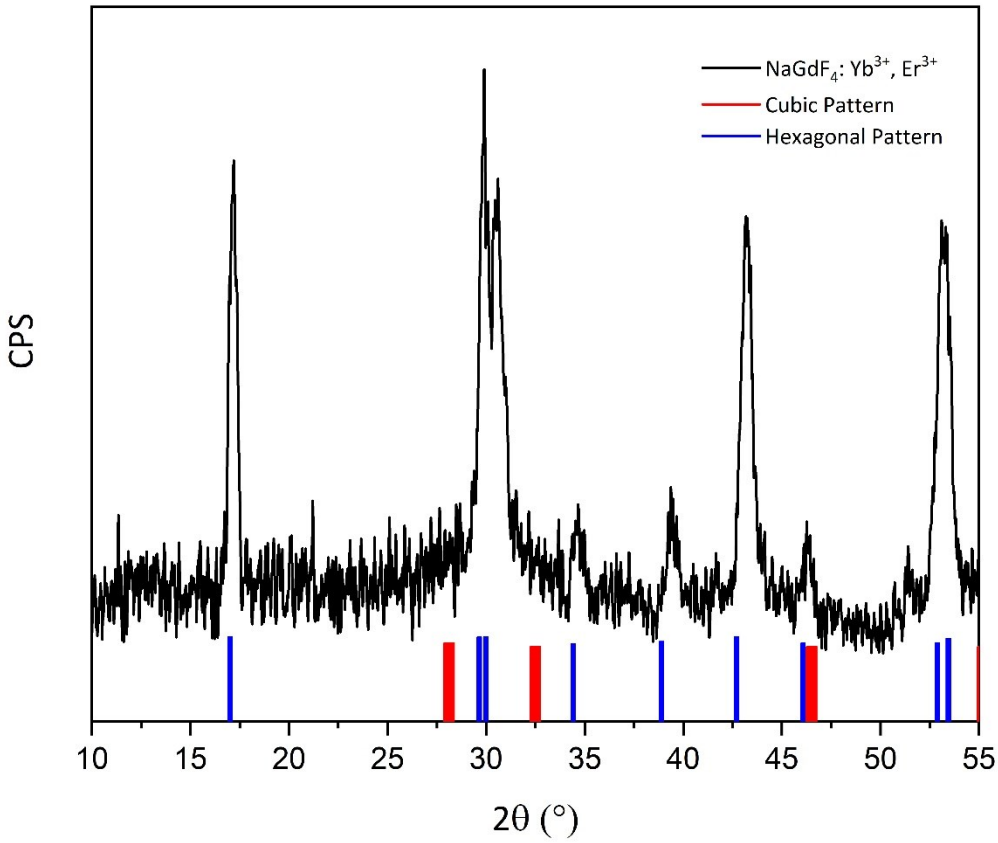

Figure S 3.1 X-ray powder diffraction of $NaGdF_4$: Yb^{3+}, Er^{3+} compared to hexagonal phase pattern (JCPDS card 27-0699) in blue, and cubic phase pattern in red (JCPDS card 27-0697). All diffraction are assigned to the hexagonal β-phase.

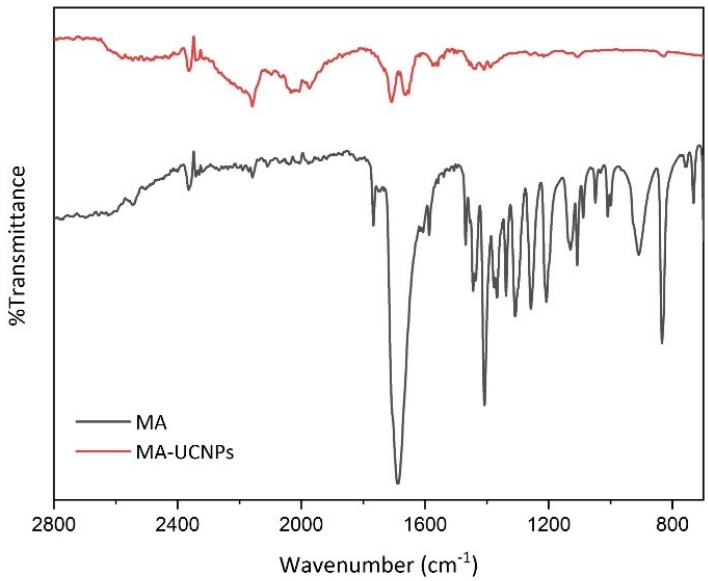

Figure S 3.2 FT-IR spectroscopy (Black) 6-maleimidohexanoic acid (MA), (Red) $NaGdF_4$: Yb^{3+}, Er^{3+} conjugated with MA. All measurements were performed on powder samples. The free MA exhibits an intense carbonyl stretch at 1693 cm^{-1} which splits into two bands when conjugated on the UCNP surface, attributed to symmetric (υ_s) and asymmetric (υ_{as}) carboxylate stretches at 1578 cm^{-1}, and 1443 cm^{-1} respectively. Maleimide group stretching modes of C-N (υ_s 1405 cm^{-1}, υ_{as} 1109 cm^{-1}), and =C-H bending modes (830 cm^{-1}) are also observed for both coordinated and free MA confirming linker coordination

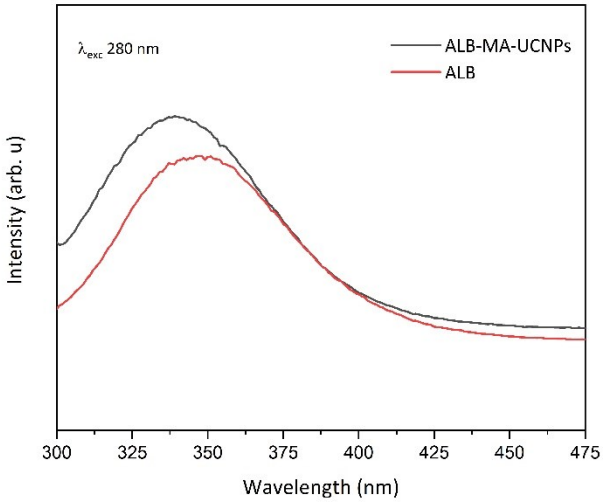

Figure S 3.3 Tryptophan fluorescence of native albumin (red) and ALB-MA-UCNPs (black) under λ_{exc} 280 nm in PBS buffer at pH 7.4.

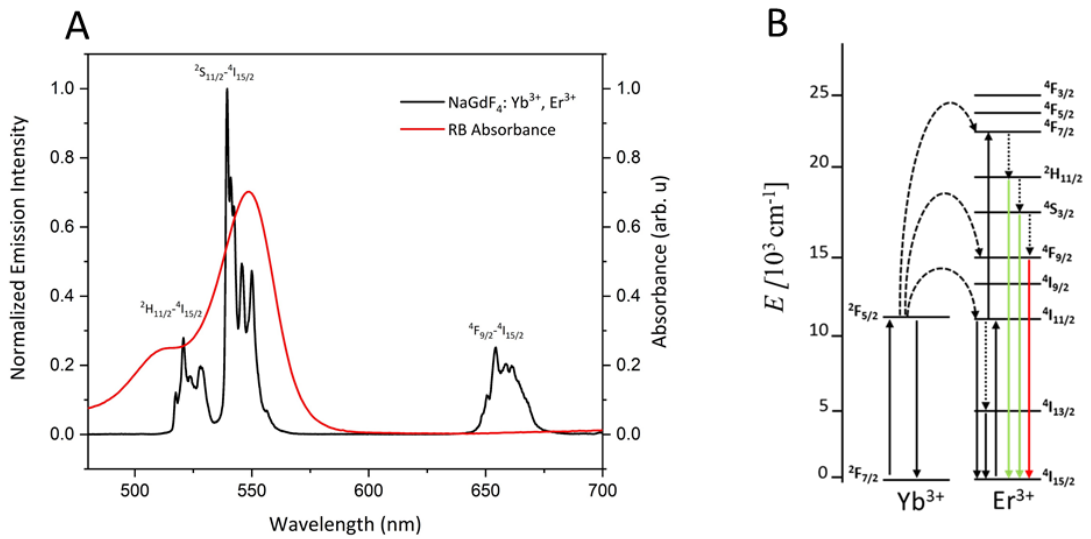

Figure S 3.4 A) Emission spectrum of UCNPs (black) irradiated at 976 nm, and RB absorbance shown in red. B) Energy level diagram showing the upconversion process of $NaGdF_4$: Yb^{3+}, Er^{3+} nanoparticles.

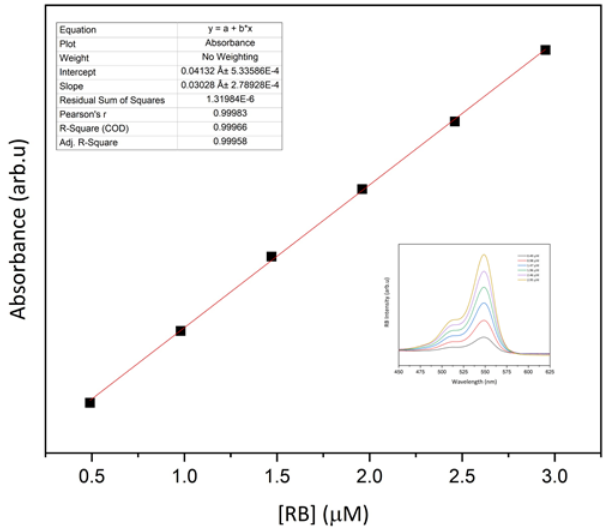

Figure S 3.5 Calibration curve of RB concentrations with corresponding RB UV-vis absorption spectra shown in the inset.

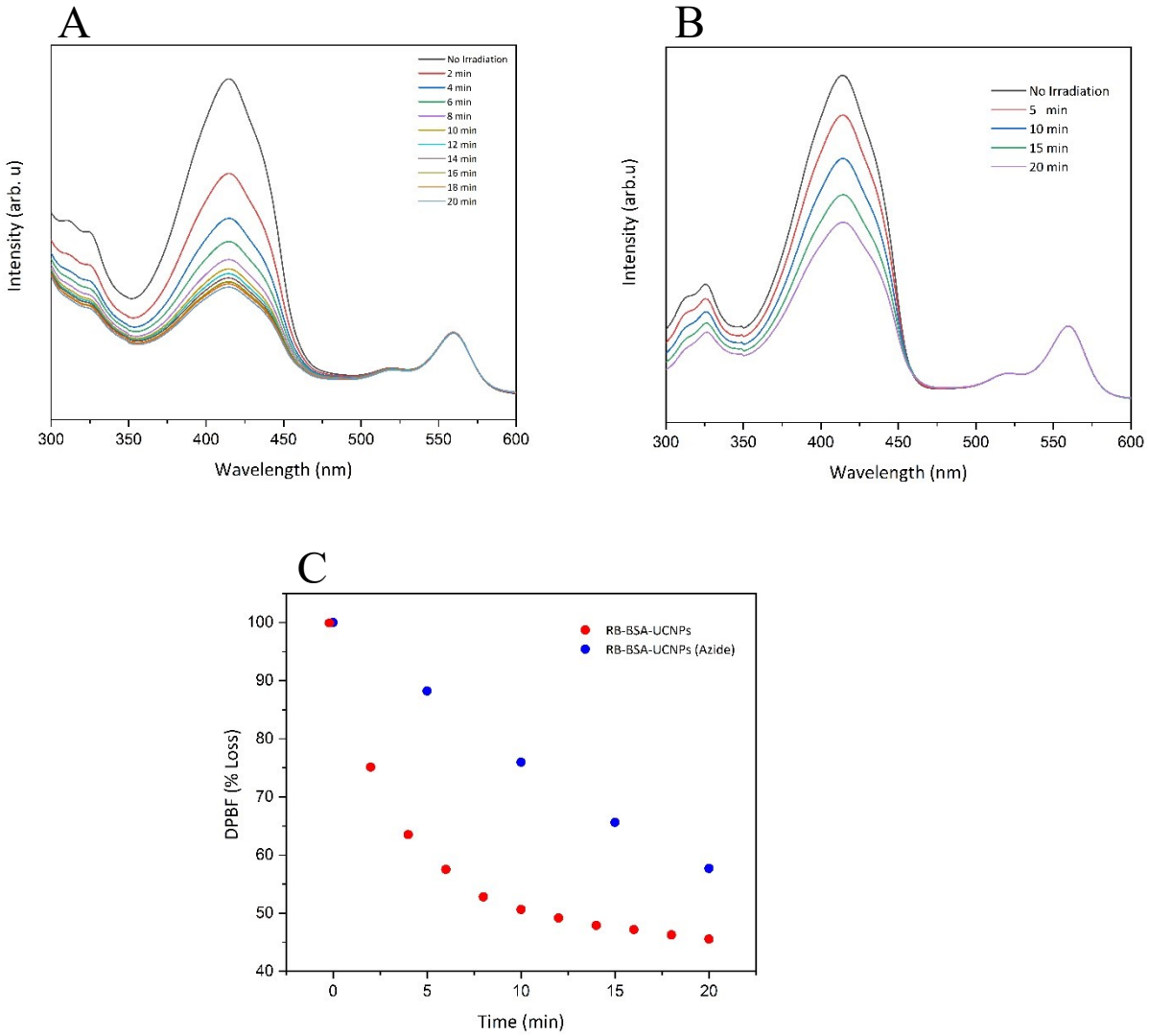

Figure S 3.6 DPBF absorption spectra as a function of irradiation time at 976 nm of 2mg.mL^{-1} of RB-ALB-UCNPs dispersed in PBS solution. (A) without sodium azide. (B) with 20 mM sodium azide. (C) Percentage decrease of the maximum absorbance for A and B.

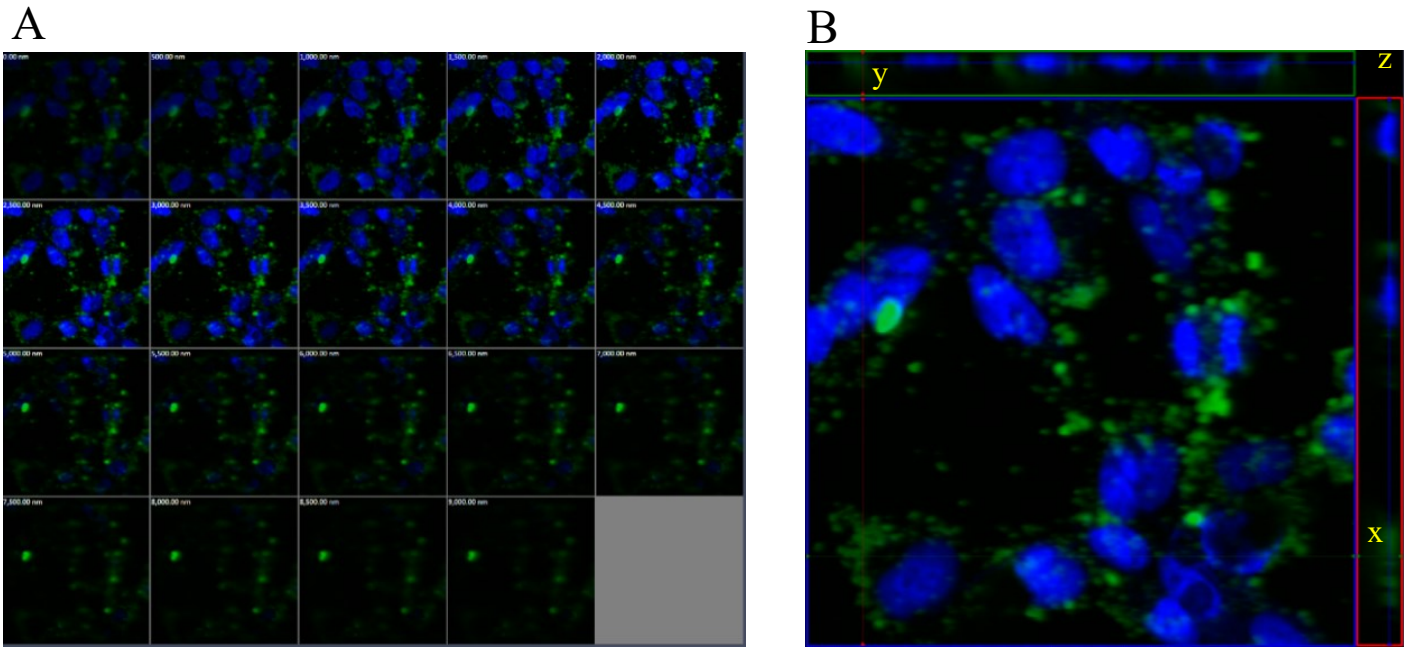

Figure S 3.7 A) confocal images of z-stack using U251N cells treated with ALB-UCNPs for 4 hours. B) Orthogonal projections representing cross sectional slices obtained from z-stack with 9 μM depth. Green is emission from ALB-UCNPs excited with 980 nm, with DAPI in blue as nuclear stain.

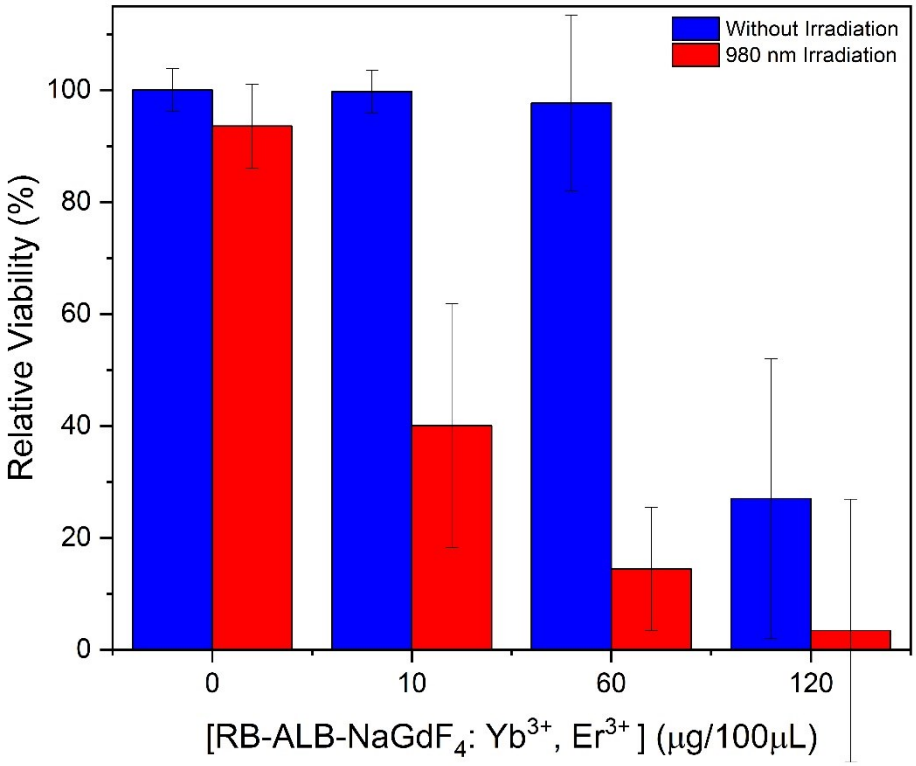

Figure S 3.8 Cell viability assays of different RB-ALB-UCNPs using U251N cancer cells without irradiation (blue) and with 976 nm irradiation (red).

Chapter 4. An intense, narrow, and sharp blue light emissive band from ultra-small lanthanides upconversion nanoparticles with active and inert shells

In preparation (Nanoscale advances)

Tarek Sabri, Steven Maurizio, John A. Capobianco*

Department of Chemistry and Biochemistry, and Centre for NanoScience Research, Concordia University. 7141 Sherbrooke St. West, Montreal, Quebec H4B 1R6, Canada.

4.1 Abstract

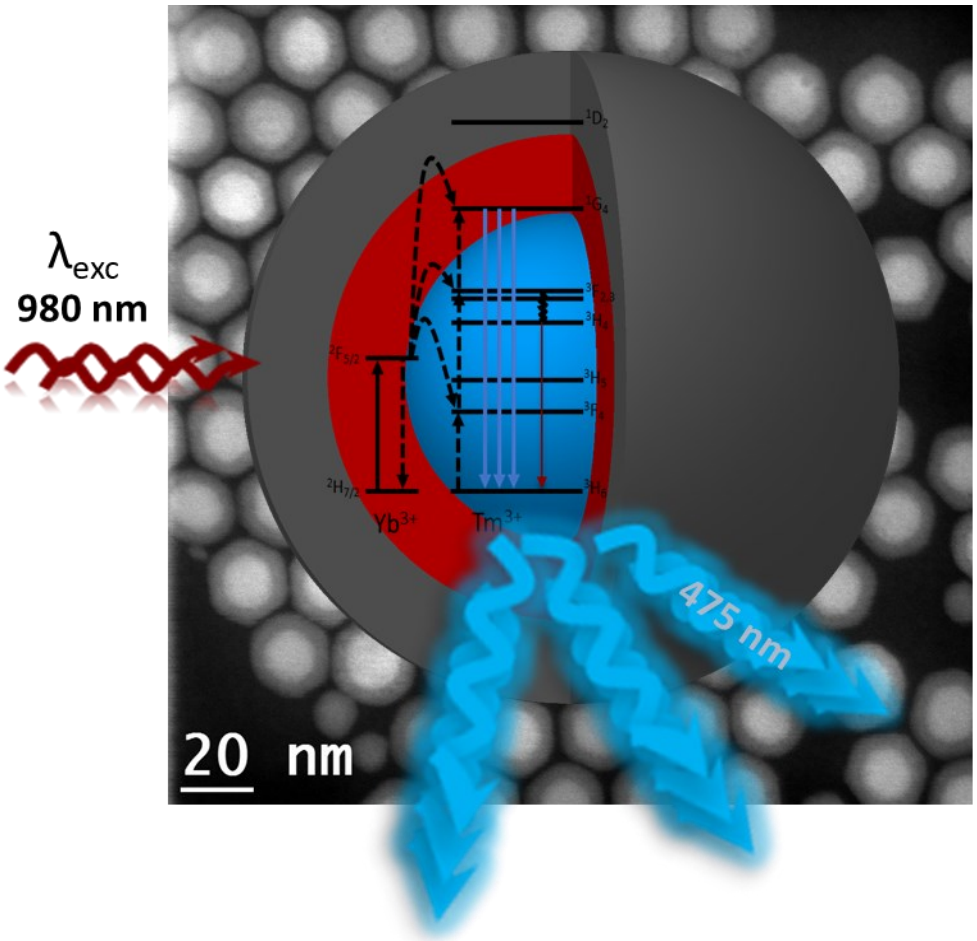

Scheme 4.1 Graphical representation of sub 10 nm core $NaGdF_4$:Yb^{3+},Tm^{3+} with active $NaGdF_4$:Yb^{3+} and inert $NaYF_4$ shell.

We report the synthesis of ultrasmall lanthanides upconversion nanoparticles, with an active, and inert shell. An intense 475 nm generated from Tm^{3+} core emitting center attributed to $^1G_4 \rightarrow {}^3H_6$ transmission is identified which surpass all of the transitions reported for similar lanthanides upconversion nanoparticles, including the 800 nm transition $^3H_4 \rightarrow {}^3H_6$.

4.2 Introduction

Lanthanide upconverting nanoparticles (UCNP) are efficient energy transducers with large anti-stokes shift that can absorb light efficiently in the near-infrared (NIR), while emitting *via* the process of upconversion in the UV-VIS-NIR regions of spectrum[7, 161].UCNPs are photostable, non susceptible to photobleaching, and have tunable emission profile based on lanthanides doping system[162, 163]. In addition, the low energy excitation radiation (NIR) can travel deeper into biological tissues [164]. These luminescent properties are ideal in developing of bio-application platforms. UCNPs have been extensively employed for imaging[165], biosensing [166], and cancer therapeutics[160, 167].

Currently there are new emerging efforts in designing blue light emitting UCNPs for its therapeutic functions. For example blue light affect harmfully human retina[168], and interfere with the circadian cycle[169]. Also, there are intrinsic naturally occurring photoreceptors present in human cells such as, flavin, porphyrin, and nitrosated proteins that are activated with blue light [170, 171], which are used for photodynamic therapy applications. Further, opsin protein (channelrhodopsins, ChR) channels are fired with blue light activation (470 nm) that manipulate neuronal signal behaviors , which could be employed for mental disorders such as, addiction, autism and anxiety [172]. However, for UCNPs to be employed in biological applications, it is required to have an intense emission to circumvent the quenching effects generated by O-H vibrations from water, and biomolecules that are deposited on UCNPs surface [173].

There are many efforts are employed to enhance luminesce intensity. Applying high power could be utilized to enhance all emission transitions. This pathway generate heat which provokes cellular toxicity, and should avoided for biological applications [174]. Luminesce intensity could also enhanced by varying dopant concentration of sensitizer/activator [15], or using dye sensitization that

can harvest excitation energy facilitating efficient upconversion emission [175, 176]. For example, Lowering Tm^{3+} concentration assist in decreasing cross relaxation mechanism, which enhance luminescence intensity. This has been reported for $LiYF_4$ host crystals, and showed only increase in the intensity of UV transition [177]. Similar approach was reported with $NaYYbF_4$:Tm^{3+} doped with varying Yb^{3+}, and Tm^{3+} concentration. However, 800 nm ($^3H_4 \rightarrow {}^3H_6$) was the major transition that showed significant enhancement. Surface plasmon resonance (SPR) is another approach applied to selectively enhance emission using metallic (Ag, Au) nanoparticles [178, 179]. Although SPR show strong enhancement, majority of the investigated transitions are related to green and red emissions in Er^{3+}doped UCNPs. Although these approaches are successful in enhancing different transitions, so far to our knowledge there have not been studies related to enhancing $^1G_4 \rightarrow {}^3H_6$ (475 nm) emission exclusively in Tm^{3+}doped UCNPs.

Herein, we report the synthesis of low Tm^{3+} concentration doped ultrasmall $NaGdF_4$ upconversion nanoparticles. Two layers of active and inert shell are added respectively, showing an intense, sharp blue light (475 nm) emission exceeding all other transitions emitting from Tm^{3+} ions, including the most intense 800 nm attributed to $^3H_4 \rightarrow {}^3H_6$ transition. Cross relaxation mechanism of Tm^{3+} processes of the high intensity transitions is analyzed. Using lifetime measurements, we identified a new mechanism that never been addressed for populating $^1G_4 \rightarrow {}^3H_6$ and $^3H_4 \rightarrow {}^3H_6$ states which is responsible for the blue bright emission. To use this design for PDT application, the core-shell-shell nanoparticles are coated with riboflavin (Rf) photosensitizer that has excellent spectral overlap with nanoparticles. Cytotoxic reactive singlet oxygen species are released and detected under NIR irradiation.

4.3 Discussion

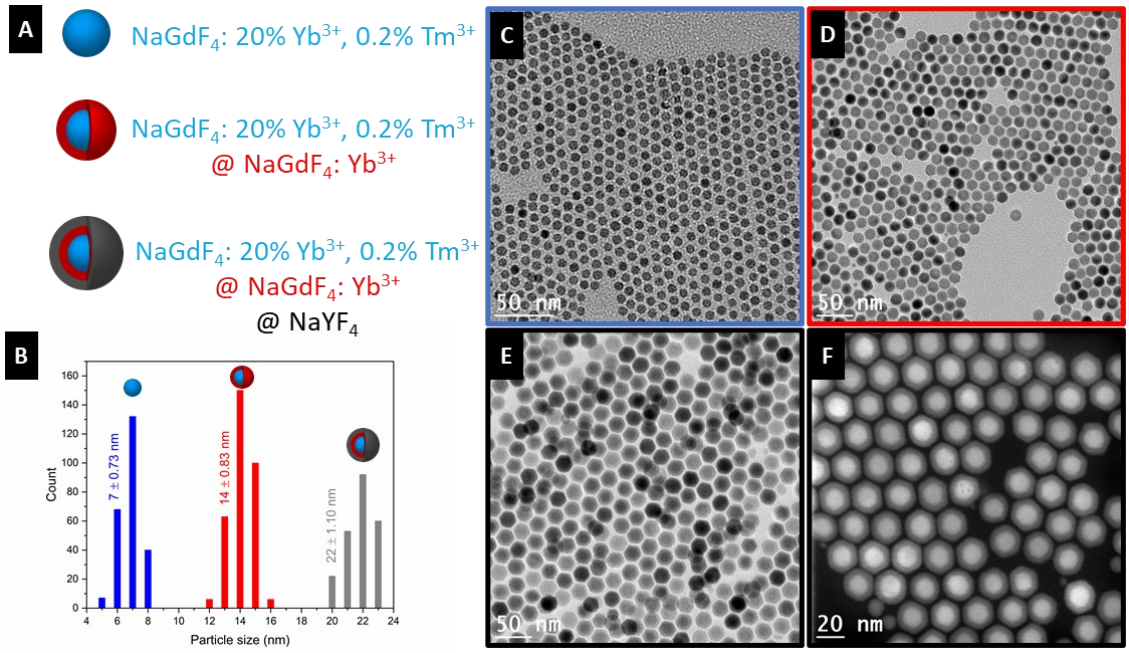

Figure 4.1 (A) Studied nanoparticle compositions. (B) Particle size distributions. (C-F) Transmission electron microscopy images (TEM) of (C) $NaGdF_4$: Yb^{3+}, Tm^{3+} ,(D) $NaGdF_4$: Yb^{3+}, Tm^{3+} @ $NaGdF_4$: Yb^{3+} ,(E) $NaGdF_4$: Yb^{3+}, Tm^{3+} @ $NaGdF_4$: Yb^{3+} @ $NaYF_4$ and (F) High resolution dark field TEM image of "E".

In the present study, we synthesized hexagonal phase ultrasmall oleate capped core $NaGdF_4$: 20% Yb^{3+}, 0.2% Tm^{3+} with additional of two concentric shells: an active $NaGdF_4$:20%Yb^{3+} and inert $NaYF_4$ (Figure S4.1) using a modified version of coprecipitation method [147]. The average size of the core/shell/shell ($NaGdF_4$:20% Yb^{3+}, 0.2% Tm^{3+}@$NaGdF_4$:20%Yb^{3+}@$NaYF_4$) are 7, 14, 22 nm based on transmission electron microscopy images (Figure 4.1).

The upconversion luminescence spectra of the core (C), core/shell (CS) and core/shell/shell (CSS) UCNPs in powder are presented in Figure 4.2. With the addition of a 3.5 nm thick Yb^{3+}-doped shell on the 7 nm core nanoparticles doped with Tm^{3+} and Yb^{3+}, there is an increase in overall luminescence intensity by approximately 60%. The addition of a shell typically results in brighter nanoparticles by distancing the luminescent ions from solvent or ligand phonons and defects on the surface, thereby decreasing quenching effects [180, 181]. However, with only a 3.5 nm shell, there have been previous reports that this is not sufficiently thick to minimize these quenching effects, and the luminescent dopants will still interact with the surface [173, 182]. Furthermore, by adding a shell doped with Yb^{3+}, there is an increase in the relative Yb^{3+} concentration with respect to Tm^{3+} in the host lattice. This is also problematic, as there is the possibility for energy migration between Yb^{3+} ions, resulting in a prolonged lifetime of their excited state that can be quenched *via* the quenching processes previously mentioned [183].

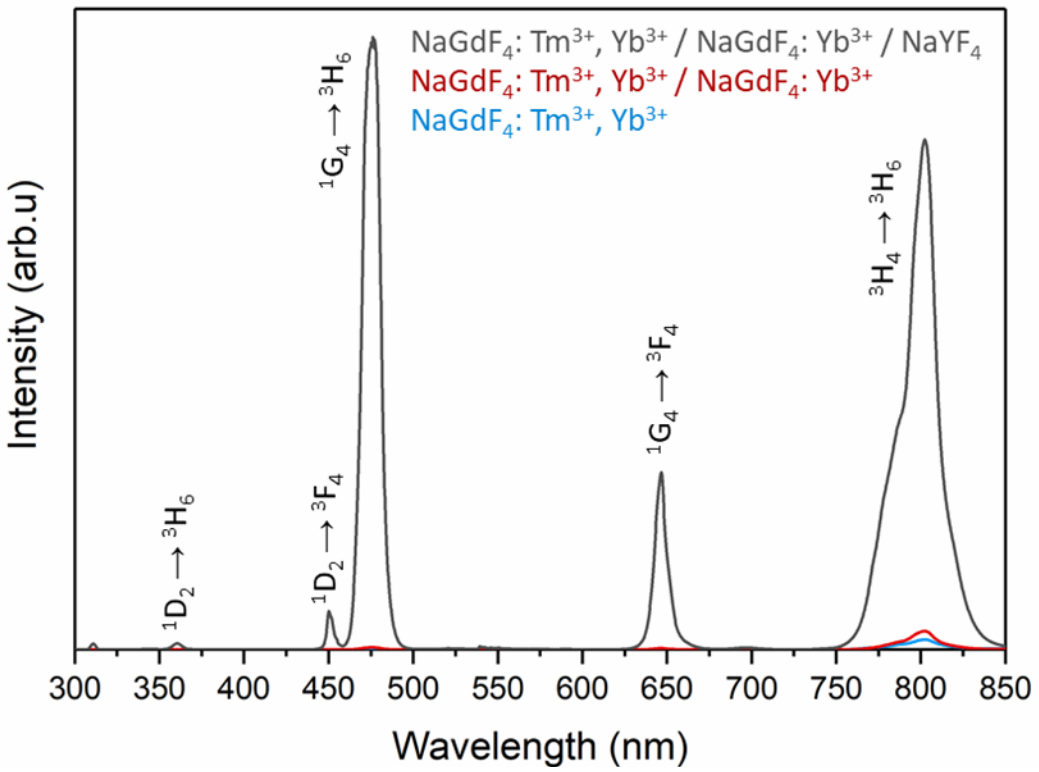

Figure 4.2 Upconversion emission spectra of different nanoparticles under 980 nm excitation in powder.

Only after the growth of an additional 4 nm shell of spectroscopically inert $NaYF_4$ is there over one magnitude of increase in luminescence intensity. This extra shell achieves the expected threshold for this composition to properly protect the core Tm^{3+} ions from possible surface quenching [182].

Another interesting point of discussion is the observed Tm^{3+} emissions. Focusing primarily on the CSS-UCNPs, the radiative transitions originate from the $^1D_2$, $^1G_4$, and $^3H_4$ levels, as depicted with an energy level diagram in Figure S4.2. This spectrum however, has drastically different relative intensities for each excited state, compared to previously described nanoparticles of similar structure [162]. With a concentration of 0.2% Tm^{3+}, a core nanoparticle size of 7 nm (equaling 1.8×10^5 Å^3) and a unit cell size of 114.05 Å^3 (Figure S4.3), there is the probability of only four Tm^{3+} ions to exist in each nanoparticle [184]. This greatly limits the possibility for Tm^{3+} cross-

relaxation processes that are responsible for the population of the $^1D_2$ state, evident by the relatively weak emissions originating from this level (at 360 and 450 nm) [185, 186]. In contrast, the $^1G_4 \rightarrow {}^3F_4$, $^3H_6$ and $^3H_4 \rightarrow {}^3H_6$ transitions (at 475, 650 and 800 nm, respectively) are strong, owing to the Tm^{3+} dopant concentration as well. Previously reported cross-relaxation mechanisms between these excited states are known to quench their emissions in favor of the population of the $^3F_4$ level, which is avoided by having only four Tm^{3+} ions in each nanoparticle [187, 188]. This ultimately results in bright nanoparticles in the blue and NIR regions, with almost no UV emissions.

To further elucidate the dynamics of Tm^{3+} in these nanoparticles, luminescence lifetimes were recorded for the $^1G_4$ and $^3H_4$ levels, presented in Figure 4.3, and their rise and decay times are presented in Table S4.1 and 4.1, respectively. As expected, increasing the shell thickness prolongs all the excited state lifetimes, by preventing surface interactions with the Tm^{3+} ions. However, this does not affect both excited states equally. By observing the decay times of the core $NaGdF_4$: Tm^{3+}, Yb^{3+} nanoparticles, the $^3H_4$ state relaxes faster than the $^1G_4$ state, and for the $NaGdF_4$: Tm^{3+}, Yb^{3+} / $NaGdF_4$: Yb^{3+} / $NaYF_4$ nanoparticles, the $^3H_4$ state relaxes slower than the $^1G_4$ state. This can be explained by studying the vulnerability of these levels to quenching. With respect to phonon-related processes, the $^1G_4$ level relaxes to the next lowest state, being the $^3F_{2,3}$ level, and the $^3H_4$ level relaxes to the $^3H_5$ level. It is expected that the $^1G_4 \rightarrow {}^3F_{2,3}$ transition (≈6000 cm^{-1}) is less susceptible to quenching than the $^3H_4 \rightarrow {}^3H_5$ transition (≈4000 cm^{-1}) due to the larger energy gap. Therefore, the increase in shell thickness is more effective in stabilizing the $^3H_4$ level over the $^1G_4$ level.

Composition	Decay Time (μs)	
	$^1G_4 \rightarrow {}^3H_6$	$^3H_4 \rightarrow {}^3H_6$
$NaGdF_4$: Tm^{3+}, Yb^{3+}	273.7	207.9
$NaGdF_4$: Tm^{3+}, Yb^{3+}@$NaGdF_4$: Yb^{3+}	492.8	484.4
$NaGdF_4$: Tm^{3+}, Yb^{3+} @ $NaGdF_4$: Yb^{3+} @ $NaYF_4$	1321.5	1947.3

Table 4.1 Luminescence decay times from the curves in Figure 3

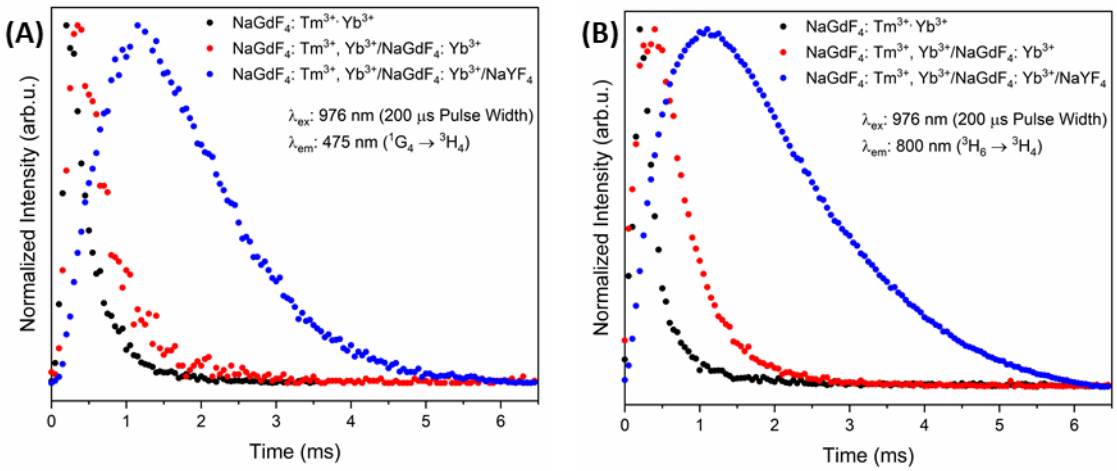

Figure 4.3 Nanoparticle luminescence decay curves, after a 200 μs pulse of 976 nm irradiation, of the (A) $^1G_4 \rightarrow {}^3H_6$ transition (475 nm) and the (B) $^3H_4 \rightarrow {}^3H_6$ transition (800 nm).

Furthermore, the emission spectra normalized to the $^3H_4 \rightarrow {}^3H_6$ transition (presented in Figure S4.4) show that there is an increase in intensity of the $^1G_4 \rightarrow {}^3F_4$, $^3H_6$ transitions by over one magnitude with each additional shell. With a prolonged lifetime of the $^3H_4$ level, there is more opportunity for energy transfer upconversion to populate the $^1G_4$ level, which greatly enhances its emissions with increasing shell thickness.

To utilize $^1G_4 \rightarrow {}^3H_6$ transition for PDT application, vitamin B2 also called Riboflavin 5'-phosphase sodium salt (Rf) is grafted on the surface of the CSS nanoparticles. Rf is naturally occurring photosensitizer that is involved in redox homeostasis. Also, Rf has an excellent spectral overlap with CSS emission that is necessary for its activation and for singlet oxygen production ($^1O_2$) (Supporting S4.5). The as-synthesized CSS-UCNPs are oleate-capped. To this end, oleate-free UCNPs were prepared using $NOBF_4$ approach [189]. The phosphate moiety of Rf coordinates with the positively charged surface of the oleate free CSS-UCNP surface. Rf grafting was confirmed by comparing stretching modes of free and loaded Rf on CSS-UCNPs surface (Supporting S4.6). Thermogravimetric assays (TGA) were employed to estimate the number of Rf molecules present on CSS-UCNPs. It is calculated that 455 µg Rf/mg(CSS-UCNPs), corresponding to 289 molecules per single nanoparticle (figure 4.4).

The nanoconstruct CSS-UCNPs were evaluated with respect to its production of $^1O_2$ under 980 nm irradiation. The reaction oxygen species released was detected by DPBF (1,3-diphenylisobenzofuran) a known probe that possess high sensitivity towards $^1O_2$ [152]. The decrease in the absorption peak of DPBF at 415 nm represent the amount $^1O_2$ released from grafted Rf.

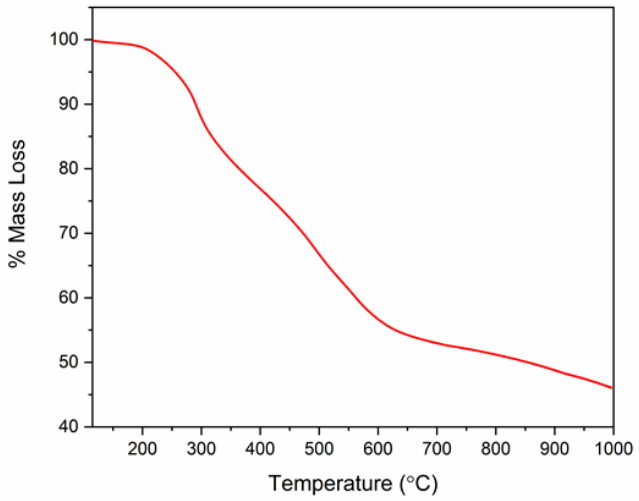

Figure 4.4 Thermogravimetric assay (TGA) of Riboflavin coated CSS nanoparticles. 45.29 % mass loss corresponding to 455 ug of Rf / 1 mg nanoparticles

Employing 40 min exposure at 10 min interval (supporting S4.7), almost 15 % DPBF is consumed that indicates the potential CSS-UCNPs as PDT vehicle for intrinsic riboflavin.

In summary, we designed a narrow band and highly blue emissive CSS-UCNPs. Employing ultra-small core nanoparticles with low Tm^{3+} doping concentration, the CSS-UCNPs emission generated under 980 nm irradiation produced a new pattern that has not been identified for similar Tm^{3+} doped UCNPs. Analysis of decaytimes of different transitions, we proposed a new cross relaxation mechanism responsible for populating $^1G_4 \rightarrow {}^3H_6$ and $^3H_4 \rightarrow {}^3H_6$ that is responsible for the emission pattern detected. To validate the significant enhancement of blue emission, naturally occurring photosensitizer Rf in grafted on the surface of the CSS-UCNPs, that showed $^1O_2$ release under 980 nm irradiation which is required for PDT application. The model presented, provide a great potential for a wide range of growing and demanding field of the blue light responsive materials.

4.4 Experimental Procedures

4.4.1 Synthesis Core $NaGdF_4$: 20 % Yb^{3+}, 0.5 % Tm^{3+}

Lanthanides chlorides (0.75 mmol $GdCl_3$, 0.2 mmol $YbCl_3$, & 0.05 mmol$TmCl_3$) are mixed with 6 mL oleic acid and 15mL 1-octadecene. The mixture is heated up to 120 ˚C under argon for 25 minutes, and the temperature increased to 160 ˚C and kept stirring at 500 rpm for 30 minutes. While keeping the solution under inert atmosphere, the temperature is decreased to 50 ˚C. Using injection pump with a rate of 1 mL/min, 8 mL of methanol containing 2.5 mmol NaOH, and 4 mmol NH_4F are injected to the solution, and left stirring for 30 minutes. Methanol was removed by gradually heating the solution under vacuum at 80 ˚C for 10-15 minutes, and 120 ˚C under argon for additional 15 minutes. The solution is heated up to 300 ˚C with a rate of 10 ˚C/ minute for period of 90 minutes. The mixture is cooled down to room temperature under inert atmosphere and the nanoparticles are precipitated using ethanol using and centrifuged of 3400 rpm for 15 minutes. Two additional washes are done to the particles using 5 ml hexanes and 45 mL ethanol to remove any residual products of the reaction mixture.

4.4.2 Synthesis of First Active Shell $NaGdF_4$: 20 % Yb^{3+}

The same procedure was followed as above. However, 0.8 mmol $GdCl_3$, 0.2 mmol $YbCl_3$ are mixed with 6 mL oleic acid and 8 mL 1-octadecene. In addition, at 50 ˚C 170 mg of sodium trifluoroacetate in added over the mixture, and 25 mg core nanoparticles are dispersed in 2 mL hexanes and added over the reaction mixture. The solution stirred for 10 minutes, and gradually heated to 120 ˚C for a period of 10 minutes to make sure all hexanes are removed using inert atmosphere (Argon flow). The reaction temperature increased to 290 ˚C for 80 minutes, and nanoparticles collected similar to the core nanoparticles.

4.4.3 Synthesis of Second Inert shell $NaYF_4$

The synthesis is similar for the first shell. However, 0.5 mmol of YCl_3 is used with 6 mL oleic acid and 8 mL 1-octadecene, and 136 mg sodium trifluoroacetate is used at 50 ˚C. In addition the reaction temperature is increased to 290 ˚C for 60 minutes.

4.4.4 X-Ray Powder Diffraction

X-ray diffraction patterns were measured using a Scintag XDS-2000 diffractometer equipped with a Si(Li) Peltier-cooled solid state detector, Cu Kα source, at a generator power of 45 kV and 40 mA, beam divergent (2 mm and 4 mm), and receiving beam slits (0.2-0.5 mm). The measurement scan covered the range 10-90° 2Θ with a step size of 0.02° and count time of 2 seconds. All samples were measured using a quartz zero background inert disk.

4.4.5 Transmission Electron Microscopy

A 5 mg sample of nanoparticles was dispersed in 5 mL of toluene to yield an approximate 0.1 wt % solution, and sonicated for 20 minutes. The nanoparticle dispersion allowed to rest for 5 minutes, and 10 µL dropped over a TEM cupper grid 3 mm in diameter coated with formavar carbon film. The solution was evaporated for 10 minutes at room temperature. TEM images were obtained using a JEM-2100F (Jeol microscope) operating power of 200 kV equipped with a charge coupled device camera (CCD-Gatan).

4.4.6 Emission Spectra and Excited State Decay Times of Upconverting nanoparticles

Different nanoparticles emission spectra are recorded using coherent 6-pin 15 fibver-coupled F6 series laser diode with 976 nm excitation source. The laser is CW controlled by ILX lightwave LDC-3744B driver. For pulsed mode LDP-3811 ILX lightwave driver is used. For UV emissions measurements Hamamatsu R4632 PMT used, and emission dispersion (2400 groves/mm) done by Oriel 77250 1/8 m monochromator. Jarrell-Asj Czerny-Turner 25-102 1 m (1180 groves/mm)

double monochromator coupled to R943-02 Hamamatsu PMT. The processing of the signal was done by SR440 Stanford research systems preamplifier, and gated photon counter system. For all measurement concentration of nanoparticles is used 1mg/mL in Toluene for comparative studies. Dry powder samples of different nanoparticles are used for lifetime measurements, with instrumentation as mentioned of the emission spectra. However, the diode laser was pulsed with 200 µs width controlled with ILX Lightwave LDP-3811.

4.4.7 Oleate removal and Riboflavin coating

10 mg of oleate nanoparticles are dispersed in 5 ml cyclohexane, while stirring NaBF4 (10mg/2ml) in DMF are added over the nanoparticles and the solution stirred for 30 minutes. DMF layer is extracted and washed with 1:1 solution of hexane and toluene. The collected pellet is washed again with same solution, and a transparent solid noticed in the bottom. The solid is redispersed in 2 ml DMF, and 5mg of phosphate riboflavin in 2 ml distilled water is added. The solution is stirred for 24 hours, and the particles linked to phosphate riboflavin precipitated by centrifugation 13 000 r.pm. for 10 minutes. The pellet is washed with distilled 3 ml water twice and precipitated by centrifugation.

4.4.8 Thermogravimetric assay

TGA measurements were carried out using TA instrument Q50 analyzer. Dried pellet of nanoparticles and its conjugates (6-8 mg) were placed into a platinum pan and heated under nitrogen flow from 25 to 800 °C at a heating rate of 10 °C/minutes.

4.4.9 Singlet Oxygen generation and detection

Rf-CSS upconverting nanoparticles are dispersed in deuterated DMSO (2mg/mL), and irradiated with 980 nm with a power density of 13 W/cm^{-2} for 10 minutes exposure time.1,3-Diphenylisbenzofuran (DPBF)trap is used to detect singlet oxygen generated. DPBF has a

maximum absorbance at 415-420 nm depending in the solvent used. The decrease in the maximum intensity is measured by using Cary 5000 series with a 1 nm resolution, and 600 nm.s^{-1} scan rate. A calibration curve is used to quantify the amount of singlet oxygen released.

4.5 Supporting Information

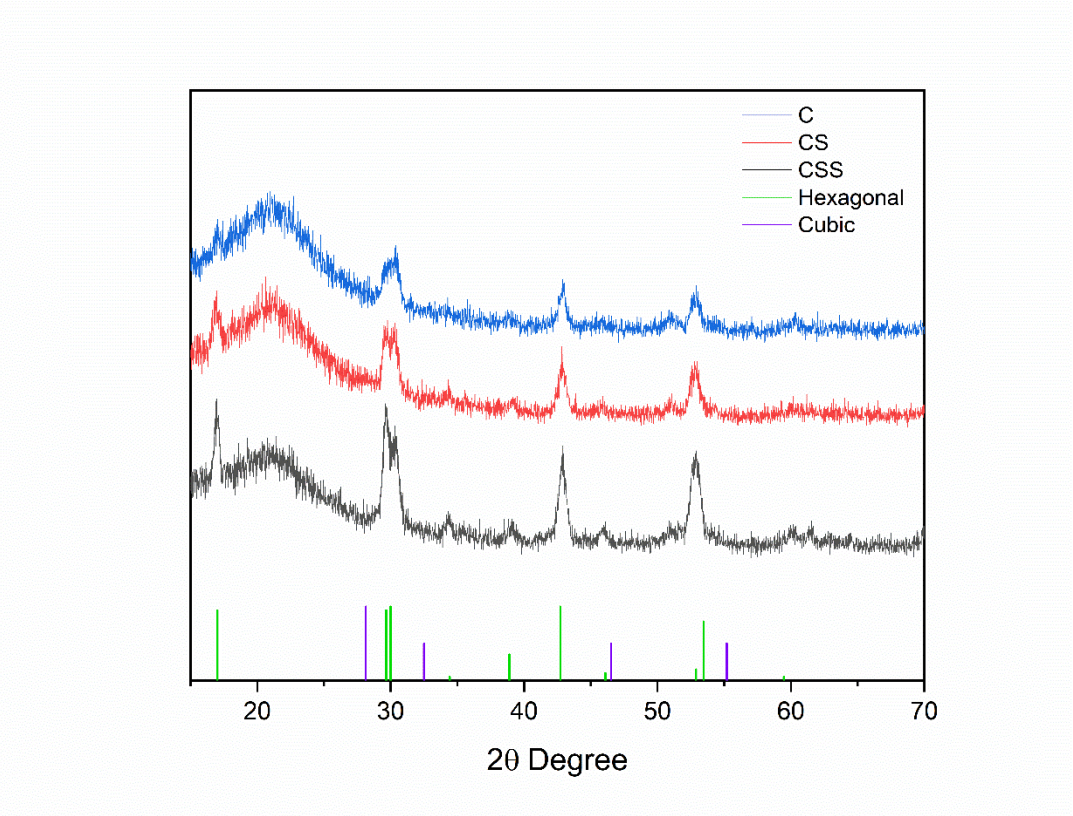

Figure S 4.1 X-ray powder diffraction of (XRPD) of nanoparticles. C, CS and CSS represent $NaGdF_4$: Yb^{3+}, Tm^{3+} / $NaGdF_4$: Yb^{3+}, Tm^{3+} @ $NaGdF_4$: Yb^{3+} / and $NaGdF_4$: Yb^{3+}, Tm^{3+} @ $NaGdF_4$: Yb^{3+} @ $NaYF_4$ respectively. At the bottom are theoretical patterns of hexagonal and cubic phase.

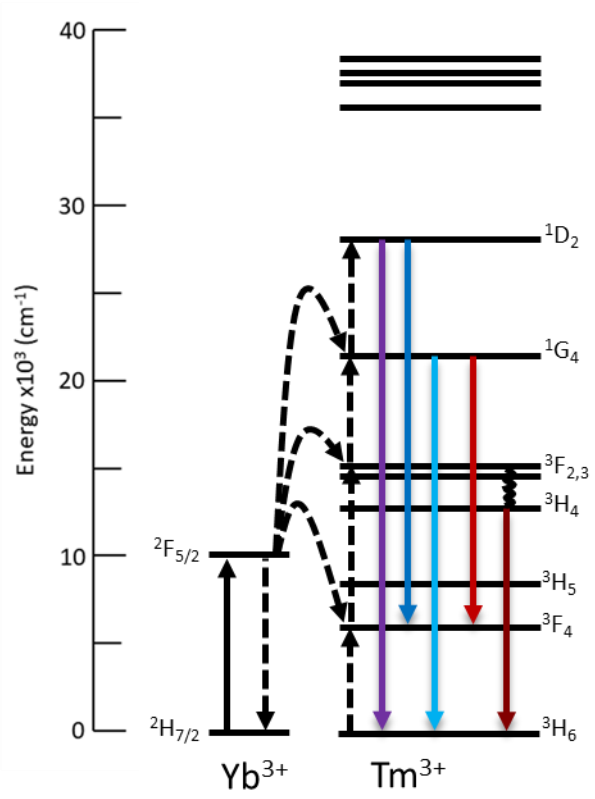

Figure S 4.2 : Energy level diagrams of Yb^{3+}, Tm^{3+} and Gd^{3+}, depicting energy transfer upconversion between Yb^{3+} and Tm^{3+}.

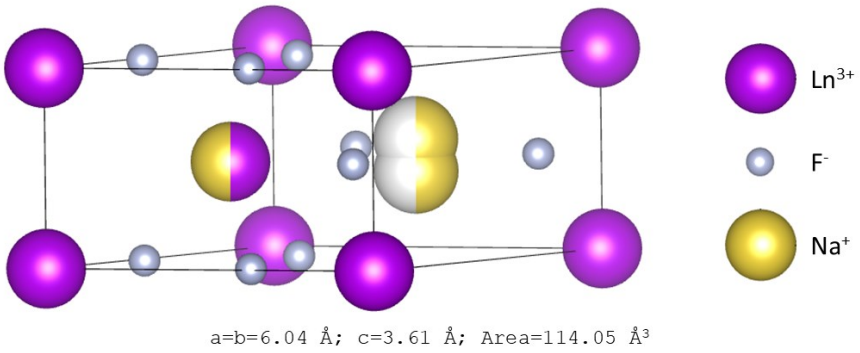

Figure S 4.3 Unit cell parameters and structure of β-$NaGdF_4$

Composition	Rise Time (μs)	
	$^1G_4 \rightarrow {}^3H_6$	$^3H_4 \rightarrow {}^3H_6$
$NaGdF_4$: Tm^{3+}, Yb^{3+} / $NaGdF_4$: Yb^{3+}	90.2	167.2
$NaGdF_4$: Tm^{3+}, Yb^{3+} / $NaGdF_4$: Yb^{3+} / $NaYF_4$	578.5	360.6

Table S 4.1 Luminescence rise times from the curves in Figure 3

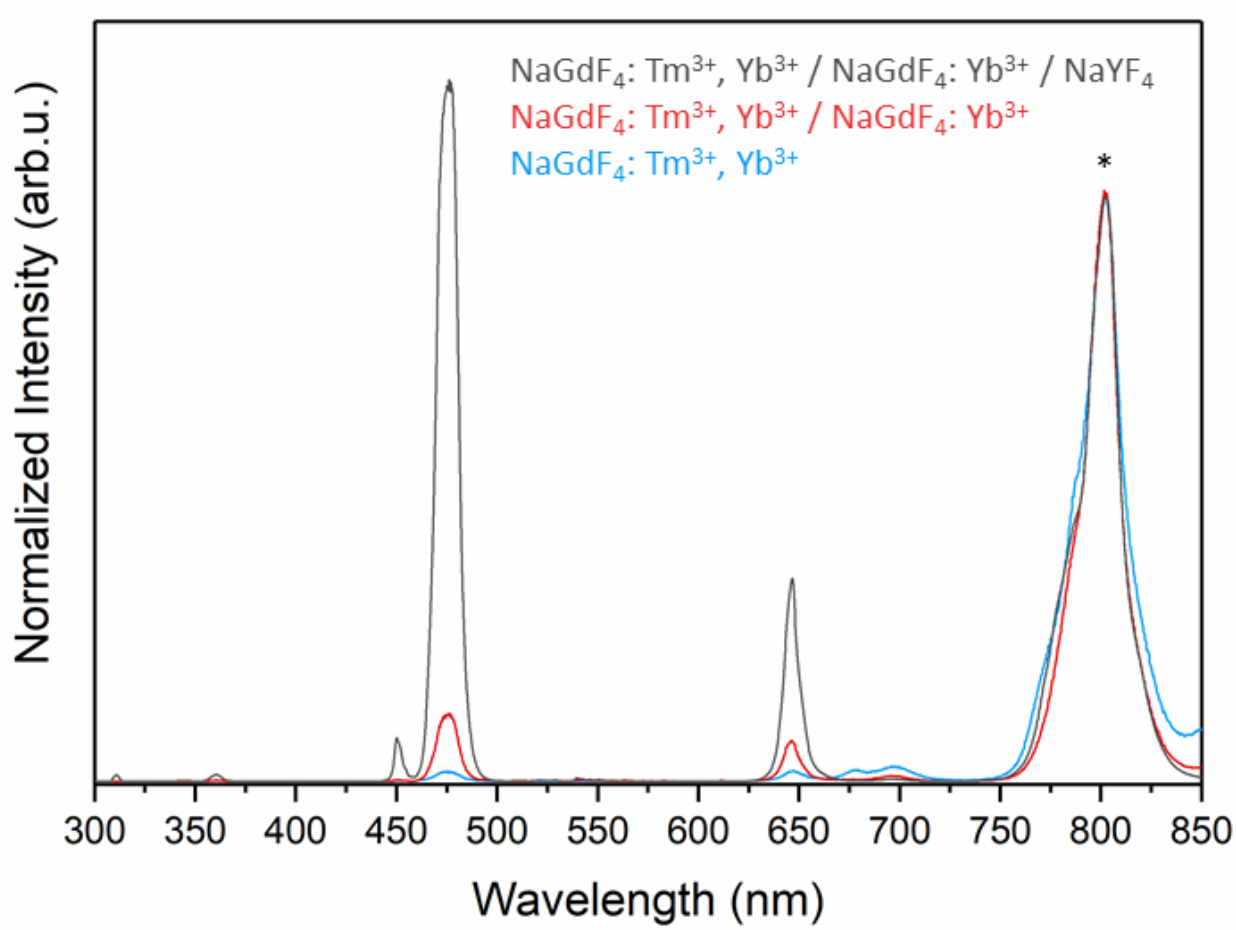

Figure S 4.4 Emission spectra for all compositions studied, upon 976 nm excitation, normalized to the $^3H_4 \rightarrow {}^3H_6$ transition indicated by the asterisk

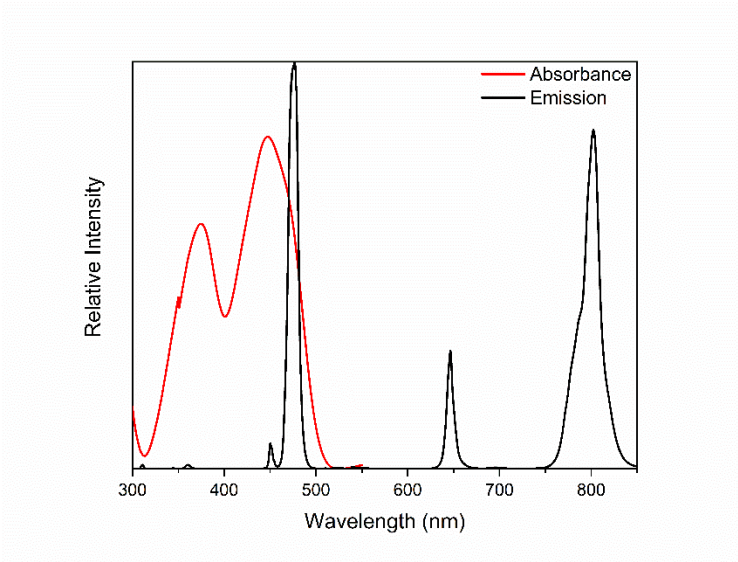

Figure S 4.5 Spectral overlap of CSS nanoparticles emission upon 976 nm excitation shown in black, and riboflavin absorbance in red

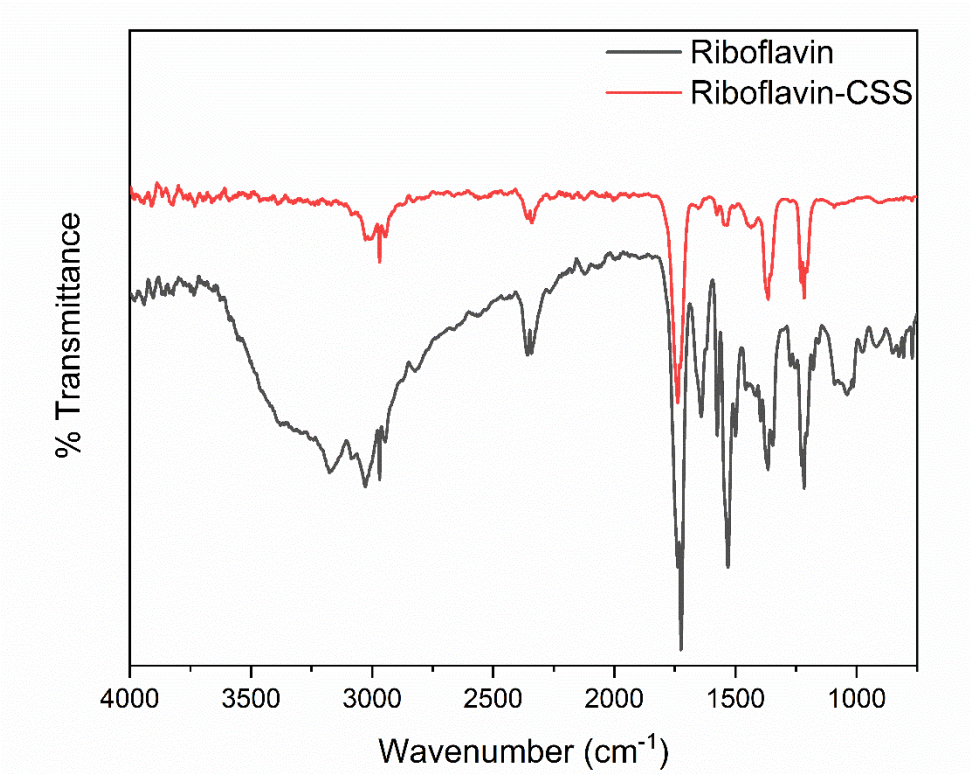

Figure S 4.6 FTIR of CSS nanoparticles surface coated with phosphate riboflavin. In black native phosphate riboflavin, and Rioflavin coated CSS shown in red

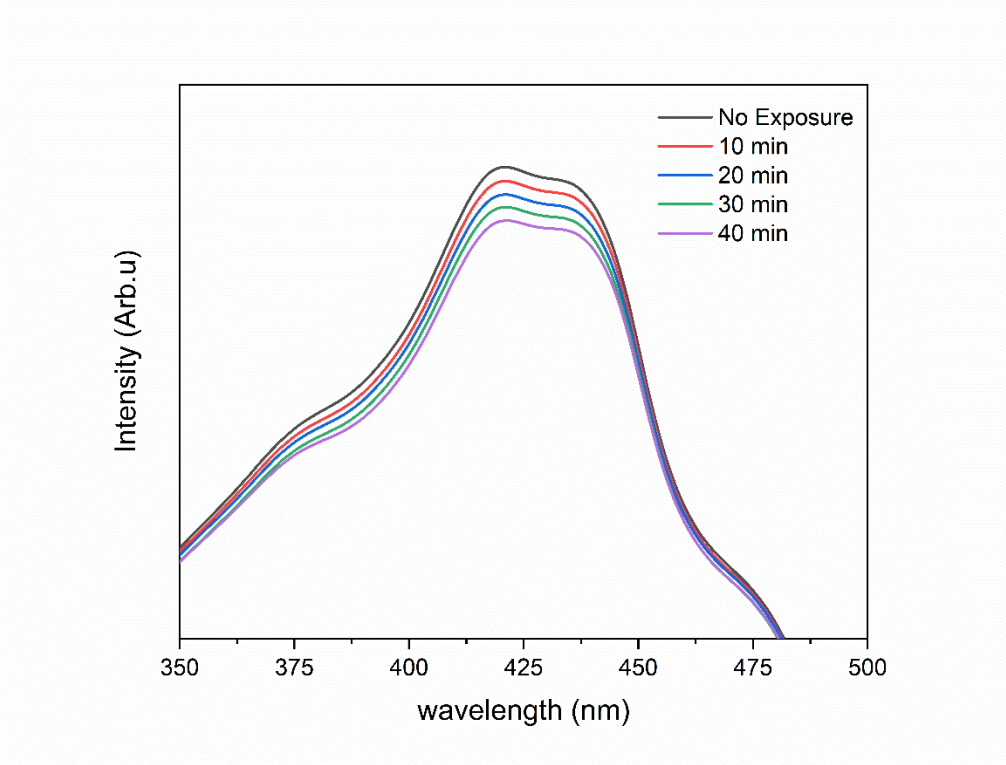

Figure S 4.7 DPBF absorption after irradiation of Rf-CSS nanoparticles with 980 nm. 2 mg/mL of nanoparticles are dispersed in (1:1) deuterated DMSO and D_2O in the presence of 37 μM DPBF

Chapter 5. Conclusions

In the past few years there are numerous nanoparticles advancement permitted their uses in a wide range of applications. Nanoparticles have wide range of chemical composition, sizes, loading properties, and surface coatings depending on the nature of the application. Lanthanides upconversion nanoparticles (Ln-UCNPs) are unique among nanoparticles with its optical activity and their response to NIR irradiation. The low toxicity, non photobleaching, and their remarkable low photodamage to living tissues, Ln-UCNPs has been extensively used in a wide range of biological application. This includes, biosensing, imaging, and light mediated therapeutics (PDT). Nevertheless, there are biological limitations for translating Ln-UCNPs as probes for cancer therapeutics such as selective targeting, renal clearance, preserving the identity in biological milieu, and maintaining its optical activity in vivo. In this thesis, new approaches of Albumin (ALB) conjugated Ln-UCNPs for PDT therapeutics were developed. The aim is to surpass some of the obstacles that hinder the biological relevance of these nano-materials, and improve their efficacy for PDT applications.

A modified version of desolvation method was developed to render Ln-UCNPs ($NaGdF_4$: Yb^{3+}, Er^{3+}) water dispersible and biocompatible for PDT. ALB desolvation (unfolding) in presence of ethanol cause 80 % loss of α-helical content. This exposed hydrophobic amino acids side chains enabling hydrophobic interaction with oleate surface, which act as a scaffold for generating a ~2 nm thick shell on $NaGdF_4$: Yb^{3+}, Er^{3+} surface. This covering was quantified by thermogravimetric analysis, and it is estimated that approximately 112 molecules of ALB were present to cover 15290 nm^2 area of single $NaGdF_4$: Yb^{3+}, Er^{3+} nanoparticle. This amount of ALB provided dispersibility in biological relevant media, and provided surface functionality due to the presence of primary

amine and carboxylic acid residues. Also, ALB presence prevents luminescence quenching in aqueous media. ALB shielded high energy vibrations solvent molecules (H_2O) to interact with $NaGdF_4$: Yb^{3+}, Er^{3+} optically active ions Er^{3+} and Yb^{3+} and persevered nanoparticle emission. Additionally, to utilize the nanoconstruct as a PDT probe, the photosensitizer Rose Bengal (RB) was structurally modified, to enhance coupling efficiency for grafting on Ln-UCNPs surface. Energy transfer of different RB loaded on $NaGdF_4$: Yb^{3+}, Er^{3+} surface was studied under 980 nm irradiation, and obtained a maximum of 63% efficiency. This energy transfer is responsible for inducing cytotoxic release of reaction singlet oxygen ($^1O_2$). Further, *in vitro* studies showed that RB presence permitted cellular internalization of ALB-$NaGdF_4$: Yb^{3+}, Er^{3+}, and inducing toxicity to human alveolar lung cancer cells (A549) within a 10-minute exposure time under 980 nm excitation. Thus, RB modified ALB-$NaGdF_4$: Yb^{3+}, Er^{3+} provided biocompatible surface coating, targeting and cytotoxicity capabilities that all enhance PDT efficacy.

New model of ALB conjugated to $NaGdF_4$: Yb^{3+}, Er^{3+} is also developed. Bifunctional linker possessing maleimide group as an ALB-thiol targeting moiety is exchanged with oleate capping ligand. Native ALB with a single active thiol group (cysteine 34) is covalently linked to $NaGdF_4$: Yb^{3+}, Er^{3+} through thioether linkage rendering Ln-UCNPs biocompatible and dispersible in aqueous environment. Analysis of ALB grafted on $NaGdF_4$: Yb^{3+}, Er^{3+} showed an asymmetric facet clustering, with 18 ALB residing on a single $NaGdF_4$: Yb^{3+}, Er^{3+}. *In vitro* evaluation of the cellular activity of ALB presence on UCNPs revealed a substantial selective cellular internalization effect using glioblastoma tumor cells (U251N), in comparison to alveolar lung cancer cells (A549). To take advantage of the cellular uptake, different concentrations of RB are incorporated with the nanoconstruct for PDT application. It is estimated that 5 molecules present induced 74% energy transfer under 980 nm irradiation. Further, spectrophotometric analysis of the

RB photoreaction processes identified type II energy transfer mechanism, and the release of toxic reactive singlet oxygen ($^1O_2$). However, using electron paramagnetic resonance (EPR), type I oxygen independent energy transfer pathway is detected through the release of thiol radical, and hydroxyl radical ($HO^{\bullet}$). *In vitro* cellular toxicity assay of the nanoconstruct using U251N irradiated with 980 nm, revealed an intense cellular toxicity effect as a result of the enhanced cellular uptake, and the release of various toxic reactive oxygen radicals.

New Ln-UCNPs design was also exploited to enhance the intensity of specific transition emission. An ultrasmall ~7 nm $NaGdF_4$: Yb^{3+}, Tm^{3+} is synthesized with the addition of two layers, an active ($NaGdF_4$: Yb^{3+}) and inert shell ($NaYF_4$) respectively. The former shell provides higher absorption of 980 nm irradiation, and through energy transfer will feeds into the core emitting centers. The latter shell offer an energy barrier by decreasing surface phonon quenching. An intense, narrow blue light (475 nm) emission attributed for $^1G_4 \rightarrow {}^3H_6$ transition is detected under 980 nm excitation. The transition exceeds all other transitions emitting from Tm^{3+}, including the most intense 800 nm attributed to $^3H_4 \rightarrow {}^3H_6$ transition in Tm^{3+} doped Ln-UCNPs. Using lifetime measurements, a new mechanism that have not been addressed for populating $^1G_4 \rightarrow {}^3H_6$ and $^3H_4 \rightarrow {}^3H_6$ states is identified, that is responsible for the emission pattern detected. To apply this design for PDT application, the nanoconstructs are coated with riboflavin (Rf) a naturally occurring photosensitizer. Rf is characterized on the surface of the nanoconstructs, and cytotoxic reactive singlet oxygen species are released and detected under 980 irradiation.

The essence of the work presented herein is to improve the efficacy of Ln-UCNPs as therapeutic nanoprobes for PDT applications. The NIR light source required to activate Ln-UCNPs provide a solution for the conventional superficial uses of the high energy radiation employed in PDT. The transducing or energy conversion ability of Ln-UCNPs designed in this work, permits

the use of many abandon visible light activated PS that posses the highest $^1O_2$ quantum yield. Ln-UCNPs surface coating strategies *via* employing biomolecule protein (ALB) provide biocompatibility and dispersibility in biological relevant media. Also, ALB intrinsic property permits the loading of different PS (hydrophobic/hydrophilic), and more importantly acting as a targeting sensor of definitive cancer cell type. Furthermore, Ln-UCNPs optical properties were utilized in different research applications (see appendix).

Chapter 6. Future Directions

Although most of the determined goals for the investigation of this thesis have been accomplished, there are several approaches that could be done to levitate the efficacy of the design in cancer therapeutic.

The model presented for albumin coated Ln-UCNPs is based on using binary dopant system $NaGdF_4$: Yb^{3+}, Er^{3+} for activating photosensitizer RB. The centered emission at 525 nm, and 550 nm attributed to $H_{11/2} \rightarrow {}^4I_{15/2}$, and ${}^4S_{3/2} \rightarrow {}^4I_{15/2}$ respectively are responsible for activating RB grafted into the surface of the nanoparticles. However, there is a relatively intense 650 nm emission attributed to ${}^4F_{9/2} \rightarrow {}^4I_{15/2}$ transition that could be employed to load a second PS alongside RB. This will enhance the flux of ${}^1O_2$ produced from the nanoconstruct under 980 nm irradiation, increase the rate of cellular toxicity, and enhance PDT efficacy. Chlorin e6 (Ce6) an FDA approved PS have a very strong spectral overlap with ${}^4F_{9/2} \rightarrow {}^4I_{15/2}$ emission, and characterized by high sensitization [190]. Ce6 used for skin and neck cancers, and show rapid elimination from the body [191]. The major limitation with Ce6 is its poor dispersibility in water. However, ALB presence permits loading Ce6 through hydrophobic interaction. Also, Ce6 posses three carboxylic acids residue that enable covalent coupling into the surface of the nanoconstruct.

Although the release of ${}^1O_2$ in the vicinity of the cell membrane or cellular organelles induce cellular toxicity, targeting of the nanoparticles into internal organelles precisely to the mitochondria will cause a surge in cellular toxicity. Mitochondria provide energy to the cells (powerhouse), and responsible for maintaining reaction oxygen species homeostasis. Triphenylphosphonium (TPP) is among several ligands that are used to target nanoparticles and therapeutic drugs towards mitochondria [192]. Guan et al. was the first to use a modified TPP structure with extending aliphatic chain to enhance Ln-UCNPs surface conjugating, and

mitochondria internalization [193]. Modified TPP could be covalently linked with ALB desolvated on $NaGdF_4$: Yb^{3+}, Er^{3+} surface. Along side RB with cell surface internalization ability, TPP presence will permits $NaGdF_4$: Yb^{3+}, Er^{3+} mitochondrial delivery. Consequently, the release of $^1O_2$ will be localized in the mitochondria that enhance the PDT efficacy of the nanoconstruct.

Additionally, ALB has been proved for solubilizing hydrophobic cancer drug. Chemotherapeutic agent could be coupled, and utilized to provide an additional toxicity and enhance treatment efficacy to the targeted cancerous tissues. Paclitaxel (PTX) is naturally occurring drug isolated from the bark of *Taxius brevifolia*, and has been used for treating different cancerous tissues [194]. PTX effectiveness is based on arresting cell division by targeting cell cytoskeleton predominantly preventing microtubules disassembly [194]. PTX has a high binding affinity to ALB, and their fusion is employed for generating an FDA approved drug Abraxane® that is used for metastatic breast cancer. ALB presence on the surface of $NaGdF_4$: Yb^{3+}, Er^{3+} allows PTX loading permitting bimodal cancer treatment PDT and chemotherapy.

Another significant study is to use *in vivo* models for targeting specific cancerous tumor. ALB has great tendency to accumulate in various cancerous tissues such glioma, colon, breast, and lung. However, each tumor holds unique endothelial fenestrations depending on the nature of its residing tissue. Selection of specific tumor require tunning the sizes of the $NaGdF_4$: Yb^{3+}, Er^{3+}. Varying the sizes will influence nanoconstructs biodistribution, and their passive targeting ability (EPR) for successfully reaching tumor site. To study the biodistribution of $NaGdF_4$: Yb^{3+}, Er^{3+}, it is necessary to adjust its emission pattern. $NaGdF_4$: Yb^{3+}, Er^{3+} has visible emission, in this range of spectra light is highly absorbed *in vivo* through biological tissues. This will prevents live imaging, or trancing of the nanoconstruct in different organs. To overcome this limitation, Tm^{3+}

doping will be essential since it will provide an 800 nm emission, which is least absorbing wavelength in all biological tissues.

APPENDIX

Manuscript 4: Intrinsic Time-Tunable Emissions in Core-Shell Upconverting Nanoparticle System

Published as:

Gabriella Tessitore, Steven L. Maurizio, Tarek Sabri and John A. Capobianco*

Angew. Chem. 2019, 131, 9844–9853

Department of Chemistry and Biochemistry, and Centre for NanoScience Research, Concordia University. 7141 Sherbrooke St. West, Montreal, Quebec H4B 1R6, Canada.

Abstract

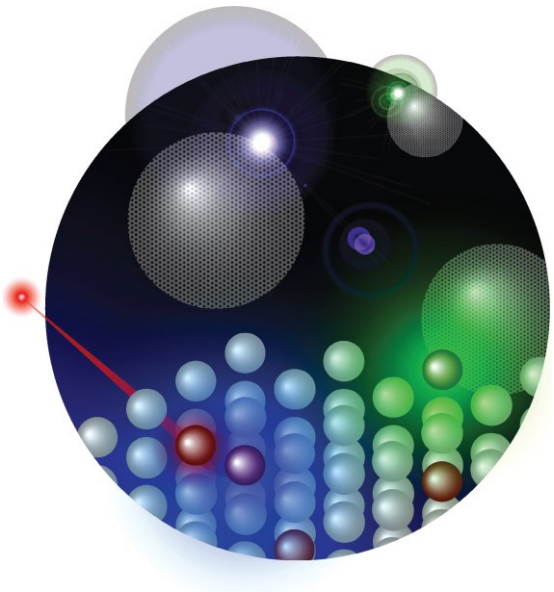

Schematic representation of Core shell Ln-UCNPs with surface emitting centers.

Color-tunable luminescence has been extensively investigated in upconverting nanoparticles for diverse applications, each exploiting emissions in different spectral regions. Manipulation of the emission wavelength is accomplished by varying the composition of the luminescent material or the characteristics of the excitation source. Here we propose core-shell β-$NaGdF_4$: Tm^{3+}, Yb^{3+}/ β-$NaGdF_4$: Tb^{3+} nanoparticles as intrinsic time-tunable luminescent materials. The time dependency of the emission wavelength only depends on the different decay time of the two emitters, without additional variation of the dopant concentration or pumping source. The time-tunable emission was recorded with a commercially available camera. The dynamics of the emissions is thoroughly investigated, and we established that the energy transfer from the $^1D_2$ excited state of Tm^{3+} ions to

the higher energy excited states of Tb^{3+} ions to be the principal mechanism to the population of the $^5D_4$ level for the Tb^{3+} ions.

Introduction

The emission wavelength is the main characteristic of a luminescent material, and it can be varied by manipulation of the external excitation source [195-199] and combining the luminescent characteristics of multiple optically active ions by co-doping [197-205].The pumping current, pulse width, and duty cycle of the excitation source can be varied, which results in changes in power density or flux, altering the relative intensity of the emissions, resulting in tuning the color of the light produced. For applications in lighting, luminescent materials are used to shift the main excitation of the pumping source, commonly ultra-violet light, to wavelengths in the visible region[206-211].Several luminescent materials are based on the emissions from lanthanide ions, whose sharp emission bands determine the high color rendering of lanthanide-doped phosphors [212-214].

Lanthanide-based nanoparticles undergoing upconversion luminescence (UCL) have been produced mainly because of their biological applications[137, 160, 172, 215-219]. Upconverting nanoparticles (UCNPs) have been investigated with respect to their color tuning in a variety of co-doped systems. The possibility to obtain multiple emissions from a single system is of particular interest given the different reported applications. Consequently, the coupling of the characteristic UV, blue, and NIR emissions from Tm^{3+} ions to the luminescence from other lanthanide ions has been exploited [39, 220, 221].In particular, the efficient green and red emissions from Tb^{3+} and Eu^{3+} have been reported to efficiently emit in Tm^{3+} co-doped systems, resulting in multicolor emissions. When the particles are co-doped with Tm^{3+} and Tb^{3+} ions together with Yb^{3+} as a sensitizer, energy transfer upconversion (ETU) favors the population of Tm^{3+} over the other dopant ions[197].Non-radiative energy transfer or Förster resonance energy transfer (FRET) occurs from Tm^{3+} to the

other ions, and it yields a tunable emission depending on the relative ion concentrations and the characteristics of the excitation source[197]. When the two emitting ions are separated, such as in a core–shell structure in which Yb^{3+} and Tm^{3+} ions are present in the core and the other emitting lanthanide ion only in the shell, the dynamics of the system are different[39, 220, 221].FRET is limited to a certain width at the core–shell interface, in which the distance between the two ions is small enough to favor the transfer process[222].The distance between ions can be manipulated by varying the concentration of the emitters in the shell, the shell thickness, or co-doping with ions capable of further promoting FRET[39, 220, 221].

Gd^{3+} is of particular interest for the high absorption cross-sections of its UV bands and strong resonance with efficient emitters, such as Tb^{3+} and Eu^{3+} [206, 207, 209-211]. In the absence of any other dopant ion, the Gd^{3+} ions in β-$NaGdF_4$ can be excited using 273 nm light to the ^6I_J states, producing the characteristic emission from the $^6P_{7/2}$ states at 312 nm [223, 224]. Energy migration through the ^6P_J excited states is efficient and can propagate energy transfer within ions at considerable distances [39, 220, 221]. When β-$NaGdF_4$ is doped with Yb^{3+} and Tm^{3+} ions in the core and Tb^{3+} or Eu^{3+} ions in the shell, it has been proposed that energy can migrate within Gd^{3+} ions in core–shell systems, fostering emissions from the ions in the shell. This mechanism, also known as energy migration-mediated upconversion, has been recently proposed in the literature [39, 220, 221]. Together with cooperative upconversion, in which the dimerization of Yb^{3+} ions can lead to emissions in the blue region[225-228],or transfer this energy to resonant levels of the two considered emitters, these are the two principal mechanisms reported to explain the luminescence mechanism in such core–shell systems [39, 220, 221].

Power studies of luminescence dynamics in nanoparticles have underlined that the population mechanism depends not only on the relative stability of the emitting levels of the ions but also on

the nanoparticle dimensions [98].Smaller nanoparticles are more affected by quenching phenomena, requiring a larger number of incident photons for the population of a specific level and reaching the saturation or steady-state at higher power values [229].When complex systems are considered, the power and pulse width of the pumping source at which saturation is achieved for different ions can influence the relative emission of the involved transitions [98]. Recently, core–shell systems have also been shown to achieve time-tunable color emissions [198, 199].The concentration of the dopant ions is varied to obtain a tunable emission, recorded under dynamic scanning [198].The difference in emissions from core–shell systems doped with five different lanthanides was also reported as temporal full-color tunable nanomaterials by changing the pulse width of the pumping NIR pulsed laser [199]. In the studied core–shell systems, contrarily, time-tunability of emissions was obtained without varying the power and pulse width of the pumping source.

Core-shell systems are investigated because of their higher luminescence efficiencies in comparison to UCNPs constituted by the core only[180-182, 230]. Herein, we studied the luminescence mechanism in UCNPs passivated by a thicker shell with respect to similar systems reported in the literature. It has been recently demonstrated that quenching mechanisms in nanoparticles arise in the absence of passivation by a thick protective shell[182]. We consequently concentrated our investigations to β-$NaGdF_4$: Tm^{3+}, Yb^{3+}/β-$NaGdF_4$: Tb^{3+} core–shell systems of 20 nm with a shell thickness of about 6 nm. Moreover, the study of dynamics from samples in solution can introduce further quenching phenomena that have the same characteristics of FRET to the solvent molecules [231], which can result in misinterpreting the time-dependent measurements. Consequently, luminescence analyses are performed on powder samples and in dilute solutions of toluene, to avoid further solvent quenching by hydroxy-containing media. A non-statistical distribution of ions has been reported in the literature [232], and it has been kept in consideration in the discussion

of our results. We report a thorough investigation of the luminescence dynamics in β-$NaGdF_4$: Tm^{3+}, Yb^{3+}/β-$NaGdF_4$: Tb^{3+} core–shell materials. Considering the intrinsic differences in luminescence decay characteristics of Tm^{3+} and Tb^{3+} in these core–shell UCNPs, we propose the applicability of their time-tunable emissions in anti-counterfeiting systems.

Results and Discussion

Comparative spectroscopic investigations between samples require perfect control of the synthesis with respect to the particle size, crystalline phase, and composition. Minor differences can result in significant errors in analyzing the decrease in emission intensity with dopant concentrations and the luminescence dynamics. β-$NaGdF_4$: 1% Tm^{3+}, 49% Yb^{3+}/ β-$NaGdF_4$: x% Tb^{3+} core-shell nanoparticles with varying Tb^{3+} concentration (x = 0, 10, 20) have been synthesized from the same core nanoparticles, undergoing epitaxial growth of the shell by a multiple-step process. All the samples show the characteristic diffractions of the hexagonal β-phase and phase purity, as shown in **Figure S1** of the Supporting Information (SI).

Information on particle size, size distribution, morphology, and crystal phase were obtained by the analyses of the micrographs in **Figure 1**. The average size of the core-shell nanoparticles recorded

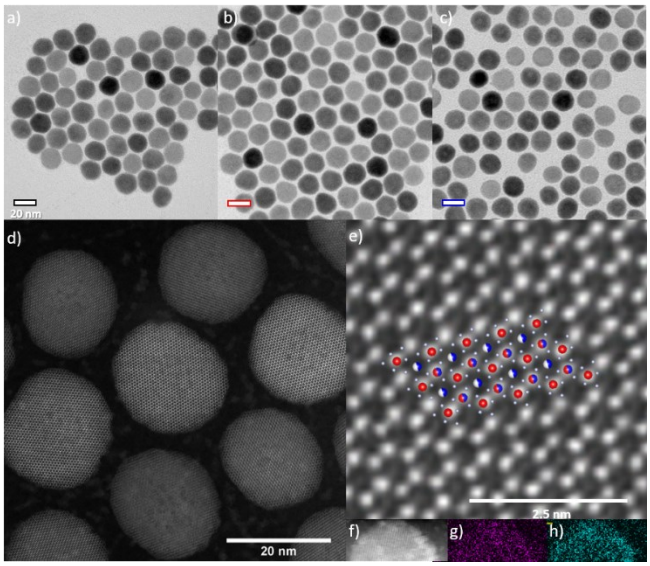

Figure 1 a,b,c) TEM micrographs of β-$NaGdF_4$: 1% Tm^{3+}, 49% Yb^{3+}/ β-$NaGdF_4$: x% Tb^{3+} core-shell nanoparticles for x = 0, 10. And 20, respectively. Scale bar of 20 nm is reported in the figures. d) HAADF STEM micrographs of β-$NaGdF_4$: 1% Tm^{3+}, 49% Yb^{3+}/ β-$NaGdF_4$: 20% Tb^{3+} core-shell nanoparticles, and e) magnification of a selected area. The unit cells reported as a visual guide for the atomic structure are obtained for the hexagonal β-$NaGdF_4$ phase with *P-6* space group (a = 6.0304 Å, c = 3.6111 Å). Lanthanide, sodium, fluorine, and vacancies are presented in the atomic model as red, blue, grey, and white spheres, respectively. Half spheres indicate the relative occupancies of the two sodium sites. f,g,h) EELS measurements with respect to the Tb^{3+} (g) and Gd^{3+} (h) concentration on a particle section (f).

for UCNPs with a Tb^{3+} concentration in the shell of 0, 10, and 20%, respectively was found to be 20 nm from the low-resolution transmission electron microscopy (TEM) micrographs (**Figures 1 a**, **b**, and **c**), with a maximum variance between nanoparticles of 1.5 nm by the analysis of 300 UCNPs. TEM micrographs of the core nanoparticles (8.9 ± 1.1 nm) are shown in **Figure S2**, and their comparison with the core-shell samples shows that the shell thickness is 5.55 ± 1.3 nm. High-angle annular dark-field (HAADF) images in **Figures 1 d** and **e** provide further evidence of the crystallinity of the samples. In **Figure 1e** the brighter atoms were assigned to lanthanide sites, due to the more efficient scattering of the incident electron from a lanthanide nucleus compared to sodium or fluorine. The atomic positions perfectly match with the unit cell of β-$NaGdF_4$ for the *P-6* space group [233].The results from electron energy loss spectroscopy (EELS) analyses shown in **Figures 1 f**, **g**, and **h** prove that all the facets of the UCNPs are covered by the shell. The

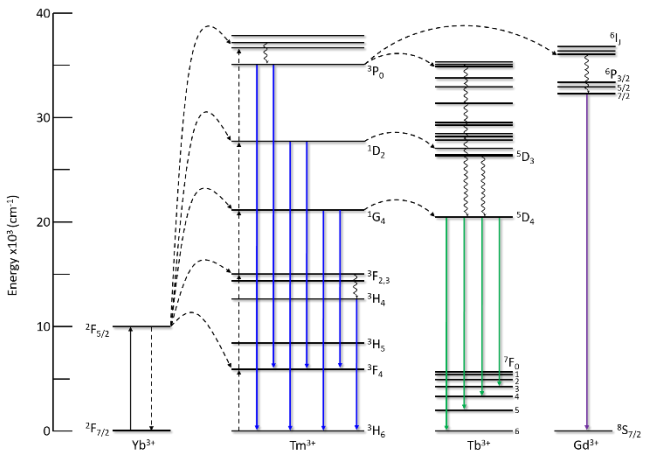

Figure 2 Energy level diagram of the optically active ions with respect to upconversion luminescence. The relevant levels and transitions are reported for each ion.

concentration of Tb^{3+} and Gd^{3+} does not change significantly within the particle, while an incomplete coverage would result in differences of the ionic concentration between the core and the shell. The crystal plane orientation for the majority of the particles does not change along the radial coordinate, further proving a uniform growth of the shell as shown by analyses with scanning transmission electron microscope (STEM) in **Figure S3**. These results prove complete passivation of the particle surface, considering that even the highly concentrated Yb^{3+} ions in the core cannot be detected.

The top facets of the UCNPs shown in **Figures 1 a**, **b**, and **c** correspond to the (001) crystal plane, while the hidden side facets grow along the (100) plane[147]. In the presence of oleic acid as a coordinating ligand, it has been demonstrated that a higher ligand affinity with the (001) facet determines the preferential growth along the (100) side facets[147]. Due to the different coverage of the facets with this ligand, epitaxial growth of the shell would first cover the less coordinated side facets in platelet-shaped particles. Complete passivation results in limited quenching phenomena from the solvent, as it will be further proven in the next section.

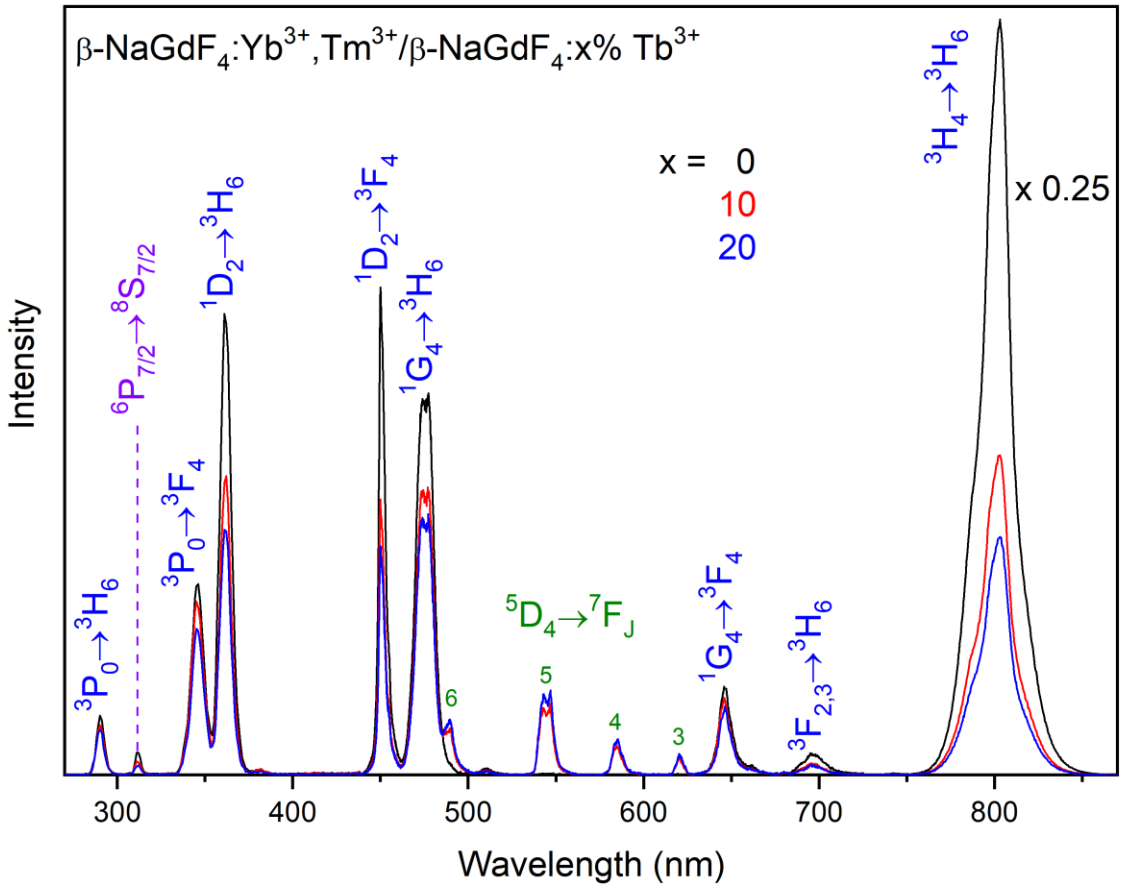

Figure 3 Emission spectra of β-$NaGdF_4$: 1% Tm^{3+}, 49% Yb^{3+}/ β-$NaGdF_4$: x% Tb^{3+} core-shell nanoparticles in solution under excitation from a 976 nm CW laser for x = 0, 10, and 20 (black, red, and blue curve, respectively). Main emissions from Tm^{3+}, Tb^{3+}, and Gd^{3+} are labeled in blue, green, and purple, respectively. The $^3H_4 \rightarrow {}^3H_6$ transition at 803 nm is scaled for clarity.

Inductively coupled plasma mass spectrometry (ICP-MS) provides the total concentration of the samples in the solutions used for comparative luminescence measurements and confirms that the concentration of Tm^{3+} and Yb^{3+} remains constant between the samples within the experimental error of the measurements, as shown in **Table S1**. Such preliminary analyses guarantee that differences between the luminescence response and dynamics arise only from the influence of Tb^{3+} on the emission mechanism and ion distribution.

Luminescence mechanism

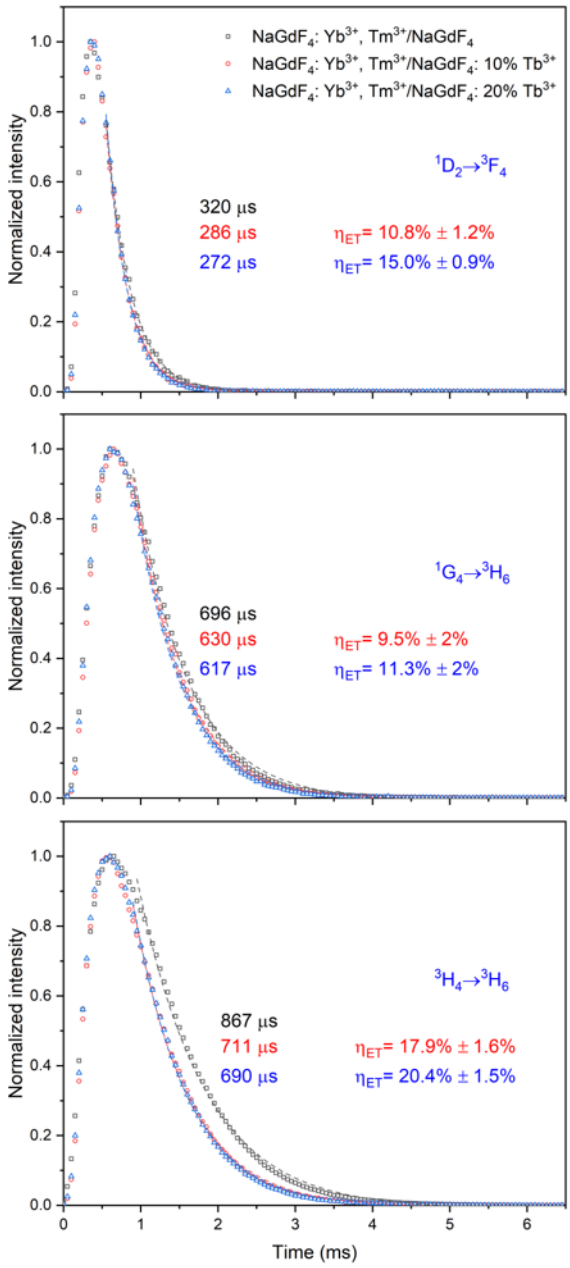

Figure 4 Decay time curves of Tm^{3+} transitions, relative decay times, and energy transfer efficiencies of β-$NaGdF_4$: 1% Tm^{3+}, 49% Yb^{3+}/ β-$NaGdF_4$: x% Tb^{3+} core-shell nanoparticles powder samples under excitation from a 976 nm pulsed laser with a 200 µs pulse width and 1 W/cm^2 peak power for x = 0, 10, and 20 (black, red, and blue curve and values, respectively).

The luminescence mechanism in the core-shell systems under investigation can be simplified as shown in **Figure 2**, where the Yb^{3+}, Tm^{3+} co-doped core results in sensitization of the Tb^{3+} ions in the shell. Gd^{3+} ions can constitute an additional excitation source to promote the emissions from

Tb^{3+} by energy migration. These two components, the core and the shell of the nanostructure, can transfer energy between each other *via* several mechanisms, both non-radiative, such as FRET and energy migration, and radiative. The complexity of the systems requires a detailed investigation of each possible pathway for clear identification of the main excitation mechanism of Tb^{3+}.

The core of all the nanoparticles under investigation contains an equivalent concentration of the sensitizer and activator ions and only the concentration of the Tb^{3+} ions in the shell varies, to avoid the introduction of ulterior differences between the samples. The UCL mechanism of Yb^{3+}, Tm^{3+} co-doped materials continues to be under investigation, as the population of the high-energy states is disputed[7, 186, 234-237]. Co-doped materials with Yb^{3+} and Tm^{3+} undergo upconversion luminescence mainly *via* ETU. After excitation of the sensitizer, Yb^{3+}, the energy is transferred to Tm^{3+} ions, which undergo radiative decay as shown in **Figure 2**. The number of photons required to populate each Tm^{3+} level by ETU is clearly shown in **Figure 2**, ranging from two photons for the NIR emission to four or five to promote transitions in the UV spectral region. The relative emission intensity from a level can be affected by the occurrence of other non-radiative phenomena, such as energy migration or cross-relaxation. These two processes are omitted in **Figure 2** for clarity.

The UCL spectra of a colloidal solution of β-$NaGdF_4$: 1% Tm^{3+}, 49% Yb^{3+}/ β-$NaGdF_4$: x% Tb^{3+} nanoparticles are shown in **Figure 3**, and the characteristic emissions from Tm^{3+}, Tb^{3+}, and Gd^{3+} ions are clearly observed. It is evident that the $^3H_4 \rightarrow {}^3H_6$ transition of the Tm^{3+} ions dominate the emission spectra, due to the lower number of photons involved in the population of the $^3H_4$ state. The lack of spectroscopic overlap between the emissions from the $^3P_0$ level of the Tm^{3+} ions with the ^6I_J and ^6P_J levels of Gd^{3+} ions (see **Figure S4**) results in the weak emission from the $^6P_{7/2}$ excited state to the $^8S_{7/2}$ ground state, which occurs *via* phonon-assisted FRET. Spectra have been

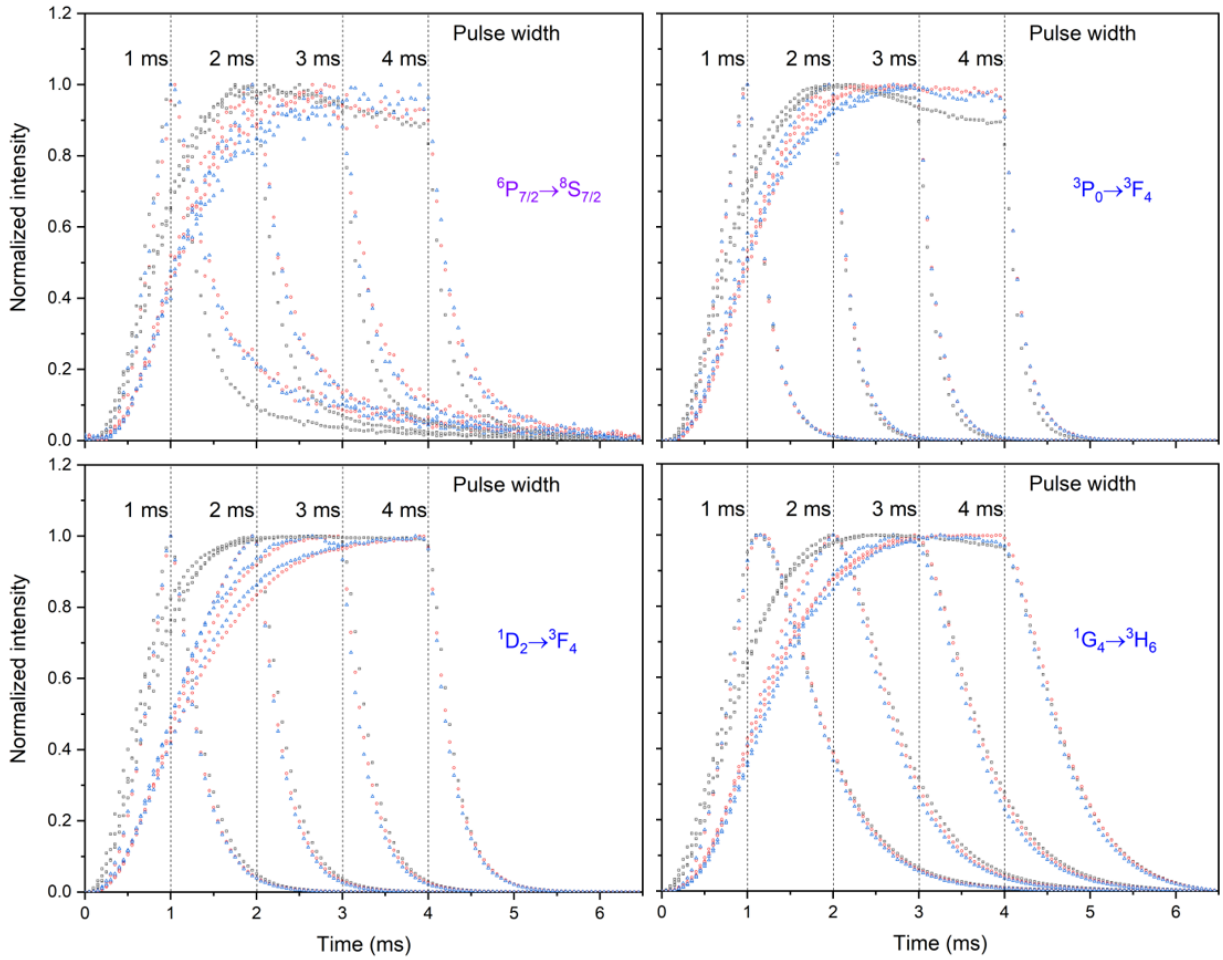

Figure 5 Decay time curves of Gd^{3+} and Tm^{3+} of β-$NaGdF_4$: 1% Tm^{3+}, 49% Yb^{3+}/β-$NaGdF_4$: x% Tb^{3+} core-shell nanoparticle powder samples under excitation from a 976 nm pulsed laser with 1, 2, 3, and 4 ms pulse widths and 4, 7, 10 and 14 W/cm^2 peak power for x = 0, 10, and 20 (black, red, and blue curves, respectively). The vertical dotted lines for each pulse width are reported as a visual guide.

corrected for the particle concentration obtained from ICP-MS (**Table S1**). Diluted solution samples are chosen to verify the variation in luminescence intensity between samples with different concentrations of Tb^{3+} ions. The use of colloidal solutions to analyze luminescence trends is preferred over the powder samples, because of the limited extent of reabsorption of light in diluted solutions with respect to the powder samples, although the spectra from powder samples follow the same trend with minor discrepancies as shown in **Figure S5a**.

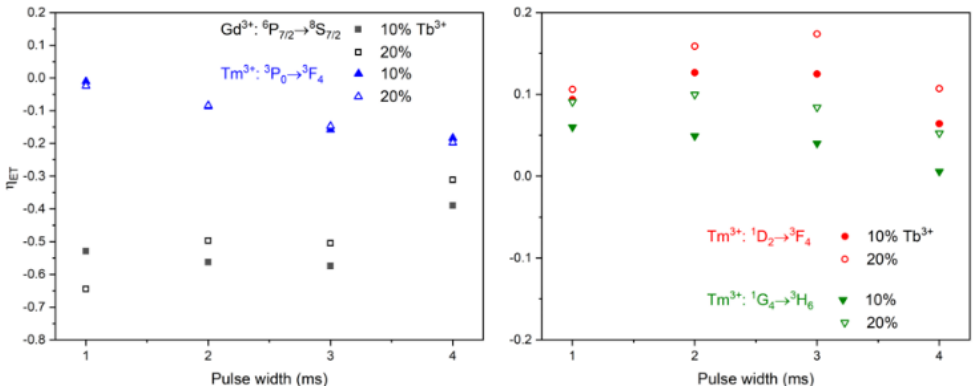

Figure 6 Energy transfer efficiencies as a function of the Tb^{3+} concentration and pulse width. The evaluated experimental error is 5% and is omitted for clarity.

The depopulation of the Tm^{3+} and Gd^{3+} ion levels in the presence of Tb^{3+} ions displayed in **Figure 3** can be attributed to radiative and non-radiative phenomena. In spite of the involved phenomena, the energy from Tm^{3+} and Gd^{3+} ions propagates from the core to the shell and populates the Tb^{3+} emitting states, or it can be quenched by surface traps after Tb^{3+} or Gd^{3+} are excited. The solvent quenching is verified by a comparison of the luminescence spectra from powder samples and in solution, evidencing that only the Tb^{3+} ions are quenched by energy transfer to resonant vibrational modes of the solvent (**Figure S5b**). The occurrence of non-radiative energy transfer can be verified by the study of the luminescence decay times of the donor (Tm^{3+} or Gd^{3+}) transitions in the absence and presence of Tb^{3+}. An efficient FRET has to correspond to a decreasing decay time of the donor emissions in the presence of the acceptor ions. Furthermore, if the emission intensities are quenched by a significantly larger percentage than the FRET efficiency, it would suggest that the energy transfer mechanism occurs *via* a radiative pathway. Consequently, when the light emitted from a donor is reabsorbed, the dynamics of the donor are unaffected, since radiative energy transfer does not occur by coupling of dipole momenta.

The bands in the emission spectra shown in **Figure 3** were integrated, and the relative decrease in intensity of the emissions of Tm^{3+} and Gd^{3+} by the addition of Tb^{3+} is reported in **Table S2**. It is evident that the transitions $^1D_2 \rightarrow {}^3H_6, {}^3F_4$, $^1G_4 \rightarrow {}^3H_6$ and $^3H_4 \rightarrow {}^3H_6$ from the Tm^{3+} ions and the

emission of Gd^{3+} from the $^6P_{7/2}\rightarrow{}^8S_{7/2}$ transition are affected to a greater extent by the presence of Tb^{3+} in the shell. The emission intensities from the Tm^{3+} ions are significantly stronger than the emission arising from Gd^{3+}. Due to the difference in the relative intensities between the Tm^{3+} and Gd^{3+} emissions, the major contribution to the Tb^{3+} population arises from the Tm^{3+} emissions, which is consistent with the results reported in the literature for β-$NaYF_4$: Tm^{3+}, Tb^{3+}, Yb^{3+} microparticles[197]. In these materials, it has been demonstrated that the population of the $^5D_4$ state of the Tb^{3+} ions occurs mainly through the $^1D_2$ and $^1G_4$ states of the Tm^{3+} ions, favoring Tm^{3+} to Tb^{3+} FRET from one of these two levels, depending on the power of the pumping source[197].

In order to study the dynamics of the Tm^{3+} ions, we performed luminescence lifetime measurements. **Figure 4** shows the decay curves of the $^1D_2\rightarrow{}^3F_4$, $^1G_4\rightarrow{}^3H_6$, and $^3H_4\rightarrow{}^3H_6$ transitions for the core-shell nanoparticles, β-$NaGdF_4$: 1% Tm^{3+}, 49% Yb^{3+}/ β-$NaGdF_4$: x% Tb^{3+} powder samples, using a 976 nm pulsed laser excitation with a 200 µs pulse width and a 1 W/cm^2 peak power density. The power density of the pumping source is obtained from the beam profile shown in **Figure S6**. The fitting of the decay times is achieved using a single exponential, ensuring that the residuals of the fittings are stochastically distributed. The FRET efficiencies (η_{ET}) were calculated as a percent difference between the sample without Tb^{3+} with those that contain either 10 or 20% Tb^{3+} in the shell and are reported in **Figure 4**.

From the analyses of the rise times for the $^1D_2$, $^1G_4$ and $^3H_4$ states, it is possible to evaluate the relative influence of cross-relaxation pathways on their dynamics. The rise times of the three levels under investigation are significantly different. The $^1D_2$ level is characterized by a shorter rise and decay time with respect to the $^1G_4$ and $^3H_4$ levels. These two states are characterized by similar dynamics, with a clear relationship between their rise times (**Figure 4**). After the population of the $^1G_4$ and $^3H_4$ excited states, the probability of cross-relaxation to populate the $^1D_2$ state is more

likely than their radiative decay[186, 234], which is evidenced by their longer rise times. The population of the $^1D_2$ state through ETU from the Yb^{3+} ions to the Tm^{3+} $^1G_4$ is unlikely, due to a lack in resonance. Therefore the process is phonon-assisted, being less probable than the more resonant cross-relaxations involving several transitions from the Tm^{3+} $^1G_4$ and $^3H_4$ states [186, 234]. Increasing the Yb^{3+} concentration favors the population of the $^1D_2$ states, which has been recently demonstrated in the literature[238].

In the presence of Tb^{3+}, the decay time of the three emissions decreases, indicating the occurrence of non-radiative pathways depopulating the Tm^{3+} levels (**Figure 4**). Considering that we proved that the only difference between the samples is the inclusion of Tb^{3+} in the shell and that other non-radiative quenching mechanisms for emissions from Tm^{3+} ions can be excluded in powder samples, the differences in decay time can be directly correlated to the efficiency of $Tm^{3+}\rightarrow Tb^{3+}$ non-radiative FRET. The depopulation of the $^1G_4$ and $^3H_4$ levels *via* non-radiative processes is partially due to the quenching of the $^1D_2$, to the same extent in which these levels contribute to its population. The transfer from this state to Tb^{3+} pushes the equilibrium of its population through more efficient cross-relaxations from the $^1G_4$ and $^3H_4$ states. Furthermore, non-radiative $Tm^{3+}\rightarrow Tb^{3+}$ FRET has been demonstrated to involve the Tm^{3+} metastable $^3F_4$ states, whose excitation can also involve the $^3H_4$ level *via* cross-relaxation[197].This additional process explains the higher $Tm^{3+}\rightarrow Tb^{3+}$ FRET efficiencies from the $^3H_4$ state. As discussed previously, FRET from $^1D_2$ and $^3F_4$ states of Tm^{3+} to the $^5D_4$ and ^7F_J states of Tb^{3+} corresponds to an increased transfer rate from the $^3H_4$ to repopulate these two Tm^{3+} levels. It is evident from the schematic luminescence mechanism in **Figure 2** that there are no absorption bands from the Tb^{3+} ground states, which are resonant with the 803 nm emission for the $^3H_4\rightarrow{}^3H_6$ transition of the Tm^{3+} ion.

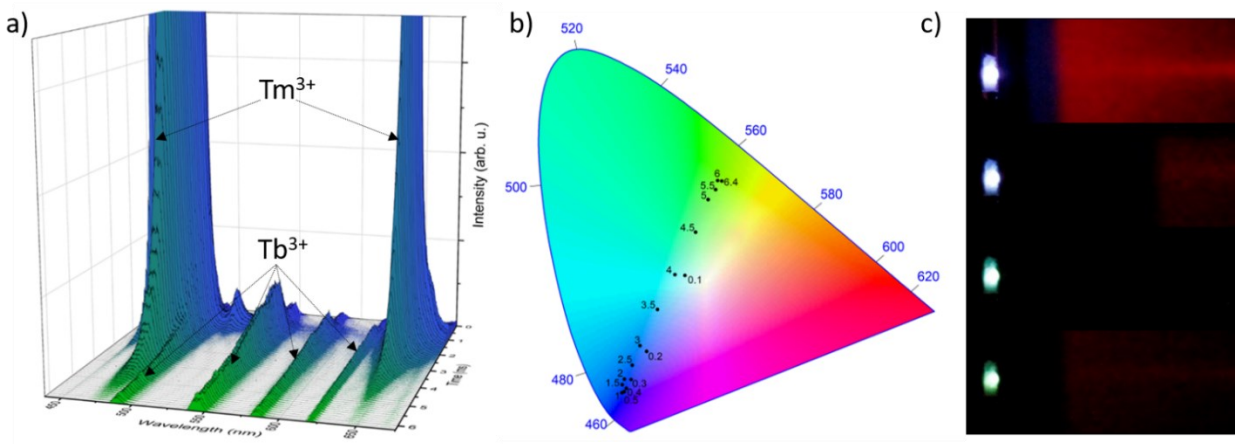

Figure 7 a) Time-resolved spectra of β-$NaGdF_4$: 1% Tm^{3+}, 49% Yb^{3+}/β-$NaGdF_4$: 10% Tb^{3+} core-shell nanoparticles powder samples under excitation from a 976 nm pulsed laser with 1 ms and 4 W/cm^2 peak power. The emissions from the Tb^{3+} and Tm^{3+} ions are indicated by arrows for clarity. B) CIE diagram as a function of time (in ms), obtained from the spectra in Fig. 7a. c) Digital photographs depicting color-tunable emissions as a function of luminescence decay time, taken with a Canon EOS 7D digital camera (operating at a 2.5 ms integration time and ISO6400). A NIR card is present as an indication of the excitation source.

Considering that the error on the FRET efficiency is less than 5% (**Figure S7**), the principal source of depletion for this emission *via* non-radiative pathways is assumed to be dependent on the FRET of the Tm^{3+} ion emissions from the $^1D_2$ and the $^3F_4$ states to Tb^{3+} ions.

It is worth noting that there is a large discrepancy between the FRET efficiencies obtained from the analysis of the decay curves shown in **Figure 4** and the relative decrease in the emission intensities obtained by integration of the spectra shown in **Figure 3**. The considered emissions are quenched by approximately 50% (**Table S2**), which cannot be explained without taking into account a radiative component of the energy transfer. An efficient non-radiative energy transfer requires proximity of the coupled ions, as well as the spectral overlap between the emission of the donor and the excitation of the acceptor [239].The Tm^{3+} ions in the investigated system reside in the core, there will be a defined region at the interface between the core and the shell, in which the distance between the Tm^{3+} and Tb^{3+} ions is sufficiently short to allow efficient FRET. On the

contrary, the emitted light from the core can be attenuated by the Tb^{3+} ions *via* a radiative energy transfer throughout the entire shell.

While radiative energy transfer occurs for the Tm^{3+} emissions overlapping with excitation bands from Tb^{3+} (see excitation spectra in **Figure S4**), non-resonant transitions from Tm^{3+} with respect to Tb^{3+} are quenched in the presence of Tb^{3+}. As an example, the $^3H_4 \rightarrow {}^3H_6$ transition at 803 nm does not correspond to any excitation of the Tb^{3+} ion from its ground states. We performed dual excitation experiments to verify the effect of reabsorption of this emission from the $^5D_4$ state of the Tb^{3+} ion on the emission spectra, reported in the **Figures S8** and **S9**. The dual excitation experiments prove that only the emissions from the $^1G_4$ state of Tm^{3+} are being populated *via* a multiple-step absorption of the 800 nm photons. An increased probability of UCL from the $^1G_4$ state after excitation with an 800 nm pumping source has been confirmed by the results in Tm^{3+}-doped $NaYF_4$ nanoparticles[240]. Cooperative UC was also excluded as a possible mechanism to sensitize Tb^{3+}, being generally less efficient[225], as confirmed from the spectra shown in **Figure S10**. The dual excitation experiments prove that, although an absorption from the $^5D_4$ emitting state of the Tb^{3+} ion is possible due to its relatively long lifetime, it would not result in an increase in the $^5D_4$ emissions or to transitions from higher energy states, due to cross-relaxation pathways. In the absence of any other process explaining the decrease in the luminescence intensity for all the Tm^{3+} ion emissions in the presence of Tb^{3+}, we have shown that the emissions from the $^1D_2$ and $^1G_4$ levels directly populate the excited states of the Tb^{3+} ion *via* radiative and non-radiative pathways. Emissions from Tm^{3+} states, which are not resonant with any absorption band from the Tb^{3+} ground states will not increase the $^5D_4$ emissions. This is confirmed by an increase in the rise time of the Tb^{3+} $^5D_4$ emissions, which will be discussed in the next section to ascertain the influence of the pulse width and peak pulse power density on the luminescence mechanisms.

Pulse and power modulation

The dynamics of emissions varies with both the pulse width and the power density. Studies of UCL after short pulse excitation or a pulse width long enough to obtain a steady-state emission from a specific level has been previously reported [241, 242]. When an ion undergoing UCL is excited with a short pulse, the excitation energy will be distributed within the levels of the ion depending on the absorption cross-section, resonance with the excitation wavelength, and decay time of the metastable intermediate states, allowing for a further population of the higher energy levels. This multiple-step process should result in an increase in the rise time of the emissions for the higher energy states unless the population pathway does not follow a sequential absorption of photons, characteristic of ETU [241, 242].The occurrence of non-radiative phenomena such as cross-relaxation involving metastable levels of an ion is an example of such a deviation, as discussed in the previous section. Decay occurs according to the relative emission probabilities and the occurrence of non-radiative pathways. The rise and decay time are characteristics of the system and represent an indicator of the pathways by which the population and depopulation of a level occur. After emission from an ion reaches the steady-state, the rise time is influenced by the characteristics of the decay time, since the depopulation of the state occurs while further photons are pumped to the level[242]. Also, the decay time will acquire a faster component, determined by a faster response of the emission from the level after achieving saturation or steady-state [242].If the excited levels reach their respective steady-states, the decay time does not change with the pulse width. A proof of this principle is provided in **Figure S11**, where the dynamics of the $^1G_4$ level is reported as a function of the pulse width, without changing the duty cycle, i.e., keeping the peak power density constant. The decay curves are overlapping in the limit of the experimental error, which is due to a minor

oscillation of the peak power reported in **Figure S11**. The error in the measurements with varying the pulse width also takes into account the instrumental response curves shown in **Figure S12**.

The curves shown in **Figure 5** were obtained with different pulse widths and duty cycles, in order to keep the excitation frequency constant, with increasing peak power. Excitation with 1, 2, 3 or 4 ms pulse widths corresponds to a 4, 7, 10 or 14 W/cm^2 peak power density. In general, the decay curves in **Figure 5** show a faster decay with increasing the peak pulse power, as the dynamics are influenced by the pumping power of the excitation source.[37] In **Figure 5**, a decreased decay time of the emissions from the $^1D_2$ and $^1G_4$ levels of the Tm^{3+} ion is observed as a function of Tb^{3+} concentration in the shell. These two levels of Tm^{3+} are the predominant source of excitation for the Tb^{3+} ions, which is consistent with the results obtained for a shorter pulse of 200 µs as discussed in the previous section. This analysis was limited to the emissions that have been shown to contribute to the luminescence from the Tb^{3+} ions. These measurements were also performed on colloidal solutions, reported in **Figure S13**, which follows the same trend as the powder samples presented in **Figure 5**.

The emissions from the $^3P_0$ level of the Tm^{3+} ions and the $^6P_{7/2}$ of Gd^{3+} ions is characterized by longer decay times with increasing Tb^{3+} concentration as provided in **Figure 5**. The weak absorption from Tb^{3+} from the high energy levels resonant with the $^3P_0$ level of the Tm^{3+} ion represent the major limitation for an efficient $Tm^{3+}\rightarrow Tb^{3+}$ FRET from this level (**Figure S4**). The presence of Tb^{3+} ions in the shell has the same influence as an optically inert ion to the depopulation of the $^3P_0$ level of the Tm^{3+} ion. Radiative emission from this level becomes more probable than energy transfer to Gd^{3+} ions and corresponds to an additional depletion of the inefficient population of the Gd^{3+} states through the Tm^{3+} $^3P_0$ level. Consequently, a portion of the $^6P_{7/2}\rightarrow{}^8S_{7/2}$ Gd^{3+} emission decreases because of the presence of Tb^{3+} in the shell. The decay time

of the Gd^{3+} ion shows a longer lifetime as the luminescence from the Tb^{3+} ion increases. Such a result can be interpreted considering a decrease in the probability of energy migration and recombination with surface traps in the presence of the Tb^{3+} ions, due to the decrease in concentration of the Gd^{3+} ions in the shell.

A part of the Gd^{3+} ion emission can be efficiently transferred to the Tb^{3+} ions, as reported in the literature [39, 220-222], and is the origin of the high quantum cutting efficiencies of $Gd^{3+}\rightarrow Tb^{3+}$ co-doped materials [206-208]. However, in the system under study, the major effect of the inclusion of the Tb^{3+} ion in the shell is equivalent to the dilution of the Gd^{3+} with inert ions. Furthermore, a portion of the luminescence is depleted by the less efficient population from the $^3P_0$ state of the Tm^{3+} ion. The Gd^{3+} emission is further reabsorbed from the Tb^{3+} ions, whose location we considered more probable on the surface, given the low FRET efficiency of $Tm^{3+}\rightarrow Tb^{3+}$.

The thickness of the shell in the UCNPs under investigation is considerably larger in comparison with the systems reported in the literature. The inefficient FRET process in the system under investigation in comparison to the large values of the FRET efficiencies reported in the literature for Yb^{3+}, Tm^{3+}, Tb^{3+} co-doped samples suggest that the distance between Tm^{3+} and Tb^{3+} ions is considerably large [197], inhibiting the non-radiative energy transfer processes between the two ions. Nevertheless, the experimental evidence suggests that the Gd^{3+} dynamics does not follow a trend consistent with the literature. The $Gd^{3+}\rightarrow Tb^{3+}$ FRET is efficient in several systems previously studied [206-208]. However, if the Tb^{3+} ions are predominantly present at the particle surface, excited Gd^{3+} in the shell will not transfer energy efficiently to these ions. Clustering in nanomaterials has been observed and proven spectroscopically in β-$NaGdF_4$: Tb^{3+} nanoparticles [230], and it provides an explanation to validate our results. The dynamics of the system further suggests a significant influence of the shell thickness on the Tb^{3+} population mechanism.

The lifetimes in **Figure 5** were analyzed by integrating the curves from the maximum after the pulse has ceased, to take into account the deviation from the single exponential discussed previously for levels reaching the steady-state emission. FRET efficiencies are reported in **Figure 6** as a function of Tb^{3+} concentration. The values for samples in solution and from the powder samples have been calculated as well, from the decay times obtained by a double-exponential fitting, shown in **Figure S14**. From the reported values, it is clear that the $^6P_{7/2}$ level of $Gd^{3+}$and the $^3P_0$ level of Tm^{3+} does not contribute to the Tb^{3+} emission *via* non-radiative energy transfer. The main contribution arises from the $^1D_2$ levels of the Tm^{3+} ion. Such a result is consistent with the reported trend observed when varying the laser power for microparticles co-doped with Yb^{3+}, Tm^{3+}, Tb^{3+} at low pumping power densities [197]. The $^1G_4$ levels have been proven to promote the emission from the Tb^{3+} ions under higher values of the power density[197]. For the core-shell nanomaterials under investigation, the main contribution from the $^1D_2$ level is confirmed even at higher power density values up to the saturation point, as reported in **Figure S15** by correlating the integrated emission intensity of each transition with the $^5D_4 \rightarrow {}^7F_5$ transition of the Tb^{3+} ion at different power densities. The luminescence rise and decay characteristics of the Tb^{3+} ions are shown in **Figure S16**. The temporal difference between the rise time of the Tm^{3+} ion emissions with the rise time from the Tb^{3+} ion arises from the described luminescence mechanism.

From **Figure 7** it is evident that the longer rise and decay times of the $^5D_4$ emissions from Tb^{3+} ions in comparison to the emissions from Tm^{3+} guarantee a large delay between the blue and green emissions from the samples, which can be exploited for easy access to time-dependent luminescence tuning. From the time-resolved spectra in **Figure 7a**, it is evident that the Tb^{3+} ions are emitting after all the Tm^{3+} emissions have decayed. The points in the CIE diagram in **Figure 7b** are obtained from the spectra in **Figure 7a** as a function of time. We propose the use of intrinsic

differences in decay time between the two ions as an efficient way to temporally tune the wavelength of the emission. Time-tunable emissions have been demonstrated to have application in anti-counterfeiting, but the proposed devices require special cameras for the detection of the emissions or pumping sources with tunable powers or pulse widths, which can be expensive[198, 199]. Because the discrepancy between the luminescence decay times of the Tm^{3+} and Tb^{3+} ions are on the scale of μs and ms respectively, the different colors can be observed with a simple digital camera operating with a shutter speed of 2.5 ms to discriminate the emission wavelengths, as shown in **Figure 7c**. Overall, this intrinsic property of the studied nanoparticle system can be a versatile candidate in applications where color tuning is necessary.

Conclusion

We report a comprehensive investigation of the luminescence dynamics in β-$NaGdF_4$: Tm^{3+}, Yb^{3+}/β-$NaGdF_4$: Tb^{3+} core-shell nanoparticles. The study is limited to particles with a size of 20 nm and a thick shell of 6 nm. The use of a thick shell is of paramount importance to avoid quenching of the emissions from the core, which are responsible for the excitations of Tb^{3+} ions in the shell. The results prove that the principal mechanism for the population of the $^5D_4$ emitting state of Tb^{3+} is radiative energy transfer from the $^1D_2 \rightarrow {}^3H_6$ transition of Tm^{3+}. The differences in the proposed mechanism to the results reported in the literature arise from the shell thickness, which contributes to the clustering of Tb^{3+} ions on the particle surface. The $Tm^{3+} \rightarrow Tb^{3+}$ radiative energy transfer results in delayed Tb^{3+} emissions from the $^5D_4$ state with respect to the transitions from Tm^{3+}, which arise from the different intrinsic dynamic properties of the two ions and the Tb^{3+} excitation mechanism. As a proof of concept, emissions from the two ions were detectable at a diverse time after the excitation source as ceased. The proposed intrinsic time-tunability of the emissions can be applied to other systems in which the decay time of the emitters differs

significantly as in the studied core-shell nanoparticles. Further investigations would be required to determine the optimal configuration of the core-shell system for the Tb^{3+} co-localization in the core and the role of the shell thickness in preventing its luminescence quenching. Finally, we underline the importance of systemic spectroscopic investigations to elucidate the luminescence mechanisms at the nanoscale.

Experimental Procedures

1- Materials

All chemicals and reagents were purchased from Sigma-Aldrich. Lanthanide chloride hexahydrates ($LnCl_3 \cdot 6\ H_2O$) were purchased of highest available purity ($GdCl_3$: 99.999%, $YbCl_3$: 99.998%, $TmCl_3$: 99.99% and $TbCl_3$: 99.999%). Trace metal grade sodium hydroxide (99.99%), ammonium fluoride (99.99%) and sodium trifluoroacetate (98%) were used. Technical grade oleic acid and 1-octadecene (90%) were used without further purification.

2- Synthesis of β-$NaGdF_4$: 49% Yb^{3+}, x% Tm^{3+} Core Nanoparticles

Core nanoparticles were synthesized using an established co-precipitation synthesis method.[46] 1.0 mmol of $LnCl_3 \cdot 6\ H_2O$ (51-x% $GdCl_3$, 49% $YbCl_3$ and x% $TmCl_3$, where x = 0 or 1%) were degassed and dissolved in 15 mL 1-octadecene and 6 mL oleic acid at 160 °C for 30 minutes under vacuum with stirring of 350 rpm. The reaction solution was then cooled to 50 °C, and the vacuum was released to inject 10 mL of methanol containing 2.5 mmol NaOH and 4 mmol NH_4F at a rate of 1 mL/min. Stirring was maintained for 30 minutes after the injection was completed. Methanol removal was then completed at about 68 °C with regulated vacuum and Ar-flow as to avoid over-bubbling of the solution. The reaction solution was then increased to 90 °C for 10 minutes and then 120 °C for 10 minutes as to evaporate any residual methanol or water. The vacuum was then released and replaced with a gas bubbler to regulate the Ar-flow. The reaction was then ramped to

300 °C for 2 hours (at a rate of 10 °C/min). The reaction vessel was cooled to room temperature in ambient conditions. Core nanoparticles were collected by dispersion in hexanes and precipitation in ethanol, followed by centrifugation at 4000 rpm in 50 mL centrifuge tubes. This washing process was repeated three times, and the collected samples were stored as solid pellets blanketed in ethanol.

3- Synthesis of β-$NaGdF_4$: 49% Yb^{3+}, x% Tm^{3+}/$NaGdF_4$: x% Tb^{3+} Core/Shell

1.0 mmol $LnCl_3 \cdot 6\ H_2O$ (100-x% $GdCl_3$, x% $TbCl_3$, where x = 0, 10 and 20%) were combined in 8 mL 1-octadecene and 6 mL oleic acid, followed by degassing and dissolving at 160°C for 40 minutes with stirring at 350 rpm and an Ar-flow. The reaction was cooled to 80 °C, followed by the addition of 1.25 mmol sodium trifluoroacetate and 5 minutes of stirring. The reaction temperature was then increased to 100 °C, followed by the addition of 1 mL of hexanes containing 25 mg of oleate-capped core nanoparticles. This solution was left at 100 °C for 10 minutes, and then ramped to 280 °C for 80 minutes at a rate of 10 °C/min. The reaction solution was then cooled to room temperature in ambient conditions and washed/stored using the same method as core nanoparticles.

4- Spectroscopic Characterization

Upconversion emission spectra were obtained using 976 nm excitation from a Coherent 6-pin 15 fiber-coupled F6 series laser diode, controlled using an ILX Lightwave LDC-3744B driver in CW mode and a ILX Lightwave LDP-3811 driver in pulsed mode. For comparative measurements, 1 mg/mL samples of UCNPs in toluene were prepared and verified using ICP-MS. Visible emissions were recorded at a right angle to the incident beam, dispersed by a Jarrell-Ash Czerny-Turner 25-102 1 m double monochromator (1180 grooves/mm) coupled to a cooled Hamamatsu R943-02 photomultiplier tube. UV emissions were recorded at the right angle of the incident beam,

dispersed using an Oriel 77250 1/8 m monochromator (2400 grooves/mm) and detected with a Hamamatsu R4632 photomultiplier tube. Signals were processed through an SR440 Stanford Research Systems preamplifier and converted using an SR400 Stanford Research Systems gated photon counter. Further experimental details are provided in the SI.

Supporting Information

Physical Characterization of β-$NaGdF_4$: Ln^{3+} Upconverting Nanoparticles

A) Emission Spectra

Upconversion emission spectra were obtained using 976 nm excitation from a Coherent 6-pin 15 fiber-coupled F6 series laser diode, controlled using an ILX Lightwave LDC-3744B driver in CW mode and a ILX Lightwave LDP-3811 driver in pulsed mode. For comparative measurements, 1 mg/mL samples of UCNPs in toluene were prepared. Visible emissions were dispersed by a Jarrell-Ash Czerny-Turner 25-102 1 m double monochromator (1180 grooves/mm) coupled to a cooled Hamamatsu R943-02 photomultiplier tube. UV emissions were dispersed using an Oriel 77250 1/8 m monochromator (2400 grooves/mm) and detected with a Hamamatsu R4632 photomultiplier tube. Signals were processed through an SR440 Stanford Research Systems preamplifier and converted using an SR400 Stanford Research Systems gated photon counter.

B) Excitation Spectra

A 150 W Xenon Arc lamp dispersed using an Oriel 77250 1/8 m monochromator (2400 grooves/mm) was used to excite solid powder UCNP samples with varying wavelengths. Emissions were recorded using the same experimental setup as the emission spectra, with a single observed emission wavelength. Spectra are corrected for the efficiency of the exciting source dispersed by the same monochromator.

C) Dual-Excitation Emission Spectra

Emission spectra were recorded using two distinct excitation sources simultaneously, an 800 nm diode laser (Shanghai Laser and Optics Century, model IRM800T3) with either a 488 nm argon ion laser (INNOVA Sabre) or a 976 nm diode laser (Coherent 6-pin 15 fiber-coupled F6 series laser diode, controlled using an ILX Lightwave LDC-3744B). Emissions were recorded using the same experimental setup as the emission spectra.

D) Transmission Electron Microscopy

10 μL of a 1 mg/mL solution of UCNPs in toluene was evaporated on a formvar/carbon film supported on a 300 mesh copper grid (3 mm in diameter). Transmission electron microscopy (TEM) micrographs were taken using a Jeol JEM-2100F microscope operating at 200 kV equipped with a charge-coupled device (CCD) camera (Gatan).

Electron energy loss spectroscopy (EELS) and scanning transmission electron microscopy (STEM) micrographs were completed on the TEM grids of a similar preparation method, using high-angle annular dark-field imaging (HAADF) from an FEI Titan 80-300 HB electron microscope.

E) Powder X-Ray Diffraction

Powder x-ray diffraction (PXRD) patterns were recorded on solid sample UCNPs using a Scintag XDS-2000 diffractometer equipped with a Si(Li) Peltier-cooled solid-state detector, CuKα source at a generator power of 45 kV and 40 mA, divergent beam (2 mm and 4 mm) and receiving beam slits (0.5 mm and 0.2 mm). Scan range was set from 10-90° 2θ with a step size of 0.02° and an integration time of 2 s.

F) Inductively Coupled Plasma – Mass Spectrometry

UCNP samples were digested in preparation for inductively coupled plasma – mass spectrometry (ICP-MS) analysis. 100 µL of a 1 mg/mL UCNP solution in toluene were combined with 1 mL of concentrated HCl and 100 µL of H_2O_2 in duplicates. Test tubes were covered and heated to 115°C for 16 hours to dissociate nanoparticles. The solvent was then evaporated, and the resulting precipitate was dissolved in 5% aqueous HNO_3, producing 5 ppm solutions to analyze. The analysis was completed using an Agilent 7500ce ICP-MS equipped with a quartz Scott-type spray chamber, focused with an off-axis Omega ion lens and an octopole reaction system with a quadrupole mass spectrometer analyzer (operating at a frequency of 3 MHz).

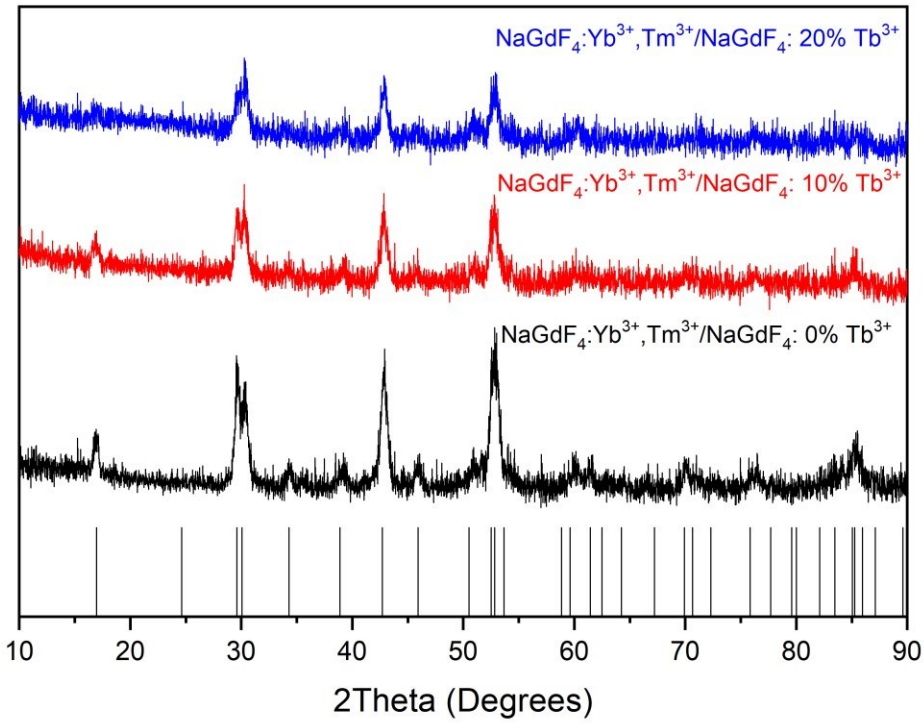

Figure S1 Powder XRD of β-$NaGdF_4$: 1% Tm^{3+}, 49% Yb^{3+}/ β-$NaGdF_4$: x% Tb^{3+} core-shell nanoparticles with x = 0, 10, and 20 (black, red, and blue curves, respectively). The theoretical pattern shown at the bottom was calculated for the P-6 space group, for a = 6.0304 Å and c = 3.6111 Å.[S2] All the diffractions are assigned to the hexagonal β-phase.

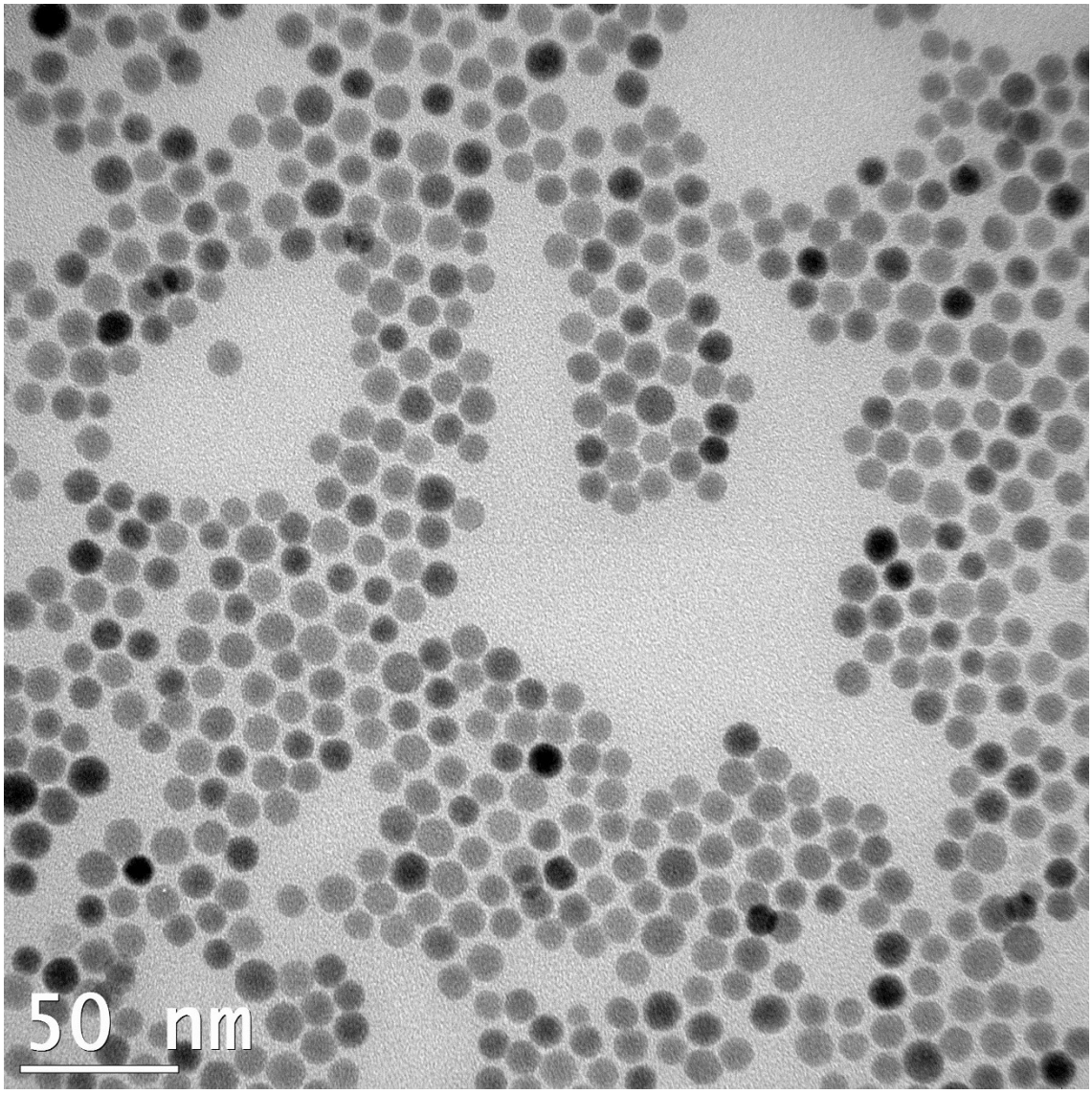

Figure S2 TEM micrographs of β-$NaGdF_4$: 1% Tm^{3+}, 49% Yb^{3+} core nanoparticles. From sizedistribution analyses, the dimension of the core is 8.9 ± 1.1 nm.

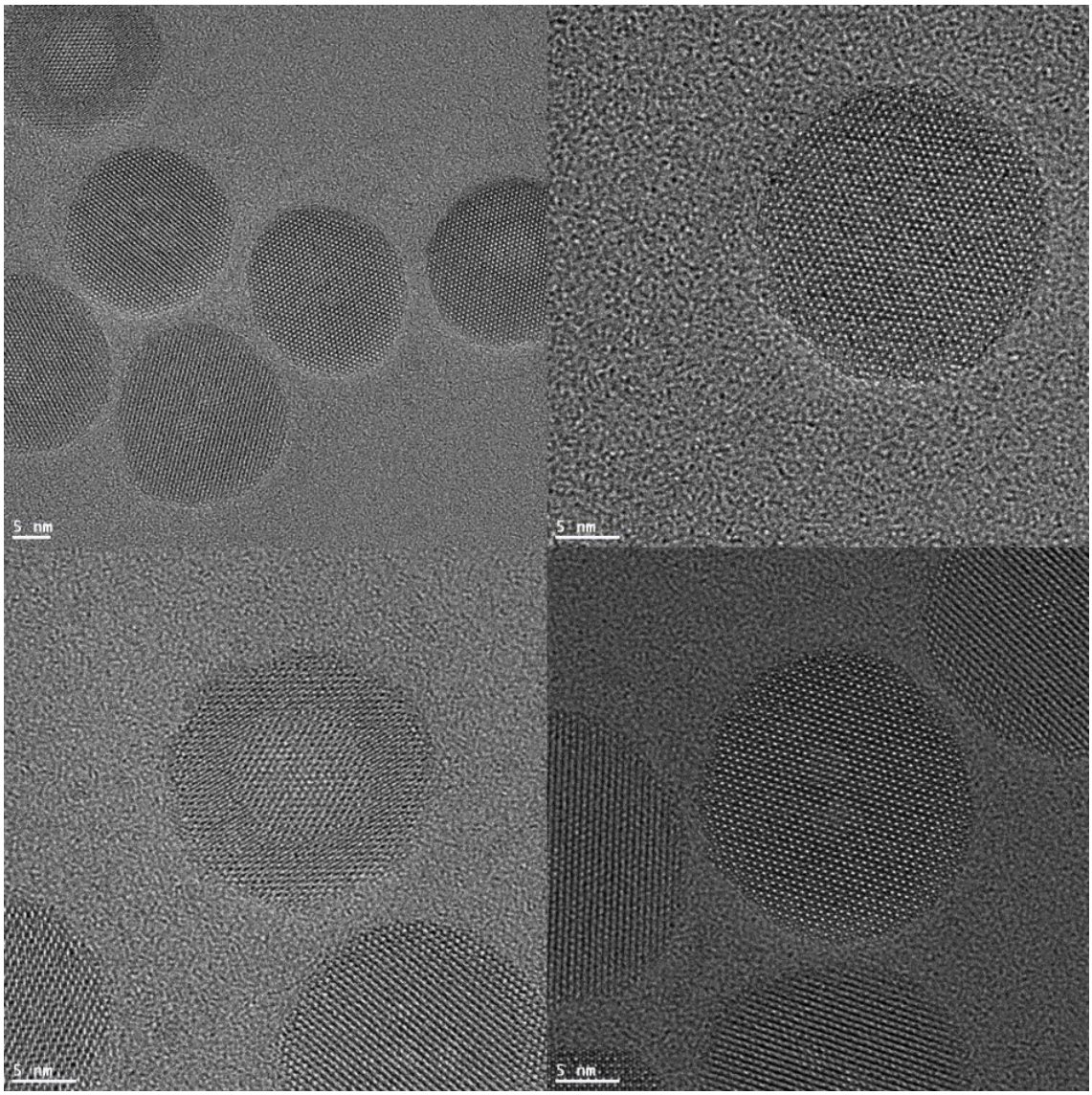

Figure S3 STEM micrographs of β-$NaGdF_4$: 1% Tm^{3+}, 49% Yb^{3+}/ β-$NaGdF_4$: 20% Tb^{3+} core-shell nanoparticles with different magnifications. Most of the particles are uniformly covered, with only a few cores visible, as shown by the distinct crystal planes orientations in one of the particles (bottom left), reported as an example.

Table S1 Molar concentration expressed as ionic percentage and total mass concentration of nanoparticles in solutions of toluene from ICP-MS measurements. The error of the measurements was propagated to include an experimental error of 5%, as provided by the instrument specifications.

Ion	0% Tb^{3+}	10% Tb^{3+}	20% Tb^{3+}
Gd^{3+}	87.5 ± 0.47%	81.06 ± 5.76%	73.79 ± 3.98%
Tb^{3+}	0.09 ± 0.02%	8.1 ± 0.60%	15.97 ± 0.94%
Tm^{3+}	0.26 ± 0.02%	0.25 ± 0.02%	0.24 ± 0.03%
Yb^{3+}	12.15 ± 1.46%	10.59 ± 0.92%	10.01 ± 0.62%
Concentration [mg/ml]	1.084	1.211	0.954

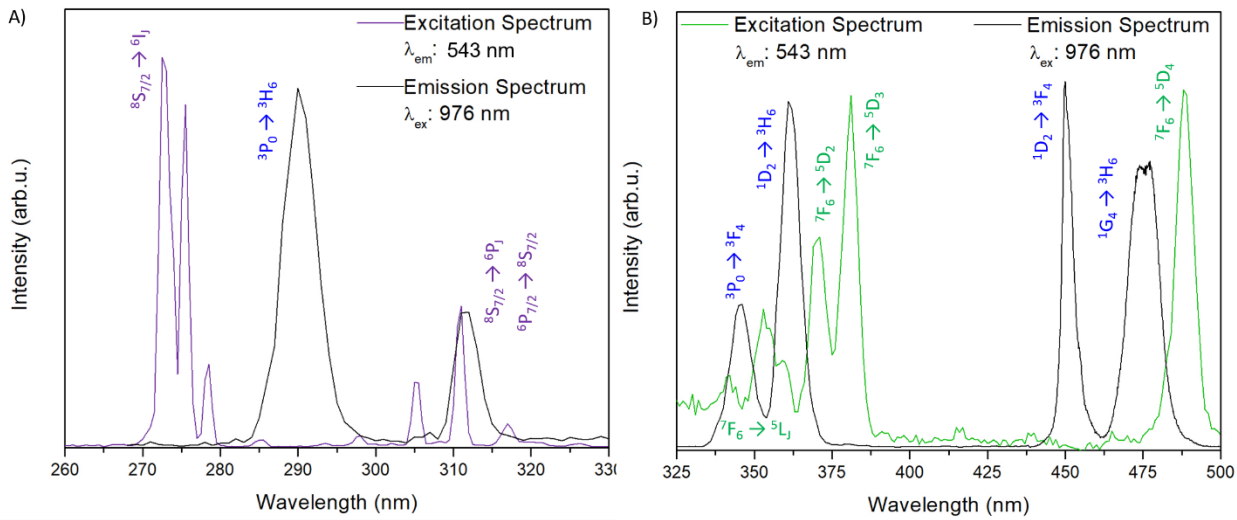

Figure S4 A) Spectroscopic overlap of the excitation bands from Gd^{3+} with the emission band of Tm^{3+} in the UV region. B) Spectroscopic overlap of the excitation bands from Tb^{3+} and the Tm^{3+} emissions in the UV and visible spectral regions. Excitation spectra are recorded for the Tb^{3+} $^5D_4 \rightarrow {}^7F_5$ emission at 543 nm, and emission spectra are excited with a 976 nm CW laser.

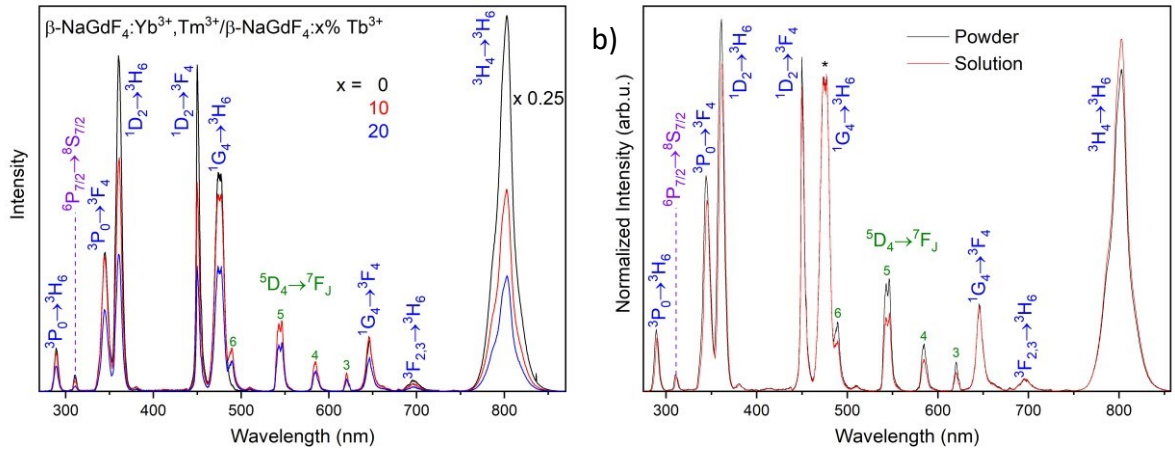

Figure S5 a) Emission spectra of the powder samples and b) comparison between spectra in powder samples and solution under excitation with 976 nm CW laser. Spectra in b) are normalized for the emission indicated by an asterisk. The decrease in the emission intensities for the powder samples is comparable to the one in solution, and the difference between spectra in powder samples and solution can be easily assigned to solvent quenching (emissions from Tb^{3+}) and difference of absorbed power for the small deviations of the other transitions.

Table S2 Percentage of decrease in luminescence intensity for the reported emissions obtained by integration of the spectra in solution in Figure 3 of the main text. All the reported transitions are arising from Tm^{3+} ions, except for the Gd^{3+} $^6P_{7/2}\rightarrow{}^8S_{7/2}$ emission at 312 nm.

Integrated emission		Luminescence depletion percentage	
λ_{em} (nm)	Transition	10% Tb^{3+}	20% Tb^{3+}
293	$_3P_0\rightarrow{}_3H_6$	15.7%	22.1%
312	$_6P_{7/2}\rightarrow{}_8S_{7/2}$	31.0%	49.3%
345	$_3P_0\rightarrow{}_3F_4$	11.1%	25.2%
362	$_1D_2\rightarrow{}_3H_6$	35.5%	46.4%
450	$_1D_2\rightarrow{}_3F_4$	43.4%	52.3%
475	$_1G_4\rightarrow{}_3H_6$	25.1%	32.6%
650	$_1G_4\rightarrow{}_3F_4$	15.7%	26.2%
803	$_3H_4\rightarrow{}_3H_6$	56.8%	67.7%

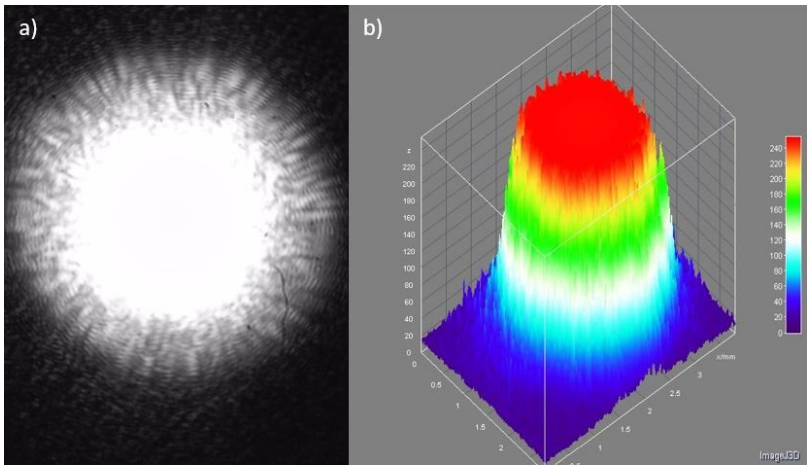

Figure S6 Beam profile obtained using the method described previously in the literature.[S3]

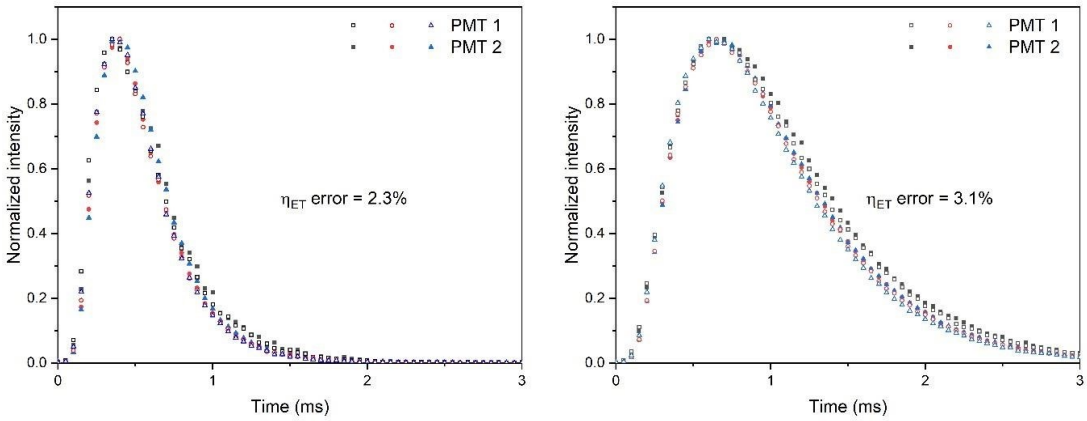

Figure S7 Evaluation of the error on the energy transfer efficiencies achieved by comparing two sets of data obtained on the two PMTs used for the emission from the Tm^{3+} $^1D_2$ and $^1G_4$ levels (left and right, respectively).

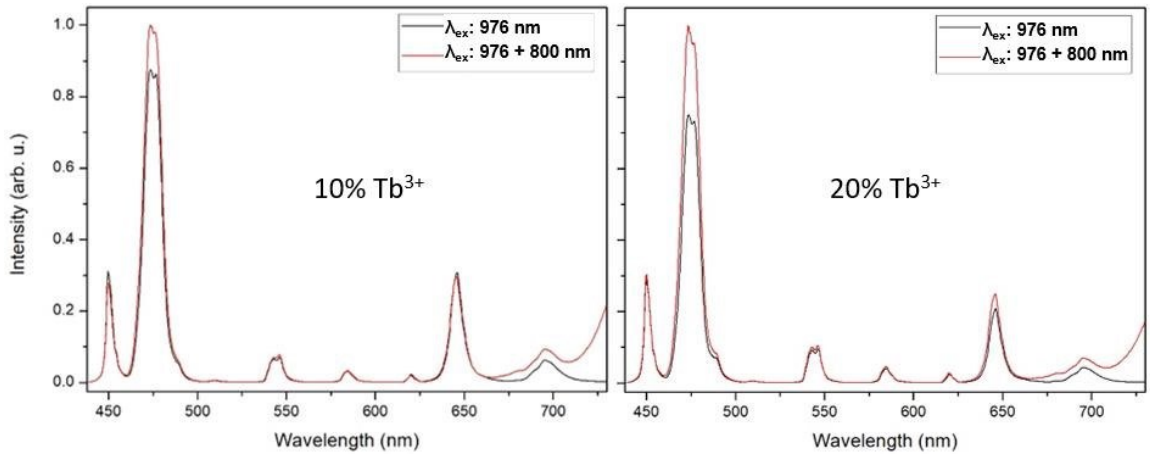

Figure S8 Emission spectra under dual excitation with 976 and 800 nm CW lasers. The increase of the $^1G_4 \rightarrow {}^3H_6, {}^3F_4$ emissions arise from the direct population after excited state absorption of the 800 nm from the metastable Tm^{3+} intermediate levels.

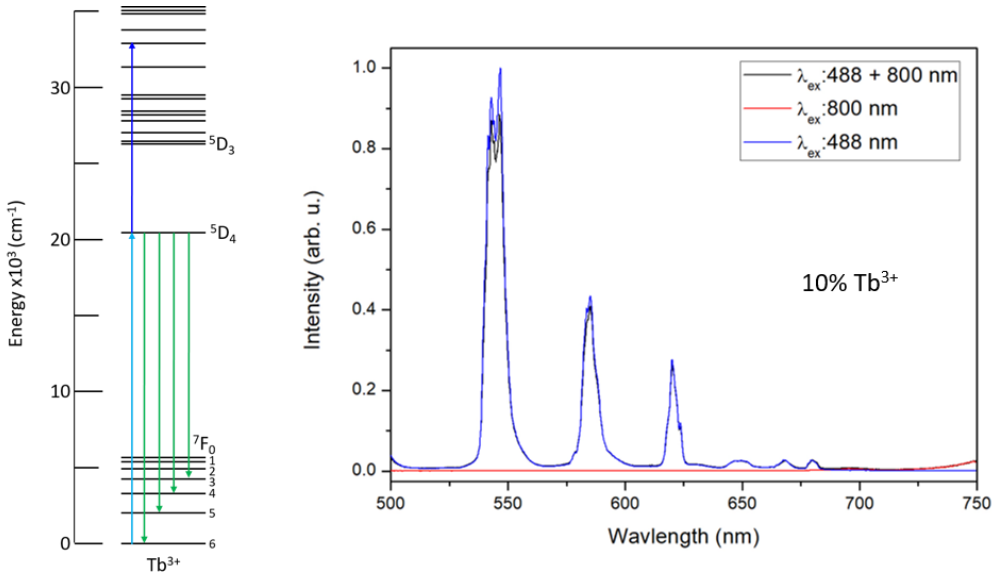

Figure S9 Energy level diagram of Tb^{3+}, representing the dual excitation experiment. Emission from the $^5D_4$ level is represented after successive excitation with 488 and 800 nm CW lasers, and the resulting emission spectra.

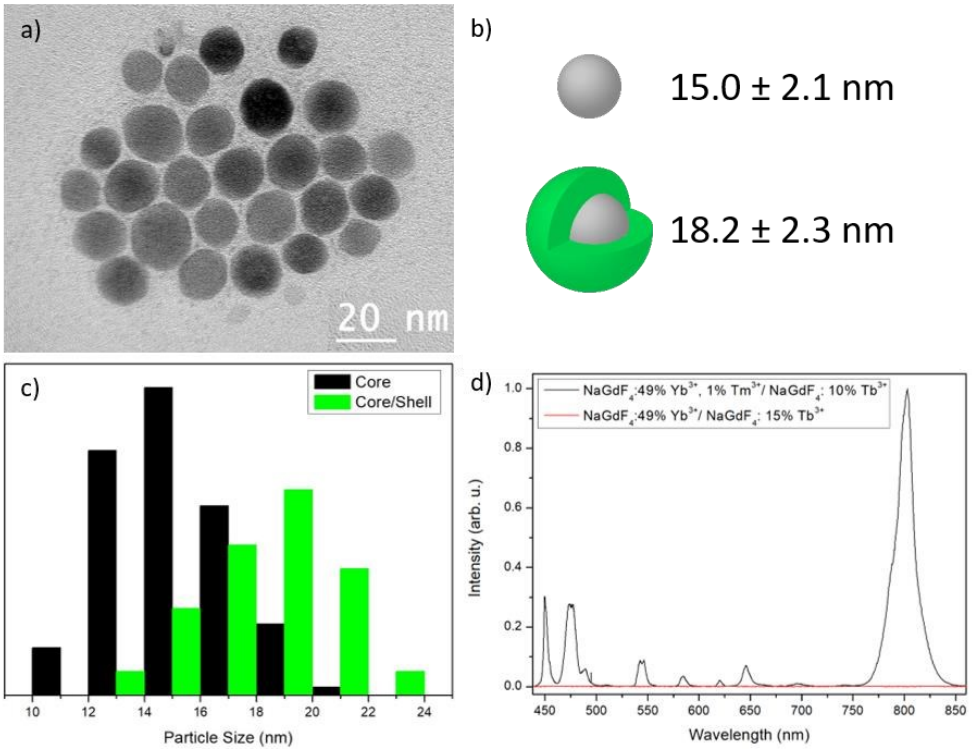

Figure S10 a) TEM micrographs of β-$NaGdF_4$: 49% Yb^{3+}/ β-$NaGdF_4$: 15% Tb^{3+} core-shell nanoparticles and b,c) relative size distribution of the core (black bars) and core-shell (green bars). d) Emission spectra of β-$NaGdF_4$: 1% Tm^{3+}, 49% Yb^{3+}/ β-$NaGdF_4$: 10% Tb^{3+} (black curve) and β-$NaGdF_4$: 49% Yb^{3+}/ β-$NaGdF_4$: 15% Tb^{3+} (red curve) core-shell nanoparticles in solution under excitation from a 976 nm CW laser.

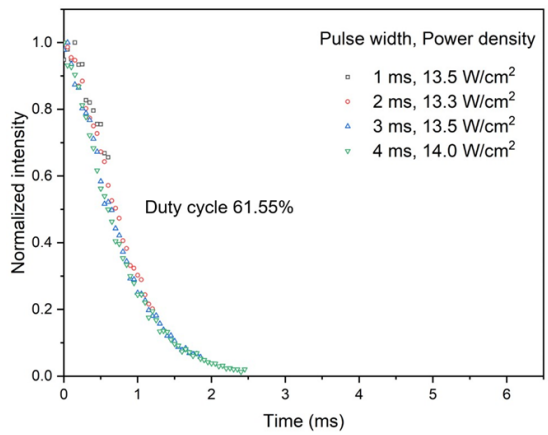

Figure S11 Decay time of the $^1G_4 \rightarrow {}^3H_6$ emission after excitation with a 976 nm pulsed laser with 1, 2, 3, and 4 ms pulse widths at a constant duty cycle, corresponding to the peak powers reported in legend. To depict the overlapping of the decay profiles, they are reported after the excitation source has ceased.

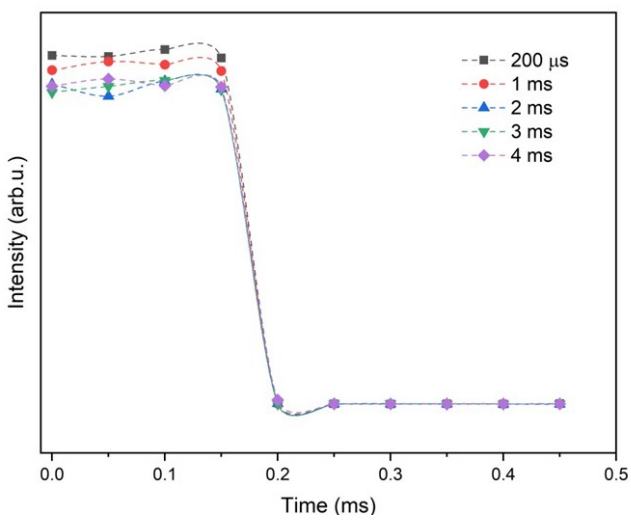

Figure S12 Instrumental response curves varying the pulse width of the excitation source at 976 nm. The derived error in the lifetime measurements is less than 10 µs.

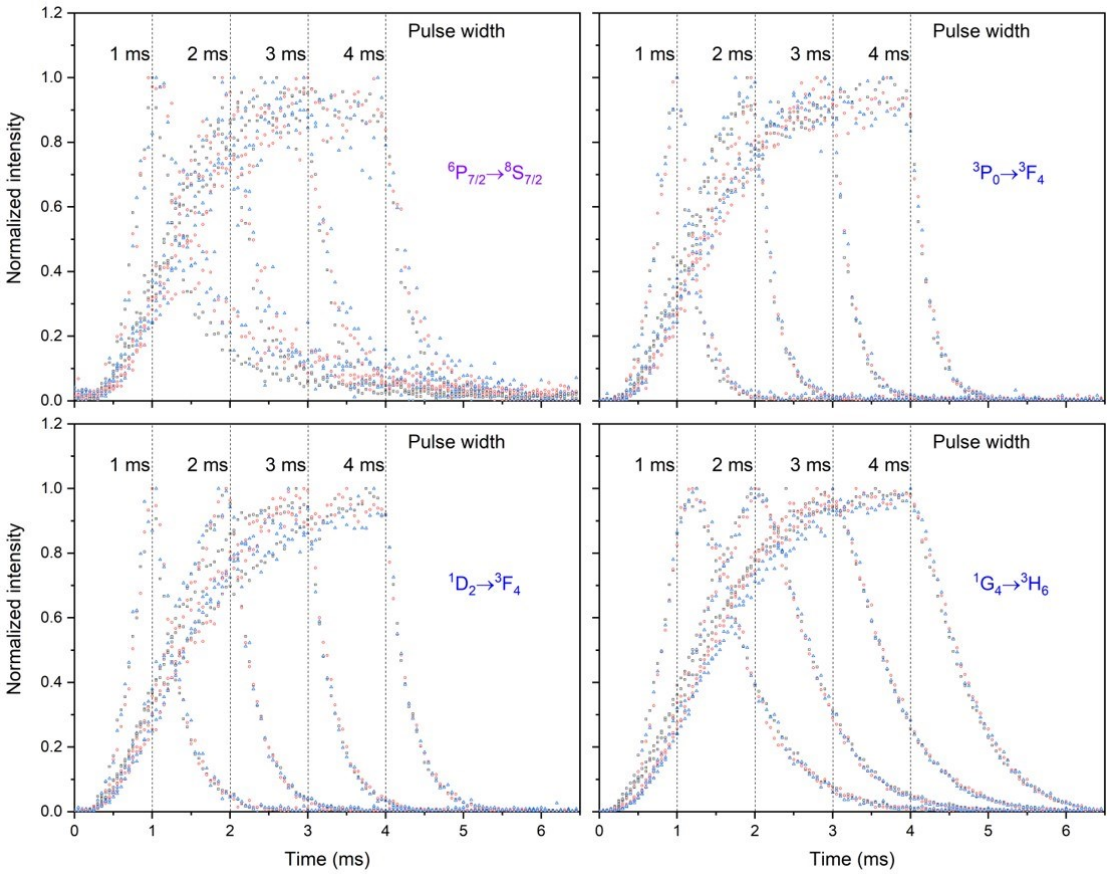

Figure S13 Decay time curves of Gd^{3+} and Tm^{3+} emissions for β-$NaGdF_4$: 1% Tm^{3+}, 49% Yb^{+3}/ β-$NaGdF_4$: x% Tb^{3+} core-shell nanoparticles from samples in solution under excitation from a 976 nm pulsed laser with 1, 2, 3, and 4 ms pulse widths and 4, 7, 10 and 14 W/cm^2 peak powers for x = 0, 10, and 20 (black, red, and blue curves, respectively).

The vertical dotted lines for each pulse width are reported as a visual guide.

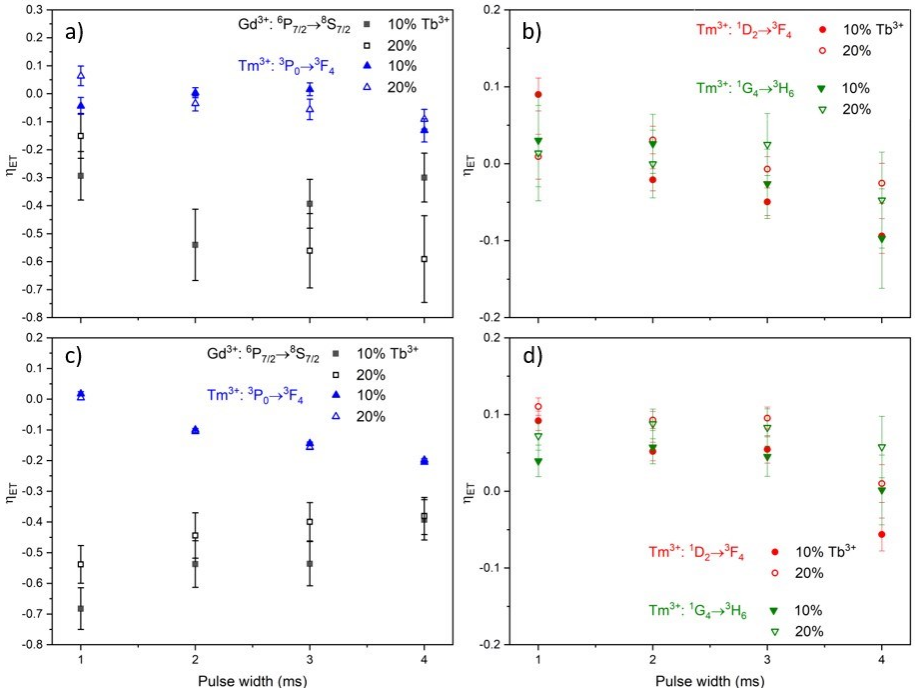

Figure S14 Energy transfer efficiencies calculated from the decay curves in Figure S13 for the solutions (a,b) and for the powder samples in Figure 5 (c,d) as a function of the Tb^{3+} concentration for 10 and 20% doping, and pulse widths. The values of decay times are obtained by a double exponential fitting and the errors bar are obtained by propagating the error of the fitting to the experimental error for the calculation of the energy transfer efficiencies.

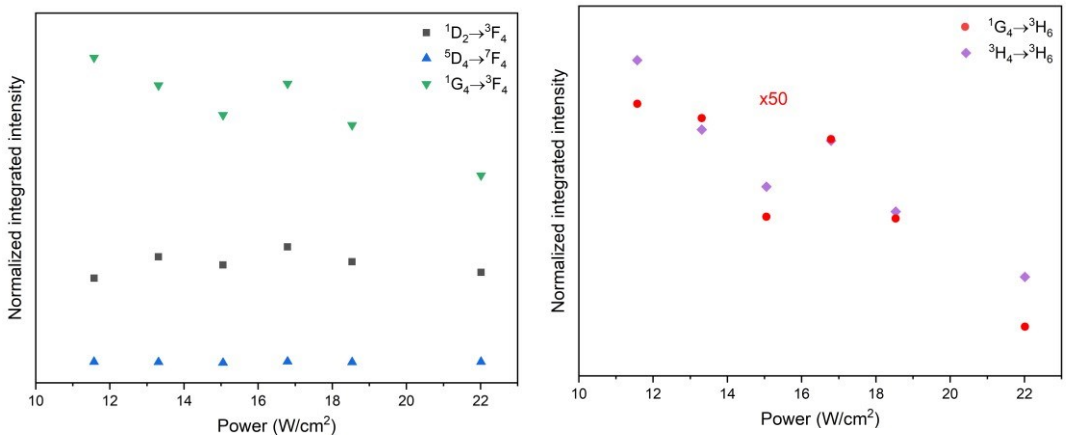

Figure S15 Integrated intensities of the Tm^{3+} emissions reported in the legends, normalized for the Tb^{3+} $^5D_4 \rightarrow {}^7F_5$ integrated intensity as a function of the power density of a 976 nm CW laser. The Tb^{3+} $^5D_4 \rightarrow {}^7F_4$ emission is reported to show the constant linear trend for emissions correlating with the Tb^{3+} ones.

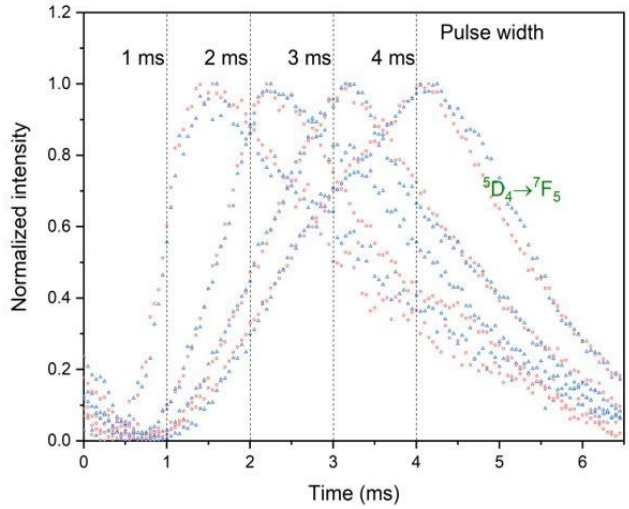

Figure S16 Decay time curves of Tb^{3+} of β-$NaGdF_4$: 1% Tm^{3+}, 49% Yb^{3+}/ β-$NaGdF_4$: x% Tb^{3+} core-shell nanoparticles for powder samples under excitation from a 976 nm pulsed laser with 1,2, 3, and 4 ms pulse widths and 4, 7, 10 and 14 W/cm^2 peak powers for x = 0, 10, and 20 (black,red, and blue curves, respectively). The vertical dotted lines for each pulse width are reported asa visual guide.

Manuscript 5: The key role of intrinsic lifetime dynamics from upconverting nanosystems in multi-emission particle velocimetry

Published as:

Gabriella Tessitore, Steven L. Maurizio, Tarek Sabri, Cameron D. Skinner, and John A. Capobianco*

Advanced Materials. 2020, 32(42):2002266

Department of Chemistry and Biochemistry, and Centre for NanoScience Research, Concordia University. 7141 Sherbrooke St. West, Montreal, Quebec H4B 1R6, Canada

Abstract

Evaluation of particle dynamics at the nano- and microscale poses a challenge to the development of novel velocimetry techniques. Established optical methods implement external or internal calibrations of the emission profiles by varying the particle velocity and are limited to specific experimental conditions. The proposed multiemission particle velocimetry approach aims to introduce a new concept for a luminescent probe, which guarantees accurate velocity measurements at the microscale, independent of the particle concentration or experimental setup, and without need for calibration. The simplicity of these analyses relies on the intrinsic luminescence dynamics of core–shell upconverting nanoparticles. Upon excitation with a focused near-infrared pulsed laser, the nanoparticle emits photons at different wavelengths. The time interval between emissions from different excited states is independent of the local environment or particle velocity. The velocity of the particles is calculated by measuring the distance between the maxima of two different emissions and dividing it by the known difference in luminescence lifetimes. This method is demonstrated using simple digital imaging of nanoparticles flowing in 75–150 μm diameter capillaries. Using this novel approach typically results in a relative standard deviation of the experimental velocities of 5% or lower without any calibration.

Introduction

Particle velocimetry aims to evaluate the velocity field of a particulate probe submerged in a flowing fluid. This technique generally exploits the optical properties of a probe by detecting the luminescence or scattered light after an incident excitation source irradiates the liquid-solid flow under inquiry [243, 244]. The particle velocity can be obtained by measuring the luminescence or scattering from the probe and using a mathematical relationship with the velocity via an external or internal calibration [243, 244].

An external calibration involves the correlation of a measurable optical property of the probe with a known external parameter, such as the flow rate, to ascertain the particle velocity. This type of calibration applies to the majority of velocimetry methods based on the use of a luminescent probe, whose luminescent profile can be recorded and calibrated with varying the flow velocity[245-247]. Lanthanide-doped upconverting nanoparticles (UCNPs) have been previously adopted for velocity measurements, and the ratio between specific emissions provided the velocity after calibration [246, 247]. The limitations of these methods reside in the propagation of the errors to the measured velocities arising from the external parameters used for calibration and from the deconvolution of the luminescence profile, and the necessity to repeat the calibration after any modifications of the experimental setup.

An internal calibration allows evaluation of the particle velocity by tracking the probes within defined time intervals or recording an internal optical property of the probe that varies with the velocity, using a known mathematical equation. Particle imaging velocimetry (PIV) and particle tracking velocimetry (PTV) belong to the first class of techniques relying on an internal calibration, i.e., PIV and PTV are self-calibrated methods[248-250]. The luminescence or scattering from particulate probes is recorded usually after excitation with double-pulse lasers within a known time

interval in sequential images, which are collected and analyzed via algorithms predicting the motion and trajectory of the particles [248-252]. The use of UCNPs in PIV has been proposed to simultaneously measure the velocity and temperature field of these nanoparticles in microfluidics. This self-calibrated method is strictly limited to dilute samples, and the sophisticated algorithms used for the particle tracking change depending on the experimental conditions. The time between sequential images is determined by the recording speed and is consequently affected by the response time of the detector and the delay between pulses, which has to be significantly short to achieve meaningful velocity measurements. These requirements limit the choice of a feasible detector and excitation source to expensive high-speed cameras and fast double-pulse lasers. While PTV allows for the resolution of the instantaneous velocity field of the single particles, other methods, such as molecular tagging velocimetry (MTV), take in consideration the average instantaneous velocity of an ensemble of particles [253, 254]. MTV mainly employs photochromic molecules as tracers, whose luminescence or absorbance can be tailored by the use of multiple light sources, or recorded via multiple detectors recording different wavelengths. As a consequence, the use of MTV generally requires a complex experimental setup. Finally, several ways are described in the literature to achieve 2D and 3D characterization of particle velocity, by use of laser masks to obtain a discretization of the control volume and allow the evaluation of the displacement in all the directions[248, 250, 253, 254].

The limitations of the reported techniques can be overcome and the experimental setup can be significantly simplified if the probe provides not only a luminescent signal to track, but information about the time interval between consecutive recordings. Therefore, it is required to find a system that undergoes two consecutive events with a known time interval between them, independent of the flow conditions. Such a system would provide an opportunity to obtain velocity measurements

without calibration, neither external nor internal. The intrinsic luminescence characteristics of UCNPs offers such a possibility, since the time interval between two intercorrelated emissions does not change with the velocity of the nanoparticle and can act as such a reference [162]. In this communication, we prove that the emissions from Tm^{3+} and Tb^{3+} in $NaGdF_4$:49% Yb^{3+}, 1% Tm^{3+}/$NaGdF_4$:20% Tb^{3+} core–shell UCNPs respect the requirements for such a reference value. Consequently, velocity measurements were performed with these core–shell UCNPs in a toluene flow without the need for calibration or a sophisticated experimental setup. The simplicity and accuracy of this technique stands out in particular with respect to MTV, considering that the average axial velocity profile of an ensemble of nanoparticles was obtained by using a single excitation and detection system. The possible advantages of the use of multiemission particle velocimetry with respect to and in concomitance with other techniques are also discussed.

Results and Discussion

The engineered core–shell UCNPs have a characteristic hexagonal prism shape (20 × 10 nm), forming colloidal suspensions in toluene.[14] The flow of toluene in the investigated velocity range between 1 and 1000 mm s^{-1} follows the so-called laminar flow regime. The flow immediately around a nanoparticle with the same geometry of the proposed nanoprobes was pre-emptively simulated to verify that homogeneous flow was not disrupted by the particles during the measurements and to evaluate the flow characteristics before performing the experiments [255](Appendix S1, Supporting Information).

From the simulated flow conditions in the simplest flow path (a cylindrical tube), it was shown that, depending on the inlet velocity, the particle in the stream modifies the velocity field of the solvent only in a small area around the particle (Figure S1, Supporting Information). More importantly, for the simulated velocity range, the flow lines do not indicate the appearance of

turbulence due to the presence of the particle in the flow (Figure S6.1, Supporting Information). The Reynolds number for the liquid phase (Re_L) ranges between 0.1 and 230 over the simulated velocity regime. This range corresponds to the requirements of laminar flow and produces the expected parabolic axial velocity u (Equation S1, Supporting Information) in the fully developed region (Video S1a, Supporting Information)[256]. The capillary dimensions and velocities used here ensure that this parabolic profile exists over the majority of the capillary length. Simulations and Equation S2 (Supporting Information) predict that the transition to the parabolic profile after the so-called entrance region (x_E in Equations S1 and S2, Supporting Information) occurs, at worst, in the first few mm of capillary (Table S1 and Figure S2, Supporting Information).

Another significant dimensionless number yielding insights into the particle motion is the Reynolds number for the particle phase (Re_p)[255]. Re_p indicates whether the particle flow results in a colloidal dispersion governed by Brownian forces ($Re_p < 10^{-6}$), in a homogeneous ($10^{-6} < Re_p < 0.1$), pseudo homogeneous ($0.1 < Re_p < 2$) or heterogeneous ($Re_p > 2$) flow.[15] Flow regimes other than the homogeneous flow lead to segregation of the velocity field of the nanoparticles from the parabolic profile [255], which would generate errors in the evaluation of the theoretically predicted velocities, making the validity of the proposed technique impracticable to prove. From the analysis of Re_p (Equations S3–S5, Supporting Information, $2.5E\text{-}5 < Re_p < 0.025$), the solid–liquid system can be described in terms of homogeneous flow, and the particle dynamics can be modeled according to the solvent dynamics. Consequently, the Brownian forces acting on each nanoparticle can be neglected in the considered velocity regime with respect to the measurement of velocity for an ensemble of nanoparticles, which follows the solvent flow lines.

Finally, the analysis of the pressure and viscous forces acting on the nanoparticle walls with respect to the other force components further confirms that the resistance offered by the

nanoparticle to the flow is negligible. The contribution to the force balance from drag is orders of magnitude higher than the other forces and ranges between 10^{-13} and 10^{-10} N (Table S2, Supporting Information), comparable with values previously reported in the literature for nanoparticles [257-259]. The small magnitude of the simulated drag forces also guarantees that the nanoparticles follow the liquid phase dynamics without significant resistance. The obtained simulated values and the reported analysis of the dimensionless numbers guarantee that a particle in regions of flow where the interactions with the wall are minimized follows the expected parabolic profile. The maximum flow velocity at the center of the capillary can be expressed as [256]

vp(x,0) = u(x,0) = 2⟨$u$avg⟩ = $2Q/A$ $\quad for\ x$>>xEvpx,0 = ux,0 = 2uavg = 2Q/A

for x>>xE (6.1)

where the particle velocity v_p can be calculated from the fluid axial velocity u at the center of the capillary (r = 0) doubling the average fluid velocity, u_{avg}, obtained by dividing the flow rate Q by the cross-section A for any axial coordinate, provided that x is larger than x_E.

In summary, measurements of the theoretically predicted velocity of the UCNPs in the middle of the capillary are expected to follow Equation **1**. For a full development of the flow lines, the nanoprobes were irradiated by a NIR pulsed laser with a focused beam profile (Figure S3, Supporting Information) after 7 cm from the flow inlet in 10 cm long capillaries (I.D. 150, 100, and 75 μm). The distance between the inlet and the excitation source guaranteed that the measurements were performed in the fullydeveloped region, where Equations S1 and S2 (Supporting Information), and Equation 1 are respected. The excitation source was pulsed to avoid overheating, which would arise for continuous-wave excitation and result in convective motion of the particles around the heated spots, consequently modifying the flow conditions (Appendix S1, Supporting Information for the thermal balances). Digital images of the particle profiles were

recorded with a mobile phone camera mounted on a simple microscope focused on the plane containing the irradiated area in the capillary and analyzed with the software ImageJ (Schematic S1 and Appendix S2, Supporting Information).

The luminescent dynamics of $NaGdF_4$:49% Yb^{3+}, 1% Tm^{3+}/$NaGdF_4$:20% Tb^{3+} core–shell nanoprobes have been thoroughly investigated in a previous article [162]. The green emission (540 nm) from the $^5D_4$ state of Tb^{3+} originates directly from the $^1D_2$ emission of Tm^{3+}, maximized in the blue region (450 nm) [162]. The maxima of the Tm^{3+} emission at 450 nm always occurs 252 ± 10 μs before the maxima of the Tb^{3+} emission at 540 nm. This time interval is independent of the pulse width for short pulses before reaching the emission steady-state (Figures S4 and S5, Supporting Information) [162, 241], i.e., this time interval does not depend on the residence time of the particles within the excitation beam and is therefore independent of the velocity. Moreover, the time interval is not influenced by the particle concentration, being the same in powder samples and colloidal dispersions of these nanoparticles [162]. In energy transfer upconversion, after near-infrared (NIR) excitation, a sensitizer transfers energy to an activator, which in turn emits light at specific wavelengths [237, 260]. Due to this sequential excitation pathway, the emission rise time of the activator is a function of the sensitizer dynamics only, in the absence of quenching phenomena, which can be achieved by protecting the sensitizer ions in a core NP with a thick outer shell. This dependency between two emissions of sensitizer and activator respects the requirements for the definition of an internal time reference essential for velocity measurements. The key aspect for the accomplishment of such a time reference resides in summary in the impossibility to quench the Tm^{3+} emissions, due to the protection with a thick shell, and the almost insensitivity of Tb^{3+} emissions to solvent quenching. The large energy gap between Tb^{3+} levels guarantees that the luminescence dynamics of the emissions from the $^5D_4$ level are unaffected by the solvent

quenching from aromatic moieties. The use of a different solvent containing OH functionalities can, however, cause minor solvent quenching of Tb^{3+} dynamics. We can conclude that using solvent similar to toluene with respect to vibrational modes and refractive index would not influence the difference between maxima, considering that the lifetimes for powder and solutions have been demonstrated to be the same, and that further studies of the luminescence lifetimes have to be performed when solvents with functionalities characterized by high energy vibrational modes are used.

Color digital images of the flowing UCNPs taken through a visible bandpass filter (400 nm < transmittance < 750 nm) show a spatially differentiated multicolor emission profile (Figure 1a), which arises from the difference in luminescence lifetimes between emissions from Tm^{3+} (blue emission) and Tb^{3+} (green emission) (Figure S6, Supporting Information). Ten digital images (minimum) were averaged, the RGB space was converted to the *X, Y, Z* coordinates of the CIE XYZ space, and plotted into the 2D CIE diagram (Figure 1b). The coordinates in the 2D CIE diagram correspond to previously obtained results from time-resolved spectra (Figure 1c)[162]. Two points in the CIE diagram in Figure 1b correspond to the distance between points in Figure 1a and a time interval between two time-resolved spectra in Figure 1c. These results allow for a

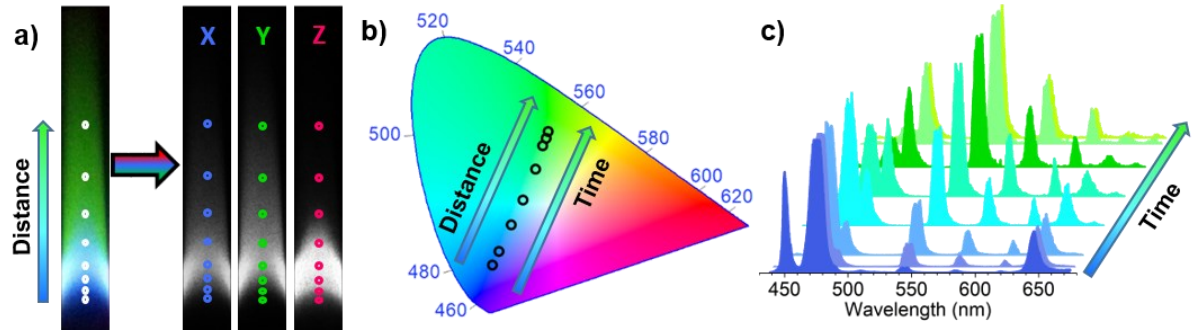

Figure 1 a) Digital image and converted images to the CIE XYZ color space of the typical multiemission flow lines. b) 2D CIE 1931 diagram showing the obtained color coordinates. c) UCNPs time-resolved spectra characterized by the same color coordinated as the points in (b).

correlation between the traveled distance of the nanoparticles and the time delay with the color coordinates, which results in the calculation of the particle velocities.

From previous results [162], it appears that the time-resolved spectra can change with the excitation pulse width, resulting in differences in the reported values on the CIE diagram. However, the time differences between time-resolved spectra representative of two points on the CIE diagram is constant, due to the discussed independency of the emission time interval from the pulse width. With increasing pulse widths, the time at which one emission reaches a maximum shift to the same extent of a second emission sensitized by the first (Figure S4, Supporting Information). Consequently, the delay between the two emissions is unaffected by the pulse width, i.e., the time between two coordinates on the CIE diagram is independent of the velocity. This color-coordinate method requires the use of the same detector for the flow imaging and the time-resolved spectra, which can be obtained by fiber arrays or modern cameras, which allow for both imaging and spectroscopic analyses. The use of different detectors to capture the digital images and record the time-resolved spectra can limit the effectiveness and accuracy of this method if their color sensitivities are different. Also, it requires calibration of the CIE coordinates with time, resulting in a similar approach to the ones already reported in the literature [245-247].

A more flexible way to obtain the particle velocities, without any need for calibration, is achieved by applying blue and green bandpass filters (BP450 and BP540, respectively) to capture the flow as images. In contrast to the color-coordinate method, the influence of the sensitivity of different detectors does not constitute a source of error when the multiple emissions are recorded separately. The luminescent lifetimes (Figure 2a) can be recorded inside the capillary with a photomultiplier tube, under the same excitation conditions used for capturing their profile with a mobile phone camera (Figure 2b). The difference in maximum emission with the time in Figure 2a corresponds to a difference in maximum emission with the distance in Figure 2c, obtained by plotting the intensity of each emission within a rectangular area from the images in Figure 2b. The distance between the two maxima for the blue and green emissions in Figure 2c can be measured and divided by the known delay of 252 μs to obtain the velocity of the particles.

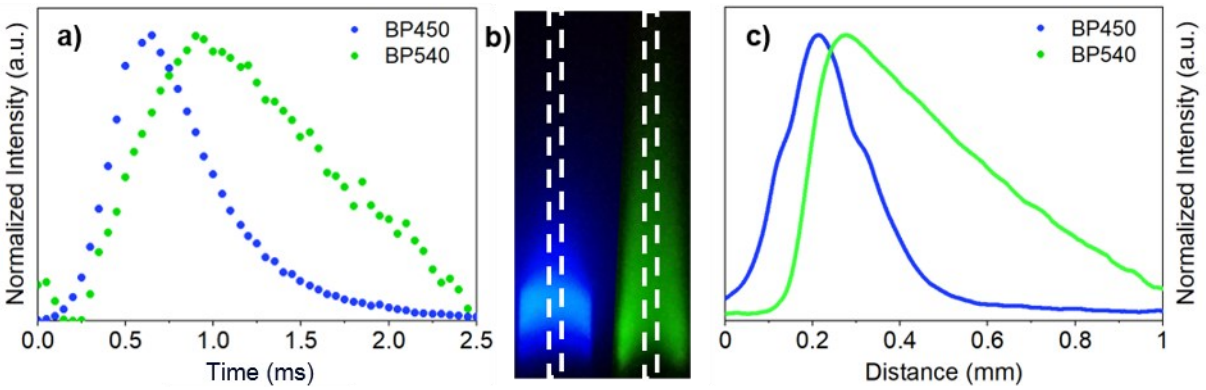

Figure 2 a) Luminescence lifetimes, b) digital images, and c) luminescence profiles within a rectangular area of the microcapillary for the blue and green UCNPs emissions, obtained by alternating blue (BP450) and green (BP540) bandpass filters.

This multiemission approach provides the steady-state velocity of the particles with a very simple luminescence imaging setup and without any need for calibration. With respect to the other methods,[3-13] only two images are needed to establish the travelled distance by these nanoprobes, allowing for maximum flexibility of their use and reducing the experimental error. With respect to

MTV [253, 254], the proposed approach yields the same 1D information without the necessity for multiple excitation sources or detectors. The implementation of similar techniques to mask the excitation source can further produce the 2D or 3D velocity fields when coupled to detection system with tunable in-focus planes. As an example, detection of multiple emissions can be performed with a confocal microscope, where different bandpass filters can be alternated, or by using a setup with two synchronized detectors equipped with different filters, which was recently discussed in the literature [261]. Moreover, we are currently exploring if the RGB filters incorporated into inexpensive digital cameras provide sufficient spectral discrimination to eliminate the need for separate filters. Furthermore, considering the reported possibility to use UCNPs in concomitance with PIV, we are confident that these nanoprobes can be adopted for 2D and 3D velocimetry by masking the laser source to form a grid, as described for the other techniques[248-250, 253, 254], with the substantial advantage of using an inexpensive excitation source other than the double-pulse lasers required for PIV and PTV.

These UCNP nanoprobes were tested with the same experimental setup in a broad range of flow rates (Figure 3a) with three different capillaries. The optical window offered by the microscope, with a 10× lens, was less than 1.5 mm with a spatial resolution smaller than 350 nm for all the images. The obtained results were compared with the theoretically predicted velocities from Equation 1 (Figure 3b), and errors for the experimental and predicted velocities were calculated (Tables S3–S5 and Appendix S3, Supporting Information). The experimental velocities do not vary significantly from the theoretically predicted values. The primary source of error on the experimental measurements originates from the uncertainty in the lifetime (252 ± 10 μs), while the dominant error in the theoretically predicted values arises from the uncertainty of the capillary diameter (≈±4 μm). Without direct measurement of the capillary diameter, the theoretically

predicted values are affected by an error (5% < error < 8%), which is larger than the experimental error (<5%). These results confirm that this strategy avoids calibrating the velocities and therefore folds in less errors in the measurements. Considering the good agreement between the experimental and theoretical values, the accuracy of the technique has been proven, which guarantees its applicability to any flow regime and the whole capillary, as shown in Figure S7 (Supporting Information). Although an accuracy lower than 5% is in good agreement with the results provided in the literature,[3-13] an even higher accuracy can be achieved by reducing the uncertainty on the lifetimes, i.e., by increasing the number of repetitions or using a detector with a faster response time.

The results in Figure 3 can be easily extended to other flow rates by changing the diameter of the capillary, the magnification of the microscope, or choosing another multiemission nanosystem. Higher velocities would require a shorter time delay between sensitizer and activator emissions to minimize the distance between sequential emissions, which can be achieved using a sensitizer with a shorter decay time compared to Tm^{3+}. Inversely, determining lower flow velocities would require a longer delay between emissions to assure the differentiation of the emissions. This new approach indeed provides maximum versatility, considering the range of possible combinations between lanthanide ions to synthesize multi-emission probes for velocimetry[198, 262].

The novelty of multiemission particle velocimetry resides in the use of the intrinsic time-tunable emissions of UCNPs without any need for calibration, no limitations on the particle concentration or shape, and exploiting these nanoprobes with a simple and economical experimental apparatus.

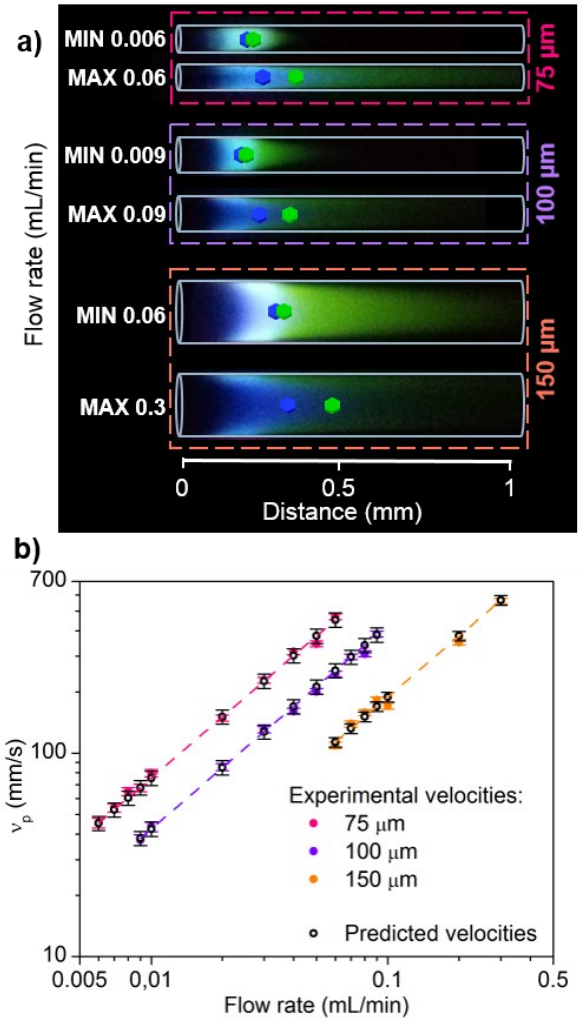

Figure 3 a) Schematic summary of the performed measurements with digital images of the multiemission flow lines for the minimum and maximum flow rates adopted for each capillary (I.D. 75, 100, and 150 µm). The blue and green hexagons represent the maximum for the blue and green emissions, respectively. b) Summary of the experimental (colored symbols) and predicted (black symbols) velocities from multiemission particle velocimetry.

We proved the accuracy of multiemission particle velocimetry by the evaluation of the errors on the measurements, which is lower than the error on the theoretically predicted values.

Therefore, it is desirable to develop UCNPs with a series of chronological emissions, whose differences in rise time are known. Because the correlation of space and time is derived by the intrinsic properties of the proposed nanoprobes, the velocity measurements do not require any data deconvolution or sophisticated algorithms. A more nuanced view is that the calculated velocity

represents the average distance travelled by the particle(s) over the time resulting from the difference in luminescent lifetimes. These nanoprobes yield the definition of an internal reference for the time measurements and the perspective to evaluate motion in any zone of a capillary and flow condition. Although this work focusses on a specific core–shell nanosystem, the idea of this new class of optical probes can be extended to sets of luminophores that are characterized by energy transfer between a sensitizer with long rise times, like in UCNPs, and any activator with resonant states, as long as quenching is avoided by a core-shell approach. Finally, further functionalization can be investigated to achieve dispersibility in several other solvents, proving the great versatility of these nanoprobes and the interest in exploring their application in velocimetry even further.

Supporting Information

Appendix S1 – Simulations

The behavior of particles in nano and microfluidics deviates from the classical models for solid-liquid flow, similar to the plethora of physical and chemical differences that nanoparticles display compared to their bulk material properties. Simulations of the flow dynamics around a nanoparticle were performed, first, studying the flow of pure toluene in a 2D geometry resembling a 100 µm capillary, and then, using the velocity profiles obtained from the 2D model as input for a 3D model of a section of the capillary. The 3D geometry contained a particle in the middle of the flow. 2D and 3D models were implemented following respectively the axisymmetric and symmetric assumptions for the resolution of the Navier-Stokes equations.

The 2D geometry for the simulations represents a 10 cm long and 100 µm diameter capillary, while the 3D section of the same capillary was 10 µm thick, with the particle placed on the symmetry

plane 3 μm from the inlet. The hexagonal particle was 20 x 10 nm in size. The meshes of both the 2D and 3D models were optimized checking the output velocity profiles and verifying the minimum number of cell elements required to obtain no variance between the simulations with increasing number of cells. The size of the meshes in terms of cells for the 2D and 3D models were respectively 50000 and 430000. The results for the simulations are shown in Figure S1.

Validation of the results for the 2D simulation was performed considering the laws governing laminar flow. The flow profile in laminar conditions can be expressed by the parabolic law:

$$u(x,r) = u_{MAX}(x,0)\left(1 - \frac{r^2}{R^2}\right) \; for \; x > x_E \qquad \text{(S1)}$$

Equation S1 expresses the axial velocity *u(x,r)* for an axial *(x)* and radial *(r)* coordinate as a function of the maximum velocity on the axis of the parabolic profile $u_{MAX}(x,0)$ and the capillary radius *R*. This equation is valid for axial coordinates after the entrance region, defined as the axial coordinate where the velocity profile turns from flat to parabolic at $x = x_E$, i.e. in the fully-developed region. For laminar flow, the axial coordinate x_E can be expressed as in Equation S2:

$$x_E = 0.06 Re_L D \qquad \text{(S2)}$$

where *D* is the capillary diameter. The coordinate x_E was calculated (Table S1) from Equation S2 using the same values of density and viscosity for toluene as in the simulations (867 kg m^{-3} and 5.91e-4 $kgm^{-1}s^{-1}$, respectively). The simulated velocity profiles are reported in Figure S2. Comparison of the values of the entrance region in Table S1 and velocity profiles in Figure S2 produced similar results validating the 2D simulations. The simulated forces acting on the nanoparticle wall were summarized in Table S2.

The particle's Reynolds number (Re_p) was obtained using a sphere with a radius such that its volume was the same as the nanoparticle. Knowing the distance between two vertexes of a

hexagonal particle, i.e. the diameter d (20 nm), the volume can be calculated by determining the side length l and the apothem a by:

$$a = \frac{d \sin 60}{2} = 8.66\ nm \qquad l = d \cos 60 = 10\ nm \tag{S3}$$

The volume is further calculated by:

$$V = \frac{(6la)h}{2} = 2598\ nm^3 \tag{S4}$$

Where h is the hexagonal prism height (10 nm). The radius of a sphere with the same volume is r_{eq} = 8.53 nm, from which Re_p can be calculated as:

$$Re_p = \frac{2\rho u r_{eq}}{\mu} = \{2.5E-5\ , 0.025\} \tag{S5}$$

Obtained for u ranging between 1 and 1000 mm/s.

Table S 6.1 Reynolds number for the liquid phase (Re_L) and axial coordinate of the entrance region x_E

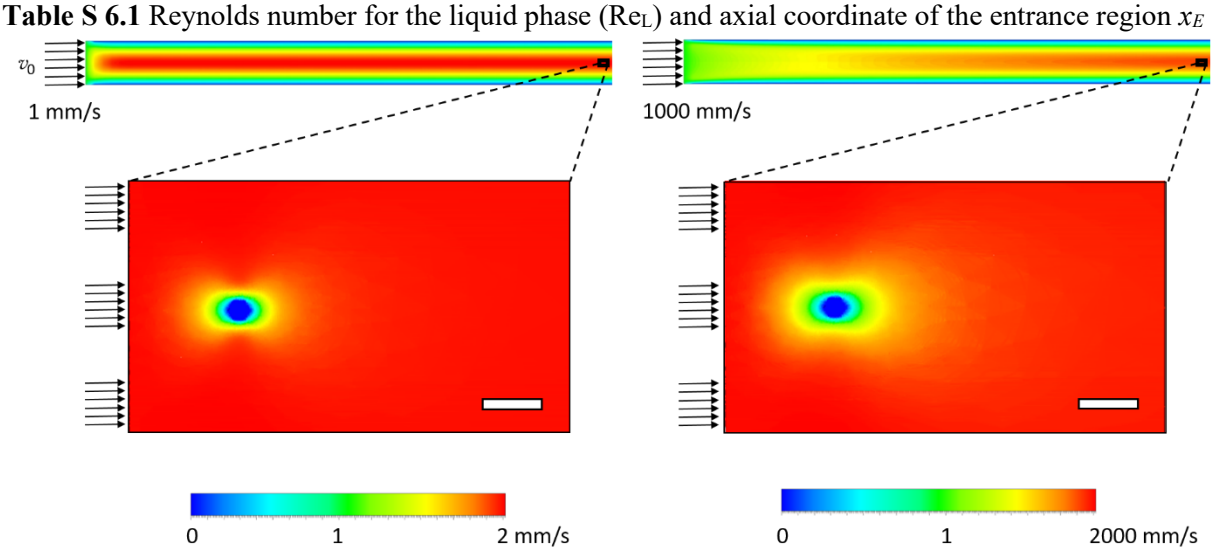

Figure S1 (top) Simulated 2D flow dynamics for toluene in an axisymmetric 100 µm capillary with inlet velocity of 1 (right) and 1000 (left) mm/s in the entrance region. (bottom) Section of the simulated 3D flow dynamics for toluene around a hexagonal particle (scale bar of 50 nm). The inlet axial velocity profile for the 3D simulations is obtained from the 2D simulations in the fully-developed region. The reference system was chosen with the x axis equidirectional with the flow.

from Equation S2 as a function of inlet velocity and diameter of the capillary.

Velocity (mm/s)	Re_L 150 µm	100 µm	75 µm	x_E (m) 150 µm	100 µm	75 µm
1	0.23	0.15	0.12	2.09E-06	9.29E-07	5.22E-07
1000	232.23	154.82	116.12	2.09E-03	9.29E-04	5.22E-04

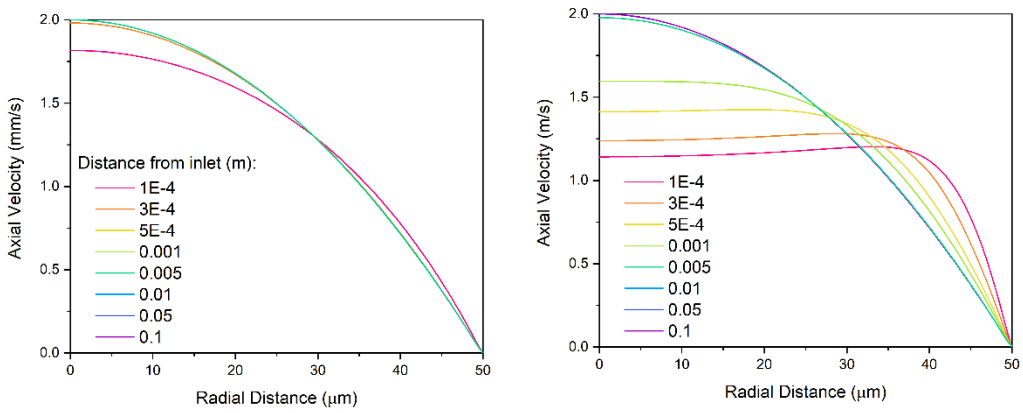

Figure S2 Axial velocity profiles from the 2D simulation of flow dynamics for toluene in a 100 µm capillary with inlet velocity of 1 (left) and 1000 (right) mm/s . The axial velocity profiles are plotted as a function of the radial distance and were calculated along lines at different distances from the inlet line.

Appendix S2 – Experimental

Table S2 Simulated forces and momenta from Figure S 6.1

Velocity / Forces	1 [mm/s]	1000 [mm/s]
F_D [N]	1.24E-13	1.17E-10
F_L [N]	-1.63E-17	4.31E-13
M_{xy} [Nm]	-5.48E-22	-5.17E-19
M_{yz} [Nm]	6.31E-27	3.84E-22
M_{xz} [Nm]	3.03E-25	2.48E-22
F_G [N]	4.32E-19	

Experimental Setup

Core-shell $NaGdF_4$:49% Yb^{3+},1% Tm^{3+}@NaGdF4:20% Tb^{3+} UCNPs were obtained *via* a modified co-precipitation synthesis previously reported.[S1] These core-shell nanosystems produce a hexagonal shape, as is common for this materials, and size of 20.5 ± 1.5 nm x 9.7 ± 1.7 nm. Their composition and luminescent properties were previously reported.[S1] The UCNPs were dispersed in toluene at a concentration of 10 mg/mL or approximately 10^{11} particles/mm^3 to ensure that the bulk properties of the solvent dominated the solution properties i.e. viscosity and density. These colloidal suspensions were sonicated for 20 minutes before use, to avoid precipitation.

The luminescence profiles of these nanoprobes were recorded in capillaries (TSP series Polymicro Flexible Fused Silica Capillary Tubing with internal diameters of 150, 100, and 75 µm, Molex, Inc.) after NIR excitation at 976 nm with a 6-pin fiber-coupled diode laser (Coherent F6 series), operating in continuous mode *via* an external driver (ILX Lightwave LDC-3744B) with a power density of 10^4 W/cm^2 and a beam size of 35 µm (Figure S3). The beam was chopped with an optical chopper at a 20 Hz frequency (model SR540, Stanford Research Systems, Inc.) and blades with adjustable duty cycle, set at 5% (chopper blade MC1F10A, Thorlabs, Inc.), resulting in a 250 µs pulse with a 5 ms overall time interval between consecutive pulses. The beam was focused into the capillary with a single-convex lens (F.D. 20.9 mm) to produce a nearly uniform excitation beam across the lumen of the capillary and in the imaging plane as shown. The lens and capillary holder were mounted on micrometer driven translation stages to achieve optical alignment. The UCNPs colloidal suspensions were injected into the capillaries *via* a syringe pump (11 Plus, Harvard Apparatus), different velocities were achieved by varying the flow rate. A simple microscope (Sixty, AO Instrument Company) was focused on ≈ 1.5 mm of the irradiated region of the capillary, using a 10x 0.25 NA objective. Bandpass filters (Thorlabs, Inc.) were applied on the microscope objective to record selected wavelengths: between 400 and 750 nm (Visible bandpass,

VisBP); 440 and 460 nm (BP450); and from 510 to 590 nm (BP540). A photomultiplier tube (PMT, Hamamatsu R4632) was directly placed on the microscope objective to record the lifetime (Figure S4) from solutions inside the capillary. The signal from the detector was processed through a preamplifier (SR440 Stanford Research Systems) and converted with a gated photon counter (SR400 Stanford Research Systems). Digital images, using automatic exposure settings, were taken by replacing the PMT with a mobile phone camera (Sony Exmor IMX362) and alternating the required bandpass filters. A schematic of the experimental setup is shown in Schematic S1. Finally, spectra of the particles in the capillary (Figure S5) are recorded with the three bandpass filters used, by a fiber-coupled CCD spectrometer (USB4000-UV-VIS-ES, Ocean Optics).

Digital Image Analyses

The analysis of the digital images was performed with the software ImageJ. A minimum of ten stacks (images) per each flow condition was averaged to improve S/N. This RGB image was converted into the CIE XYZ color space by the ImageJ plugin "Color Space Converter", which automatically converts the figure into three gray-scale images. The intensity of these stacks in a point corresponds to a coordinate into the XYZ space. The coordinates x and y in the 2D CIE 1931 diagram were obtained in different points along the capillary axis.

Image to image offsets can occur as a result of changing the filters with different refractive index. These were evaluated by calculating the translation vector using the beam profile inside the capillary in non-flow images. This vector was applied to the flow images to correct for any offsets. The resulting digital images of the blue and green filtered emissions from the nanoprobes were cropped to a rectangular area and the intensities along the axis of the capillary were plotted by

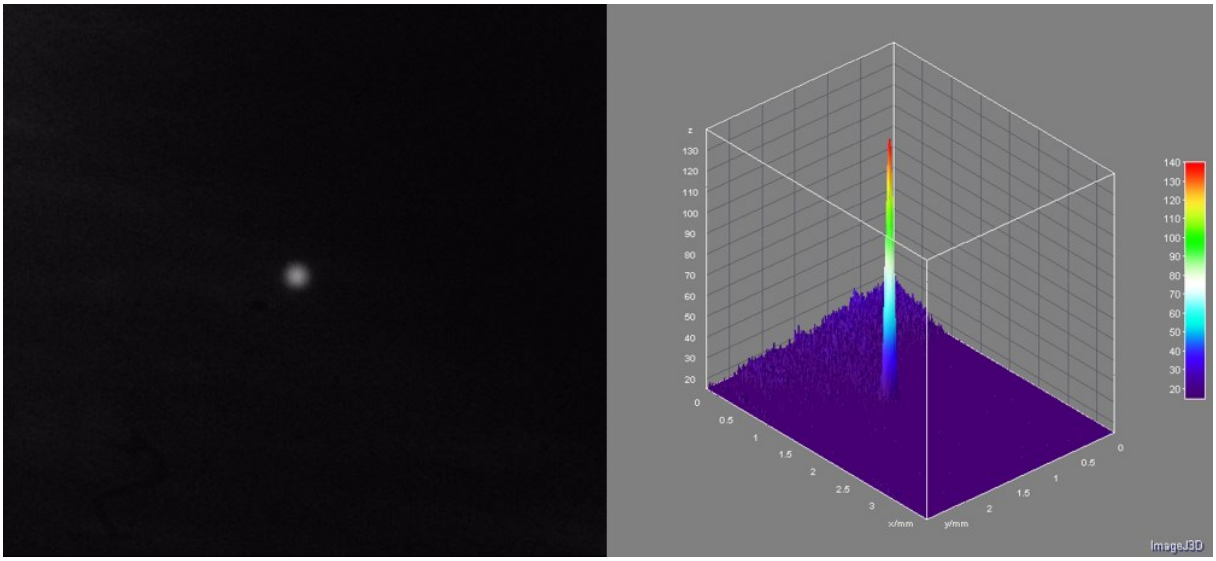

Figure S3 A picture of the focused NIR laser beam (right) was taken with a camera by using neutral density filters, as described before. The analysis of the picture with ImageJ 3D allows for a characterization of the beam profile (left) and diameter (35 µm).

means of the "Plot Profile" tool. The scale was set using the known distance between the inside walls of each capillary. The obtained curves of the luminescence as a function of the distance were plotted in Origin to search for the maximum intensity. The velocities were calculated by subtracting the distance between maxima for the blue and green emissions in each flow condition and dividing it by the measured lifetime difference of 250 µs (Figure 2). The analysis of error for the experimental and theoretically predicted velocities is reported in the next section.

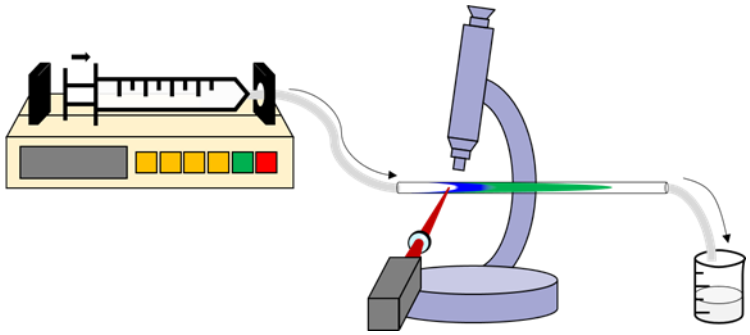

Scheme The experimental setup composed by a syringe pump, a NIR pulsed laser diode, focused with a single convex lens, the capillary and a simple microscope. Pictures are taken from the microscope objective while the pump is allowing the flow of the nanoparticle colloidal suspension at different flow rates.

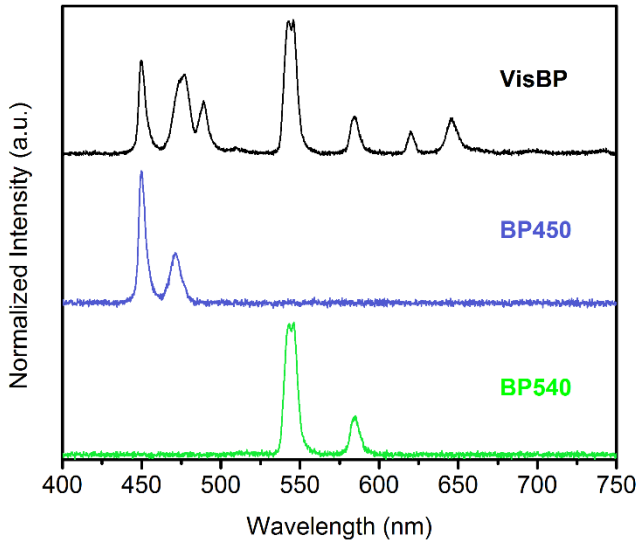

Figure S4 Luminescence spectra for the UCNP nanoprobes under 976 nm NIR pulsed laser excitation with different bandpass filters.

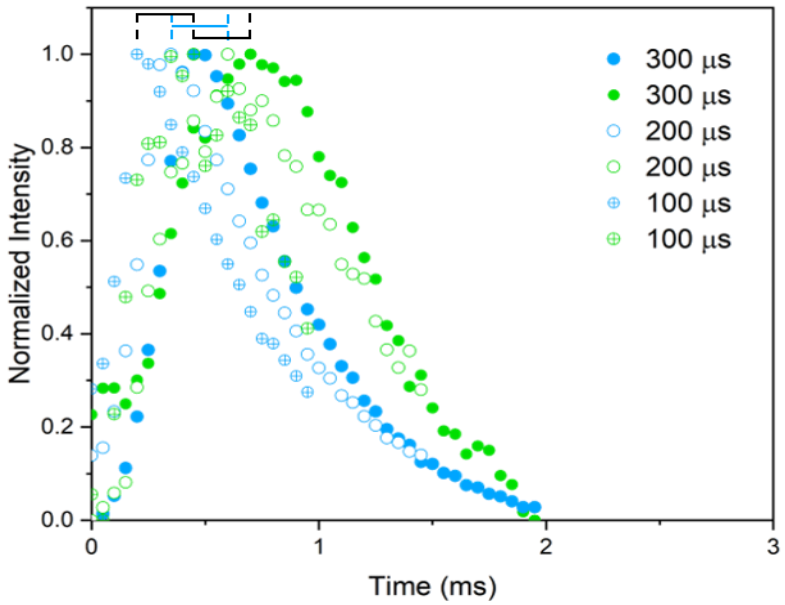

Figure S5 Lifetime curves for the proposed nanoprobes of the blue (blue symbols) and green (green symbols) emissions under NIR pulsed laser excitation with different pulse widths in the legend. The duty cycle is constant for all the measurements to avoid differences in the excitation power.

Appendix 3 – Error Evaluation

The following error evaluation considers both the experimental and theoretically predicted errors. The experimental errors arise from the image resolution and time response of the PMT used to determine the luminescence lifetimes. The axial coordinate of the maximum (x_M) of each emission was considered to occur within a range from the measured value dependent on the resolution (R) of the digital image. Consequently, the range for the distance at which the maximum intensity for an emission was achieved is $x_M \pm R$. The resolution for the recorded digital images was 350 ± 20 nm. The difference in luminescence lifetimes is 250 ± 8 μs as previously reported.[S1] The resulting error on the velocity (u_{exp} = distance between maxima / 250 μs) was obtained by propagation of the error on distance and time for each capillary and flow condition (Table S3, S4, and S5).

Similarly, the theoretically predicted errors were calculated taking into account the accuracy of the flow rate for the syringe pump and the error of the internal diameter of the capillaries. The predicted velocity u_{theo} was obtained by dividing the flow rate for the cross-sectional area of the capillary. The accuracy, provided from the manufacturer, on the volumetric flow was ±1%. The internal diameters of the capillaries were 150 ± 4 μm, 100 ± 4 μm, and 75 ± 3 μm, as reported from the manufacturer. As for the experimental error, the predicted error was evaluated by propagating the error on the flow rate and internal diameter of the capillaries.

Table S3 Measured (exp) and theoretically predicted (theo) values of the axial velocity u, respective standard deviation (S.D.), and percent deviation of the experimental from the theoretically predicted velocities for the 75 µm capillary.

Flow Rate (mL/min)	u_{exp} (mm/s)	$S.D._{exp}$ (mm/s)	u_{theo} (mm/s)	$S.D._{theo}$ (mm/s)	Exp/theo %
0.006	45.46	2.46	45.27	3.65	0.42
0.007	54.03	2.63	52.82	4.26	2.29
0.008	64.91	2.87	60.36	4.87	7.54
0.009	67.60	2.93	67.91	5.48	0.46
0.01	79.77	3.23	75.45	6.08	5.73
0.02	149.00	5.16	150.90	12.17	1.26
0.03	228.24	7.57	226.35	18.25	0.83
0.04	315.76	10.30	301.80	24.33	4.63
0.05	345.64	11.24	377.26	30.42	8.38
0.06	469.49	15.15	452.71	36.50	3.71

Table S4 Measured (exp) and theoretically predicted (theo) values of the axial velocity u, respective standard deviation (S.D.), and percent deviation of the experimental from the theoretically predicted velocities for the 100 µm capillary.

Flow Rate (mL/min)	u_{exp} (mm/s)	$S.D._{exp}$ (mm/s)	u_{theo} (mm/s)	$S.D._{theo}$ (mm/s)	Exp/theo %
0.009	37.48	2.31	38.20	3.08	1.88
0.01	43.60	2.42	42.44	3.42	2.73
0.02	85.52	3.38	84.88	6.84	0.75
0.03	130.40	4.62	127.32	10.26	2.42
0.04	160.92	5.52	169.77	13.69	5.21
0.05	201.04	6.73	212.21	17.11	5.26
0.06	245.20	8.09	254.65	20.53	3.71
0.07	297.88	9.74	297.09	23.95	0.27
0.08	308.28	10.06	339.53	27.37	9.20
0.09	385.52	12.49	381.97	30.80	0.93

Table S5 Measured (exp) and theoretically predicted (theo) values of the axial velocity u, respective standard deviation (S.D.), and percent deviation of the experimental from the theoretically predicted velocities for the 150 µm capillary**.**

Flow Rate (mL/min)	u_{exp} (mm/s)	$S.D._{exp}$ (mm/s)	u_{theo} (mm/s)	$S.D._{theo}$ (mm/s)	Exp/theo %
0.06	109.20	4.02	113.18	6.14	3.52
0.07	139.36	4.88	132.04	7.16	5.54
0.08	158.36	5.44	150.90	8.19	4.94
0.09	182.53	6.17	169.77	9.21	7.52
0.1	170.62	5.81	188.63	10.24	9.55
0.2	351.48	11.42	377.26	20.47	6.83
0.3	560.93	18.06	565.88	30.71	0.87

Manuscript 6: Wavelength-Selective Nonlinear Imaging and Photo-Induced Cell Damage by Dielectric Harmonic Nanoparticles

Published as:

Vasyl Kilin,[*,†] Gabriel Campargue,[†] Ina Fureraj,[†] Sim Sakong,[†] **Tarek Sabri,[‡]** Florian Riporto,[¶] Alice Vieren,[†] Yannick Mugnier,[¶] Christophe Mas,[§] Davide Staedler,[k] John Michael Collins,[⊥] Luigi Bonacina,[†] Alfred Vogel,[#] John A.Capobianco,[‡] and Jean-Pierre Wolf[†]

ACS Nano 2020, 14, 4, 4087–4095

† Department of Applied Physics, Universitè de Genève, 22 chemin de Pinchat, 1211 Genève 4, Switzerland

‡ Department of Chemistry and Biochemistry and Centre for NanoScience Research, Concordia University, 7141 Sherbrooke St. West, Montreal, Canada

¶ Univ. Savoie Mont Blanc, SYMME, F-74000 Annecy, France

§ OncoTheis Sàrl, 18 chemin des Aulx, CH-1228, Plan-les-Ouates, Geneva, Switzerland

k Department of Pharmacology and Toxicology, University of Lausanne, Lausanne, Switzerland

Abstract

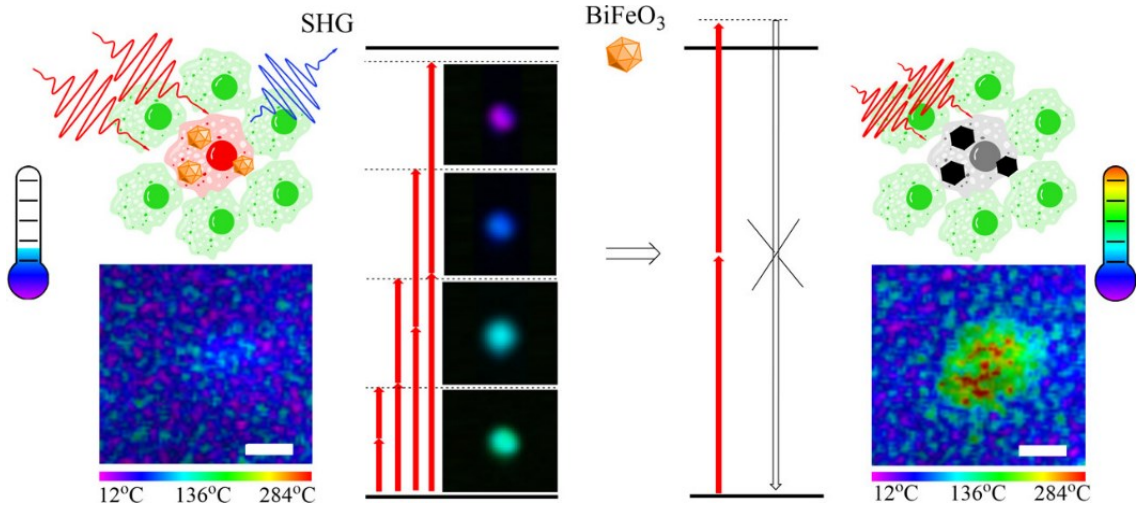

Scheme Schematic representation of harmonic generation photoinduced cell damage, and Ln-UCNPs nanothermometry

We introduce a nonlinear all-optical theranostics protocol based on the excitation wavelength decoupling between imaging and photoinduced damage of human cancer cells labeled by bismuth ferrite (BFO) harmonic nanoparticles (HNPs). To characterize the damage process, we rely on a scheme for *in situ* temperature monitoring based on upconversion nanoparticles: by spectrally resolving the emission of silica coated $NaGdF_4:Yb^{3+}/Er^{3+}$ nanoparticles in close vicinity of a BFO HNP, we show that the photointeraction upon NIR-I excitation at high irradiance is associated with a temperature increase >100 °C. The observed laser–cell interaction implies a permanent change of the BFO nonlinear optical properties, which can be used as a proxy to read out the outcome of a theranostics procedure combining imaging at 980 nm and selective cell damage at 830 nm. The approach has potential applications to monitor and treat lesions within NIR light penetration depth in tissues.

Introduction

Nanoparticle-based theranostics is often associated with multimodal interaction in which the control over diagnostics (imaging) and treatment (e.g., cell disruption, drug-release) procedures is exerted by physically distinct stimuli (e.g., optical, magnetic). In some settings, the rapid access to different kinds of interaction exploiting the same physical vector and equipment can be the key to success. Approaches based on plasmonic absorption of gold nanoparticles have been intensively studied in the past decade [263]. In this case, irradiation at low pulse energy enables the use of nanoparticles as markers, whereas an increase of pulse energy results in thermomechanical effects that can be used for localized destruction of target cells or structures. However, from the practical viewpoint, the separation between the two regimes is difficult to control, especially when thick cell layers are irradiated and the radiant exposure changes as a function of depth. In this work, we investigate the excitation wavelength decoupling between imaging and photoinduced damage of cells labeled by bismuth ferrite (BFO) harmonic nanoparticles (HNPs). It was previously shown that BFO HNPs are suitable cell markers for nonlinear microscopy [264, 265]. Their contrast is based on second- and third-harmonic generation (SHG, THG) rather than luminescence. Harmonic generation is a parametric nonlinear process where N incident photons at frequency ω interacting with a nonlinear medium are scattered as a single photon at frequency $N \times \omega$. As we previously demonstrated, the colocalization of SHG and THG typically excited between 1200 and 1300 nm leads to additional selectivity against the background; in fact, it can be exploited to detect HNP-labeled structures against endogenous sources of harmonic signals [264, 265], such as collagen or lipids [266]. Furthermore, the long excitation wavelengths strongly limit autofluorescence that may hinder the marker detection in tissues.

The procedure we demonstrate here implies harmonic generation using excitation ≥980 nm for imaging, followed by photointeraction at shorter wavelengths (820–830 nm) for localized damage of BFO labeled cells. Although the process of harmonic generation is not directly associated with photon absorption, it is known that nonlinear conversion efficiency can be enhanced when the excitation or emission frequency is tuned to a resonance [267]. In this case, concomitant with the harmonic emission, heat can be deposited onto the particle following direct multiphoton excitation or linear reabsorption of SHG [268]. Within this resonant approach, the temperature reached by a ZnO nanowire excited by two photons above the band gap frequency was recently estimated to 327 °C [269]. The amount of temperature increase does not exclusively rely on the choice of the excitation frequency, but also on other parameters playing a role in local heating dynamics, in particular, the numerical aperture (NA) of the focused beam [270],the laser repetition rate, and the dwell time [270, 271]. Keeping all other conditions identical, MHz sources are more effective for heating than kHz ones because the interpulse delay is short compared to the heat dissipation rate.

To demonstrate the possibility to select the photointeraction modality by wavelength switching, we characterize the process in three stages. (i) We study the dependence of imaging and permanent damage as a function of peak irradiance, irradiation dose, and wavelength for BFO HNPs, and unlabeled and labeled cancer cells. (ii) We devise an all-optical scheme based on $NaGdF_4:Yb^{3+}/Er^{3+}$ upconversion nanoparticles for in situ temperature monitoring around a nanometric heating source. (iii) We demonstrate the spatial selectivity of the photodamage procedure on a coculture containing labeled and unlabeled cells.

Results and Discussion

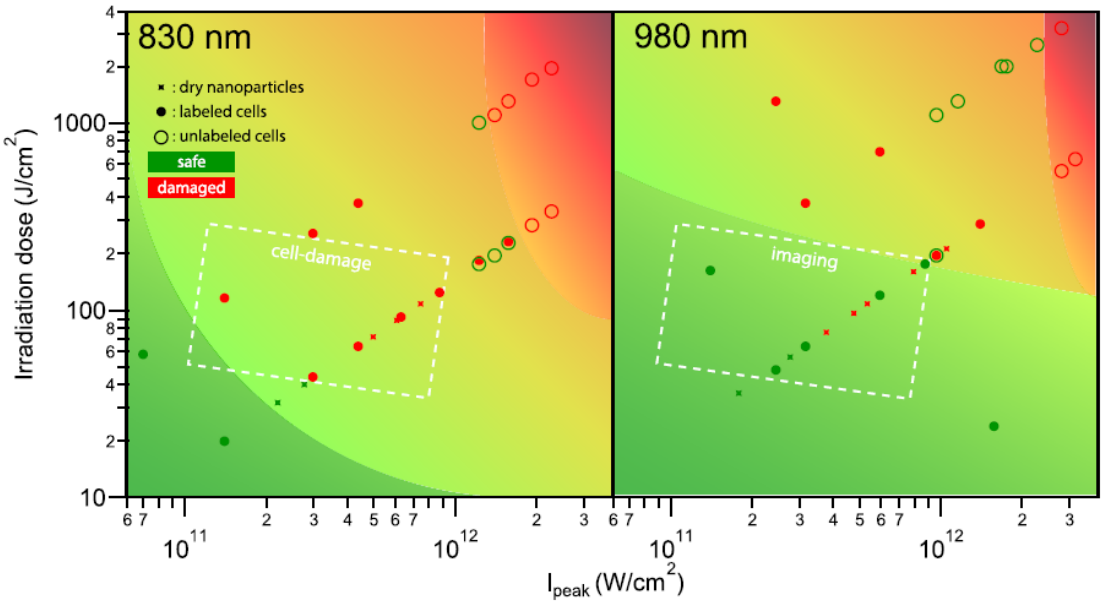

Figure 1 Assessment of photoinduced damage as a function of irradiance and irradiation dose on dry BFO HNPs dispersed on a microscope coverslip (stars), unlabeled A549 cells (open circles), and BFO-labeled A549 cells (filled circles). Green corresponds to safe exposure and red to unsafe exposure observed during the first image scan as detailed in the Materials and Methods section. Variation of irradiance goes along with a variation of the total irradiation dose that depends on pixel dwell time (4.1 µs and 23.8 µs for the measurements in the lower and upper diagonal series, respectively). The dashed box outlines the theranostics window, i.e., an irradiance/irradiation dose region characterized by a different interaction modality (imaging, photodamage) on labeled cells when the wavelength is switched between 980 and 830 nm.

Figure 1 provides an overview of the photoinduced effects of different irradiation parameters. Damage thresholds for dry particles or small particle aggregates, labeled cells, and unlabeled cells exhibit pronounced differences at 830 and 980 nm. This makes it possible to identify parameter regimes for damage-free cell imaging at 980 nm, and targeted cell destruction at 830 nm (see dashed boxes). These regimes and the underlying interaction mechanisms will now be discussed in details.

Effect of Laser Irradiation on Dry BFO HNPs on a Substrate

The direct band gap of BFO is approximately centered at 450 nm (2.7 eV) [272]. Upon resonant interaction in this spectral region, differently from what has been reported for ZnO [267, 268, 273], for two-photon excitation >800 nm we observe pristine SHG spectra and no or very weak photoluminescence (Figure S2, upper plot). The latter is normally reported for one-photon excitation of <400 nm [274]. On the other hand, we observe that the SHG signal vanishes permanently upon irradiation at intensities and irradiation doses above specific threshold values (Figure 1). As reported in Figure S 3, the dynamics of the SHG signal from a large ensemble of BFO HNPs on a substrate undergoing areal scanning irradiation follows a characteristic decay. The sudden drop at the beginning of the irradiation procedure originates from the complete loss of SHG from the larger HNP aggregates present on the substrate with concomitant emission of a broadband luminescence signal (Figure S2, lower plot). The slower decay stems from the progressive disappearance of SHG from smaller aggregates and isolated nanoparticles.

The SHG loss is likely associated with the processes affecting the noncentrosymmetric crystal structure of BFO [275]. The XRD pattern measured for BFO HNP powder irradiated at high peak irradiance at 820 nm for several consecutive hours presents several distinct features as compared to the traces obtained for samples either treated with low irradiation or not irradiated (Figure S5). In particular, the highly irradiated sample trace indicates the presence of SHG-inactive phases such as metal Bi and Fe_3O_4. This finding is likely related to a major rise in the local temperature, but it also points to a reduction of the oxidation state of the Bi^{3+} and Fe^{3+} ions. Previous work on the temperature dependence of the crystal structure already enables a rough assessment of the temperature rise associated with the structure modifications observed in the

present study. In the 447–767 °C range, bulk BFO is known to be less thermodynamically stable than the sillenite $Bi_{25}FeO_{39}$ and $Bi_2Fe_4O_9$ phases [276]. The irreversible transformation of sol–gel BFO powders to $Bi_2Fe_4O_9$ above 504 °C has also been reported [277]. In the case of nanoparticles, these temperature values should be taken as indicative, because of very probable size effects. Decomposition byproducts with different absorption properties might also contribute to local heating by changes in the optical absorptivity upon irradiation, as previously observed in the ablation of dielectric materials [278, 279].

In Figure 1, star symbols indicate all the irradiation conditions tested on dry BFO HNPs as a function of peak irradiance, irradiation dose, and wavelength (left: 830 nm, right: 980 nm). The first two parameters are calculated according to the expressions reported in Materials and Methods. The irradiation dose is computed considering exclusively a single image frame. Consequently, we report in red the data points corresponding to exposure settings leading to the observation of nanoparticles' SHG suddenly disappearing during the first image scan concomitant with the emission of luminescence, while the irradiation-safe conditions are indicated in green.

Temperature Rise around BFO HNPs

To calculate the extent of the temperature rise associated with the damage onset, we developed a specific protocol to image and quantify in situ the temperature increase of nanoparticles upon laser irradiation. We used 30 nm silica-coated $NaGdF_4:Yb^{3+}/Er^{3+}$ upconverting nanoparticles (UCNPs) as local temperature probes by exploiting the thermal sensitivity of the $^2H_{11/2}$ and $^4S_{3/2} \rightarrow {}^4I_{15/2}$ emissions of the Er^{3+} ion. The temperature can be estimated by measuring the ratio of the two fluorescence intensities centered at 525 and 545 nm [280]. This spatially resolved approach provides access to the heterogeneity of HNP individual responses. Similar procedures have already been developed with different upconversion nanomaterials in other settings, for

example, by heating gold nanorods embedded in a biological tissue and using $CaF_2:Nd^{3+},Y^{3+}$ for ratiometric temperature readoutb [281].

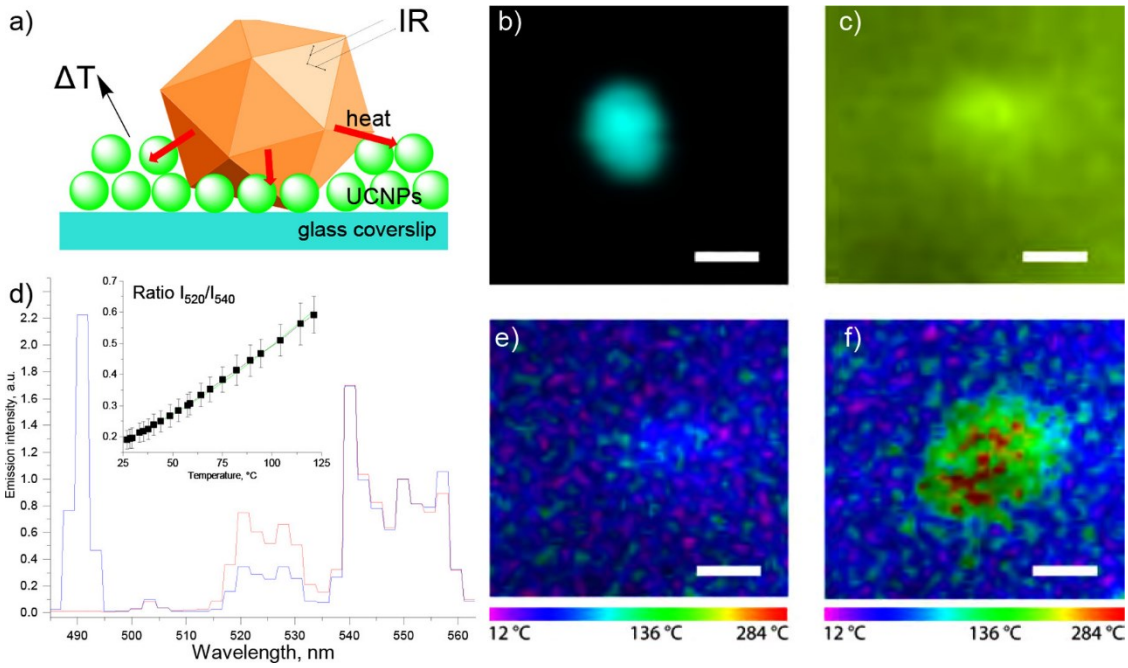

Figure 2 In situ characterization of the temperature increase around a small BFO particle aggregate probed by UCNPs nanothermometry. (a) Schematic representation of the sample. (b,c) Hyperspectral images of a BFO particle surrounded by UCNPs excited at 980 nm. The SHG emission centered at 490 nm is visible in the 485−515 nm spectral region (b). UCNP luminescence overlaps the SHG emission when the full 485−565 nm spectral range is shown (c). (d) Spectrally resolved emission of a HNP and UCNP mixture as in (a) obtained with irradiance/irradiation dose below (blue line, showing the SHG peak at 490 nm) and above threshold with loss of SHG (red line). The traces are normalized by the emission intensity at 540 nm. Inset: Temperature calibration curve showing the UCNP I520/I540 intensity ratio as a function of the substrate temperature. (e,f) Temperature-resolved images of the particle in panels (b) and (c) plotted using a false-color map extracted from the calibration curve in d). The excitation intensity corresponds to the photostable regime (b, c, and e) and permanent loss of SHG (f), respectively. Scale bar 1 μm.

As illustrated in Figure 2a, we prepared a sample by casting a drop of a mixture of BFO HNPs and UCNPs on a glass coverslip and letting the solvent evaporate. We successively acquired an image with the laser tuned to 980 nm under HNP-safe settings. The hyperspectral images obtained under these conditions are shown in Figure 2 (b,c). The former plot is limited to the spectral channels in the SHG region (480–515 nm); the latter covers the full spectral range, 480–

565 nm (Figure 2c). The images indicate the presence of a small HNP nanoparticle aggregate emitting a strong SHG signal superposed to a homogeneous layer of UCNP emission. Figure 2d shows the characteristic UCNP emission spectrum featuring the two bands in the visible region upon NIR excitation. These green bands can be conveniently separated from the narrow SHG blue emission at 490 nm when UCNPs and BFO HNPs are simultaneously excited at 980 nm. We calibrated the response of UCNPs under our imaging conditions (without HNPs) by artificially changing the temperature of the substrate where the UCNPs are deposited using a home-built Peltier element slide holder. The band intensity ratio was fitted according to I525/I540 = C exp $\Delta E/kT$, with C being an experimental constant, k the Boltzmann constant, and ΔE the energy difference among the excited states of the Er^{3+} ion leading to the I525 and I540 bands. Notably, the agreement of the data points to the fitting function is preserved throughout the entire investigated temperature range, 30–120 °C.

For visualizing the temperature distribution around BFO HNPs, the area shown in panels b and c was irradiated under excitation conditions below and above the threshold for photodamage of BFO dry nanoparticles. Note that for this specific measurement, we set the laser at 980 nm for photodamage in order to collect SHG and also resonantly trigger the upconversion process. From the analysis of the UCNP I525/I540 ratio, we found that this exposure entails a significant temperature rise, up to >200 °C for some HNPs. This value was extrapolated from the fit to the experimentally determined calibration curve measured up to 120 °C (Figure 2d). The temperature-resolved maps in Figure 2 (e,f) at low and high irradiance/dose settings, respectively, indicate that the temperature increase colocalizes with the position of the SHG-active particle.

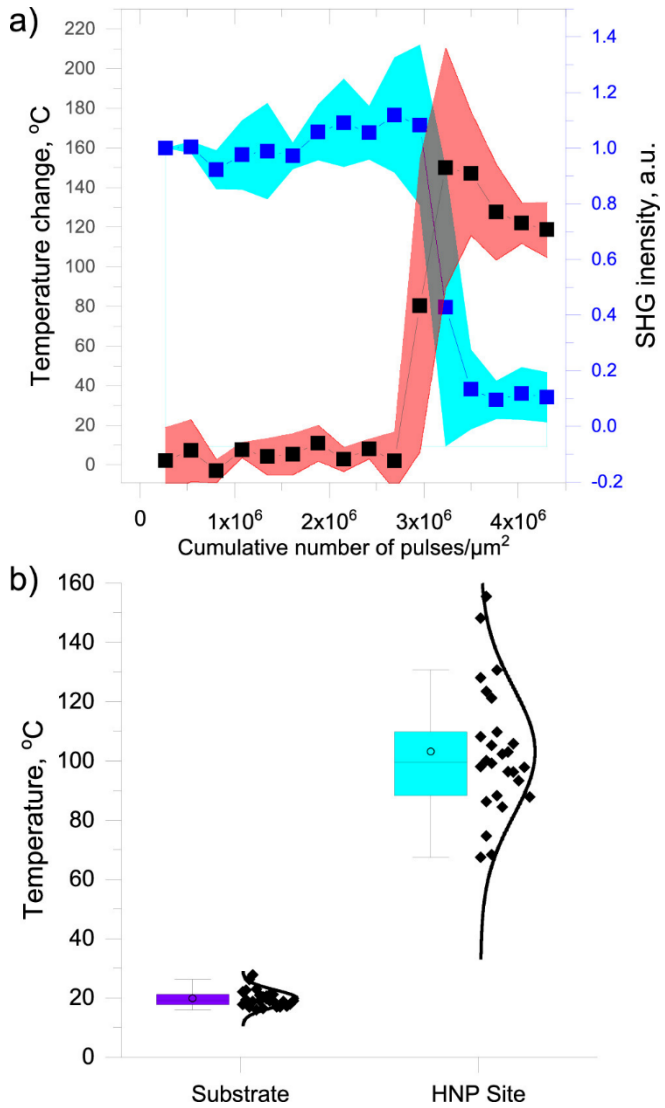

Figure 3 (a) Time evolution of the temperature change (red) and SHG intensity (blue) during irradiation. Each data point corresponds to an image of a sequence acquired at 0.25 fps. (b) Temperature distribution in the absence (left, Substrate) and in close proximity (right, HNP Site) of a BFO HNP.

Figure 3 shows the kinetics of the SHG loss under the same irradiation conditions as in Figure 2 (d,f) and the concomitant temperature rise. The kinetic traces in Figure 3a were obtained by averaging the response of a few (N = 3) HNPs. We repeated the procedure on a larger number of particles (N = 25) in order to define a statistical distribution of the temperature increase (Figure 3b). HNPs are heating up to 100 °C on average, with a fairly broad distribution indicating a large

particle-to-particle variability, which might be associated with the aggregation state or the size, according to the broad distribution measured by DLS (see Figure S1) [282]. We assume that the actual temperature is even higher than 100 °C considering that we detect time-averaged values at a slow frame rate (0.25 frame per second, fps).

BFO HNP-Mediated Cell Damage

After having assessed the photodamage on the dry particles at two selected wavelengths, we now study the effect of BFO HNP-mediated light-interaction in cell medium and on living cells. In Figure S4, we report the results of the protocol described for dry NPs applied to BFO HNPs in cell medium. The outcome of the measurement is quantitatively similar, displaying a slightly lower temperature increment consistent with the different thermal properties of the surrounding medium. For this temperature estimation, we applied the calibration of Figure 2. Although an approximation, this approach is partially justified by the findings of Balabhadra et al., who showed that the thermal calibration is only slightly dependent on the surrounding medium [283]. Quintanilla et al. have shown that this dependence can be associated with the light extinction properties of the UCNP environment. Indeed, absorption and scattering in the sample might differ at the wavelengths of the two emission bands used for the ratiometric temperature estimation [281]. This effect was recently observed in experiments on 3D cell cultures treated with different media [284]. The epi-detection configuration of our setup should minimize this effect, in fact by collecting the backward emission we ensure that upconverted photons travel through a very thin sample layer.

An increase in autofluorescence intensity correlated with cell damage upon laser irradiation has been reported by several authors [285, 286], and it is commonly referred to as hyperfluorescence

[287]. By monitoring the onset of strong hyperfluorescent spots, we first determined the intensity required for direct cell damage by irradiating adenocarcinomic human alveolar epithelial cells (A549) without nanoparticles. For this procedure, we used red fluorescent protein (RFP) expressing cells. The irradiation conditions tested for 830 and 980 nm excitation are reported in Figure 1. Unlabeled cells (open circles) appear in green when we observed no visible damage upon laser exposure, and in red when they are affected. The position of the boundaries between the two possible outcomes in the plots is wavelength-dependent, as already reported [288]. We colored in red the region of irradiation parameters unsafe for unlabeled cells and in green the region that is safe for both unlabeled and labeled cells (the shaded areas in the plots are exclusively based on the data points reported, and should be considered qualitative guidelines to ease the inspection of the plots).

Similarly, labeled cells are indicated as green and red filled circles, for safe and unsafe irradiation conditions, respectively. As compared to the case of unlabeled cells, the presence of BFO HNPs clearly shifts the threshold leading to photodamage to lower irradiance/dose values. In the case of very sparsely labeled cells (containing only a few HNPs, not shown), photodamage takes place at higher irradiance/irradiation dose values. We also notice that dry HNPs have the tendency to be photodamaged at lower irradiation parameters than labeled cells, likely because of the absence of a water environment facilitating heat dissipation.

Overall, we can now delineate three distinct regions for the interaction: (i) the green region corresponds to conditions not leading to the observation of hyperfluorescent spots in labeled cells; (ii) the yellow region characterizes laser exposure settings affecting labeled cells while preserving unlabeled cells; and finally, (iii) the red region is associated with damage both for labeled and unlabeled cells. The parameters characterizing these regions are critically sensitive to the wavelength used for the excitation. The comparison between 830 and 980 nm plots allows defining

an interaction area (dashed white square), where a different outcome on cells is expected depending only on wavelength change while maintaining identical irradiance/dose values. The existence of this region demonstrates the possibility to follow a theranostics approach based on switching the interaction modality with laser wavelength. Note that, instead of working exclusively in NIR-I, one can follow the same approach and take full advantage of NIR-II for imaging as this spectral region can be easily accessed using HNPs [264].

To mimic a situation where the laser treatment at 830 nm should selectively target a cell subpopulation preserving nonlabeled ones and maintaining single-cell resolution, we plated in a glass-bottom Petri dish a coculture containing both wild-type and BFO-preloaded cells. This scenario is illustrated in Figure S3. The cell at the center of the field of view displays a strong SHG-active area, associated with BFO HNP internalization and aggregation. After laser treatment, intracellular regions which were initially SHG-active start exhibiting a bright and spectrally broad hyperfluorescence emission.

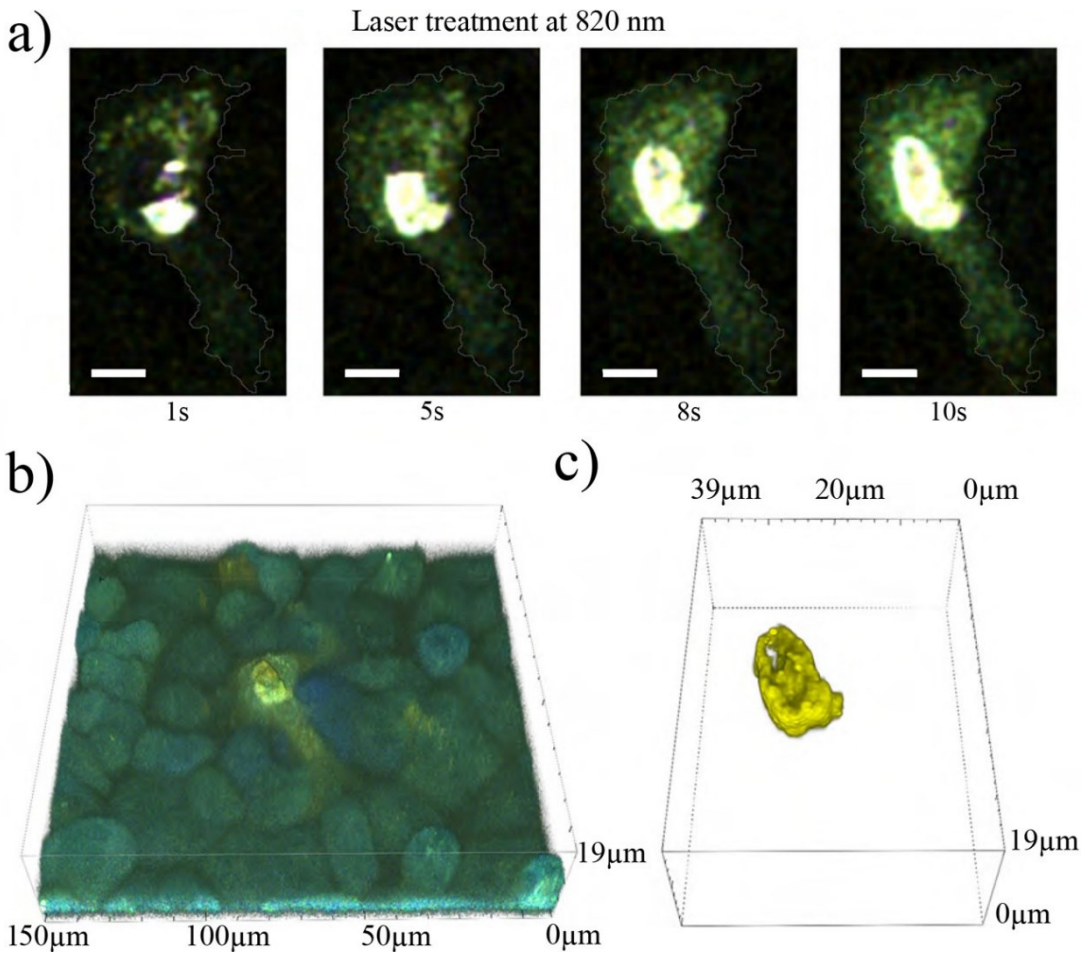

Figure 4 (a) Evolution of hyper fluorescence during the laser treatment. (b) Three-dimensional reconstruction of a coculture containing BFO labeled and unlabeled cells exposed to irradiation at 820 nm. The reconstruction was obtained by autofluorescence imaging via two-photon excitation at 720 nm. Note the presence of a damaged cell in the center. (c) Identification of the laser-ablated region obtained by spectrally unmixing the emission signal. As a reference for unmixing, the emission spectrum of ablated cells reported in Figure 5a is used.

In Figure 4, we show the evolution of the laser-induced BFO HNP-mediated cell modifications and its high spatial selectivity. During the treatment, performed on a surface of 150 × 150 μm^2 centered on a BFO labeled cell, a strongly luminescent area develops. It is initially confined in a few isolated spots and eventually covers a large fraction of the cell body. Figure 5 presents a quantitative analysis of the spectral changes in luminescence and SHG emission going

along with cell damage and the time-evolution of SHG and hyperfluorescence signals. Spectrally, we observe a clear red-shift from autofluorescence to hyperfluorescence (Figure 5a). This feature is consistent with the spectra reported by Qu's group in a series of recent works on femtosecond laser surgery [289, 290]. As shown in Figure 5b, hyperfluorescence sets in upon the loss of SHG, which is indicative of a temperature rise >80 °C (Figure 3a). Interestingly, Hovhannisyan et al. have also described a similar signal kinetics with a clear temporal correlation between the loss of SHG from collagen fibers irradiated by a femtosecond laser and the appearance of hyperfluorescence, and attributed it to free-electron mediated damage [291].

After the treatment, we acquired a volume image of the whole irradiated region by autofluorescence (Figure 4b). We observe that the unlabeled cells surrounding the target cell are not visibly affected by the laser irradiation. By applying a spectral-deconvolution procedure to isolate the image regions associated with the characteristic hyperfluorescence of damaged cells (orange trace in Figure 5a), we were able to precisely delineate the photointeraction volume (Figure 4c). Its interior is not fluorescent, suggesting either material ablation or, alternatively, a complete bleaching of the fluorescing/hyperfluorescing species. The former scenario is compatible with the expansion of a thermally generated cavitation bubble as previously reported for direct femtosecond laser ablation [270].

Our results demonstrate the existence of distinct parameter regions for damage-free SHG image of BFO labeled cells and selective modifications. The photoinduced damage remains confined within HNP-labeled cells and preserves neighboring structures, because of the difference in the damage threshold among BFO HNPs and unlabeled cells (Figure 1). The mechanism of cell damage relies on different effects. Under the irradiation conditions we explored, nonlinear

photochemistry and free-electrons mediated effects play a major role in cellular modifications [270, 292].

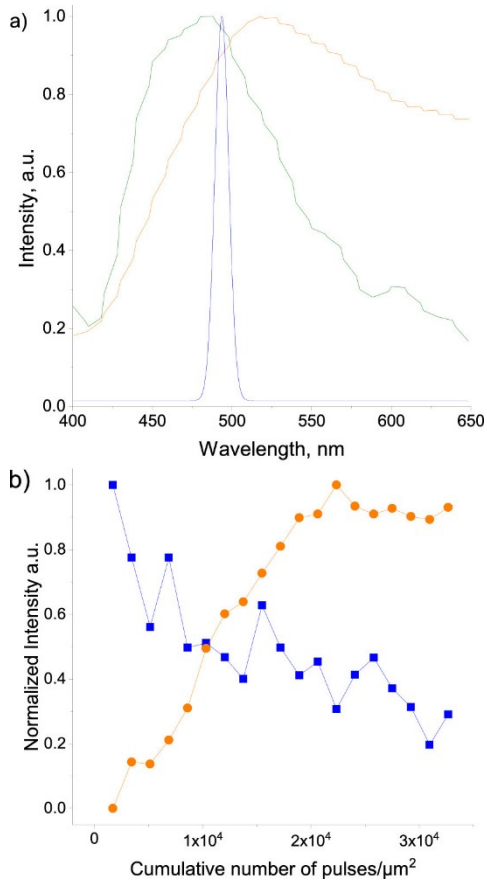

Figure 5 (a) Normalized emission spectra of a selected cell before (green) and after (orange) laser treatment along with the SHG emission spectrum (cyan). (b) Time evolution of SHG (blue) and hyper fluorescence (orange) intensity from a laser-damaged region within the cell.

On the other hand, the interaction is associated with a rise of the local temperature around the HNP. By the UCNPs-based protocol (Figures 2 and 3), we have demonstrated that the temperature increase in the immediate vicinity of a photoexcited BFO HNP can easily exceed 100 °C. This temperature rise, although essential to the process, is not the unique element of the

disruption mechanism. Thermal denaturation cannot play a leading role at the short heat exposure times (microsecond dwell times) to which the cells are exposed [293]: the temperature needed to produce photodenaturation within microseconds is higher than the threshold for explosive vaporization [294]. The cell damage produced by BFO HNPs is most likely a mixture of thermomechanical effects and free-electron-mediated molecular modifications. This scenario is corroborated by the observation of the cavity in Figure 4c, which can arise either from vaporization of tissue water at the heterogeneous nucleation threshold (at the HNP/cytoplasm interface) or from disintegration of biomolecules into non-condensable gas via nonlinear chemistry or free-electron-mediated bond breaking.

Conclusions

Use of optical probes such as BFO HNPs combined with different irradiation parameters could enable theranostics applications. The inherent nonlinear dependence of the photointeraction by BFO HNPs exploited in this work leads to the efficient wavelength decoupling between imaging at 980 nm and photointeraction at 830 nm and confines the instantaneous interaction to a very small focal volume which can be displaced in three dimensions. As a drawback, nonlinear excitation requires comparatively higher intensities than linear photothermal methods and relies on raster-scanning rather than large area irradiation [295]. Conveniently, the wavelengths needed for our approach can be selected in the first and second transmission windows of biological tissues (NIR-I: 650–950 nm, and NIR-II: 1100–1350 nm), which entails optimal conditions in terms of optical penetration depth [296]. Thanks to recent progresses in femtosecond laser technologies, nowadays the whole 700–1300 nm range can be covered by a single tunable source, enabling a rapid switching between the two interaction modalities.

The temperature rise that we were able to characterize by using $NaGdF_4:Yb^{3+}/Er^{3+}$ UCNPs together with free-electron-mediated effects lead to a complete loss of SHG emission, which can be used as a real-time optical readout of the success of the photointeraction and may be amenable to achieve homogeneous effects through relatively thick target layers. Based on all these considerations, we believe that cell disruption in conjunction with BFO HNPs could be an enabling theranostic tool in medical procedures such as margin resection and cleanup after cancer surgery because of the complete and highly selective disruption of labeled cells and the immediate readout of the success of the procedure associated with the sudden disappear of narrow-banded SHG emission by HNPs upon laser-induced decomposition [297]. To overcome constraints given by the limited optical penetration depth of biological tissues, the technique could, for in vivo applications inside the body, be implemented in a nonlinear endoscopy setup [298].

Materials and Methods

1- BFO Nanoparticles

BFO nanoparticles provided by the company FEE GmbH (Idar-Oberstein, Germany) were obtained as ethanol stabilized colloidal suspensions. As reported earlier [282], the synthesis is based on the autocombustion method with Bi and Fe nitrate salts first dissolved in an acidic solution. After addition of a fuel, namely, 2-amino-2-hydroxymethylpropane-1,3-diol, and drying at 105 °C, the obtained dried resin ignites itself leading to BFO powders showing secondary phases of different oxides. Phase purity is then improved by a 1 h calcination step at 600 °C. Because of the autoignition procedure, this scalable approach results in batch-to-batch variation in terms of residual impurities and the absence of size and shape control for the HNPs [282]. Stable suspensions of BFO are, however, readily obtained after wet milling of the calcined powder on a rolling bench. The final average size of BFO HNPs suspended in ethanol is approximately 140 nm as estimated from dynamic light scattering (DLS, Figure S1) [282].

2- Synthesis of Lanthanide Upconversion Nanoparticles $NaGdF_4$:20% Yb^{3+}/2% Er^{3+} (Ln-UCNPs)

A previously reported thermal decomposition approach was used for the synthesis of monodisperse upconverting $NaGdF_4$:20% Yb^{3+}/2% Er^{3+} [160]. In brief, lanthanide precursors were prepared under reflux (80 °C) by mixing of Yb_2O_3 (2.5×10^{-4} mol, 0.0985 g), Er_2O_3 (2.5×10^{-5} mol, 0.0096 g), and Gd_2O_3 (9.75×10^{-4} mol, 0.534 g) with 5 mL distilled water and 5 mL trifluoroacetic acid for 12 h. The transparent liquid precursors were air-dried at 60 °C for 16 h, forming a white solid powder. Dried precursors were heated to 125 °C in the presence of 7.5 mL 1-octadecene, 7.5 mL oleic acid, and sodium trifluoroacetate (2.5×10^{-3} mol, 0.34 g). Simultaneously, in a three neck 100 mL flask (receiving flask), 12.5 mL 1-octadecene and 12.5 mL oleic acid were heated under vacuum to 150 °C for a period of 30 min. The temperature of the receiving flask was increased to 310 °C, under an inert atmosphere (argon), followed by the injection of the precursor using a syringe pump system at a rate of 1.5 mL/min. The reaction mixture was stirred for 60 min after which the solution was cooled down to room temperature. Absolute ethanol (100 mL) was added to the solution, and the nanoparticles were precipitated by centrifugation at 3400 rpm for 15 min. The precipitate was washed twice using a hexane/ethanol (1:4) mixture.

3- Silica Coated $NaGdF_4$:20% Yb^{3+}/2% Er^{3+}

The $NaGdF_4$:20% Yb^{3+}/2% Er^{3+} nanoparticles are oleate capped, and dispersible in nonpolar organic solvents. A silica shell was added to render nanoparticles water dispersible using a water-in-oil reverse microemulsion method [299]. First, 20 mg of the oleate capped $NaGdF_4$:20% Yb^{3+}/2% Er^{3+} nanoparticles were dispersed in cyclohexane (10 mL) and sonicated for 10 min. The nonionic surfactant Igepal CO-520 (octylphenoxy poly(ethyleneoxy)ethanol) (0.1 mL) was added to the nanoparticles under sonication for 10 min and the mixture stirred at 600 rpm for 20 min. Another two portions of 0.4 mL Igepal CO-520 were added with 10 min intervals between each portion.

Ammonium hydroxide (80 μL, 28%) was added to the solution followed by sonication until the solution became clear. Tetraethyl orthosilicate (TEOS, 20 μL) was added to the reaction mixture and stirred for 48 h. For purification, 20 mL of acetone was added to the mixture followed by centrifugation at 3400 rpm. The precipitate was washed twice using an ethanol–water (1:1) mixture, and the nanoparticles were stored in the same solution.

4- Laser Irradiation Parameters

The measurements were performed with a Mai-Tai or altenatively an Insight tunable laser (Newport Spectra-Physics) at 80 MHz repetition rate. The pulse duration at the sample after transmission through the microscope optics and the air objective (Plan APO 20× WI N.A. 0.75) is t_{pulse} = 190 fs at fwhm.

Assuming a spatial Gaussian profile of focal diameter $\lambda/2NA$, the peak irradiance (or peak intensity) is calculated at fwhm of the laser temporal and spatial profile as (24)

$$I_{peak} = (16P_{av}NA^2)/(Rt_{pulse}\,\pi\lambda)$$

where Pav is the average incident power and R the laser repetition rate. Pulse density is defined for a specific scan as

$$d_{pulse} = R/vP_{size} = R \text{ x } t_d / P^2_{size}$$

where v is the scanning speed of the laser focal spot, P_{size} the lateral pixel dimension, and t_d the dwell time.

The corresponding irradiation dose associated with a single image frame is

$$F_{total} = d_{pulse} \text{ x } E_{pulse}$$

where E_{pulse} is the pulse energy.

5- Cells and Cell Cocultures

For the measurements in Figure 1, we used Red Fluorescent Protein (RFP) expressing adenocarcinomic human alveolar basal epithelial cells A549.For the coculture measurements (Figures 4 and S 4), wild-type A549 and cells preloaded of BFO HNPs by *g*-force method were cocultured by simultaneous plating on glass-bottom dishes (35 mm Glass Bottom Dishes, No 1.5 Uncoated, MatTek Corporation). The coculture was suspended in a total of 2 mL cell culture medium. Cells were allowed to adhere for 24 h before imaging. The coculture plated on a 20-mm-diameter glass bottom dish containing 10^3 A549 cells preloaded with BFO and 10^5 nonlabeled A549, yielding a ratio of 1:100. The number of cells was determined using a hemocytometer.

6- *g*-Force Induced Internalization of BFO into Cells

To internalize BFO nanoparticles into cells used for cocultures, the *g*-force based delivery method was used [300]. Briefly, adherent A549 cells were detached by incubation for 5 min in trypsin/EDTA (ethylenediaminetetraacetic acid) 0.25% solution diluted in DPBS (Dulbecco's phosphate-buffered saline). After removing trypsin using centrifugation precipitation of cells, the cell pellet was resuspended in 1 mL of cellular media with a final cellular count of 10^6 cells. BFO nanoparticles were presonicated for 30 min in PBS buffer and added to the cellular suspension at a final concentration 0.2 mg/mL. After gentle vortex, cell suspension was centrifuged for 5 min at 400 *g* (MiniSpin plus, Vaudaux-Eppendorf AG. Next, the cells were resuspended and plated for culturing. For further use and imaging, BFO preloaded cells were treated using the same protocols as for normal cells.

For the assessment in Figure 1 the internalization of nanoparticles relied on overnight incubation of RFP expressing A549 cells with BFO in medium at 100 μg/mL concentration. The cells were rinsed three times in PBS before performing the experiment.

7- Hyperspectral Imaging

Hyperspectral imaging was performed using a Nikon multiphoton inverted microscope (A1R-MP) coupled with a Mai-Tai tunable Ti:sapphire oscillator from Spectra-Physics (100 fs, 80 MHz, 700–1000 nm). A Plan APO 20× WI N.A. 0.75 objective was used to focus the excitation laser and to epi-collect the SHG signal. The signal was collected and directed through an optical fiber to the spectral detector, where it was diffracted by a grating and projected on a 32-PMT array. Cellular autofluorescence was induced at 720 nm and SHG was excited at 980 nm. Spectra were acquired in the range 400–650 nm and the resolution was set to 10 nm. Live cell imaging was performed at 37 °C using Okolab incubator (Pozzuoli, NA, Italy) with humidity and CO_2 control.

8- Determination of Damage Thresholds

To determine the damage thresholds of (i) BFO HNPs, (ii) unlabeled cells, and (iii) labeled cells, we performed measurements under different scanning and laser conditions.

(i) The sample was prepared by casting a drop of BFO HNPs suspended in ethanol on a microscope coverslip and letting the solvent evaporate. An irradiation was arbitrarily labeled as unsafe (red stars) if during the first image frame we observed a drop of more than 10% of the signal from the particle ensemble and if after 100 successive frames the signal decreased by more than 20% with respect to the initial value, safe (green stars) otherwise.

(ii,iii) We measured RFP expressing live cells plated on a Petri dish not at confluence both unlabeled and with internalized BFO HNPs. An irradiation was considered unsafe (red circles) if we observed the sudden appearance of one or multiple hyperfluorescence spots during the first frame, successively developing as larger bright rings during the successive frames, eventually leaving a dark region in the middle.

The relevant scanning characteristics (dwell time, pixel size, scanning speed) to determine dpulse and other excitation parameters were obtained directly from the microscope software interface (Nikon Elements).

9- Nanothermometry

Nanothermometric imaging was performed on BFO nanoparticles dried together with upconverting nanoparticles (UCNPs) $NaGdF_4:Yb^{3+}/Er^{3+}$ with an average size of 36 nm coated with silica shell of 2 nm. Imaging was performed using 980 nm at 0.85 TW/cm^2. Emission of harmonic and upconverting nanoparticles was recorded using hyperspectral detection. The fluorescence response of UCNPs was converted to temperature change based on a calibration obtained from imaging dried UCNPs at different temperatures. For this experiment, UCNPs at 5 mg/mL were dried on a glass coverslip and the sample was deposited using a home-built Peltier element based thermostat. Acquired fluorescence of UCNPs was spectrally unmixed using UCNPs 520 nm (510–535 nm) and 540 nm (535–565 nm) bands as reference spectra. Unmixed images were used for the construction of ratiometric images. Images of HNPs mixed with UCNPs samples were acquired and also spectrally unmixed.

For the experiment in cell medium, UCNPs were suspended at final concentration of 100 µg/mL. An aliquot of presonicated BFO HNPs was added to the solution to obtain 50 µg/mL concentration. Before measurements, samples were left on the microscope stage for 25 min to allow NPs to precipitate. Imaging and temperature quantification were performed following the same protocol as for dry nanoparticles.

Supporting Information

Size distribution of BFO nanoparticles

Figure S1 provides the Dynamic Light Scattering characterization (by number) of the BFO nanoparticles obtained by autocombustion method used for the measurements reported in the manuscript.

Irradiation of BFO HNPs on a substrate

Figure S2 shows the average emission spectra of multiple dry BFO HNPs for two excitation wav elengths under a safe irradiation regime and when irradiation leads to loss of SHG.

Figure S3 shows the evolution over successive frames of the average SHG signal acquired during laser irradiation at 830 nm and 980 nm from 82 × 82 μm^2 regions of samples obtained casting a drop of BFO HNPs solution on a microscope substrate and letting the solvent evaporates. The irradiation dose, F_{total}, is calculated from the number of pulses accumulated during a single image frame and computed as reported in the Materials and Methods Section of the main text. The sudden signal drop after the first frame is identified with the unset of photodamage, which then becomes more severe over subsequent image scans. Green traces are examples of measurements retained as safe irradiations in Figure 1 of the main text.

Irradiation of BFO HNPs in cell medium

The procedure described for Figure 2 and 3 in the main text was repeated for nanoparticles in medium. The results are reported in Figure S4 UCNPs were suspended at final concentration of 100 μg/ml. An aliquot of presonicated BFO HNPs was added to the solution to obtain 50 μg/ml concentration. Before measurements, samples were let on the microscope stage for 25 minutes to

allow NPs to precipitate. Imaging and temperature quantification were performed following the same protocol as for dry nanoparticles.

X-ray powder diffraction

To elucidate the origin of SHG loss, a few mg of BFO powders were dispersed on a glass slide and underwent laser-scanning irradiation for several hours at 820 nm below and above the threshold of the photo-damage regime for dry nanoparticles. After the irradiation, a low amount of powder was collected and transferred to a zero-background Si holder for an X-ray powder diffraction analysis (PANalytical X'Pert3 Powder diffractometer equipped with a Co anticathode, 5h acquisition time). The XRD traces reported in Figure S5 not only reveal the presence of $BiFeO_3$ but also of several by-products upon laser irradiation.

The space group and identiers (ID) from the Crystallography Open Database (COD) of the $BiFeO_3$, Fe_3O_4, metal Bi and β-Bi_2O_3 phases are reported on the plot together with the corresponding references as reported in the the legend. Note that $BiFeO_3$ and β-Bi_2O_3 are SHG-active phases but no SHG is expected from the Bi and Fe_3O_4 compounds. A substantial amorphous contribution in the 25-45° 2θ range can also be noted together with an additional peak (denoted with a star) that might be attributed to a modification of the SiO_2 substrate (COD ID 4124042).

Cell co-cultures

Figure S6 shows a typical image of a cell co-culture containing both wild-type and BFOpreloaded A549 cells. The irradiation procedure leads to the emission of hyperfluorescence initially co-localized with the internalized BFO nanoparticles.

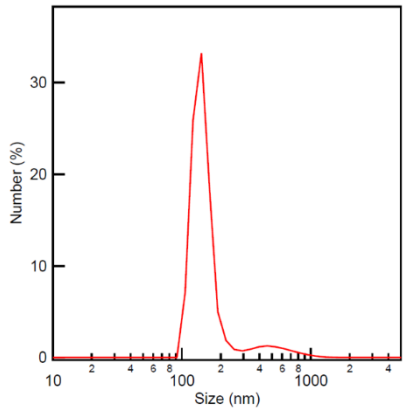

Figure S1 Size distribution by number of BFO nanoparticles by dynamic light scattering.

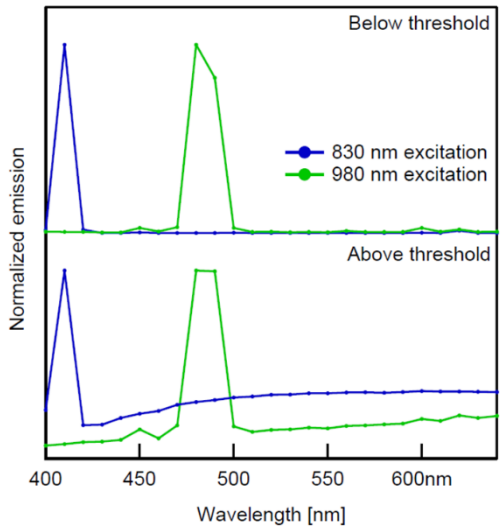

Figure S2 Emission spectra of BFO HNPs upon excitation at 830 and 980 nm under safe irradiation conditions (top) and under damaging irradiation conditions (bottom). In the latter case, SHG peak is accompanied by a spectrally large and featureless luminescence band.

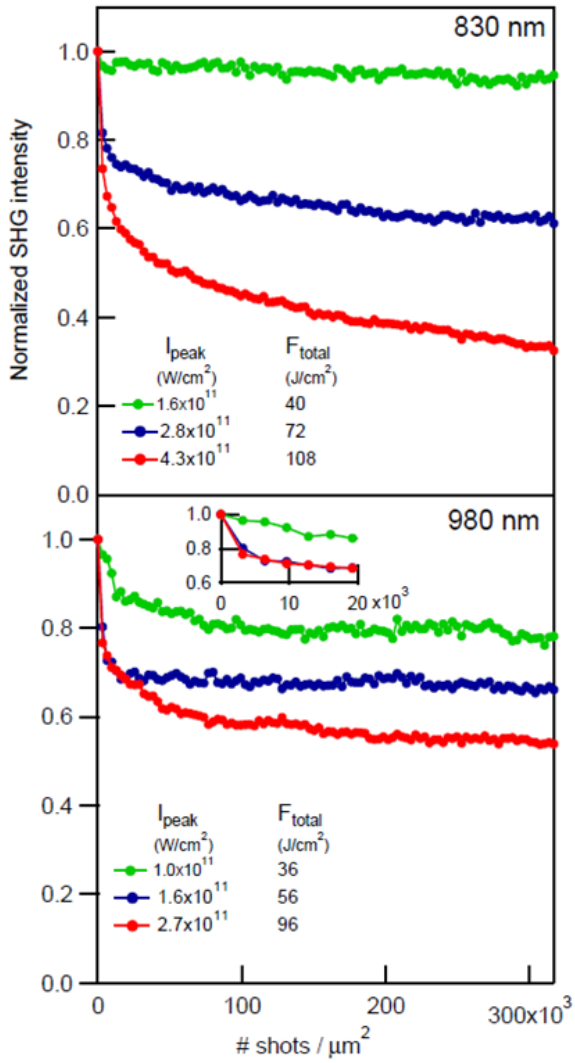

Figure S3 Evolution of the SHG signal collected from multiple nanoparticles on a substrate during laser irradiation at 830 and 980 nm for different irradiance/irradiation dose settings. The close-up evidence the different dynamics of nanoparticles irradiated at 980 nm under safe (green) and photo-damage conditions during the first image scan: the sudden drop in SHG is clearly not present for the green trace.

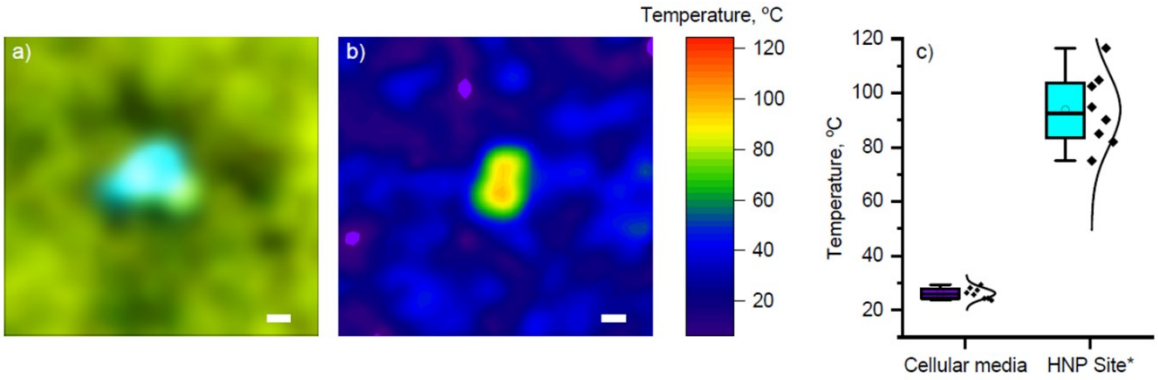

Figure S4 In Situ characterization of the temperature increase around a BFO HNPs in cell medium probed by UCNPs nanothermometry. Hyperpectral images of a BFO particle surrounded by UCNPs excited at 980 nm. b) Temperature-resolved images of the particle in panels a) plotted using a false-color map extracted from the calibration curve obtained for dry particles on a substrate. Scale bar 1µm. c) Temperature distribution in the absence and in close proximity of the BFO HNP.

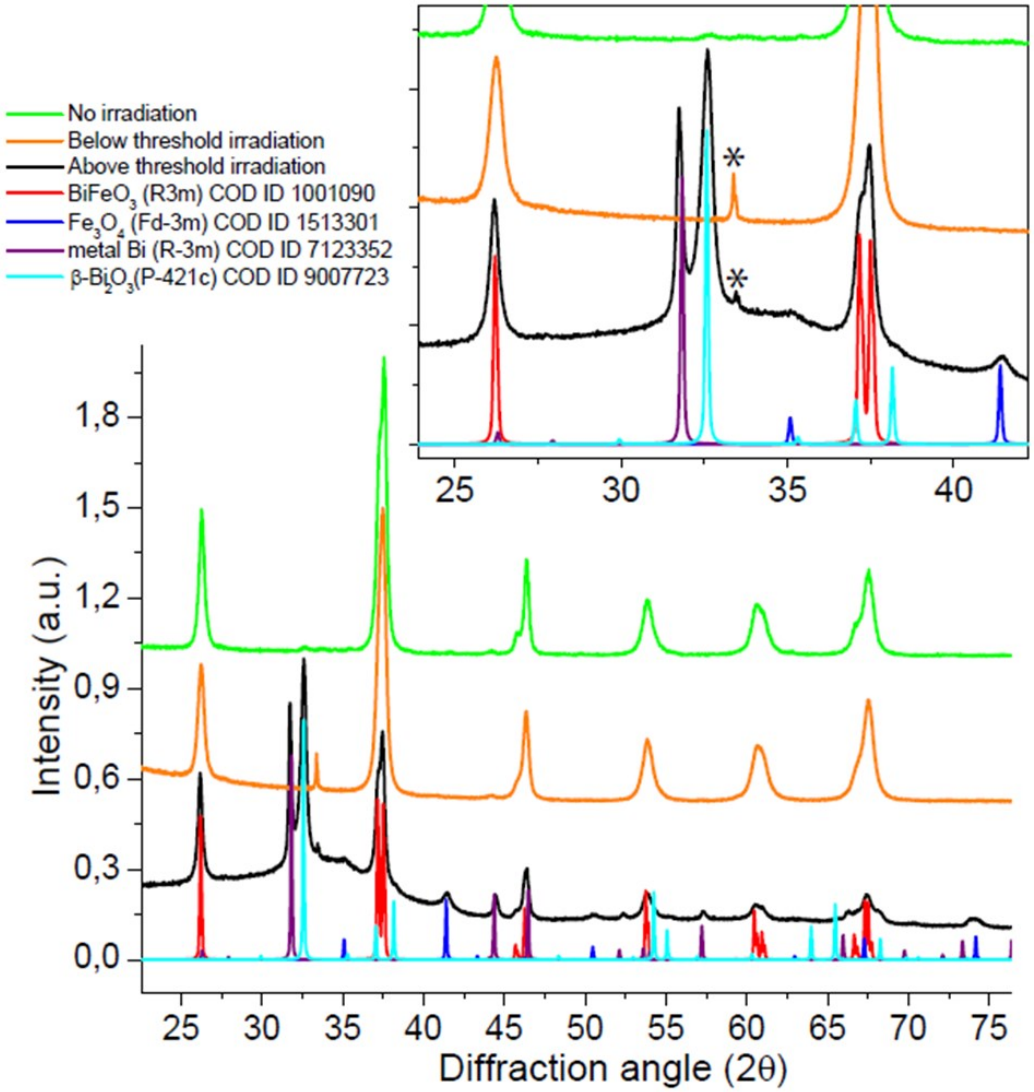

Figure S5 XRD pattern of BFO upon different irradiation conditions at 820 nm. The space group and identifiers (ID) from the Crystallography Open Database (COD) of by-products of different compositions are reported along with the experimental traces.

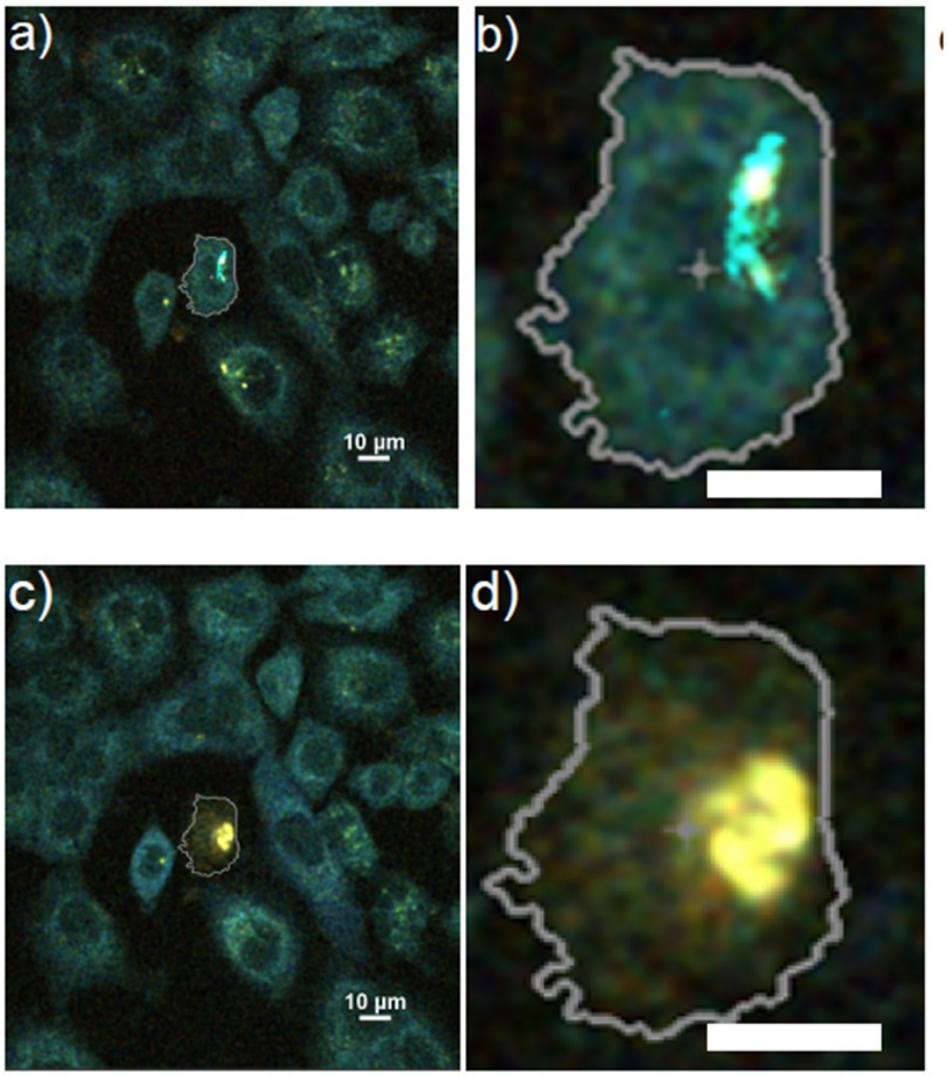

Figure S6 a) and c) Hyperspectral images of cell co-culture before (a) and after (c) laser treatment. b) and d) Close-up of a cell containing BFO before (b) and after (d) laser treatment. The region displaying SHG in a) and b) corresponds to the area showing the most intense hyperfluorescence in c) and d). All images obtained as an overlay of excitation at 720 nm (auto fluorescence) and 980 nm (SHG).

REFERENCES

1. Henderson, B.; Imbusch, G. F., *Optical spectroscopy of inorganic solids*. Oxford University Press: 2006; Vol. 44.
2. Dieke, G. H.; Crosswhite, H., The spectra of the doubly and triply ionized rare earths. *Applied optics* **1963,** *2* (7), 675-686.
3. Liu, G., Advances in the theoretical understanding of photon upconversion in rare-earth activated nanophosphors. *Chemical Society Reviews* **2015,** *44* (6), 1635-1652.
4. Scheps, R., Upconversion laser processes. *Progress in Quantum Electronics* **1996,** *20* (4), 271-358.
5. Ovsyakin, V.; Feofilov, P., Cooperative sensitization of luminescence in crystals activated with rare earth ions. *Soviet Journal of Experimental and Theoretical Physics Letters* **1966,** *4*, 317.
6. Auzel, F., Compteur quantique par transfert d'energie entre deux ions de terres rares dans un tungstate mixte et dans un verre. *CR Acad. Sci. Paris* **1966,** *262*, 1016-1019.
7. Auzel, F., Upconversion and anti-stokes processes with f and d ions in solids. *Chemical reviews* **2004,** *104* (1), 139-174.
8. Riseberg, L. A.; Moos, H.-W., Multiphonon orbit-lattice relaxation of excited states of rare-earth ions in crystals. *Physical Review* **1968,** *174* (2), 429.
9. Kropp, J. L.; Windsor, M. W., Luminescence and energy transfer in solutions of rare-earth complexes. I. Enhancement of fluorescence by deuterium substitution. *The Journal of Chemical Physics* **1965,** *42* (5), 1599-1608.
10. Boyer, J.-C.; Vetrone, F.; Cuccia, L. A.; Capobianco, J. A., Synthesis of colloidal upconverting NaYF4 nanocrystals doped with Er3+, Yb3+ and Tm3+, Yb3+ via thermal decomposition of lanthanide trifluoroacetate precursors. *Journal of the American Chemical Society* **2006,** *128* (23), 7444-7445.
11. Naccache, R.; Vetrone, F.; Mahalingam, V.; Cuccia, L. A.; Capobianco, J. A., Controlled synthesis and water dispersibility of hexagonal phase NaGdF4: Ho3+/Yb3+ nanoparticles. *Chemistry of Materials* **2009,** *21* (4), 717-723.
12. Vleck, J. V., The Puzzle of Rare-earth Spectra in Solids. *Journal of physical chemistry* **1937,** *41* (1), 67-80.
13. Sedlmeier, A.; Achatz, D. E.; Fischer, L. H.; Gorris, H. H.; Wolfbeis, O. S., Photon upconverting nanoparticles for luminescent sensing of temperature. *Nanoscale* **2012,** *4* (22), 7090-7096.
14. Suyver, J.; Grimm, J.; Krämer, K.; Güdel, H.-U., Highly efficient near-infrared to visible up-conversion process in NaYF4: Er3+, Yb3+. *Journal of luminescence* **2005,** *114* (1), 53-59.
15. Tu, L.; Liu, X.; Wu, F.; Zhang, H., Excitation energy migration dynamics in upconversion nanomaterials. *Chemical Society Reviews* **2015,** *44* (6), 1331-1345.
16. Spikes, J. D., The historical development of ideas on applications of photosensitized reactions in the health sciences. In *Primary photo-processes in biology and medicine*, Springer: 1985; pp 209-227.
17. Ackroyd, R.; Kelty, C.; Brown, N.; Reed, M., The history of photodetection and photodynamic therapy¶. *Photochemistry and photobiology* **2001,** *74* (5), 656-669.
18. Dougherty, T. J.; Grindey, G.; Fiel, R.; Weishaupt, K. R.; Boyle, D., Photoradiation therapy. II. Cure of animal tumors with hematoporphyrin and light. *Journal of the National Cancer Institute* **1975,** *55* (1), 115-121.

19. Arnold, S.; Kubo, M.; Ogryzlo, E., Relaxation and reactivity of singlet oxygen. ACS Publications: 1968.
20. Merkel, P. B.; Kearns, D. R., Remarkable solvent effects on the lifetime of 1. DELTA. g oxygen. *Journal of the American Chemical Society* **1972,** *94* (3), 1029-1030.
21. Sternberg, E. D.; Dolphin, D.; Brückner, C., Porphyrin-based photosensitizers for use in photodynamic therapy. *Tetrahedron* **1998,** *54* (17), 4151-4202.
22. O'Connor, A. E.; Gallagher, W. M.; Byrne, A. T., Porphyrin and nonporphyrin photosensitizers in oncology: preclinical and clinical advances in photodynamic therapy. *Photochemistry and photobiology* **2009,** *85* (5), 1053-1074.
23. Hino, S.; Okada, Y.; Iwasaki, K.; Kijima, M.; Shirakawa, H., Electronic structures of cumulene type carbyne model compounds: a typical example of one-dimensional quantum well. *Chemical physics letters* **2003,** *372* (1-2), 59-65.
24. Abrahamse, H.; Hamblin, M. R., New photosensitizers for photodynamic therapy. *Biochemical Journal* **2016,** *473* (4), 347-364.
25. Chilakamarthi, U.; Giribabu, L., Photodynamic therapy: past, present and future. *The Chemical Record* **2017,** *17* (8), 775-802.
26. Svaasand, L., Optical dosimetry for direct and interstitial photoradiation therapy of malignant tumors. *Progress in clinical and biological research* **1984,** *170*, 91-114.
27. Henderson, B. W., *Photodynamic therapy: basic principles and clinical applications*. CRC Press: 2020.
28. Svaasand, L. O.; Potter, W. R., The implications of photobleaching for photodynamic therapy. In *Photodynamic Therapy*, CRC Press: 2020; pp 369-386.
29. Salomatina, E. V.; Jiang, B.; Novak, J.; Yaroslavsky, A. N., Optical properties of normal and cancerous human skin in the visible and near-infrared spectral range. *Journal of biomedical optics* **2006,** *11* (6), 064026.
30. Alexandrakis, G.; Rannou, F. R.; Chatziioannou, A. F., Tomographic bioluminescence imaging by use of a combined optical-PET (OPET) system: a computer simulation feasibility study. *Physics in Medicine & Biology* **2005,** *50* (17), 4225.
31. Venturoli, D.; Rippe, B., Ficoll and dextran vs. globular proteins as probes for testing glomerular permselectivity: effects of molecular size, shape, charge, and deformability. *American Journal of Physiology-Renal Physiology* **2005,** *288* (4), F605-F613.
32. Zhao, X.; Li, H.; Lee, R. J., Targeted drug delivery via folate receptors. *Expert opinion on drug delivery* **2008,** *5* (3), 309-319.
33. Roth, L.; Agemy, L.; Kotamraju, V.; Braun, G.; Teesalu, T.; Sugahara, K.; Hamzah, J.; Ruoslahti, E., Transtumoral targeting enabled by a novel neuropilin-binding peptide. *Oncogene* **2012,** *31* (33), 3754-3763.
34. Simberg, D.; Duza, T.; Park, J. H.; Essler, M.; Pilch, J.; Zhang, L.; Derfus, A. M.; Yang, M.; Hoffman, R. M.; Bhatia, S., Biomimetic amplification of nanoparticle homing to tumors. *Proceedings of the National Academy of Sciences* **2007,** *104* (3), 932-936.
35. Greish, K., Enhanced permeability and retention (EPR) effect for anticancer nanomedicine drug targeting. In *Cancer nanotechnology*, Springer: 2010; pp 25-37.
36. Naccache, R.; Chevallier, P.; Lagueux, J.; Gossuin, Y.; Laurent, S.; Vander Elst, L.; Chilian, C.; Capobianco, J. A.; Fortin, M. A., High relaxivities and strong vascular signal enhancement for NaGdF4 nanoparticles designed for dual MR/optical imaging. *Advanced Healthcare Materials* **2013,** *2* (11), 1478-1488.

37. Wang, F.; Deng, R.; Liu, X., Preparation of core-shell NaGdF 4 nanoparticles doped with luminescent lanthanide ions to be used as upconversion-based probes. *Nature protocols* **2014,** *9* (7), 1634-1644.
38. Liu, J.; Chen, G.; Hao, S.; Yang, C., Sub-6 nm monodisperse hexagonal core/shell NaGdF 4 nanocrystals with enhanced upconversion photoluminescence. *Nanoscale* **2017,** *9* (1), 91-98.
39. Wang, F.; Deng, R.; Wang, J.; Wang, Q.; Han, Y.; Zhu, H.; Chen, X.; Liu, X., Tuning upconversion through energy migration in core–shell nanoparticles. *Nature materials* **2011,** *10* (12), 968-973.
40. Sheleg, S. V.; Zhavrid, E. A.; Khodina, T. V.; Kochubeev, G. A.; Istomin, Y. P.; Chalov, V. N.; Zhuravkin, I. N., Photodynamic therapy with chlorin e6 for skin metastases of melanoma. *Photodermatology, photoimmunology & photomedicine* **2004,** *20* (1), 21-26.
41. Bogdan, N.; Vetrone, F.; Ozin, G. A.; Capobianco, J. A., Synthesis of ligand-free colloidally stable water dispersible brightly luminescent lanthanide-doped upconverting nanoparticles. *Nano letters* **2011,** *11* (2), 835-840.
42. Dong, A.; Ye, X.; Chen, J.; Kang, Y.; Gordon, T.; Kikkawa, J. M.; Murray, C. B., A generalized ligand-exchange strategy enabling sequential surface functionalization of colloidal nanocrystals. *Journal of the American Chemical Society* **2011,** *133* (4), 998-1006.
43. Chen, J.; Chen, N.; Huang, J.; Wang, J.; Huang, M., Derivatizable phthalocyanine with single carboxyl group: synthesis and purification. *Inorganic Chemistry Communications* **2006,** *9* (3), 313-315.
44. Wang, M.; Chen, Z.; Zheng, W.; Zhu, H.; Lu, S.; Ma, E.; Tu, D.; Zhou, S.; Huang, M.; Chen, X., Lanthanide-doped upconversion nanoparticles electrostatically coupled with photosensitizers for near-infrared-triggered photodynamic therapy. *Nanoscale* **2014,** *6* (14), 8274-8282.
45. Yu, Q.; Rodriguez, E.; Naccache, R.; Forgione, P.; Lamoureux, G.; Sanz-Rodriguez, F.; Scheglmann, D.; Capobianco, J., Chemical modification of temoporfin–a second generation photosensitizer activated using upconverting nanoparticles for singlet oxygen generation. *Chemical Communications* **2014,** *50* (81), 12150-12153.
46. Lucky, S. S.; Soo, K. C.; Zhang, Y., Nanoparticles in photodynamic therapy. *Chemical reviews* **2015,** *115* (4), 1990-2042.
47. Duong, H. T.; Chen, Y.; Tawfik, S. A.; Wen, S.; Parviz, M.; Shimoni, O.; Jin, D., Systematic investigation of functional ligands for colloidal stable upconversion nanoparticles. *RSC advances* **2018,** *8* (9), 4842-4849.
48. Nsubuga, A.; Sgarzi, M.; Zarschler, K.; Kubeil, M.; Hübner, R.; Steudtner, R.; Graham, B.; Joshi, T.; Stephan, H., Facile preparation of multifunctionalisable 'stealth'upconverting nanoparticles for biomedical applications. *Dalton Transactions* **2018,** *47* (26), 8595-8604.
49. Boyer, J.-C.; Manseau, M.-P.; Murray, J. I.; Van Veggel, F. C., Surface modification of upconverting NaYF4 nanoparticles with PEG− phosphate ligands for NIR (800 nm) biolabeling within the biological window. *Langmuir* **2010,** *26* (2), 1157-1164.
50. Ding, B.; Shao, S.; Yu, C.; Teng, B.; Wang, M.; Cheng, Z.; Wong, K. L.; Ma, P. a.; Lin, J., Large-pore mesoporous-silica-coated upconversion nanoparticles as multifunctional immunoadjuvants with ultrahigh photosensitizer and antigen loading efficiency for improved cancer photodynamic immunotherapy. *Advanced Materials* **2018,** *30* (52), 1802479.

51. Juan, J.; Cheng, L.; Shi, M.; Liu, Z.; Mao, X., Poly-(allylamine hydrochloride)-coated but not poly (acrylic acid)-coated upconversion nanoparticles induce autophagy and apoptosis in human blood cancer cells. *Journal of Materials Chemistry B* **2015,** *3* (28), 5769-5776.
52. Kostiv, U.; Patsula, V.; Noculak, A.; Podhorodecki, A.; Větvička, D.; Poučková, P.; Sedláková, Z.; Horák, D., Phthalocyanine-Conjugated Upconversion NaYF4: Yb3+/Er3+@ SiO2 Nanospheres for NIR-Triggered Photodynamic Therapy in a Tumor Mouse Model. *ChemMedChem* **2017,** *12* (24), 2066-2073.
53. Ren, W.; Tian, G.; Jian, S.; Gu, Z.; Zhou, L.; Yan, L.; Jin, S.; Yin, W.; Zhao, Y., TWEEN coated NaYF 4: Yb, Er/NaYF4 core/shell upconversion nanoparticles for bioimaging and drug delivery. *RSC advances* **2012,** *2* (18), 7037-7041.
54. Maeda, H.; Wu, J.; Sawa, T.; Matsumura, Y.; Hori, K., Tumor vascular permeability and the EPR effect in macromolecular therapeutics: a review. *Journal of controlled release* **2000,** *65* (1-2), 271-284.
55. Choi, H. S.; Liu, W.; Misra, P.; Tanaka, E.; Zimmer, J. P.; Ipe, B. I.; Bawendi, M. G.; Frangioni, J. V., Renal clearance of quantum dots. *Nature biotechnology* **2007,** *25* (10), 1165-1170.
56. Tang, L.; Fan, T. M.; Borst, L. B.; Cheng, J., Synthesis and biological response of size-specific, monodisperse drug–silica nanoconjugates. *ACS nano* **2012,** *6* (5), 3954-3966.
57. Park, Y. I.; Kim, H. M.; Kim, J. H.; Moon, K. C.; Yoo, B.; Lee, K. T.; Lee, N.; Choi, Y.; Park, W.; Ling, D., Theranostic probe based on lanthanide-doped nanoparticles for simultaneous in vivo dual-modal imaging and photodynamic therapy. *Advanced materials* **2012,** *24* (42), 5755-5761.
58. Anselmo, A. C.; Zhang, M.; Kumar, S.; Vogus, D. R.; Menegatti, S.; Helgeson, M. E.; Mitragotri, S., Elasticity of nanoparticles influences their blood circulation, phagocytosis, endocytosis, and targeting. *ACS nano* **2015,** *9* (3), 3169-3177.
59. Monsky, W. L.; Fukumura, D.; Gohongi, T.; Ancukiewcz, M.; Weich, H. A.; Torchilin, V. P.; Yuan, F.; Jain, R. K., Augmentation of transvascular transport of macromolecules and nanoparticles in tumors using vascular endothelial growth factor. *Cancer Research* **1999,** *59* (16), 4129-4135.
60. Tan, W.; Donovan, M. J.; Jiang, J., Aptamers from cell-based selection for bioanalytical applications. *Chemical reviews* **2013,** *113* (4), 2842-2862.
61. Group, V. I. S. i. O. N. C. T., Year 2 efficacy results of 2 randomized controlled clinical trials of pegaptanib for neovascular age-related macular degeneration. *Ophthalmology* **2006,** *113* (9), 1508. e1-1508. e25.
62. Huang, Y.-F.; Shangguan, D.; Liu, H.; Phillips, J. A.; Zhang, X.; Chen, Y.; Tan, W., Molecular assembly of an aptamer-drug conjugate for targeted drug delivery to tumor cells. *Chembiochem: a European journal of chemical biology* **2009,** *10* (5), 862.
63. Hou, W.; Liu, Y.; Jiang, Y.; Wu, Y.; Cui, C.; Wang, Y.; Zhang, L.; Teng, I.-T.; Tan, W., Aptamer-based multifunctional ligand-modified UCNPs for targeted PDT and bioimaging. *Nanoscale* **2018,** *10* (23), 10986-10990.
64. Sarmento, B.; Neves, J. D., *Biomedical applications of functionalized nanomaterials: concepts, development and clinical translation*. William Andrew: 2018.
65. Antony, A. C., Folate receptors. *Annual review of nutrition* **1996,** *16* (1), 501-521.
66. Parker, N.; Turk, M. J.; Westrick, E.; Lewis, J. D.; Low, P. S.; Leamon, C. P., Folate receptor expression in carcinomas and normal tissues determined by a quantitative radioligand binding assay. *Analytical biochemistry* **2005,** *338* (2), 284-293.

67. D'angelica, M.; Ammori, J.; Gonen, M.; Klimstra, D. S.; Low, P. S.; Murphy, L.; Weiser, M. R.; Paty, P. B.; Fong, Y.; DeMatteo, R. P., Folate receptor-α expression in resectable hepatic colorectal cancer metastases: patterns and significance. *Modern Pathology* **2011,** *24* (9), 1221-1228.
68. Chien, Y.-H.; Chou, Y.-L.; Wang, S.-W.; Hung, S.-T.; Liau, M.-C.; Chao, Y.-J.; Su, C.-H.; Yeh, C.-S., Near-infrared light photocontrolled targeting, bioimaging, and chemotherapy with caged upconversion nanoparticles in vitro and in vivo. *Acs Nano* **2013,** *7* (10), 8516-8528.
69. Chintharlapalli, S.; Papineni, S.; Jutooru, I.; McAlees, A.; Safe, S., Structure-dependent activity of glycyrrhetinic acid derivatives as peroxisome proliferator–activated receptor γ agonists in colon cancer cells. *Molecular Cancer Therapeutics* **2007,** *6* (5), 1588-1598.
70. Cai, Y.; Xu, Y.; Chan, H. F.; Fang, X.; He, C.; Chen, M., Glycyrrhetinic acid mediated drug delivery carriers for hepatocellular carcinoma therapy. *Molecular pharmaceutics* **2016,** *13* (3), 699-709.
71. Zhang, C.; Liu, Z.; Zheng, Y.; Geng, Y.; Han, C.; Shi, Y.; Sun, H.; Zhang, C.; Chen, Y.; Zhang, L., Glycyrrhetinic acid functionalized graphene oxide for mitochondria targeting and cancer treatment in vivo. *Small* **2018,** *14* (4), 1703306.
72. Choi, J. E.; Kim, H.-K.; Kim, Y.; Kim, G.; Lee, T. S.; Kim, S.; Kim, D.; Jang, H. S., 800 nm near-infrared light-excitable intense green-emitting Li (Gd, Y) F4: Yb, Er-based core/shell/shell upconversion nanophosphors for efficient liver cancer cell imaging. *Materials & Design* **2020,** *195*, 108941.
73. Alonso-de Castro, S.; Ruggiero, E.; Lekuona Fernández, A.; Cossío, U.; Baz, Z.; Otaegui, D.; Gómez-Vallejo, V.; Padro, D.; Llop, J.; Salassa, L., Functionalizing NaGdF4: Yb, Er upconverting nanoparticles with bone-targeting phosphonate ligands: imaging and in vivo biodistribution. *Inorganics* **2019,** *7* (5), 60.
74. Scott, A. M.; Allison, J. P.; Wolchok, J. D., Monoclonal antibodies in cancer therapy. *Cancer Immunity Archive* **2012,** *12* (1).
75. Lubin, R.; Zalcman, G.; Bouchet, L.; Trédaniel, J.; Legros, Y.; Cazals, D.; Hirsch, A.; Soussi, T., Serum p53 antibodies as early markers of lung cancer. *Nature medicine* **1995,** *1* (7), 701-702.
76. Jin, Y.; Ni, D.; Zhang, J.; Han, F.; Wang, J.; Gao, L.; Zhang, H.; Liu, Y.; Cui, Z.; Yao, Z., Targeting Upconversion Nanoprobes for Magnetic Resonance Imaging of Early Colon Cancer. *Particle & Particle Systems Characterization* **2017,** *34* (3), 1600393.
77. Liang, L.; Care, A.; Zhang, R.; Lu, Y.; Packer, N. H.; Sunna, A.; Qian, Y.; Zvyagin, A. V., Facile assembly of functional upconversion nanoparticles for targeted cancer imaging and photodynamic therapy. *ACS applied materials & interfaces* **2016,** *8* (19), 11945-11953.
78. Jin, G.; He, R.; Liu, Q.; Lin, M.; Dong, Y.; Li, K.; Tang, B. Z.; Liu, B.; Xu, F., Near-infrared light-regulated cancer theranostic nanoplatform based on aggregation-induced emission luminogen encapsulated upconversion nanoparticles. *Theranostics* **2019,** *9* (1), 246.
79. Cedervall, T.; Lynch, I.; Lindman, S.; Berggård, T.; Thulin, E.; Nilsson, H.; Dawson, K. A.; Linse, S., Understanding the nanoparticle–protein corona using methods to quantify exchange rates and affinities of proteins for nanoparticles. *Proceedings of the National Academy of Sciences* **2007,** *104* (7), 2050-2055.

80. Walkey, C. D.; Chan, W. C., Understanding and controlling the interaction of nanomaterials with proteins in a physiological environment. *Chemical Society Reviews* **2012,** *41* (7), 2780-2799.
81. Vitali, M.; Casals, E.; Canals, F.; Colomé, N.; Puntes, V., Simple spectroscopic determination of the hard protein corona composition in AuNPs: albumin at 75%. *Nanoscale* **2020,** *12* (29), 15832-15844.
82. Sleep, D.; Cameron, J.; Evans, L. R., Albumin as a versatile platform for drug half-life extension. *Biochimica et Biophysica Acta (BBA)-General Subjects* **2013,** *1830* (12), 5526-5534.
83. Schnitzer, J.; Sung, A.; Horvat, R.; Bravo, J., Preferential interaction of albumin-binding proteins, gp30 and gp18, with conformationally modified albumins. Presence in many cells and tissues with a possible role in catabolism. *Journal of Biological Chemistry* **1992,** *267* (34), 24544-24553.
84. Schnitzer, J. E.; Oh, P., Albondin-mediated capillary permeability to albumin. Differential role of receptors in endothelial transcytosis and endocytosis of native and modified albumins. *Journal of Biological Chemistry* **1994,** *269* (8), 6072-6082.
85. Oh, P.; Borgström, P.; Witkiewicz, H.; Li, Y.; Borgström, B. J.; Chrastina, A.; Iwata, K.; Zinn, K. R.; Baldwin, R.; Testa, J. E., Live dynamic imaging of caveolae pumping targeted antibody rapidly and specifically across endothelium in the lung. *Nature biotechnology* **2007,** *25* (3), 327-337.
86. Lane, T. F.; Sage, E. H., The biology of SPARC, a protein that modulates cell-matrix interactions. *The FASEB Journal* **1994,** *8* (2), 163-173.
87. Cortes, J.; Saura, C., Nanoparticle albumin-bound (nab™)-paclitaxel: improving efficacy and tolerability by targeted drug delivery in metastatic breast cancer. *European Journal of Cancer Supplements* **2010,** *8* (1), 1-10.
88. Li, D.; Zhang, M.; Xu, F.; Chen, Y.; Chen, B.; Chang, Y.; Zhong, H.; Jin, H.; Huang, Y., Biomimetic albumin-modified gold nanorods for photothermo-chemotherapy and macrophage polarization modulation. *Acta Pharmaceutica Sinica B* **2018,** *8* (1), 74-84.
89. Oleinick, N. L.; Morris, R. L.; Belichenko, I., The role of apoptosis in response to photodynamic therapy: what, where, why, and how. *Photochemical & Photobiological Sciences* **2002,** *1* (1), 1-21.
90. Spikes, J. D., New trends in photobiology: Chlorins as photosensitizers in biology and medicine. *Journal of Photochemistry and Photobiology B: Biology* **1990,** *6* (3), 259-274.
91. Idris, N. M.; Gnanasammandhan, M. K.; Zhang, J.; Ho, P. C.; Mahendran, R.; Zhang, Y., In vivo photodynamic therapy using upconversion nanoparticles as remote-controlled nanotransducers. *Nature medicine* **2012,** *18* (10), 1580-1585.
92. Detty, M. R.; Gibson, S. L.; Wagner, S. J., Current clinical and preclinical photosensitizers for use in photodynamic therapy. *Journal of medicinal chemistry* **2004,** *47* (16), 3897-3915.
93. Frangioni, J. V., In vivo near-infrared fluorescence imaging. *Current opinion in chemical biology* **2003,** *7* (5), 626-634.
94. Smith, A. M.; Mancini, M. C.; Nie, S., Bioimaging: second window for in vivo imaging. *Nature nanotechnology* **2009,** *4* (11), 710-711.
95. Luan, L.; Ding, L.; Zhang, W.; Shi, J.; Yu, X.; Liu, W., A naphthalocyanine based near-infrared photosensitizer: Synthesis and in vitro photodynamic activities. *Bioorganic & medicinal chemistry letters* **2013,** *23* (13), 3775-3779.

96. Omar, G. S.; Wilson, M.; Nair, S. P., Lethal photosensitization of wound-associated microbes using indocyanine green and near-infrared light. *BMC microbiology* **2008,** *8* (1), 111.
97. Chatterjee, D. K.; Yong, Z., Upconverting nanoparticles as nanotransducers for photodynamic therapy in cancer cells. **2008**.
98. Gargas, D. J.; Chan, E. M.; Ostrowski, A. D.; Aloni, S.; Altoe, M. V. P.; Barnard, E. S.; Sanii, B.; Urban, J. J.; Milliron, D. J.; Cohen, B. E., Engineering bright sub-10-nm upconverting nanocrystals for single-molecule imaging. *Nature nanotechnology* **2014,** *9* (4), 300-305.
99. Hong, G.; Lee, J. C.; Robinson, J. T.; Raaz, U.; Xie, L.; Huang, N. F.; Cooke, J. P.; Dai, H., Multifunctional in vivo vascular imaging using near-infrared II fluorescence. *Nature medicine* **2012,** *18* (12), 1841-1846.
100. Ramasamy, P.; Kim, J., Combined plasmonic and upconversion rear reflectors for efficient dye-sensitized solar cells. *Chemical Communications* **2014,** *50* (7), 879-881.
101. Lu, Y.; Zhao, J.; Zhang, R.; Liu, Y.; Liu, D.; Goldys, E. M.; Yang, X.; Xi, P.; Sunna, A.; Lu, J., Tunable lifetime multiplexing using luminescent nanocrystals. *Nature Photonics* **2014,** *8* (1), 32-36.
102. Wu, S.; Han, G.; Milliron, D. J.; Aloni, S.; Altoe, V.; Talapin, D. V.; Cohen, B. E.; Schuck, P. J., Non-blinking and photostable upconverted luminescence from single lanthanide-doped nanocrystals. *Proceedings of the National Academy of Sciences* **2009,** *106* (27), 10917-10921.
103. Konan, Y. N.; Gurny, R.; Allémann, E., State of the art in the delivery of photosensitizers for photodynamic therapy. *Journal of Photochemistry and Photobiology B: Biology* **2002,** *66* (2), 89-106.
104. Jalil, R. A.; Zhang, Y., Biocompatibility of silica coated NaYF 4 upconversion fluorescent nanocrystals. *Biomaterials* **2008,** *29* (30), 4122-4128.
105. Boyer, J.-C.; Manseau, M.-P.; Murray, J. I.; van Veggel, F. C., Surface modification of upconverting NaYF4 nanoparticles with PEG− phosphate ligands for NIR (800 nm) biolabeling within the biological window. *Langmuir* **2009,** *26* (2), 1157-1164.
106. Zhao, Z.; Han, Y.; Lin, C.; Hu, D.; Wang, F.; Chen, X.; Chen, Z.; Zheng, N., Multifunctional core–shell upconverting nanoparticles for imaging and photodynamic therapy of liver cancer cells. *Chemistry–An Asian Journal* **2012,** *7* (4), 830-837.
107. Dou, Q. Q.; Teng, C. P.; Ye, E.; Loh, X. J., Effective near-infrared photodynamic therapy assisted by upconversion nanoparticles conjugated with photosensitizers. *International journal of nanomedicine* **2015,** *10*, 419.
108. Han, S.; Hwang, B. W.; Jeon, E. Y.; Jung, D.; Lee, G. H.; Keum, D. H.; Kim, K. S.; Yun, S. H.; Cha, H. J.; Hahn, S. K., Upconversion Nanoparticles/Hyaluronate–Rose Bengal Conjugate Complex for Noninvasive Photochemical Tissue Bonding. *ACS nano* **2017,** *11* (10), 9979-9988.
109. Monopoli, M. P.; Åberg, C.; Salvati, A.; Dawson, K. A., Biomolecular coronas provide the biological identity of nanosized materials. *Nature nanotechnology* **2012,** *7* (12), 779-786.
110. Kratz, F., Albumin as a drug carrier: design of prodrugs, drug conjugates and nanoparticles. *Journal of controlled release* **2008,** *132* (3), 171-183.
111. Ke, P. C.; Lin, S.; Parak, W. J.; Davis, T. P.; Caruso, F., A Decade of the Protein Corona. *ACS nano* **2017,** *11* (12), 11773-11776.

112. Bogdan, N.; Vetrone, F.; Roy, R.; Capobianco, J. A., Carbohydrate-coated lanthanide-doped upconverting nanoparticles for lectin recognition. *Journal of Materials Chemistry* **2010,** *20* (35), 7543-7550.
113. Weber, C.; Coester, C.; Kreuter, J.; Langer, K., Desolvation process and surface characterisation of protein nanoparticles. *International journal of pharmaceutics* **2000,** *194* (1), 91-102.
114. Maibaum, L.; Dinner, A. R.; Chandler, D., Micelle formation and the hydrophobic effect. *The Journal of Physical Chemistry B* **2004,** *108* (21), 6778-6781.
115. Bergstrm, L.; Shinozaki, K.; Tomiyama, H.; Mizutani, N., Colloidal processing of a very fine BaTiO3 powder—effect of particle interactions on the suspension properties, consolidation, and sintering behavior. *Journal of the American Ceramic Society* **1997,** *80* (2), 291-300.
116. Majorek, K. A.; Porebski, P. J.; Dayal, A.; Zimmerman, M. D.; Jablonska, K.; Stewart, A. J.; Chruszcz, M.; Minor, W., Structural and immunologic characterization of bovine, horse, and rabbit serum albumins. *Molecular immunology* **2012,** *52* (3-4), 174-182.
117. Horrocks Jr, W. D.; Sudnick, D. R., Lanthanide ion probes of structure in biology. Laser-induced luminescence decay constants provide a direct measure of the number of metal-coordinated water molecules. *Journal of the American Chemical Society* **1979,** *101* (2), 334-340.
118. Wang, J.-H.; Wang, B.; Liu, Q.; Li, Q.; Huang, H.; Song, L.; Sun, T.-Y.; Wang, H.; Yu, X.-F.; Li, C., Bimodal optical diagnostics of oral cancer based on Rose Bengal conjugated gold nanorod platform. *Biomaterials* **2013,** *34* (17), 4274-4283.
119. Liu, K.; Liu, X.; Zeng, Q.; Zhang, Y.; Tu, L.; Liu, T.; Kong, X.; Wang, Y.; Cao, F.; Lambrechts, S. A., Covalently assembled NIR nanoplatform for simultaneous fluorescence imaging and photodynamic therapy of cancer cells. *ACS nano* **2012,** *6* (5), 4054-4062.
120. Conlon, K. A.; Berrios, M., Light-induced proteolysis of myosin heavy chain by Rose Bengal-conjugated antibody complexes. *Journal of Photochemistry and Photobiology B: Biology* **2001,** *65* (1), 22-28.
121. Habeeb, A. S. A., Determination of free amino groups in proteins by trinitrobenzenesulfonic acid. *Analytical biochemistry* **1966,** *14* (3), 328-336.
122. Georgakoudi, I.; Nichols, M. G.; Foster, T. H., The mechanism of Photofrin photobleaching and its consequences for photodynamic dosimetry. *Photochemistry and photobiology* **1997,** *65* (1), 135-144.
123. Fleischer, C. C.; Payne, C. K., Nanoparticle–cell interactions: molecular structure of the protein corona and cellular outcomes. *Accounts of chemical research* **2014,** *47* (8), 2651-2659.
124. Denizot, F.; Lang, R., Rapid colorimetric assay for cell growth and survival: modifications to the tetrazolium dye procedure giving improved sensitivity and reliability. *Journal of immunological methods* **1986,** *89* (2), 271-277.
125. Qin, J.; Kunda, N.; Qiao, G.; Calata, J. F.; Pardiwala, K.; Prabhakar, B. S.; Maker, A. V., Colon cancer cell treatment with rose bengal generates a protective immune response via immunogenic cell death. *Cell death & disease* **2017,** *8* (2), e2584.
126. D'Autréaux, B.; Toledano, M. B., ROS as signalling molecules: mechanisms that generate specificity in ROS homeostasis. *Nature reviews Molecular cell biology* **2007,** *8* (10), 813-824.

127. Dolmans, D. E.; Fukumura, D.; Jain, R. K., Photodynamic therapy for cancer. *Nature reviews cancer* **2003,** *3* (5), 380-387.
128. Berg, K.; Selbo, P. K.; Weyergang, A.; Dietze, A.; Prasmickaite, L.; Bonsted, A.; Engesaeter, B.; Angell-Petersen, E.; Warloe, T.; Frandsen, N., Porphyrin-related photosensitizers for cancer imaging and therapeutic applications. *Journal of microscopy* **2005,** *218* (2), 133-147.
129. Wainwright, M., Non-porphyrin photosensitizers in biomedicine. *Chemical Society Reviews* **1996,** *25* (5), 351-359.
130. Xu, F.; Li, H.; Yao, Q.; Ge, H.; Fan, J.; Sun, W.; Wang, J.; Peng, X., Hypoxia-activated NIR photosensitizer anchoring in the mitochondria for photodynamic therapy. *Chemical science* **2019,** *10* (45), 10586-10594.
131. Stolik, S.; Delgado, J.; Perez, A.; Anasagasti, L., Measurement of the penetration depths of red and near infrared light in human "ex vivo" tissues. *Journal of Photochemistry and Photobiology B: Biology* **2000,** *57* (2-3), 90-93.
132. Hong, G.; Antaris, A. L.; Dai, H., Near-infrared fluorophores for biomedical imaging. *Nature Biomedical Engineering* **2017,** *1* (1), 1-22.
133. Cheng, L.; Yang, K.; Shao, M.; Lee, S.-T.; Liu, Z., Multicolor in vivo imaging of upconversion nanoparticles with emissions tuned by luminescence resonance energy transfer. *The Journal of Physical Chemistry C* **2011,** *115* (6), 2686-2692.
134. áMichael Dcona, M.; Matthew, C., Near infrared light mediated release of doxorubicin using upconversion nanoparticles. *Chemical Communications* **2015,** *51* (40), 8477-8479.
135. Jalani, G.; Naccache, R.; Rosenzweig, D. H.; Haglund, L.; Vetrone, F.; Cerruti, M., Photocleavable hydrogel-coated upconverting nanoparticles: a multifunctional theranostic platform for NIR imaging and on-demand macromolecular delivery. *Journal of the American Chemical Society* **2016,** *138* (3), 1078-1083.
136. Gu, B.; Zhang, Q., Recent advances on functionalized upconversion nanoparticles for detection of small molecules and ions in biosystems. *Advanced Science* **2018,** *5* (3), 1700609.
137. Wu, X.; Zhang, Y.; Takle, K.; Bilsel, O.; Li, Z.; Lee, H.; Zhang, Z.; Li, D.; Fan, W.; Duan, C., Dye-sensitized core/active shell upconversion nanoparticles for optogenetics and bioimaging applications. *ACS nano* **2016,** *10* (1), 1060-1066.
138. Zhang, Y.; Zhang, W.; Zeng, K.; Ao, Y.; Wang, M.; Yu, Z.; Qi, F.; Yu, W.; Mao, H.; Tao, L., Upconversion Nanoparticles–Based Multiplex Protein Activation to Neuron Ablation for Locomotion Regulation. *Small* **2020,** *16* (8), 1906797.
139. Kettler, K.; Veltman, K.; van de Meent, D.; van Wezel, A.; Hendriks, A. J., Cellular uptake of nanoparticles as determined by particle properties, experimental conditions, and cell type. *Environmental toxicology and chemistry* **2014,** *33* (3), 481-492.
140. Ganguly, P.; Breen, A.; Pillai, S. C., Toxicity of nanomaterials: exposure, pathways, assessment, and recent advances. *ACS Biomaterials Science & Engineering* **2018,** *4* (7), 2237-2275.
141. Monopoli, M. P.; Åberg, C.; Salvati, A.; Dawson, K. A., Biomolecular coronas provide the biological identity of nanosized materials. *Nature nanotechnology* **2012,** *7* (12), 779.
142. Stehle, G.; Sinn, H.; Wunder, A.; Schrenk, H. H.; Stewart, J. C. M.; Hartung, G.; Maier-Borst, W.; Heene, D. L., Plasma protein (albumin) catabolism by the tumor itself—implications for tumor metabolism and the genesis of cachexia. *Critical reviews in oncology/hematology* **1997,** *26* (2), 77-100.

143. Podhajcer, O. L.; Benedetti, L.; Girotti, M. R.; Prada, F.; Salvatierra, E.; Llera, A. S., The role of the matricellular protein SPARC in the dynamic interaction between the tumor and the host. *Cancer and Metastasis Reviews* **2008,** *27* (3), 523-537.
144. Zhao, P.; Yin, W.; Wu, A.; Tang, Y.; Wang, J.; Pan, Z.; Lin, T.; Zhang, M.; Chen, B.; Duan, Y., Dual-Targeting to Cancer Cells and M2 Macrophages via Biomimetic Delivery of Mannosylated Albumin Nanoparticles for Drug-Resistant Cancer Therapy. *Advanced Functional Materials* **2017,** *27* (44), 1700403.
145. Gunnoo, S. B.; Madder, A., Chemical protein modification through cysteine. *ChemBioChem* **2016,** *17* (7), 529-553.
146. Kratz, F.; Warnecke, A.; Scheuermann, K.; Stockmar, C.; Schwab, J.; Lazar, P.; Drückes, P.; Esser, N.; Drevs, J.; Rognan, D., Probing the cysteine-34 position of endogenous serum albumin with thiol-binding doxorubicin derivatives. Improved efficacy of an acid-sensitive doxorubicin derivative with specific albumin-binding properties compared to that of the parent compound. *Journal of medicinal chemistry* **2002,** *45* (25), 5523-5533.
147. Liu, D.; Xu, X.; Du, Y.; Qin, X.; Zhang, Y.; Ma, C.; Wen, S.; Ren, W.; Goldys, E. M.; Piper, J. A., Three-dimensional controlled growth of monodisperse sub-50 nm heterogeneous nanocrystals. *Nature communications* **2016,** *7* (1), 1-8.
148. Chib, R.; Butler, S.; Raut, S.; Shah, S.; Borejdo, J.; Gryczynski, Z.; Gryczynski, I., Effect of quencher, denaturants, temperature and pH on the fluorescent properties of BSA protected gold nanoclusters. *Journal of luminescence* **2015,** *168*, 62-68.
149. Stiel, H.; Teuchner, K.; Paul, A.; Leupold, D.; Kochevar, I. E., Quantitative comparison of excited state properties and intensity-dependent photosensitization by rose bengal. *Journal of Photochemistry and Photobiology B: Biology* **1996,** *33* (3), 245-254.
150. Alarcón, E.; Edwards, A. M.; Aspée, A.; Borsarelli, C. D.; Lissi, E. A., Photophysics and photochemistry of rose bengal bound to human serum albumin. *Photochemical & Photobiological Sciences* **2009,** *8* (7), 933-943.
151. Entradas, T.; Waldron, S.; Volk, M., The detection sensitivity of commonly used singlet oxygen probes in aqueous environments. *Journal of Photochemistry and Photobiology B: Biology* **2020,** *204*, 111787.
152. Mayeda, E. A.; Bard, A. J., Production of singlet oxygen in electrogenerated radical ion electron transfer reactions. *Journal of the American Chemical Society* **1973,** *95* (19), 6223-6226.
153. Davies, M. J., Detection and characterisation of radicals using electron paramagnetic resonance (EPR) spin trapping and related methods. *Methods* **2016,** *109*, 21-30.
154. Nsubuga, A.; Mandl, G. A.; Capobianco, J. A., Investigating the reactive oxygen species production of Rose Bengal and Merocyanine 540-loaded radioluminescent nanoparticles. *Nanoscale Advances* **2021,** *3* (5), 1375-1381.
155. Zhu, W.; Dong, Z.; Fu, T.; Liu, J.; Chen, Q.; Li, Y.; Zhu, R.; Xu, L.; Liu, Z., Modulation of hypoxia in solid tumor microenvironment with MnO2 nanoparticles to enhance photodynamic therapy. *Advanced Functional Materials* **2016,** *26* (30), 5490-5498.
156. Davies, M. J., Singlet oxygen-mediated damage to proteins and its consequences. *Biochemical and biophysical research communications* **2003,** *305* (3), 761-770.
157. Noh, I.; Lee, D.; Kim, H.; Jeong, C. U.; Lee, Y.; Ahn, J. O.; Hyun, H.; Park, J. H.; Kim, Y. C., Enhanced photodynamic cancer treatment by mitochondria-targeting and brominated near-infrared fluorophores. *Advanced Science* **2018,** *5* (3), 1700481.

158. Merlot, A. M.; Kalinowski, D. S.; Richardson, D. R., Unraveling the mysteries of serum albumin—more than just a serum protein. *Frontiers in physiology* **2014,** *5*, 299.
159. Lin, T.; Zhao, P.; Jiang, Y.; Tang, Y.; Jin, H.; Pan, Z.; He, H.; Yang, V. C.; Huang, Y., Blood–brain-barrier-penetrating albumin nanoparticles for biomimetic drug delivery via albumin-binding protein pathways for antiglioma therapy. *Acs Nano* **2016,** *10* (11), 9999-10012.
160. Sabri, T.; Pawelek, P. D.; Capobianco, J. A., Dual activity of rose bengal functionalized to albumin-coated lanthanide-doped upconverting nanoparticles: targeting and photodynamic therapy. *ACS applied materials & interfaces* **2018,** *10* (32), 26947-26953.
161. Wen, S.; Zhou, J.; Zheng, K.; Bednarkiewicz, A.; Liu, X.; Jin, D., Advances in highly doped upconversion nanoparticles. *Nature communications* **2018,** *9* (1), 1-12.
162. Tessitore, G.; Maurizio, S. L.; Sabri, T.; Capobianco, J. A., Intrinsic Time-Tunable Emissions in Core–Shell Upconverting Nanoparticle Systems. *Angewandte Chemie* **2019,** *131* (29), 9844-9853.
163. Mai, H.-X.; Zhang, Y.-W.; Si, R.; Yan, Z.-G.; Sun, L.-d.; You, L.-P.; Yan, C.-H., High-quality sodium rare-earth fluoride nanocrystals: controlled synthesis and optical properties. *Journal of the American Chemical Society* **2006,** *128* (19), 6426-6436.
164. Smith, A. M.; Mancini, M. C.; Nie, S., Second window for in vivo imaging. *Nature nanotechnology* **2009,** *4* (11), 710-711.
165. Rafique, R.; Kailasa, S. K.; Park, T. J., Recent advances of upconversion nanoparticles in theranostics and bioimaging applications. *TrAC Trends in Analytical Chemistry* **2019,** *120*, 115646.
166. Fan, Y.; Zhang, F., A New Generation of NIR-II Probes: Lanthanide-Based Nanocrystals for Bioimaging and Biosensing. *Advanced Optical Materials* **2019,** *7* (7), 1801417.
167. Wang, C.; Cheng, L.; Liu, Z., Drug delivery with upconversion nanoparticles for multi-functional targeted cancer cell imaging and therapy. *Biomaterials* **2011,** *32* (4), 1110-1120.
168. Wu, J.; Seregard, S.; Spångberg, B.; Oskarsson, M.; Chen, E., Blue light induced apoptosis in rat retina. *Eye* **1999,** *13* (4), 577-583.
169. Geerdink, M.; Walbeek, T. J.; Beersma, D. G.; Hommes, V.; Gordijn, M. C., Short blue light pulses (30 min) in the morning support a sleep-advancing protocol in a home setting. *Journal of biological rhythms* **2016,** *31* (5), 483-497.
170. Yang, M.-Y.; Chang, C.-J.; Chen, L.-Y., Blue light induced reactive oxygen species from flavin mononucleotide and flavin adenine dinucleotide on lethality of HeLa cells. *Journal of Photochemistry and Photobiology B: Biology* **2017,** *173*, 325-332.
171. Liebmann, J.; Born, M.; Kolb-Bachofen, V., Blue-light irradiation regulates proliferation and differentiation in human skin cells. *Journal of Investigative Dermatology* **2010,** *130* (1), 259-269.
172. Shah, S.; Liu, J.-J.; Pasquale, N.; Lai, J.; McGowan, H.; Pang, Z. P.; Lee, K.-B., Hybrid upconversion nanomaterials for optogenetic neuronal control. *Nanoscale* **2015,** *7* (40), 16571-16577.
173. Arppe, R.; Hyppänen, I.; Perälä, N.; Peltomaa, R.; Kaiser, M.; Würth, C.; Christ, S.; Resch-Genger, U.; Schäferling, M.; Soukka, T., Quenching of the upconversion luminescence of NaYF 4: Yb 3+, Er 3+ and NaYF 4: Yb 3+, Tm 3+ nanophosphors by water: the role of the sensitizer Yb 3+ in non-radiative relaxation. *Nanoscale* **2015,** *7* (27), 11746-11757.

174. McNichols, R. J.; Gowda, A.; Kangasniemi, M.; Bankson, J. A.; Price, R. E.; Hazle, J. D., MR thermometry-based feedback control of laser interstitial thermal therapy at 980 nm. *Lasers in Surgery and Medicine: The Official Journal of the American Society for Laser Medicine and Surgery* **2004,** *34* (1), 48-55.
175. Wang, X.; Valiev, R. R.; Ohulchanskyy, T. Y.; Ågren, H.; Yang, C.; Chen, G., Dye-sensitized lanthanide-doped upconversion nanoparticles. *Chemical Society Reviews* **2017,** *46* (14), 4150-4167.
176. Chen, G.; Damasco, J.; Qiu, H.; Shao, W.; Ohulchanskyy, T. Y.; Valiev, R. R.; Wu, X.; Han, G.; Wang, Y.; Yang, C., Energy-cascaded upconversion in an organic dye-sensitized core/shell fluoride nanocrystal. *Nano letters* **2015,** *15* (11), 7400-7407.
177. Maurizio, S. L.; Tessitore, G.; Mandl, G. A.; Capobianco, J. A., Luminescence dynamics and enhancement of the UV and visible emissions of Tm 3+ in LiYF 4: Yb 3+, Tm 3+ upconverting nanoparticles. *Nanoscale Advances* **2019,** *1* (11), 4492-4500.
178. Xu, W.; Lee, T. K.; Moon, B. S.; Song, H.; Chen, X.; Chun, B.; Kim, Y. J.; Kwak, S. K.; Chen, P.; Kim, D. H., Broadband plasmonic antenna enhanced upconversion and its application in flexible fingerprint identification. *Advanced Optical Materials* **2018,** *6* (6), 1701119.
179. Zhang, H.; Li, Y.; Ivanov, I. A.; Qu, Y.; Huang, Y.; Duan, X., Plasmonic modulation of the upconversion fluorescence in NaYF4: Yb/Tm hexaplate nanocrystals using gold nanoparticles or nanoshells. *Angewandte Chemie International Edition* **2010,** *49* (16), 2865-2868.
180. Vetrone, F.; Naccache, R.; Mahalingam, V.; Morgan, C. G.; Capobianco, J. A., The active-core/active-shell approach: A strategy to enhance the upconversion luminescence in lanthanide-doped nanoparticles. *Advanced Functional Materials* **2009,** *19* (18), 2924-2929.
181. Wang, Z.; Meijerink, A., Concentration quenching in upconversion nanocrystals. *The Journal of Physical Chemistry C* **2018,** *122* (45), 26298-26306.
182. Johnson, N. J.; He, S.; Diao, S.; Chan, E. M.; Dai, H.; Almutairi, A., Direct evidence for coupled surface and concentration quenching dynamics in lanthanide-doped nanocrystals. *Journal of the American Chemical Society* **2017,** *139* (8), 3275-3282.
183. Fischer, S.; Bronstein, N. D.; Swabeck, J. K.; Chan, E. M.; Alivisatos, A. P., Precise tuning of surface quenching for luminescence enhancement in core–shell lanthanide-doped nanocrystals. *Nano letters* **2016,** *16* (11), 7241-7247.
184. Grzechnik, A.; Friese, K., Crystal structures and stability of NaLnF 4 (Ln= La, Ce, Pr, Nd, Sm and Gd) studied with synchrotron single-crystal and powder diffraction. *Dalton transactions* **2012,** *41* (34), 10258-10266.
185. Yu, D.-C.; Martin-Rodriguez, R.; Zhang, Q.-Y.; Meijerink, A.; Rabouw, F. T., Multi-photon quantum cutting in Gd 2 O 2 S: Tm 3+ to enhance the photo-response of solar cells. *Light: Science & Applications* **2015,** *4* (10), e344-e344.
186. Villanueva-Delgado, P.; Krämer, K. W.; Valiente, R.; de Jong, M.; Meijerink, A., Modeling blue to UV upconversion in β-NaYF 4: Tm 3+. *Physical Chemistry Chemical Physics* **2016,** *18* (39), 27396-27404.
187. Prorok, K.; Bednarkiewicz, A.; Stręk, W., Corrigendum to "Thulium concentration quenching in the up-converting α-Tm3+/Yb3+ NaYF4 colloidal nanocrystals"[Opt. Mater. 35 (5)(2013) 1124–1128]. *OPTICAL MATERIALS-AMSTERDAM-* **2013,** *35* (9), 1759-1759.

188. Braud, A.; Girard, S.; Doualan, J.; Thuau, M.; Moncorgé, R.; Tkachuk, A., Energy-transfer processes in Yb: Tm-doped KY 3 F 10, LiYF 4, and BaY 2 F 8 single crystals for laser operation at 1.5 and 2.3 μm. *Physical Review B* **2000,** *61* (8), 5280.
189. Himmelstoß, S. F.; Hirsch, T., Long-Term Colloidal and Chemical Stability in Aqueous Media of NaYF4-Type Upconversion Nanoparticles Modified by Ligand-Exchange. *Particle & Particle Systems Characterization* **2019,** *36* (10), 1900235.
190. Kostenich, G.; Zhuravkin, I.; Zhavrid, E., Experimental grounds for using chlorin ρ6 in the photodynamic therapy of malignant tumors. *Journal of Photochemistry and Photobiology B: Biology* **1994,** *22* (3), 211-217.
191. Paul, S.; Heng, P. W. S.; Chan, L. W., Optimization in solvent selection for chlorin e6 in photodynamic therapy. *Journal of fluorescence* **2013,** *23* (2), 283-291.
192. Wang, X. H.; Peng, H. S.; Yang, L.; You, F. T.; Teng, F.; Hou, L. L.; Wolfbeis, O. S., Targetable phosphorescent oxygen nanosensors for the assessment of tumor mitochondrial dysfunction by monitoring the respiratory activity. *Angewandte Chemie* **2014,** *126* (46), 12679-12683.
193. Guan, Y.; Lu, H.; Li, W.; Zheng, Y.; Jiang, Z.; Zou, J.; Gao, H., Near-infrared triggered upconversion polymeric nanoparticles based on aggregation-induced emission and mitochondria targeting for photodynamic cancer therapy. *ACS applied materials & interfaces* **2017,** *9* (32), 26731-26739.
194. Ledwitch, K.; Ogburn, R.; Cox, J.; Graham, R.; Fritzsche, A.; Gosnell, D.; Manning, T., Taxol: efficacy against oral squamous cell carcinoma. *Mini reviews in medicinal chemistry* **2013,** *13* (4), 509-521.
195. Kraft, M.; Würth, C.; Muhr, V.; Hirsch, T.; Resch-Genger, U., Particle-size-dependent upconversion luminescence of NaYF 4: Yb, Er nanoparticles in organic solvents and water at different excitation power densities. *Nano Research* **2018,** *11* (12), 6360-6374.
196. Zhang, C.; Yang, L.; Zhao, J.; Liu, B.; Han, M. Y.; Zhang, Z., White-light emission from an integrated upconversion nanostructure: toward multicolor displays modulated by laser power. *Angewandte Chemie* **2015,** *127* (39), 11693-11697.
197. Xue, X.; Thitsa, M.; Cheng, T.; Gao, W.; Deng, D.; Suzuki, T.; Ohishi, Y., Laser power density dependent energy transfer between Tm 3+ and Tb 3+: tunable upconversion emissions in NaYF 4: Tm 3+, Tb 3+, Yb 3+ microcrystals. *Optics express* **2016,** *24* (23), 26307-26321.
198. Liu, X.; Wang, Y.; Li, X.; Yi, Z.; Deng, R.; Liang, L.; Xie, X.; Loong, D. T.; Song, S.; Fan, D., Binary temporal upconversion codes of Mn 2+-activated nanoparticles for multilevel anti-counterfeiting. *Nature communications* **2017,** *8* (1), 1-7.
199. Deng, R.; Qin, F.; Chen, R.; Huang, W.; Hong, M.; Liu, X., Temporal full-colour tuning through non-steady-state upconversion. *Nature nanotechnology* **2015,** *10* (3), 237-242.
200. Wang, F.; Liu, X., Upconversion multicolor fine-tuning: visible to near-infrared emission from lanthanide-doped NaYF4 nanoparticles. *Journal of the American Chemical Society* **2008,** *130* (17), 5642-5643.
201. Teng, X.; Zhu, Y.; Wei, W.; Wang, S.; Huang, J.; Naccache, R.; Hu, W.; Tok, A. I. Y.; Han, Y.; Zhang, Q., Lanthanide-doped Na x ScF3+ x nanocrystals: crystal structure evolution and multicolor tuning. *Journal of the American Chemical Society* **2012,** *134* (20), 8340-8343.

202. Passuello, T.; Piccinelli, F.; Pedroni, M.; Bettinelli, M.; Mangiarini, F.; Naccache, R.; Vetrone, F.; Capobianco, J.; Speghini, A., White light upconversion of nanocrystalline Er/Tm/Yb doped tetragonal Gd4O3F6. *Optical Materials* **2011,** *33* (4), 643-646.
203. Zhou, L.; Fan, Y.; Wang, R.; Li, X.; Fan, L.; Zhang, F., High-capacity upconversion wavelength and lifetime binary encoding for multiplexed biodetection. *Angewandte Chemie* **2018,** *130* (39), 13006-13011.
204. Shin, J.; Kyhm, J.-H.; Hong, A.-R.; Song, J. D.; Lee, K.; Ko, H.; Jang, H. S., Multicolor tunable upconversion luminescence from sensitized seed-mediated grown LiGdF4: Yb, Tm-based core/triple-shell nanophosphors for transparent displays. *Chemistry of Materials* **2018,** *30* (23), 8457-8464.
205. Liu, Y.; Tu, D.; Zhu, H.; Li, R.; Luo, W.; Chen, X., A strategy to achieve efficient dual-mode luminescence of Eu3+ in lanthanides doped multifunctional NaGdF4 nanocrystals. *Advanced Materials* **2010,** *22* (30), 3266-3271.
206. Wegh, R.; Van Loef, E.; Meijerink, A., Visible quantum cutting via downconversion in LiGdF4: Er3+, Tb3+ upon Er3+ 4f11→ 4f105d excitation. *Journal of luminescence* **2000,** *90* (3-4), 111-122.
207. Lorbeer, C.; Cybinska, J.; Mudring, A.-V., Reaching quantum yields≫ 100% in nanomaterials. *Journal of Materials Chemistry C* **2014,** *2* (10), 1862-1868.
208. Lorbeer, C.; Mudring, A.-V., Quantum cutting in nanoparticles producing two green photons. *Chemical Communications* **2014,** *50* (87), 13282-13284.
209. Wegh, R.; Donker, H.; Oskam, K.; Meijerink, A., Visible quantum cutting in Eu3+-doped gadolinium fluorides via downconversion. *Journal of Luminescence* **1999,** *82* (2), 93-104.
210. Van Pieterson, L.; Reid, M.; Wegh, R.; Soverna, S.; Meijerink, A., 4 f n→ 4 f n− 1 5 d transitions of the light lanthanides: Experiment and theory. *Physical Review B* **2002,** *65* (4), 045113.
211. Wegh, R. T.; Donker, H.; Oskam, K. D.; Meijerink, A., Visible quantum cutting in LiGdF4: Eu3+ through downconversion. *Science* **1999,** *283* (5402), 663-666.
212. Ogiegło, J.; Zych, A.; Jüstel, T.; Meijerink, A.; Ronda, C., Luminescence and energy transfer in Lu3Al5O12 scintillators co-doped with Ce3+ and Pr3+. *Optical materials* **2013,** *35* (3), 322-331.
213. Jüstel, T.; Nikol, H.; Ronda, C., New developments in the field of luminescent materials for lighting and displays. *Angewandte Chemie International Edition* **1998,** *37* (22), 3084-3103.
214. Zhou, X.; Qiao, J.; Zhao, Y.; Han, K.; Xia, Z., Multi-responsive deep-ultraviolet emission in praseodymium-doped phosphors for microbial sterilization. *Science China Materials* **2021**, 1-9.
215. Ibarra-Ruiz, A. M.; Rodríguez Burbano, D. C.; Capobianco, J. A., Photoluminescent nanoplatforms in biomedical applications. *Advances in Physics: X* **2016,** *1* (2), 194-225.
216. Liu, X.; Yan, C.-H.; Capobianco, J. A., Photon upconversion nanomaterials. *Chemical Society Reviews* **2015,** *44* (6), 1299-1301.
217. Chen, S.; Weitemier, A. Z.; Zeng, X.; He, L.; Wang, X.; Tao, Y.; Huang, A. J.; Hashimotodani, Y.; Kano, M.; Iwasaki, H., Near-infrared deep brain stimulation via upconversion nanoparticle–mediated optogenetics. *Science* **2018,** *359* (6376), 679-684.
218. Rojas-Gutierrez, P. A.; Bhuckory, S.; Mingoes, C.; Hildebrandt, N.; DeWolf, C.; Capobianco, J. A., A route to triggered delivery via photocontrol of lipid bilayer properties using lanthanide upconversion nanoparticles. *ACS Applied Nano Materials* **2018,** *1* (9), 5345-5354.

219. Mandl, G. A.; Rojas-Gutierrez, P. A.; Capobianco, J. A., A NIR-responsive azobenzene-based supramolecular hydrogel using upconverting nanoparticles. *Chemical Communications* **2018,** *54* (46), 5847-5850.
220. Zuo, J.; Sun, D.; Tu, L.; Wu, Y.; Cao, Y.; Xue, B.; Zhang, Y.; Chang, Y.; Liu, X.; Kong, X., Precisely tailoring upconversion dynamics via energy migration in core–shell nanostructures. *Angewandte Chemie* **2018,** *130* (12), 3108-3112.
221. Su, Q.; Han, S.; Xie, X.; Zhu, H.; Chen, H.; Chen, C.-K.; Liu, R.-S.; Chen, X.; Wang, F.; Liu, X., The effect of surface coating on energy migration-mediated upconversion. *Journal of the American Chemical Society* **2012,** *134* (51), 20849-20857.
222. Ledoux, G.; Amans, D.; Joubert, M.-F.; Mahler, B.; Mishra, S.; Daniele, S.; Dujardin, C., Modeling energy migration for upconversion materials. *The Journal of Physical Chemistry C* **2018,** *122* (1), 888-893.
223. Tessitore, G.; Mudring, A.-V.; Krämer, K. W., Room temperature synthesis of β-NaGdF4: RE3+ (RE= Eu, Er) nanocrystallites and their luminescence. *Journal of luminescence* **2017,** *189*, 91-98.
224. Tessitore, G.; Mudring, A.-V.; Krämer, K. W., Luminescence and energy transfer in β-NaGdF 4: Eu 3+, Er 3+ nanocrystalline samples from a room temperature synthesis. *New journal of chemistry* **2018,** *42* (1), 237-245.
225. Salley, G.; Valiente, R.; Güdel, H., Cooperative Yb 3+− Tb 3+ dimer excitations and upconversion in Cs 3 Tb 2 Br 9: Yb 3+. *Physical Review B* **2003,** *67* (13), 134111.
226. Prorok, K.; Bednarkiewicz, A.; Cichy, B.; Gnach, A.; Misiak, M.; Sobczyk, M.; Strek, W., The impact of shell host (NaYF 4/CaF 2) and shell deposition methods on the up-conversion enhancement in Tb 3+, Yb 3+ codoped colloidal α-NaYF 4 core–shell nanoparticles. *Nanoscale* **2014,** *6* (3), 1855-1864.
227. Qin, W.-P.; Liu, Z.-Y.; Sin, C.-N.; Wu, C.-F.; Qin, G.-S.; Chen, Z.; Zheng, K.-Z., Multi-ion cooperative processes in Yb 3+ clusters. *Light: Science & Applications* **2014,** *3* (8), e193-e193.
228. Xiao, W.; Wu, D.; Zhang, L.; Zhang, X.; Hao, Z.; Pan, G.-H.; Zhao, H.; Zhang, L.; Zhang, J., Cooperative upconversion luminescence properties of Yb3+ and Tb3+ heavily codoped silicate garnet obtained by multiple chemical unit cosubstitution. *The Journal of Physical Chemistry C* **2017,** *121* (5), 2998-3006.
229. Würth, C.; Kaiser, M.; Wilhelm, S.; Grauel, B.; Hirsch, T.; Resch-Genger, U., Excitation power dependent population pathways and absolute quantum yields of upconversion nanoparticles in different solvents. *Nanoscale* **2017,** *9* (12), 4283-4294.
230. Li, C.; Lin, J., Rare earth fluoride nano-/microcrystals: synthesis, surface modification and application. *Journal of Materials Chemistry* **2010,** *20* (33), 6831-6847.
231. Rabouw, F. T.; Prins, P. T.; Villanueva-Delgado, P.; Castelijns, M.; Geitenbeek, R. G.; Meijerink, A., Quenching pathways in NaYF4: Er3+, Yb3+ upconversion nanocrystals. *Acs nano* **2018,** *12* (5), 4812-4823.
232. Dong, C.; Pichaandi, J.; Regier, T.; van Veggel, F. C., Nonstatistical dopant distribution of Ln3+-doped NaGdF4 nanoparticles. *The Journal of Physical Chemistry C* **2011,** *115* (32), 15950-15958.
233. Aebischer, A.; Hostettler, M.; Hauser, J.; Krämer, K.; Weber, T.; Güdel, H. U.; Bürgi, H. B., Structural and Spectroscopic Characterization of Active Sites in a Family of Light-Emitting Sodium Lanthanide Tetrafluorides. *Angewandte Chemie International Edition* **2006,** *45* (17), 2802-2806.

234. Villanueva-Delgado, P.; Krämer, K. W.; Valiente, R., Simulating energy transfer and upconversion in β-NaYF4: Yb3+, Tm3+. *The Journal of Physical Chemistry C* **2015,** *119* (41), 23648-23657.
235. Krämer, K. W.; Biner, D.; Frei, G.; Güdel, H. U.; Hehlen, M. P.; Lüthi, S. R., Hexagonal sodium yttrium fluoride based green and blue emitting upconversion phosphors. *Chemistry of materials* **2004,** *16* (7), 1244-1251.
236. Suyver, J.; Aebischer, A.; Biner, D.; Gerner, P.; Grimm, J.; Heer, S.; Krämer, K.; Reinhard, C.; Güdel, H.-U., Novel materials doped with trivalent lanthanides and transition metal ions showing near-infrared to visible photon upconversion. *Optical Materials* **2005,** *27* (6), 1111-1130.
237. Auzel, F., Upconversion processes in coupled ion systems. *Journal of Luminescence* **1990,** *45* (1-6), 341-345.
238. Cao, B.; Wu, J.; Feng, Z.; Dong, B., Investigation of near-infrared-to-ultraviolet upconversion luminescence of Tm3+ doped NaYF4 phosphors by Yb3+ codoping. *Materials Chemistry and Physics* **2013,** *142* (1), 333-338.
239. Főrster, T., 10th Spiers Memorial Lecture. Transfer mechanisms of electronic excitation. *Discussions of the Faraday Society* **1959,** *27*, 7-17.
240. Zhang, H.; Jia, T.; Shang, X.; Zhang, S.; Sun, Z.; Qiu, J., Mechanisms of the blue emission of NaYF 4: Tm 3+ nanoparticles excited by an 800 nm continuous wave laser. *Physical Chemistry Chemical Physics* **2016,** *18* (37), 25905-25914.
241. Gamelin, D. R.; Gudel, H. U., Upconversion processes in transition metal and rare earth metal systems. *Transition metal and rare earth compounds* **2001**, 1-56.
242. Liu, H.; Huang, K.; Valiev, R. R.; Zhan, Q.; Zhang, Y.; Ågren, H., Photon upconversion kinetic nanosystems and their optical response. *Laser & Photonics Reviews* **2018,** *12* (1), 1700144.
243. Adrian, R. J., Particle-imaging techniques for experimental fluid mechanics. *Annual review of fluid mechanics* **1991,** *23* (1), 261-304.
244. Wright, S. F.; Zadrazil, I.; Markides, C. N., A review of solid–fluid selection options for optical-based measurements in single-phase liquid, two-phase liquid–liquid and multiphase solid–liquid flows. *Experiments in Fluids* **2017,** *58* (9), 1-39.
245. Kunst, B. H.; Schots, A.; Visser, A. J., Detection of flowing fluorescent particles in a microcapillary using fluorescence correlation spectroscopy. *Analytical chemistry* **2002,** *74* (20), 5350-5357.
246. Brites, C. D.; Xie, X.; Debasu, M. L.; Qin, X.; Chen, R.; Huang, W.; Rocha, J.; Liu, X.; Carlos, L. D., Instantaneous ballistic velocity of suspended Brownian nanocrystals measured by upconversion nanothermometry. *Nature nanotechnology* **2016,** *11* (10), 851-856.
247. Huang, H.; Huang, F.; Lin, L.; Feng, Z.; Cheng, Y.; Wang, Y.; Chen, D., Perceiving linear-velocity by multiphoton upconversion. *ACS applied materials & interfaces* **2019,** *11* (49), 46379-46385.
248. Wereley, S. T.; Meinhart, C. D., Recent advances in micro-particle image velocimetry. *Annual review of fluid mechanics* **2010,** *42*, 557-576.
249. Hinsch, K. D., Three-dimensional particle velocimetry. *Measurement Science and Technology* **1995,** *6* (6), 742.
250. Grant, I., Particle image velocimetry: a review. *Proceedings of the Institution of Mechanical Engineers, Part C: Journal of Mechanical Engineering Science* **1997,** *211* (1), 55-76.

251. Fond, B.; Abram, C.; Beyrau, F., On the characterisation of tracer particles for thermographic particle image velocimetry. *Applied Physics B* **2015,** *118* (3), 393-399.
252. Pedocchi, F.; Martin, J. E.; García, M. H., Inexpensive fluorescent particles for large-scale experiments using particle image velocimetry. *Experiments in Fluids* **2008,** *45* (1), 183-186.
253. Koochesfahani, M.; Cohn, R.; Gendrich, C.; Nocera, D., Molecular tagging diagnostics for the study of kinematics and mixing in liquid phase flows. In *Developments in Laser Techniques and Fluid Mechanics*, Springer: 1997; pp 125-144.
254. Gendrich, C.; Koochesfahani, M.; Nocera, D., Molecular tagging velocimetry and other novel applications of a new phosphorescent supramolecule. *Experiments in fluids* **1997,** *23* (5), 361-372.
255. Doron, P.; Barnea, D., Flow pattern maps for solid-liquid flow in pipes. *International journal of multiphase flow* **1996,** *22* (2), 273-283.
256. Kolin, A., Demonstration of parabolic velocity distribution in laminar flow. *American Journal of Physics* **1953,** *21* (8), 619-620.
257. Shi, Y.; Xiong, S.; Chin, L. K.; Zhang, J.; Ser, W.; Wu, J.; Chen, T.; Yang, Z.; Hao, Y.; Liedberg, B., Nanometer-precision linear sorting with synchronized optofluidic dual barriers. *Science advances* **2018,** *4* (1), eaao0773.
258. Ahmed, M.; Eslamian, M., Numerical simulation of natural convection of a nanofluid in an inclined heated enclosure using two-phase lattice Boltzmann method: accurate effects of thermophoresis and Brownian forces. *Nanoscale research letters* **2015,** *10* (1), 1-12.
259. Aminfar, H.; Motallebzadeh, R., Investigation of the velocity field and nanoparticle concentration distribution of nanofluid using Lagrangian-Eulerian approach. *Journal of dispersion science and technology* **2012,** *33* (1), 155-163.
260. Tessitore, G.; Mandl, G. A.; Brik, M. G.; Park, W.; Capobianco, J. A., Recent insights into upconverting nanoparticles: spectroscopy, modeling, and routes to improved luminescence. *Nanoscale* **2019,** *11* (25), 12015-12029.
261. Jiang, H.; Weng, X.; Li, D., Dual-wavelength fluorescent detection of particles on a novel microfluidic chip. *Lab on a Chip* **2013,** *13* (5), 843-850.
262. Wang, F.; Han, Y.; Lim, C. S.; Lu, Y.; Wang, J.; Xu, J.; Chen, H.; Zhang, C.; Hong, M.; Liu, X., Simultaneous phase and size control of upconversion nanocrystals through lanthanide doping. *nature* **2010,** *463* (7284), 1061-1065.
263. Riley, R. S.; Day, E. S., Gold nanoparticle-mediated photothermal therapy: applications and opportunities for multimodal cancer treatment. *Wiley Interdisciplinary Reviews: Nanomedicine and Nanobiotechnology* **2017,** *9* (4), e1449.
264. Dubreil, L.; Leroux, I.; Ledevin, M.; Schleder, C.; Lagalice, L.; Lovo, C.; Fleurisson, R.; Passemard, S.; Kilin, V.; Gerber-Lemaire, S., Multi-harmonic imaging in the second near-infrared window of nanoparticle-labeled stem cells as a monitoring tool in tissue depth. *ACS nano* **2017,** *11* (7), 6672-6681.
265. Ramos-Gomes, F.; Möbius, W.; Bonacina, L.; Alves, F.; Markus, M. A., Bismuth ferrite second harmonic nanoparticles for pulmonary macrophage tracking. *Small* **2019,** *15* (4), 1803776.
266. Debarre, D.; Pena, A.-M.; Supatto, W.; Boulesteix, T.; Strupler, M.; Sauviat, M.-P.; Martin, J.-L.; Schanne-Klein, M.-C.; Beaurepaire, E., Second-and third-harmonic generation microscopies for the structural imaging of intact tissues. *Medecine Sciences: M/S* **2006,** *22* (10), 845-850.

267. Riporto, J.; Urbain, M.; Mugnier, Y.; Multian, V.; Riporto, F.; Bredillet, K.; Beauquis, S.; Galez, C.; Monnier, V.; Chevolot, Y., Second harmonic spectroscopy of ZnO, BiFeO 3 and LiNbO 3 nanocrystals. *Optical Materials Express* **2019,** *9* (4), 1955-1966.
268. Urban, B. E.; Neogi, P. B.; Butler, S. J.; Fujita, Y.; Neogi, A., Second harmonic imaging of plants tissues and cell implosion using two-photon process in ZnO nanoparticles. *Journal of biophotonics* **2012,** *5* (3), 283-291.
269. Voss, T.; Kudyk, I.; Wischmeier, L.; Gutowski, J., Nonlinear optics with ZnO nanowires. *physica status solidi (b)* **2009,** *246* (2), 311-314.
270. Vogel, A.; Noack, J.; Hüttman, G.; Paltauf, G., Mechanisms of femtosecond laser nanosurgery of cells and tissues. *Applied Physics B* **2005,** *81* (8), 1015-1047.
271. Nagy, B.; Gallais, L.; Vámos, L.; Oszetzky, D.; Rácz, P.; Dombi, P., Direct comparison of kilohertz-and megahertz-repetition-rate femtosecond damage threshold. *Optics letters* **2015,** *40* (11), 2525-2528.
272. Kumar, A.; Rai, R. C.; Podraza, N. J.; Denev, S.; Ramirez, M.; Chu, Y.-H.; Martin, L. W.; Ihlefeld, J.; Heeg, T.; Schubert, J., Linear and nonlinear optical properties of Bi Fe O 3. *Applied Physics Letters* **2008,** *92* (12), 121915.
273. Lin, J.; Fujita, Y.; Neogi, A., Saturation of two photon emission in ZnO nanoparticles with second order nonlinearity. *RSC Advances* **2015,** *5* (15), 10921-10926.
274. Soram, B. S.; Ngangom, B. S.; Sharma, H., Effect of annealing temperatures on the structural and optical properties of sol–gel processed nanocrystalline BiFeO3 thin films. *Thin Solid Films* **2012,** *524*, 57-61.
275. Boyd, R. W., 1.2 Descriptions of Nonlinear Optical Processes. In *Nonlinear Optics (3rd Edition)*, Elsevier.
276. Rojac, T.; Bencan, A.; Malic, B.; Tutuncu, G.; Jones, J. L.; Daniels, J. E.; Damjanovic, D., BiFeO 3 ceramics: processing, electrical, and electromechanical properties. *Journal of the American Ceramic Society* **2014,** *97* (7), 1993-2011.
277. Kirsch, A.; Murshed, M. M.; Litterst, F. J.; Gesing, T. M., Structural, spectroscopic, and thermoanalytic studies on Bi2Fe4O9: tunable properties driven by nano-and poly-crystalline states. *The Journal of Physical Chemistry C* **2019,** *123* (5), 3161-3171.
278. Ichimura, N.; Kondo, H.; Harada, Y.; Hashimoto, S., Formation of high density color centers and laser ablation in alkali halide crystals. *Journal of luminescence* **2000,** *87*, 586-588.
279. Gaudiuso, C.; Giannuzzi, G.; Volpe, A.; Lugarà, P. M.; Choquet, I.; Ancona, A., Incubation during laser ablation with bursts of femtosecond pulses with picosecond delays. *Optics express* **2018,** *26* (4), 3801-3813.
280. Vetrone, F.; Naccache, R.; Zamarrón, A.; Juarranz de la Fuente, A.; Sanz-Rodríguez, F.; Martinez Maestro, L.; Martin Rodriguez, E.; Jaque, D.; Garcia Sole, J.; Capobianco, J. A., Temperature sensing using fluorescent nanothermometers. *ACS nano* **2010,** *4* (6), 3254-3258.
281. Quintanilla, M.; Zhang, Y.; Liz-Marzán, L. M., Subtissue plasmonic heating monitored with CaF2: Nd3+, Y3+ nanothermometers in the second biological window. *Chemistry of Materials* **2018,** *30* (8), 2819-2828.
282. Schwung, S.; Rogov, A.; Clarke, G.; Joulaud, C.; Magouroux, T.; Staedler, D.; Passemard, S.; Jüstel, T.; Badie, L.; Galez, C., Nonlinear optical and magnetic properties of BiFeO3 harmonic nanoparticles. *Journal of Applied Physics* **2014,** *116* (11), 114306.

283. Balabhadra, S.; Debasu, M. L.; Brites, C. D.; Ferreira, R. A.; Carlos, L. D., Upconverting nanoparticles working as primary thermometers in different media. *The Journal of Physical Chemistry C* **2017,** *121* (25), 13962-13968.
284. Quintanilla, M.; García, I.; de Lázaro, I.; García-Alvarez, R.; Henriksen-Lacey, M.; Vranic, S.; Kostarelos, K.; Liz-Marzán, L. M., Thermal monitoring during photothermia: hybrid probes for simultaneous plasmonic heating and near-infrared optical nanothermometry. *Theranostics* **2019,** *9* (24), 7298.
285. König, K.; Becker, T.; Fischer, P.; Riemann, I.; Halbhuber, K.-J., Pulse-length dependence of cellular response to intense near-infrared laser pulses in multiphoton microscopes. *Optics letters* **1999,** *24* (2), 113-115.
286. Supatto, W.; Débarre, D.; Farge, E.; Beaurepaire, E., Femtosecond pulse-induced microprocessing of live Drosophila embryos. *Medical Laser Application* **2005,** *20* (3), 207-216.
287. Orzekowsky-Schroeder, R. B.; Martensen, B.; Vogel, A.; Hüttmann, G.; Klinger, A.; Blessenohl, M.; Gebert, A., In vivo spectral imaging of different cell types in the small intestine by two-photon excited autofluorescence. *Journal of biomedical optics* **2011,** *16* (11), 116025.
288. Kuetemeyer, K.; Rezgui, R.; Lubatschowski, H.; Heisterkamp, A., Influence of laser parameters and staining on femtosecond laser-based intracellular nanosurgery. *Biomedical optics express* **2010,** *1* (2), 587-597.
289. Qin, Z.; Sun, Q.; Lin, Y.; He, S.; Li, X.; Chen, C.; Wu, W.; Luo, Y.; Qu, J. Y., New fluorescent compounds produced by femtosecond laser surgery in biological tissues: the mechanisms. *Biomedical optics express* **2018,** *9* (7), 3373-3390.
290. Sun, Q.; Qin, Z.; Wu, W.; Lin, Y.; Chen, C.; He, S.; Li, X.; Wu, Z.; Luo, Y.; Qu, J. Y., In vivo imaging-guided microsurgery based on femtosecond laser produced new fluorescent compounds in biological tissues. *Biomedical optics express* **2018,** *9* (2), 581-590.
291. Hovhannisyan, V.; Lo, W.; Hu, C.; Chen, S.-J.; Dong, C. Y., Dynamics of femtosecond laser photo-modification of collagen fibers. *Optics express* **2008,** *16* (11), 7958-7968.
292. Liang, X.-X.; Zhang, Z.; Vogel, A., Multi-rate-equation modeling of the energy spectrum of laser-induced conduction band electrons in water. *Optics express* **2019,** *27* (4), 4672-4693.
293. Lee, H.; Alt, C.; Pitsillides, C. M.; Lin, C. P., Optical detection of intracellular cavitation during selective laser targeting of the retinal pigment epithelium: dependence of cell death mechanism on pulse duration. *Journal of biomedical optics* **2007,** *12* (6), 064034.
294. Simanovskii, D.; Mackanos, M.; Irani, A.; O'Connell-Rodwell, C.; Contag, C.; Schwettman, H.; Palanker, D., Cellular tolerance to pulsed hyperthermia. *Physical Review E* **2006,** *74* (1), 011915.
295. Abadeer, N. S.; Murphy, C. J., Recent progress in cancer thermal therapy using gold nanoparticles. *The Journal of Physical Chemistry C* **2016,** *120* (9), 4691-4716.
296. Sordillo, L. A.; Pu, Y.; Pratavieira, S.; Budansky, Y.; Alfano, R. R., Deep optical imaging of tissue using the second and third near-infrared spectral windows. *Journal of biomedical optics* **2014,** *19* (5), 056004.
297. Harmsen, S.; Teraphongphom, N.; Tweedle, M. F.; Basilion, J. P.; Rosenthal, E. L., Optical surgical navigation for precision in tumor resections. *Molecular imaging and biology* **2017,** *19* (3), 357-362.

298. Lukic, A.; Dochow, S.; Bae, H.; Matz, G.; Latka, I.; Messerschmidt, B.; Schmitt, M.; Popp, J., Endoscopic fiber probe for nonlinear spectroscopic imaging. *Optica* **2017,** *4* (5), 496-501.
299. Kostiv, U.; Janoušková, O.; Šlouf, M.; Kotov, N.; Engstová, H.; Smolková, K.; Ježek, P.; Horák, D., Silica-modified monodisperse hexagonal lanthanide nanocrystals: synthesis and biological properties. *Nanoscale* **2015,** *7* (43), 18096-18104.
300. Ocampo, S. M.; Rodriguez, V.; de La Cueva, L.; Salas, G.; Carrascosa, J. L.; Rodríguez, M. J.; García-Romero, N.; Cuñado, J. L. F.; Camarero, J.; Miranda, R., g-force induced giant efficiency of nanoparticles internalization into living cells. *Scientific reports* **2015,** *5* (1), 1-9.